Weak gravitational lensing as a probe of large-scale structure and galaxy formation

Malin Nicole Renneby

München 2019

Weak gravitational lensing as a probe of large-scale structure and galaxy formation

Malin Nicole Renneby

Dissertation
an der Fakultät für Physik
der Ludwig-Maximilians-Universität
München

vorgelegt von
Malin Nicole Renneby
aus Göteborg

München, den 23 Januar 2019

"By Endurance We Conquer."
– Family motto of Sir Ernest Shackleton, Irish polar explorer 1874-1922.

Erstgutachter: Prof. Dr. Andreas Burkert
Zweitgutachter: Prof. Dr. Volker Springel
Tag der mündlichen Prüfung: 1 März 2019

Contents

List of Figures

List of Tables

Zusammenfassung

Die Untersuchung der Beziehung zwischen Galaxien und der umgebenden Halos aus dunkler Materie ist ein fundamentaler Bestandteil für das Verständnis der Entwicklung der großräumigen Struktur des Universums. In dieser Arbeit untersuchen wir, wie der Galaxie-Galaxie-Gravitationslinseneffekt, die Verzerrung der Bilder von Hintergrundgalaxien nahe ausgewählter Galaxien im Vordergrund, beim Verständnis des Zusammenhangs zwischen sichtbarer und dunkler Materie helfen kann. Einerseits erlaubt der Gravitationslinseneffekt eine direkte Abschätzung der Masse innerhalb eines gegebenen Radius für verschiedene nach ihren Eigenschaften (z.B. Sternenmasse oder Farbe) ausgewählte Galaxien. Andererseits beschreibt die Galaxien-Galaxien-Häufung die räumliche Verteilung von Galaxien und erlaubt, in Verbindung mit der Korrelation der Galaxien und der sie beherbegenden Halos, kosmologische Parameter zu bestimmen.

Diese Dissertation ist in drei Teile gegliedert, in der sich jeder Teil mit je einer von drei offenen Problemen des Galaxie-Galaxie-Gravitationslinseneffekts beschäftigt, um sich als konkurrenzfähige Methode zur Bestimmung kosmologischer Parameter für derzeitige und zukünftige großskalige Himmelsdurchmusterungen zu behaupten. In Kapitel 3 (Renneby et al., 2018) untersuchen wir wie ein kosmologischer Reskalierungsalgorithmus, welcher schnell und kosteneffizient Partikel- und Haloverteilungen einer kosmologischen Mehrkörpersimulation in eine andere Simulation mit anderen kosmologischen Parametern überführt, angepasst werden kann, um präzise Massenprofile durch den Galaxie-Galaxie Gravitationslinseneffekt hervorzusagen und etwaige verursachte Fehler abzuschätzen. Das darauffolgende Kapitel 4 (Renneby et al., prepa) befasst sich mit Vorhersagen für semi-analytische Modelle der Galaxieentstehung (SAMs) und hydrodynamische Simulatione. In Kapitel 5 (Renneby et al., prepb) werden schliesslich die wichtigsten systematischen Einflüsse für die Masseprofile durch den Galaxie-Galaxie Gravitationslinseneffekt, baryonische Prozesse, mithilfe einer Vielzahl hydrodynamischer Simulationen untersucht.

Die wichtigsten Ergebnisse sind: In Kapitel 3 erbringen wir den Nachweis, dass eine kosmologische Mehrkörpersimulation mit gegebenen kosmologischen Parametern (Ω_m, σ_8) verwendet werden kann, um Masseprofile zentraler Galaxien ohne Beschränkung der gewählten Hintergrundkosmologie durch zwei Biasparameter für die Halokonzentration Δc und der Positionen der Halo-Brandungsradien Δr_sp nachzubilden. Diese beiden Parameter können gut durch die Konzentration-Masse-Rotverschiebung-Relationen, die in Ludlow et al. (2016) präsentiert werden, und der Brandungsradius-Masse-Rotverschiebung-Relationen, die in Diemer et al. (2017) präsentiert werden, vorausgesagt werden.

Weiterhin zeigen wir, dass die Beobachtungen der räumichen Galaxienkorrelation und des Gravitationslinseneffekts in Kapitel 4 ein einheitliches Bild für Rückwirkungsmodelle liefern. Die Ergebnisse für die hydrodynamischen IllustrisTNG Simulationen stimmen dabei mit den derzeitigen Messungen der KiDS+GAMA-Himmelsdurchmusterungen, wie auch für eine

Auswahl von Galaxien in SDSS, sowohl lokal hellster Galaxien (LBGs) und solcher, die nur nach ihrer stellaren Masse ausgewählten wurden, überein. Beobachtungen des Gravitationslinseneffekts um LBG und der Galaxienkorrelation liefern in Verbindung mit dem Münchner SAM L-Galaxies Modell implizieren eine schwächere Radiomodus-AGN-Rückwirkung und eine geringere dynamische Reibungszeitskala für Galaxieverschmelzungen gegenüber dem neusten Model von Henriques et al. (2015). Dieser Vergleich zeigt gleichzeitig die Probleme der beiden Modellierungssystemen auf, z.B. für das Signal durch rote Galaxien mittlerer Masse unter $10^{11}\,M_{\odot}$, für welche Beobachtungen niedrigere Massen der beherbergenden Halos sternentstehungsgeminderter Galaxien nahelegen. Dies zeigt die Notwendigkeit für verbesserte umgebungsabhängige Mechanismen für Sternentstehungsminderung und Verschmelzung in Galaxiengruppen und Galaxienhaufen auf.

In Übereinstimmung mit der Literatur (z.B. Leauthaud et al., 2017) finden wir, dass baryonische Effekte zu einer Reduzierung der Masseprofile um 10-20 Prozent im Bereich $0.1 < r\,[h^{-1}\,\mathrm{Mpc}] < 1$ führt. Weiterhin zeigen wir, dass dieses Verhalten auf eine Vielzahl von Galaxien verschiedener stellarer Masse zutrifft, sowie für zentrale Galaxien in Galaxiegruppen. Trotz verschiedener Beschreibungen der Galaxieentstehung erzeugen die Eagle und IllustrisTNG Simulationen ähnliche Profile des schwachen Gravitationslinseneffekts, die konsistent mit den beobachteten sind. Der erhebliche Gasausstoß durch die Implementierung der AGN-Rückwirkung in den Illustris Simulation führen zu einer Reduktion der Massenprofile bis zu einem extremen Radius von $r \sim 5 - 6\,h^{-1}\,\mathrm{Mpc}$, wohingegen dieser bei den Nachfolgersimulationen IllustrisTNG etwa $r \sim 1 - 2\,h^{-1}\,\mathrm{Mpc}$ betrug. Diese Radien sind grösstenteils unabhängig von der stellaren Masse der gewählten Galaxieklasse. Jedoch existiert eine etwas größerer Effekt für Halos von Galaxiegruppen, in welchen die AGN-Rückwirkung am effizientesten ist und nur eine geringe zeitliche Entwicklung bis zu einer Rotverschiebung von $z = 1$ eintritt. Wir versuchen diesen Effekt mithilfe des baryonischen Korrekturmodells von Schneider & Teyssier (2015) und der IllustrisTNG300 Simulation für Halos von Galaxiegruppen und Galaxiehaufen zu parametrisieren. Wir stellen fest, dass das Modell die wichtigsten Deformationscharakteristika abbildet, jedoch sind weitergehende Arbeiten notwendig um die Massenprofile in rein gravitativen Simulationen zu korrigieren.

Abstract

The study of the relation between galaxies and their surrounding haloes of dark matter is a fundamental component to understand the evolution of the large-scale structure of the Universe. In this thesis, we investigate how galaxy-galaxy lensing, the distortion of the shapes of background galaxies around selected foreground lens galaxies, can help to elucidate this interplay together with complementary galaxy clustering measurements. Galaxy-galaxy lensing, on one hand, provides a direct estimate of the mass inside a given aperture and also its distribution, which allows for connecting certain classes of galaxies, chosen according to properties such as stellar mass and colour, to the mass and shape of the encompassing dark host structures. Galaxy clustering, on the other hand, describes the spatial distribution of galaxies and the combination of the two probes can be used to jointly constrain the cosmological parameters for the matter fraction Ω_m and the amplitude of the matter fluctuations σ_8.

This thesis is split into three parts addressing three outstanding challenges each for small-scale galaxy-galaxy lensing to act as a competitive probe for current and future large-scale structure surveys. In Chapter 3 (Renneby et al., 2018), we investigate how a cosmological rescaling algorithm, which fast and cost-efficiently maps particle and halo distributions from one N-body simulation to another one with a different set of cosmological parameters, can be adapted to accurately predict galaxy-galaxy lensing profiles and quantify the induced errors. The subsequent Chapter 4 (Renneby et al., prepa) deals with verifying that both lensing and clustering probes yield consistent predictions in semi-analytical models of galaxy formation (SAMs) and hydrodynamical simulations. To conclude in Chapter 5 (Renneby et al., prepb), we examine the main systematic effect on lensing profiles, namely the imprint of baryonic processes, using a range of hydrodynamical simulations.

The major findings are the following: In Chapter 3 we establish that an N-body simulation with a set of parameters (Ω_m, σ_8) can be used to emulate the lensing profiles for central galaxies with no further restriction in a different background cosmology with two principal biases in halo concentrations Δc and the positions of the halo splashback radii Δr_sp. These biases can be predicted well with the concentration-mass-redshift relations presented in Ludlow et al. (2016) and the splashback radius-mass-redshift relations from Diemer et al. (2017).

To continue, we discover that lensing and clustering observations in Chapter 4 point towards a consistent picture for the feedback prescriptions. The hydrodynamical IllustrisTNG simulation suite is in agreement with current constraints from the KiDS+GAMA surveys for stellar mass only selected samples as well as locally brightest galaxies (LBGs) in SDSS. For the Munich SAM L-Galaxies, constraints from LBG lensing and general clustering demand a weaker radio-mode AGN feedback and shorter dynamical friction merger time than the default setup in the latest model from Henriques et al. (2015). Still, this comparison also highlights difficulties in the two modelling frameworks to accurately predict the signal for

intermediate mass red galaxies below $< 10^{11}\,M_{\odot}$, where the observations suggest lower host halo masses for quenched satellite galaxies. This calls for improved environmental quenching and merging mechanisms in galaxy groups and clusters.

Finally, we retrieve a similar baryonic imprint as previously established in the literature for specific lens samples (e.g. Leauthaud et al., 2017) with suppressions of $10 - 20\,\%$ for $0.1 < r\,[h^{-1}\,\mathrm{Mpc}] < 1$ and show that it is generalisable to a large range of stellar masses and for central galaxies in groups. Despite their different galaxy formation recipes, the Eagle and IllustrisTNG simulations produce similar lensing profile descriptions consistent with observations. The considerable gas ejection of the AGN feedback implementation in the Illustris simulation puts it at the extreme end in terms of the extent of the suppression up to $r \sim 5 - 6\,h^{-1}\,\mathrm{Mpc}$ whereas its successor IllustrisTNG achieves mass convergence at $r \sim 1 - 2\,h^{-1}\,\mathrm{Mpc}$. These radii are largely independent of the stellar mass of the samples, with a slightly larger impact for group class haloes where the AGN feedback is most efficient, and there is little redshift evolution to $z = 1$. We attempt to parameterise the effect using the baryonic correction model of Schneider & Teyssier (2015) for group and cluster-size haloes in the TNG300 simulation. We find that the model captures the main deformation features but that further work is required for it to properly adjust the gravity-only mass profiles.

Keywords: gravitational lensing: weak – galaxies: evolution – galaxies: haloes – cosmology: theory – methods: numerical

Chapter 1 Introduction

1.1 Prologue

At the smallest nodes of the cosmic web, galaxies sit as luminous beacons tracing the encompassing structures of dark matter. Their immediate matter field overdensity surroundings are known as dark matter haloes which are on average ellipsoidal in shape and co-evolve with the galaxies across time. Investigating this rich relation with statistical 1-pt, 2-pt and higher order correlations can help us to understand galaxy formation as well as constraining cosmological parameters governing the overall growth of structure and matter and energy content of the Universe. However, at these small scales, linear perturbation theory breaks down and thus numerical and empirical tools must be used in the modelling of the relationship between different galaxy and host halo properties, such as stellar mass or star formation rate with respect to halo mass and shape. This thesis focuses on how gravitational weak lensing, with a special emphasis on the subcategory of galaxy-galaxy lensing (GGL), the bending of light rays due to spacetime perturbations by objects along the line-of-sight, can act as a suitable probe capturing the "dark-luminous" cross-correlations of the cosmic web together with complementary measurements of the clustering of galaxies, the "luminous-luminous" correlations. Jointly, these two probes can constrain the cosmological parameters governing the matter fraction $\Omega_{\rm m}$ and the amplitude of the matter fluctuations σ_8. For this joint parameter combination, there is currently a small tension between early Universe (cosmic microwave background) and late Universe probes (weak lensing) for the standard ΛCDM cosmological model, which might signify new fundamental physics. This stresses the urgent need for a better theoretical understanding of the signal; especially in the small-scale regime which offers the best signal-to-noise ratios.

The thesis follows a theoretical approach where numerical predictions are compared to measurements from observational surveys. Three main areas are covered: (i) how a rescaling algorithm can map the lensing signal produced by different $N-$body simulations of cold dark matter using different cosmological parameters to one-another in Chapter 3, (ii) how lensing and clustering working in tandem can rule out certain models of galaxy formation based on the implementation of feedback processes in Chapter 4, and (iii) how galactic baryons modify the signal in hydrodynamical simulations and how to deform the signal in dark matter only runs to compensate for this effect in Chapter 5. We list the main numerical simulations used in this work and the concepts behind them in Chapter 2.

In this Chapter, we introduce the basic phenomenology of cosmic structure formation focusing on haloes and galaxies respectively and the statistical probes used to examine it. In addition, the Chapter serves to put the results of this thesis into a more general perspective. We start by reviewing the standard cosmological model (Section 1.2.1) and then move on to correlation functions (Section 1.2.2) and the large-scale structure (Section 1.2.3). Then we

detail the basic steps of halo formation (Section 1.2.4), describe the most used halo profiles (Section 1.2.5) and express the process in the excursion set framework as well as provide an interpretation of the cosmological rescaling algorithm studied in this thesis in the same language (Section 1.2.6). Consecutively we introduce the two main observables in this thesis; weak gravitational lensing (Section 1.3) (and specifically GGL in Section 1.3.1) and galaxy clustering (Section 1.4). We proceed by highlighting their cosmological constraining power (Section 1.5) and how they can inform on the galaxy-halo connection (Section 1.6). To conclude, we give a brief overview of the feedback process which impedes star formation at the massive end (Section 1.7).

1.2 Statistical properties of cosmic structure formation

In the framework of general relativity (Einstein, 1915), the presence of matter induces gravitational perturbations through the field equations

$$G_{\mu\nu} = 8\pi G/c^4 T_{\mu\nu}, \tag{1.2.1}$$

where $G_{\mu\nu}$ is the Einstein tensor (curvature), G the gravitational constant, c the speed of light and $T_{\mu\nu}$ the stress-energy tensor (matter-energy).

1.2.1 Background solution - geometry and dynamics

In this thesis we investigate if the standard cosmological model together with state-of-the art recipes to populate the resulting structures with galaxies can produce realistic weak lensing and galaxy clustering observations. This Section details its main ingredients and is based on Baumann (2018); Weinberg (2008); Padmanabhan (2010); Mo et al. (2010) and extensive details can be found in most standard textbooks on cosmology. For the spacetime geometry, the background solution for a homogeneous, isotropic, expanding Universe has the Friedmann-Robertson-Lemaître-Walker (FLRW) metric to define distances

$$\mathrm{d}s^2 \overset{\mathrm{def}}{=} g_{\mu\nu}\mathrm{d}X^\mu \mathrm{d}X^\nu = -c^2\mathrm{d}t^2 + a(t)^2\gamma_{ij}\mathrm{d}x^i\mathrm{d}x^j, \tag{1.2.2}$$

where $\mathrm{d}s^2$ is the invariant line element, $g_{\mu\nu}$ the metric, $X^\mu = (t, x^i)$ with t as the time coordinate and x^i the comoving spatial coordinates, γ_{ij} the spatial metric and $a(t)$ the scale factor. Physical coordinates are given as $x^i_{\mathrm{phys}} = a(t)x^i$ and we define the Hubble parameter H as the normalised time derivative $H = \dot{a}/a$. We can split the spatial line element $\mathrm{d}l^2 = \gamma_{ij}\mathrm{d}x^i\mathrm{d}x^j$ into a radial and an angular component $\mathrm{d}l^2 = \mathrm{d}\chi^2 + f_K^2(\chi)\mathrm{d}\omega^2$ where χ is the comoving radial distance and $f_K(\chi)$ the comoving angular-diameter distance

$$f_K(\chi) = \begin{cases} K^{-1/2}\sin(K^{1/2}\chi), & K > 0 \text{ (spherical)} \\ \chi, & K = 0 \text{ (flat)} \\ (-K)^{-1/2}\sinh\left[(-K)^{1/2}\chi\right], & K < 0 \text{ (hyperbolical)} \end{cases} \tag{1.2.3}$$

for different spatial curvature K. Photons travel along geodesics. Their 4-momentum P^μ satisfies

$$P^\alpha \frac{\mathrm{d}P^\mu}{\mathrm{d}X^\alpha} = -\Gamma^\mu_{\alpha\beta}P^\alpha P^\beta, \tag{1.2.4}$$

where $\Gamma^{\mu}_{\alpha\beta}$ are the Christoffel symbols

$$\Gamma^{\mu}_{\alpha\beta} \stackrel{\text{def}}{=} \frac{1}{2} g^{\mu\nu} \left(\partial_\alpha g_{\beta\nu} + \partial_\beta g_{\alpha\nu} - \partial_\nu g_{\alpha\beta} \right). \tag{1.2.5}$$

Homogeneity implies that $\partial_i P^\mu$ vanishes in Eq. (1.2.4) for a photon on a radial trajectory which leaves the zero:th component. Since the energy $E \stackrel{\text{def}}{=} P^0$, the $\mu = 0$ part tells us that

$$E \frac{\mathrm{d}E}{\mathrm{d}t} = -\frac{\dot{a}}{a} p^2, \;\; p^2 = a^2(t) \gamma_{ij} P^i P^j, \tag{1.2.6}$$

and with the four-component of the momentum satisfying $E^2 - p^2 = m^2$, where m is the mass of the particle, $p \sim a^{-1}$ both for massive and massless particles. The wavelength of light λ in a quantum mechanical description is inversely proportional to the momentum $\lambda = h/p$ with h as Planck's constant. As the momentum decays as a^{-1}, λ scales as a leading to a redshift z of the wave,

$$z \stackrel{\text{def}}{=} \frac{\lambda_0 - \lambda_1}{\lambda_1}, \tag{1.2.7}$$

with λ_1 as the original wavelength emitted at time t_1 and λ_0 the wavelength observed at time t_0. Setting $a(t_0) = 1$ yields

$$z + 1 = \frac{1}{a(t_1)}. \tag{1.2.8}$$

For sources nearby we can expand the denominator $a(t_1) \approx a(t_0)[1 + H_0(t_1 - t_0) + \ldots]$. $H_0 \stackrel{\text{def}}{=} \dot{a}(t_0)/a(t_0)$ is the Hubble constant which is measured in units of $H_0 \stackrel{\text{def}}{=} 100\, h\, \mathrm{kms}^{-1}\mathrm{Mpc}^{-1}$ with $h \approx 0.68$ from cosmic microwave background (CMB) temperature and lensing data from the Planck satellite (Planck Collaboration, 2016a, 2018). We will henceforth use h for the Hubble constant throughout this thesis. There is still some tension in the value of the Hubble constant between these early-time measurements and observations using late-time Cepheid[1] calibrated supernovae Type Ia distance ladders and strong gravitational lensing time delays (Riess et al., 2016; Bonvin et al., 2017), which some authors claim to be of the order of $3.8\,\sigma$ (Riess et al., 2018). This motivates some flexibility in the modelling scheme and new probes such as multi-messenger gravitational waves observations could provide tighter constraints in the future (Abbott et al., 2017b).

We can now give an expression for the comoving distance χ in Eq. (1.2.3) between us and an astronomical object at z

$$\chi = \int_{t_1}^{t_0} \frac{\mathrm{d}t'}{a(t')} = \int_0^z \frac{\mathrm{d}z'}{H(z')}. \tag{1.2.9}$$

Hubble-Lemaître's law gives that galaxies move with 3-velocity $v = H_0 d$ as a part of the Hubble flow with d as the proper distance. Inside groups and clusters, the velocities can deviate from this base value from peculiar velocities v_{pec}, causing a Doppler shift which can be translated as a shift in redshift z_{pec}

$$1 + z_{\mathrm{pec}} = \sqrt{\frac{1 + v_{\mathrm{pec}}/c}{1 - v_{\mathrm{pec}}/c}}, \tag{1.2.10}$$

and the observed redshift z_{obs} is then

$$1 + z_{\mathrm{obs}} = (1 + z_{\mathrm{pec}})\,(1 + z_H)\,, \tag{1.2.11}$$

[1] A class of variable stars.

with z_H as the cosmological redshift.

Homogeneity and isotropy constrain the elements of the stress-energy tensor $T_{\mu\nu}$. Isotropy dictates that the mean value of any 3-vector should vanish, i.e. that $T_{i0} = T_{0j} = 0$, and isotropy around a point $\boldsymbol{x} = 0$ forces the mean value of any 3-tensor T_{ij} to be proportional to δ_{ij} and the 3-metric $g_{ij} = a(t)^2\delta_{ij}$ at $\boldsymbol{x} = 0$ where δ_{ij} is the Kronecker delta. Since this is a proportionality between two 3-tensors it must remain invariant under arbitrary spatial coordinate transformations. Homogeneity in turn demands that the proportionality constant can only be a function of time. Thus, the stress-energy tensor takes the form of a perfect fluid with respect to an observer with relative 4-velocity[2] U^μ,

$$T^\mu{}_\nu = g^{\mu\alpha}T_{\alpha\nu} = -\left(\rho(t) + \frac{P(t)}{c^2}\right)U^\mu U_\nu + P(t)\delta^\mu{}_\nu, \tag{1.2.12}$$

where ρ is the density and P the pressure in the rest-frame of the fluid. The conservation equation $\nabla_\mu T^\mu{}_\nu = 0$ gives for the energy density at index $\nu = 0$, that

$$\dot{\rho} + 3\frac{\dot{a}}{a}\left(\rho + \frac{P}{c^2}\right) = 0, \tag{1.2.13}$$

which can easily be solved with an equation-of-state $P = P(\rho) = wc^2\rho$ with a solution $\rho \propto a^{-3-3w}$. This implies that the cold matter density for which $|P| \ll \rho$, i.e. $w = P = 0$, evolves as $\rho \propto a^{-3}$. This applies to baryonic (ordinary) matter and *cold dark matter* (CDM). This latter type of matter interacts only gravitationally and we can infer its existence from gravitational lensing (e.g. Brainerd et al., 1996; Bacon et al., 2000), baryonic acoustic oscillations (e.g. Eisenstein et al., 2005), the CMB (e.g. Hinshaw et al., 2013; Planck Collaboration, 2016a) and galactic rotation curves (e.g Rubin et al., 1980). The solution $w = 1/3$ applies for relativistic matter, i.e. photons and neutrinos at early times and those energy densities decay as $\rho \propto a^{-4}$. This thesis focus on the late time Universe where those terms are less important and we neglect the impact of massive neutrinos. One can also construct a solution for $w = 1$, i.e. with negative pressure $P = -c^2\rho$, which gives a constant density, a cosmological constant[3] Λ. This term is known as *dark energy* and was first observationally inferred from supernovae type Ia measurements where the luminosities at $z \approx 0.5$ were fainter than allowed in a matter-dominated Universe, but instead this suggested a flat Universe with an accelerated expansion (Riess et al., 1998; Perlmutter et al., 1999). Solving Eq. (1.2.1) with Eq. (1.2.12) at this background level yields the Friedmann equations:

$$H^2 = \frac{8\pi G}{3}\rho - \frac{cK}{a^2}, \tag{1.2.14}$$

$$\frac{\ddot{a}}{a} = -\frac{4\pi G}{3}(\rho + 3P). \tag{1.2.15}$$

We can define a critical density $\rho_{\rm crit}(t)$ and density parameter $\Omega(t)$ as

$$\rho_{\rm crit}(t) \stackrel{\rm def}{=} \frac{3H^2(t)}{8\pi G}, \quad \Omega(t) \stackrel{\rm def}{=} \frac{\rho}{\rho_{\rm crit}}, \tag{1.2.16}$$

[2]The 4-velocity for a locally comoving observer in the inertial Cartesian frame is simply $U^\mu = (1, 0, 0, 0)$.

[3]This term can also be added to the righthand side of the field equations Eq. (1.2.1) as $-\Lambda g_{\mu\nu}$ which does not alter the conservation equation since $\nabla^\mu g_{\mu\nu} = 0$. Modifying the righthand side of the field equations is standard in modified gravity. In this thesis we only deal with standard ΛCDM cosmologies.

which allows us to rewrite the first Friedmann equation at $t = 0$ as

$$H^2 = H_0^2 \left(\Omega_{\mathrm{m}} a^{-3} + \Omega_{\mathrm{r}} a^{-4} + \Omega_K a^{-2} + \Omega_\Lambda \right), \tag{1.2.17}$$

for the different energy density components with $\Omega_K \overset{\mathrm{def}}{=} -Kc/(H_0^2)$. From the CMB temperature, polarisation, lensing and additional baryonic acoustic oscillation data it has been established that $|\Omega_K| \approx 0$ (Planck Collaboration, 2016a), specifically from the position of the first peak in the angular CMB power spectra telling us that the geometry of the Universe is flat. The matter fraction can be separated into the two components $\Omega_{\mathrm{m}} = \Omega_{\mathrm{b}} + \Omega_{\mathrm{cdm}}$ where the total matter density and the baryonic matter density can be inferred from the peaks in the CMB power spectra (Planck Collaboration, 2016a).

The different scalings of the different density components implies that they were the dominant components of the Universe at certain epochs (radiation, matter and dark energy). As we are treating the late-time Universe we are primarily interested in the two latter eras.

This summarises the current cosmological standard model, flat ΛCDM, i.e. the solution for a spatially flat Universe governed by the Einstein field equations with an FLRW metric with a stress-energy tensor for ordinary matter, radiation and a so-far unknown cold dark matter component and a cosmological constant of unknown origin.

1.2.2 Correlation functions

In this Section we provide the mathematical foundations of the statistical treatment of structure formation, i.e. how we extract information about the cosmic web. In later Sections we relate these expressions to lensing and clustering correlation functions. This introduction is primarily based on the following references Lim (2012); Baldauf (2018); Bartelmann & Schneider (2001).

Consider a scalar field $\phi(\boldsymbol{x})$, $\phi : \mathcal{U} \subseteq \mathbb{R}^d \to \mathcal{M}$, $\boldsymbol{x} \mapsto \phi(\boldsymbol{x})$. The space $\mathcal{M}$ is either $\mathbb{R}$ or $\mathbb{C}$ here. Assume that there exists a suitable measure on the ensemble of field configurations $\{\phi\}$ and that they obey a functional probability distribution $P[\phi(\boldsymbol{x})]$. We define the expectation value to obtain the functional of a specific field configuration $\phi(\boldsymbol{x})$, $\mathcal{F}[\phi(\boldsymbol{x})]$, as

$$\langle \mathcal{F}[\phi(\boldsymbol{x})] \rangle \overset{\mathrm{def}}{=} \int \mathcal{F}[\phi(\boldsymbol{x})] \, P[\phi(\boldsymbol{x})] \, \mathcal{D}\phi \,, \tag{1.2.18}$$

where the integral is performed over the set of all possible field configurations. Here, functionals of certain interest are *$n-$point correlation functions*, which can be expressed as $\langle \phi(\boldsymbol{x}_0)\phi(\boldsymbol{x}_1) \ldots \phi(\boldsymbol{x}_n) \rangle$. If the mapping ϕ is to $\mathbb{C}$, it may be convenient to reformulate the expression by complex-conjugating some of the field configuration terms. Moreover, we are interested in the case where ϕ is a random field. A *random field* is a generalisation of a stochastic process, which given a parameter set T is a collection of random variables $\phi(t)$ with $t \in T$, in the sense that the underlying parameter space can consist of $n-$dimensional vectors where T is of dimension d, i.e. each element of $\{\phi\}$ is a realisation of the random field. A subset of interest of these fields are the *homogeneous* random fields. Such fields are defined over the whole of $\mathbb{R}^d$ whose mean functions are constant and whose covariances only depend on the distance $\boldsymbol{x} - \boldsymbol{x}'$, i.e. the field $\phi(\boldsymbol{x})$ is statistically indistinguishable from $\phi(\boldsymbol{x} + \boldsymbol{x}')$, i.e. translational invariant. If the covariances only depend on the Euclidean distance $|\boldsymbol{x} - \boldsymbol{x}'|$, these are known as *isotropic*. Should the random field satisfy the latter criteria in the absence of stationarity, one would name this property *rotational invariance*. We can write the

two-point correlation function for a homogeneous random field as

$$\langle \phi^*(\boldsymbol{x}_i)\phi(\boldsymbol{x}_j)\rangle = \xi_{\phi^*{}_i\phi_j}\left(\boldsymbol{x}_i - \boldsymbol{x}_j\right), \tag{1.2.19}$$

with $\xi_\phi(\boldsymbol{x}) \stackrel{\text{def}}{=} \langle\phi(\boldsymbol{x})\phi(0)\rangle$ valid for $\phi : \mathbb{R}^d \to \mathbb{C}^n$, $\boldsymbol{x} \mapsto \phi(\boldsymbol{x})$. If the field is isotropic as well, the righthand side simplifies to $\xi_{\phi^*{}_i\phi_j}(|\boldsymbol{x}_i - \boldsymbol{x}_j|)$. We can compute the Fourier transform of this correlation function with the definition $f : \mathbb{R}^d \to \mathcal{M}$ with $\mathcal{M} = \mathbb{R}$ or $\mathbb{C}$ as

$$f(\boldsymbol{k}) \stackrel{\text{def}}{=} \int f(\boldsymbol{x})\, \mathrm{e}^{-\mathrm{i}\boldsymbol{k}\cdot\boldsymbol{x}}\, \mathrm{d}^d\boldsymbol{x}, \quad f(\boldsymbol{x}) \stackrel{\text{def}}{=} \frac{1}{(2\pi)^d}\int f(\boldsymbol{k})\, \mathrm{e}^{\mathrm{i}\boldsymbol{k}\cdot\boldsymbol{x}}\, \mathrm{d}^d\boldsymbol{k}, \tag{1.2.20}$$

leading to

$$\begin{aligned}\langle \phi^*(\boldsymbol{k}_i)\phi(\boldsymbol{k}_j)\rangle &= \int \mathrm{e}^{\mathrm{i}\boldsymbol{k}_i\cdot\boldsymbol{x}_i}\left(\int \mathrm{e}^{-\mathrm{i}\boldsymbol{k}_j\cdot\boldsymbol{x}_j}\,\langle\phi^*(\boldsymbol{x}_i)\phi(\boldsymbol{x}_j)\rangle\,\mathrm{d}^d\boldsymbol{x}_j\right)\mathrm{d}^d\boldsymbol{x}_i \\ &= \int \mathrm{e}^{-\mathrm{i}(\boldsymbol{k}_j-\boldsymbol{k}_i)\cdot\boldsymbol{x}_i}\hat{\xi}_{\phi^*{}_i\phi_j}(\boldsymbol{k}_j)\,\mathrm{d}^d\boldsymbol{x}_i = (2\pi)^d\delta^d\left(\boldsymbol{k}_j - \boldsymbol{k}_i\right)\hat{\xi}_{\phi^*{}_i\phi_j}(\boldsymbol{k}_j),\end{aligned} \tag{1.2.21}$$

with $\delta^d(\boldsymbol{k}_j - \boldsymbol{k}_i)$ as the d-dimensional Dirac delta function and $\hat{\xi}_{\phi^*{}_i\phi_j}(\boldsymbol{k}) \stackrel{\text{def}}{=} P(\boldsymbol{k})$ as the power spectrum.

In an astrophysical and cosmological context, the two-point function for matter density fluctuations with $\rho = \bar{\rho} + \delta\rho = \bar{\rho}(1+\delta)$ can be defined according to

$$\begin{aligned}\langle\rho(\boldsymbol{x}_i)\,\rho(\boldsymbol{x}_j)\rangle = \bar{\rho}^2\,\langle(1+\delta(\boldsymbol{x}_i))\,(1+\delta(\boldsymbol{x}_j))\rangle = \bar{\rho}^2\,(1+\langle\delta(\boldsymbol{x}_i)\,\delta(\boldsymbol{x}_j)\rangle) = \\ \bar{\rho}^2\left(1+\xi_{\delta_i\delta_j}(\boldsymbol{x}_i - \boldsymbol{x}_j)\right),\end{aligned} \tag{1.2.22}$$

where we have used that the mean of the density fluctuations, $\langle\delta(\boldsymbol{x})\rangle$, is zero.

In the early Universe, as viewed from the surface of the CMB (Planck Collaboration, 2016b), the statistical properties of the matter field could be well described by a homogeneous and rotational invariant Gaussian random field, i.e. that any linear combinations of the random field is Gaussian and that the joint probability distribution is a multivariate Gaussian for a number of linear combinations of the random variables. Around the mean of zero, the Gaussian probability density function is even under parity which means that all odd n-point correlation functions vanish and it is possible to use Wick's theorem to rewrite all even n-point correlation functions in terms of the sum of all possible two-point correlation functions, meaning that the Gaussian random field is fully characterisable by its power spectrum. In this thesis we work in a late-time epoch where the assumption of Gaussianity for the matter field is no longer valid, but we will still use two-point correlation functions as main characterisers.

An ansatz for the linear power spectrum of matter density fluctuations is

$$P(k,\, z=0) = T^2(k)Ak^{n_\mathrm{s}}, \tag{1.2.23}$$

assuming the primordial power spectrum can be captured by an amplitude A and spectral tilt n_s. Inflationary models predict a value of n_s close to 1 (e.g. Mukhanov & Chibisov, 1981), i.e. that the power spectrum is nearly scale-invariant. For the rescaling algorithm in this thesis, we study a subset of cosmologies with scale-invariant linear power spectra but nothing per se restricts the algorithm to such configurations. We will measure the power spectrum amplitude in terms of the parameter σ_8 explained in Section 1.2.6. $T(k)$ is known as the transfer function which defines a map between the evolution of the density contrast at

scale k compared to the superhorizon case at an arbitrary large scale $k = 0$ (e.g. Eisenstein & Hu, 1998). In the radiation dominated era, subhorizon[4] perturbations were frozen and superhorizon perturbations grew as $\delta \propto a^2$, until they entered the horizon due to the expansion of the Universe, leading to a difference in growth as a function of scale k encapsulated in $T(k)$.

We have to introduce a few additional tools before we can generalise these results to the statistical observables of a cosmological survey. Firstly, we are working on finite domains where homogeneity and isotropy are not directly applicable. The latter symmetry can be approximately satisfied on scales smaller than the domain size and if we restrict the consideration to fields with periodic boundary conditions, one can obtain translation invariance. Secondly, in a cosmological survey we measure correlations between the projected fields and not the full 3D information. These two quantities can be related to one another through the *Limber approximation* (Limber, 1953). For an isotropic and homogeneous random field with two-point correlation function $\xi_{ij}\left(|\boldsymbol{r}_i - \boldsymbol{r}_j|\right)$ with $\boldsymbol{r} = (\boldsymbol{x}, \chi)$ where χ is the coordinate along the line-of-sight projection this approximation reads

$$\int\int G(\chi_1, \chi_2)\xi_{ij}\left(|\boldsymbol{r}_i - \boldsymbol{r}_j|\right)\,\mathrm{d}\chi_1\,\mathrm{d}\chi_2 \approx \int\int G(\chi_1, \chi_2)\xi_{ij}\left(|\boldsymbol{x}_i - \boldsymbol{x}_j|\right)\delta^d(\chi_i - \chi_j)\,\mathrm{d}\chi_1\,\mathrm{d}\chi_2\,, \tag{1.2.24}$$

with

$$\xi_{ij}\left(x\right) = \int \xi_{ij}\left(\sqrt{x^2 + \chi^2}\right)\,\mathrm{d}\chi\,. \tag{1.2.25}$$

This approximation is valid if the function $G(\chi_1, \chi_2)$ only varies weakly with χ_1 and χ_2 on scales where the correlation has dominant contributions which is the case in this thesis. We will primarily explore projected cross-correlations between the matter and the galaxy fields (gravitational lensing) and auto-correlations of the galaxy field (galaxy clustering).

1.2.3 Perturbations and the Zel'dovich approximation

Having introduced the mathematical toolset to describe structure formation, we now proceed by discussing the evolution of matter density perturbations and how they yield the large-scale structure of the Universe. Broadly, this Section draws heavily from the following books and reviews: Dodelson (2003); Mo et al. (2010); Kilbinger (2015).

We can introduce first-order scalar perturbations to the FLRW metric induced by matter perturbations. In the Newtonian gauge, the perturbations can be expressed using solely the diagonal elements of the metric. The line element then takes the form

$$\mathrm{d}s^2 = -\left(1 + \frac{2\Psi}{c^2}\right)c^2\mathrm{d}t^2 + a^2(t)\left(1 - \frac{2\Phi}{c^2}\right)\mathrm{d}l^2, \tag{1.2.26}$$

where Ψ and Φ are the Bardeen potentials and they satisfy Ψ/c^2, $\Phi/c^2 \ll 1$. In the absence of anisotropic stress, which is true in the standard cosmological paradigm[5], $\Phi = \Psi$. This assumption can be tested by combining weak gravitational lensing (which as we shall see is

[4] Perturbations on scales smaller (greater) than the Hubble radius are known as subhorizon (superhorizon). During inflation, superhorizon perturbations were in causal contact.

[5] This equality can be computed using the trace-free part of the stress-energy tensor. Baryons and dark matter can be described as perfect fluids and the photonic anisotropic stress component only starts to appear during the matter-dominated epoch when the corresponding energy density is subdominant. The only source of note are free-streaming neutrinos, which are expected to have a small impact.

sensitive to the combination $\Phi + \Psi$ which describe the path of photons) and galaxy clustering observations (since the gravitational acceleration of non-relativistic particles, i.e. galaxy components, is solely determined by Ψ) where deviations could point towards modifications of gravity (e.g. Weinberg et al., 2013; Reyes et al., 2010; Leonard et al., 2015). This is one of the reasons why it is interesting to compute the joint predictions for these probes as is done in this thesis. We will primarily concern ourselves with subhorizon perturbations whose evolution can be described in a purely Newtonian formalism. In the matter-dominated era, perturbations are sourced through the Poisson equation (the 00:th component of the field equations) as

$$\Phi_{\boldsymbol{k}} = -\frac{3}{2}H^2\Omega_{\mathrm{m}}a^2\frac{\delta_{\boldsymbol{k}}}{k^2}, \tag{1.2.27}$$

where $\delta_{\boldsymbol{k}}$ are the amplitude of the fluctuations and k their wave modes[6]. These fluctuations occur around the mean density $\bar{\rho}$, i.e. $\delta = (\rho - \bar{\rho})/\bar{\rho}$ and can be shown to evolve as (e.g. Peebles, 1993)

$$\ddot{\delta} + 2H(t)\dot{\delta} - 4\pi G\rho\delta = 0. \tag{1.2.28}$$

The evolution can be decomposed into a growing and a decaying mode, where we neglect the latter as surviving perturbations observed today come from the growing mode. Eq. (1.2.28) expressed in terms of the linear growth factor $D(t)$

$$\ddot{D} + 2H\dot{D} - \frac{3}{2}H_0^2\Omega_{\mathrm{m}}(1+z)^3 D = 0, \tag{1.2.29}$$

and matter perturbations evolve as $\delta(\boldsymbol{x}, t_1) = D(t_1)/D(t_0)\delta(\boldsymbol{x}, t_0)$ for $t_1 > t_0$ where one typically normalises the linear growth such that $D(t_0) = 0$. We can write an analogous expression for the power spectrum since the linear growth affects all perturbations independent of position and thus all their wave modes equally. This means that the density field, as well as the gravitational acceleration and the peculiar velocities, have a self-similar time evolution. Can we describe how the particles themselves move as the perturbations evolve? To first order in Lagrangian perturbation theory[7], the result is captured by the *Zel'dovich approximation* (Zel'Dovich, 1970), where one computes an initial displacement field for the particles, considered as individual fluid elements, and then assume that they will continue to move in this direction. In physical coordinates, this can be expressed as (Peacock, 2003)

$$\boldsymbol{x}(t) = a(t)\boldsymbol{q} + b(t)\boldsymbol{\Psi}(\boldsymbol{q}), \tag{1.2.30}$$

where $b(t)$ is a function which scales the initial displacement $\boldsymbol{\Psi}(\boldsymbol{q})$ where $\boldsymbol{q}$ is the initial comoving position (Lagrangian position) and $\boldsymbol{x}$ the final position at t (Eulerian position). This field can be computed from the gradient of the potential $\boldsymbol{\Psi}(\boldsymbol{q}) = \nabla\Phi(\boldsymbol{q})$. Linearising the density relation yields $\delta = -b/a\nabla\cdot\boldsymbol{\Psi}$ which means that the ratio $b(t)/a(t) = D(t)$, i.e. that

$$\boldsymbol{x}(t) = a(t)\left(\boldsymbol{q} + D(t)\boldsymbol{\Psi}(\boldsymbol{q})\right), \tag{1.2.31}$$

[6] At linear order all k are decoupled from one another.

[7] We can write Eq. (1.2.30) as $\boldsymbol{x} = \boldsymbol{q} + \boldsymbol{\Psi}(\boldsymbol{q}, t)$ with $\boldsymbol{\Psi} = \boldsymbol{\Psi}^{(1)} + \boldsymbol{\Psi}^{(2)} + \ldots$ with $\boldsymbol{\Psi}^{(1)}$ as the Zel'dovich approximation (White, 2014).

where the approximation was suggested to be valid for extrapolations of structure growth into the regime $\delta \sim 1$ where displacements no longer are small[8]. We will use this expression for the cosmological rescaling algorithm to modify the large-scale perturbations to account for residual differences in the power spectrum between the target and rescaled cosmologies.

1.2.4 Halo formation

This Section details how dark matter haloes form from matter perturbations in the nonlinear regime. We consider the classical Einstein-de Sitter solution, then point out the steps to generalise the relation and conclude by introducing the basic principles of Press-Schechter theory and excursion sets. This Section draws inspiration from Shi (2017); Mo et al. (2010). Consider the classical spherical collapse model in an Einstein-de Sitter universe ($\Omega_\mathrm{m} = 1$) (Gunn & Gott, 1972; Lahav et al., 1991), for a spherically symmetric overdense shell with initial amplitude $\Delta_i = (M_i - \bar{M}_i)/\bar{M}_i$ within a radius R_i of where $\bar{M}_i = (4\pi/3)\bar{\rho}R_i^3$. As the shell expands, it encloses the same mass unless different shells start to cross. In this universe without a cosmological constant, the radius R evolves according to the Newtonian potential

$$\ddot{R} = -\frac{GM_i}{R^2}, \tag{1.2.32}$$

which can be readily integrated to

$$\dot{R}^2 = \frac{2GM_i}{R} - K, \tag{1.2.33}$$

with curvature $K = 8\pi G\rho(t_i)R^2\Delta_i$ set by the initial conditions. Setting $K = 0$ is equivalent to computing the Hubble expansion for the Einstein-de Sitter universe itself, for which we can integrate the equation once more to arrive at:

$$R_\mathrm{EdS} = \frac{1}{2}(GM_i)^{1/3}(6t)^{2/3}, \tag{1.2.34}$$

from which we realise that $R \to \infty$ as $t \to \infty$. For $K > 0$, i.e. for an initial matter overdensity, the equation has a solution

$$R(\theta) = \frac{GM_i}{K}(1 - \cos\theta), \tag{1.2.35}$$

$$t(\theta) = \frac{GM_i}{K^{3/2}}(\theta - \sin\theta), \tag{1.2.36}$$

from initial times $t = 0$ and $R = 0$. At $\theta = \pi$, R reaches its maximum $R_\mathrm{max} = GM_i/K$ at time $t_\mathrm{max} = \pi GM_iK^{3/2}$, which is known as the turnaround time marking the transition between the weakly non-linear and non-linear regimes, and the structure collapses again at $\theta = 2\pi$ for $t_\mathrm{coll.} = 2t_\mathrm{max}$. If we compare the radial solution for the whole universe and the one for the overdensity at t_max we find

$$\frac{\rho_\mathrm{max}}{\bar{\rho}} = \frac{R^3_\mathrm{EdS}(t_\mathrm{max})}{R^3_\mathrm{max}} = \left(\frac{3\pi}{4}\right)^2 \approx 5.55, \tag{1.2.37}$$

i.e. the sphere is 5.55 denser than the average density of the universe. Of course, it is physically implausible for the sphere to collapse fully due to imperfections in the symmetry

[8] At this point mode coupling becomes important.

coming from gradient instabilities which appear as soon as shell-crossing occurs. Instead a virialised nonlinear structure supported by its velocity dispersion is formed at $R_{\rm vir}$ following the virial theorem $T = U/2$ where T is the kinetic and U the potential energy. That is

$$T = \frac{U(R_{\rm vir})}{2} = -\frac{GM}{2R_{\rm vir}} = U(R_{\rm max}) = -\frac{GM}{2R_{\rm max}}, \tag{1.2.38}$$

which means that $R_{\rm vir} = 1/2R_{\rm max}$ at which Eq. (1.2.37) reads

$$\frac{\rho_{\rm vir}}{\bar{\rho}} = \frac{R^3_{\rm EdS}(t_{\rm coll.})}{R^3_{\rm vir}} = 18\pi^2 \approx 178, \tag{1.2.39}$$

which is the origin of the density threshold $\Delta = 200$ in common halo definitions. Using linear theory, this threshold corresponds to $\delta_{\rm c}(t_{\rm coll.}) \approx 1.686$. For a more realistic, flat universe with a cosmological constant $\Lambda > 0$, one has to modify Eq. (1.2.32) by adding a term $+\Lambda/3R$ to the lefthand side and the whole derivation can easily be modified to account for it (Lahav et al., 1991; Lacey & Cole, 1993). This has the net effect of slightly increasing Δ which can be approximated as (Bryan & Norman, 1998)

$$\Delta \approx \frac{18\pi^2 + 82x - 39x^2}{\Omega_{\rm m}(t_{\rm vir.})}, \quad x = \Omega_{\rm m}(t_{\rm vir.}) - 1. \tag{1.2.40}$$

The new spherical collapse threshold can be approximated by the following expression with 1 % accuracy (Mo et al., 2010)

$$\delta_{\rm c}(t_{\rm coll.}) \approx 1.686 \left(\Omega_{\rm m}(t_{\rm coll.})\right)^{0.0055}, \tag{1.2.41}$$

which implies a very weak scaling with the background cosmology. It is not true in general that perturbations grow with perfect spherical symmetry. More realistic models consider ellipsoidal collapse (e.g. Bond & Myers, 1996; Sheth et al., 2001). The first structures to form are sheet-like pancakes (collapse along the first, shortest ellipsoidal axis), then filaments (collapse along the second axis) and lastly virialised dark matter haloes (third axis). Together they constitute the *cosmic web*.

Going beyond this simple setup analytically is a daunting task and that is why halo formation is studied numerically using gravity-only $N-$body simulations (see Section 2.2). These simulations allow us to track the entire history of a halo and identify the initial Lagrangian patch in the initial conditions corresponding to a proto-halo. These smaller regions gradually collapse and merge with each other to form larger haloes. A general feature of ΛCDM universes is that they predict structures on multiple scales. Within a virialised halo, additional density peaks corresponding to bound substructures can be present. These are known as *subhaloes*. Linking the evolution of these subhaloes across cosmic time in a cosmological simulation allows the construction of merger trees.

1.2.5 Halo profiles

We measure the spatial cross-correlation between the halo and matter fields in our simulations to obtain mass profiles in 3D and 2D. In 3D, we consider spherically averaged radial matter density profiles for haloes as a function of halo mass. As a model for comoving matter density profiles of haloes, we consider the *NFW profile* (Navarro et al., 1996, 1997):

$$\rho_{\rm NFW}(r) = \frac{\rho_{\rm crit}(z)\delta_{\rm c}}{(r/r_{\rm s})(1 + r/r_{\rm s})^2}. \tag{1.2.42}$$

Here, δ_c denotes the characteristic density of the halo, r_s its scale radius, and $\rho_{crit}(z)$ the comoving critical density at halo redshift z. For a spatially flat universe with cold dark matter (CDM) and a cosmological constant Λ, $\rho_{crit}(z) = 3H_0^2(8\pi G)^{-1}E(z)^2(1+z)^{-3}$, where G is the gravitational constant, and $E(z)^2 = \Omega_m(1+z)^3 + (1-\Omega_m)$.

For a given overdensity threshold Δ, one may define the halo radius $r_{\Delta c}$ as the radius at which the mean interior density is $\Delta \times \rho_{crit}(z)$. The halo concentration $c_{\Delta c}$ is then defined by $c_{\Delta c} = r_{\Delta c}/r_s$ with the associated halo mass $M_{\Delta c} = \Delta(4/3)\pi r_{\Delta c}^3 \rho_{crit}(z)$ and the characteristic density δ_c

$$\delta_c = \frac{\Delta}{3}\frac{c_{\Delta c}^3}{\ln(1+c_{\Delta c}) - c_{\Delta c}/(1+c_{\Delta c})}. \tag{1.2.43}$$

We also consider as halo radius $r_{\Delta m}$, at which the halo's mean interior density is Δ times the cosmic mean. The associated halo concentration $c_{\Delta m} = r_{\Delta m}/r_s$, and the halo mass $M_{\Delta m} = \Delta(4/3)\pi r_{\Delta m}^3 \Omega_m \rho_{crit}(0)$.

In addition, we also model the density field with *Einasto profiles* (Einasto, 1965):

$$\rho_{Einasto}(r) = \rho_s \exp\left(-\frac{2}{\alpha}\left[\left(\frac{r}{r_s}\right)^\alpha - 1\right]\right), \tag{1.2.44}$$

where α denotes a profile shape parameter, r_s the scale radius, and ρ_s is a density normalisation parameter. The shape parameter is connected to the local average density in the initial field, encompassing the peak curvature (Gao et al., 2008; Ludlow & Angulo, 2017). Following L16, we fix $\alpha = 0.18$.

1.2.6 Press-Schechter and excursion sets

We would like to describe how many haloes are formed given a certain cosmology and how they can be related to the evolution of density fluctuations, given the threshold of collapse presented in the previous Section. This Section mainly traces the following references: Musso (2016); Desjacques et al. (2018). We will also sketch an interpretation of the cosmological rescaling algorithm of Angulo & White (2010), which we extend in this thesis in Chapter 3, in this light.

The number of haloes at a given mass can be computed from the *halo mass function* (HMF) which can be written as

$$\mathrm{d}n = n(M)\,\mathrm{d}M\,, \tag{1.2.45}$$

with $\mathrm{d}n$ being the distribution of haloes with masses $M \pm \mathrm{d}M/2$.

Suppose that we would like to find an analytic expression for Eq. (1.2.45) based on the formation model of cosmic structures from the evolution of the density field. We can filter the density fluctuations $\delta(\boldsymbol{x})$ with $\boldsymbol{x} = \boldsymbol{x}(t)$, so that we neglect fluctuations below a certain radial scale R_*, by convolving the field with a filter function $\mathcal{W}_{R_*}$,

$$\delta(\boldsymbol{x};\, r_*) = \int \delta(\boldsymbol{x'})\mathcal{W}_{R_*}(\boldsymbol{x}-\boldsymbol{x'})\,\mathrm{d}^3x'\,. \tag{1.2.46}$$

A popular choice is a spherical top-hat function,

$$\mathcal{W}_{r_*}(\boldsymbol{x}-\boldsymbol{x'}) = \begin{cases} 1, & |\boldsymbol{x}-\boldsymbol{x'}| < r_*, \\ 0. \end{cases} \tag{1.2.47}$$

Enclosed within this (Lagrangian) radius R_* is a mass $M = 4\pi/3 \cdot \bar{\rho}_\mathrm{m} R_*^3$, with $\bar{\rho}_\mathrm{m}$ as the mean density of the universe at a certain redshift. We can measure the amplitude of the power spectrum convolved with a spherical top-hat function as the variance of the spectrum given by

$$s(z) = \sigma_M^2(z) = \sigma_{R_*}^2(z) = \frac{1}{2\pi^2} \int k^2 P_\mathrm{m}(k,\, z) \hat{\mathcal{W}}_{R_*}^2(k)\, \mathrm{d}k\,, \tag{1.2.48}$$

which depends on redshift which can be factored out as

$$\begin{aligned} \sigma^2(R,\, z) &= D^2(z) \int_0^\infty \frac{1}{4\pi} k^2 P(k,\, 0) \mathcal{W}^2(kR)\, \mathrm{d}k \\ &= D^2(z) \sigma^2(R,\, 0). \end{aligned} \tag{1.2.49}$$

The special case with a spherical top-hat function with radius $R = 8\,h^{-1}\,\mathrm{Mpc}$ yields the cosmological parameter σ_8. The RMS of the fluctuations in galaxy numbers within such spheres has been found to be close to unity (e.g. Davis & Peebles, 1983; White et al., 1993) and this is why it is conventional to measure the amplitude of the density fluctuations using this normalisation. For a power spectrum $P(k) \propto k^n$, the variance scales as $\sigma^2(R) \propto R^{-(n+3)}$, which allows us to write (Mo et al., 2010)

$$\sigma^2(R,\, t) = \left(\frac{M}{M^*(t)} \right)^{-(n+3)/3}, \tag{1.2.50}$$

where

$$M^*(t) \propto (D(t))^{6/(n+3)}. \tag{1.2.51}$$

The spectral index n is greater than > -3 for all length scales for cold dark matter (and for baryons on scales greater than the Jeans length, see Section 1.6). This means that structures form bottom-up, i.e. smaller structures gradually grow to form larger ones.

With these definitions, we outline the principles of *excursion sets*[9] (e.g. Bond et al., 1991; Lacey & Cole, 1993). Each position $\boldsymbol{x}_i$ has an associated matter overdensity, $\delta_R(\boldsymbol{x}_i)$ on the smoothing scale given by R, whose stochastic trajectory over the different smoothing scales we follow. The overdensity field δ is then the ensemble of all trajectories. Haloes form from (i) the largest patches whose initial mean density evolved linearly to the present exceeds the threshold of spherical collapse δ_c with radius R. We can scale this threshold with the linear growth rate as $\delta_c/D(z)$ to acquire the threshold at higher redshift. Since the barrier height shrinks with $1/D(z)$ the barrier is the lowest at $z = 0$ and is higher for higher redshifts. (ii) The smoothing scales are ordered[10] in such a way that $\delta(R') > \delta(R)$ for $R' < R$, which translates to an axis of $1/R$ vs. δ_R. As σ is a monotonic function of $1/R$, they are equivalent variables. This setup is illustrated in Fig. 1.1 for the linear density field, which follows a stochastic trajectory for the different smoothing scales measured at two points $\boldsymbol{x}_i$ and $\boldsymbol{x}_j$. The first up-crossing of the barrier marks the halo formation. Since $\boldsymbol{x}_i$ crosses at a larger radius, the corresponding halo is more massive.

We would like to find a function[11] $f(s)$, which describes this barrier crossing yielding the HMF through

$$\frac{\mathrm{d}n}{\mathrm{d}M} = \frac{\bar{\rho}}{M} \frac{\mathrm{d}s}{\mathrm{d}M} f(s). \tag{1.2.52}$$

[9] Also known as extended Press-Schechter theory.
[10] This circumvents the cloud-in-cloud problem (e.g. Peacock & Heavens, 1990).
[11] Equivalently $f(R)$ or $f(M)$.

Press and Schechter (Press & Schechter, 1974) constructed a mass function

$$f_{\mathrm{PS}}\left(\sigma_{\mathrm{m}}\right)=\sqrt{\frac{2}{\pi}}\frac{\delta_{\mathrm{c}}}{\sigma_{\mathrm{m}}}\,\mathrm{e}^{-\frac{1}{2}\left(\frac{\delta_{\mathrm{c}}}{\sigma_{\mathrm{m}}}\right)^{2}} \tag{1.2.53}$$

which corresponds to any crossing of the barrier and had to be normalised by hand by a factor of two to reconcile it with observations. This fudge factor comes from that underdense regions at scale R could be embedded in overdense regions at $R'>R$, which is known as the cloud-in-cloud problem (e.g. Peacock & Heavens, 1990), i.e. the crossing at any radii. Semi-analytical extensions of this formula have attained a better agreement with observational data. A popular choice is the Sheth-Tormen (Sheth & Tormen, 1999) halo mass function.

We will now discuss the concept of cosmological rescaling (Angulo & White, 2010). Suppose that we would like to match the growth history and variance of the linear matter power spectrum between two different simulations. This could be expressed as the minimisation of the integral

$$\delta_{\mathrm{rms}}^{2}\left(\alpha,\,z'\right)=\frac{1}{\ln R_{1}-\ln R_{2}}\int_{R_{1}}^{R_{2}}\left[1-\frac{\sigma\left(\alpha^{-1}R,\,z'\right)}{\sigma'\left(R,\,z_{\mathrm{fin}}\right)}\right]^{2}\frac{\mathrm{d}R}{R}, \tag{1.2.54}$$

between two smoothing scales R_1 and R_2 which are dilated by a length scale factor α.

In this language, varying σ_8 translates to varying the smoothing radii $1/R$, since the matter field on average is smoother on large scales and less smooth on smaller scales. Varying Ω_{m} induces a variation in the growth rate, which for a flat ΛCDM cosmology depends on Ω_{m} and z, which causes a variation of the barrier height. Finding the rescaling parameters α and z'_* is equivalent to evaluating the variance of the ensemble of trajectories between two smoothing lengths $1/R_2$ and $1/R_1$ for different barrier heights which constrains δ and its derivative $\mathrm{d}\delta/\mathrm{d}R$ or equivalently $\mathrm{d}\delta/\mathrm{d}\sigma$. Alternatively, we can consider the scenario with a fixed barrier $\delta_{\mathrm{crit.}}$ over all redshifts, switch variables to σ on the x-axis and rescale σ according to Eq. (1.2.49) with the linear growth rate. Then, finding the rescaling parameters correspond to adjusting a range of scales between $1/R_2$ and $1/R_1$ with α in the fiducial cosmology and progressively sweep smaller and larger scales with $D(z)$. Trajectories with a less steep initial slope $\mathrm{d}\delta/\mathrm{d}R$ at large radii will then eventually cross the barrier at smaller scales (higher redshifts) with a steep slope. The first setup is slightly preferable intuitively as the variations in σ_8 and Ω_{m} are confined to separate axes.

The steepness of the derivative $\mathrm{d}\delta/\mathrm{d}R$ at the barrier first-crossing determines the concentration of the haloes (e.g. Lacey & Cole, 1993), as the time derivative of the mass accretion $\dot{M}$ is inversely proportional to the derivative.

Varying the redshift z_* in the target cosmology imposes a constraint on the growth rate, which helps to better constrain the derivative $\mathrm{d}\delta/\mathrm{d}R$. δ and its derivative $\mathrm{d}\delta/\mathrm{d}R$ form a system of differential equations which determine $f(R)$, at the first crossing of the barrier of the trajectories (Bond et al., 1991; Musso & Sheth, 2012) with correlated steps. However, to make it work properly, one must introduce an additional correlation between density trajectories of positions $\boldsymbol{x}_i$, $\boldsymbol{x}_j$ which are close in real space, which can be done by appropriately rescaling the Press-Schechter mass function (Sheth & Tormen, 1999) or by imposing a peak constraint (Paranjape & Sheth, 2012; Paranjape et al., 2013) from peak theory (Bardeen et al., 1986) as well as introduce scatter in the barrier height, for instance as $\delta_{\mathrm{crit.}}\rightarrow\delta_{\mathrm{crit.}}+\beta\sigma$ with β as a log-normal distributed random variable to account for a worse agreement at low masses, since such haloes do not exclusively form around peaks in the initial overdensity

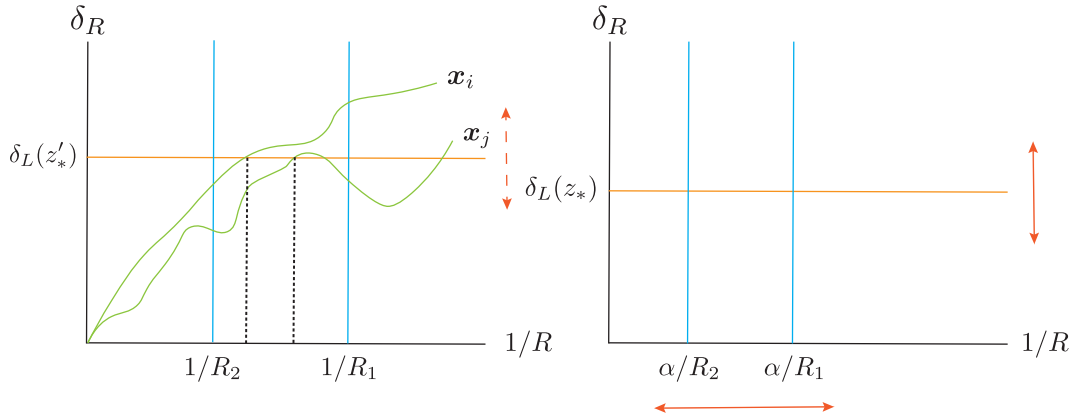

Figure 1.1: Here, we illustrate cosmological rescaling in an excursion set framework with the barrier threshold for halo formation on the y-axis and corresponding smoothing radii on the x-axis. In this simplified picture, rescaling can be imagined as the minimisation of the ensemble of density trajectories between certain smoothing radii, given by the halo masses one would like to study. Varying the smoothing scale through the length rescaling parameter α changes the interval on the x-axis and variation of the redshift parameter z^* translates to different halo formation thresholds.

field. Still, the nature of β is not completely clear, although it has recently been related to tidal shear forces in the initial density field (Castorina et al., 2016), and the peak constraint alone cannot properly account for the actual ellipticities of protohaloes (Ludlow & Porciani, 2011; Hahn & Paranjape, 2014). By rescaling a simulation we implicitly assume that these correlations evolve in a similar manner in the fiducial and the target cosmology from similar initial conditions. We continue this argument in Chapter 3, where we show what rescaling implies for the internal structure of dark matter haloes.

The final tuning of the algorithm involves computing the Lagrangian displacements of the particles using the Zel'dovich approximation (see Section 1.2.3) to compensate for residual differences in the linear power spectrum, which can be computed easily, see Chapter 3. Practically, one computes the smoothing scale $R_{\rm NL}$ which corresponds[12] to $\sigma'(R_{\rm NL}, z^*) = 1$. All modes that are larger than this scale lies in the linear regime, and can then be adjusted through the approximation which can be expressed as

$$\boldsymbol{q}_i = \boldsymbol{x} - D(z) S_{\boldsymbol{k}}(\boldsymbol{q};\, \alpha^{-1} R_{\rm nl}) \tag{1.2.55}$$

for the displacement field S computed according to the following low-pass filter which allows for the separation of the long modes.

$$D(z) S_{\boldsymbol{k}}(\boldsymbol{q};\, \alpha^{-1} R_{\rm nl}) = \begin{cases} D(z) S_{\boldsymbol{k}}(\boldsymbol{q}), & |k| < \alpha / R_{\rm NL}, \\ 0, & |k| > \alpha / R_{\rm NL}. \end{cases} \tag{1.2.56}$$

Afterwards, these modes are added back in when they have been scaled by the square-root of the target-to-fiducial ratio of the linear power spectrum as

$$D'(z') S'(\boldsymbol{q};\, R_{\rm nl}) = \begin{cases} \alpha D(z) \left[\frac{P'(k)}{\alpha^3 P(\alpha k)} \right]^{1/2} S_{\alpha \boldsymbol{k}}(\boldsymbol{q}), & |k| < 1/R_{\rm NL}, \\ 0, & |k| > 1/R_{\rm NL}. \end{cases} \tag{1.2.57}$$

[12] Or by picking something slightly more conservative like $\sigma' = 0.7$.

We use this additional correction in Chapter 3 for one of our extreme cosmologies and show that it has negligible impact for the measured small-scale halo profiles as all particles are moved jointly.

1.3 Gravitational lensing

We now continue by reviewing the basic principles of gravitational lensing with a focus on weak gravitational lensing which is the main observable in this thesis. This Section generally charts the following reviews and references Bartelmann & Schneider (2001); Schneider (2003); Kilbinger (2015). Photons travel along null geodesics, i.e. $\mathrm{d}s = 0$, which means that Eq. (1.2.26) with $\Phi = \Psi$ tells us that at first order

$$t = \frac{1}{c}\int \left(1 - \frac{2\Phi}{c^2}\right) \mathrm{d}x_{\mathrm{phys}}, \tag{1.3.1}$$

with $n = 1 - 2\Phi/c^2$ as an effective refractive index in the neighbourhood of the perturbation. We can apply Fermat's principle $\delta t = 0$ (e.g. Schneider, 1985; Blandford & Narayan, 1986) to arrive at the Euler-Lagrange equations for this index, i.e. the geodesic equation for the transverse motion. Integrating these equations along the light path gives a relation for the local deflection angle $\boldsymbol{\alpha}$ between the received and emitted light rays as

$$\boldsymbol{\alpha} = -\frac{2}{c^2}\int \nabla_\perp \Phi \, \mathrm{d}x_{\mathrm{phys}}, \tag{1.3.2}$$

where the gradient is taken perpendicular to the light path. This equation has to be generalised for cosmological applications. For a potential Φ located at comoving distance χ' from an observer the deflection reads $\mathrm{d}\boldsymbol{\alpha} = -2/c^2 \nabla_\perp \Phi(\boldsymbol{x}, \chi')\mathrm{d}\chi'$ in the comoving frame. Given two neighbouring geodesics in an FLRW universe, their unperturbed transverse separation $\boldsymbol{x_0}$ for an observer at comoving distance χ would be proportional to the comoving angular distance $f_K(\chi)$ in Eq. (1.2.3) for a small angle $\boldsymbol{\theta}$ (e.g. Schneider et al., 1992; Seitz et al., 1994)

$$\boldsymbol{x_0} = f_K(\chi)\boldsymbol{\theta}, \tag{1.3.3}$$

which means that the differential displacement of the source at χ as seen from the deflecting potential at χ' is $\mathrm{d}\boldsymbol{x} = f_K(\chi - \chi')\mathrm{d}\boldsymbol{\alpha}$ and the total deflection for the observer is obtained by integrating this quantity along the line-of-sight, i.e. along χ' from χ to 0, that is

$$\boldsymbol{x}(\chi) = f_K(\chi)\boldsymbol{\theta} - \frac{2}{c^2}\int_0^\chi f_K(\chi - \chi') \left[\nabla_\perp \Phi(\boldsymbol{x}(\boldsymbol{\theta}, \chi'), \chi') - \nabla_\perp \Phi_0(\chi')\right] \mathrm{d}\chi', \tag{1.3.4}$$

where Φ_0 denotes the potential along a second undeflected light ray. If we let $\boldsymbol{\beta}$ denote the un-lensed observed angle for the observer, i.e. $\boldsymbol{\beta} = \boldsymbol{x}/f_K(\chi)$, Eq. (1.3.4) gives the difference between the apparent angle $\boldsymbol{\theta}$ and the deflection angle $\boldsymbol{\alpha}$ in the *lens equation* $\boldsymbol{\beta} = \boldsymbol{\theta} - \boldsymbol{\alpha}$ with

$$\boldsymbol{\alpha} = \frac{2}{c^2}\int_0^\chi \frac{f_K(\chi - \chi')}{f_K(\chi)} \left[\nabla_\perp \Phi(\boldsymbol{x}(\boldsymbol{\theta}, \chi'), \chi') - \nabla_\perp \Phi_0(\boldsymbol{x}(\chi')\right] \mathrm{d}\chi', \tag{1.3.5}$$

This equation can be simplified by replacing $\boldsymbol{x}$ in the integral with its 0:th order solution in Eq. (1.3.3) which is possible under the assumption that the change in the comoving separation due to deflection between the actual light rays is small w.r.t. comoving separation of

unperturbed rays. This is known as the Born approximation and allows one to replace the difference between the perpendicular potential gradients with the perpendicular gradient of the difference between the two potentials, i.e. that we compute the potential gradient along the unperturbed ray. Computing the potential difference is thus equivalent to adding a term which depends on χ' only, which means that we can rename the difference $\Delta\Phi = \Phi$. Moreover, we can construct a linearised mapping between the source and image plane through the Jacobian $\boldsymbol{A} = \boldsymbol{\partial\beta}/\boldsymbol{\partial\theta}$, i.e.

$$A_{ij} = \delta_{ij} - \frac{2}{c^2}\int_0^\chi \frac{f_K(\chi-\chi')f_K(\chi')}{f_K(\chi)}\frac{\partial^2}{\partial x_i \partial x_j}\Phi(f_K(\chi')\boldsymbol{\theta},\chi')\,\mathrm{d}\chi', \tag{1.3.6}$$

where the second term can be considered as a gradient of a 2D lensing potential ψ

$$\psi \stackrel{\mathrm{def}}{=} \frac{2}{c^2}\int_0^\chi \frac{f_K(\chi-\chi')f_K(\chi')}{f_K(\chi)}\Phi(f_K(\chi')\boldsymbol{\theta},\chi')\,\mathrm{d}\chi', \tag{1.3.7}$$

which allows us to parameterise the matrix $\boldsymbol{A}$ as

$$\boldsymbol{A} = \begin{pmatrix} 1-\kappa-\gamma_1 & -\gamma_2 \\ -\gamma_2 & 1-\kappa+\gamma_1 \end{pmatrix}, \tag{1.3.8}$$

with the scalar convergence $\kappa = 1/2\nabla^2\psi$ and the spin-2 shear $\gamma = \gamma_1 + \mathrm{i}\gamma_2$ with components $\gamma_1 = 1/2(\partial_1\partial_1 - \partial_2\partial_2)\psi$ and $\gamma_2 = \partial_1\partial_2\psi$ with $\kappa, |\gamma| \ll 1$ in the case of *weak gravitational lensing*. In this limit the mapping between the source and image plane is one-to-one. We can distinguish between different cases of weak lensing depending on the objects involved; lensing of the large-scale structure of the Universe by itself is known as *cosmic shear* and lensing of background galaxies by specific foreground galaxies is called *galaxy-galaxy lensing* (e.g. Brainerd et al., 1996; Fischer et al., 2000), which is the subject of this thesis. Cosmic shear, first detected by Bacon et al. (2000); Kaiser et al. (2000); Van Waerbeke et al. (2000); Wittman et al. (2000), can be used solely (e.g. Heymans et al., 2013; Hildebrandt et al., 2017; Hikage et al., 2018) or in combination with galaxy-galaxy lensing and galaxy clustering to constrain cosmological parameters (Joudaki et al., 2018; van Uitert et al., 2018; Abbott et al., 2017a) in so-called 3×2-pt correlation function measurements.

The inverse determinant of $\boldsymbol{A}$ describes a magnification of the sources. Extracting $(1-\kappa)$ from Eq. (1.3.8) which only affects the size, one discovers that the shape distortion of the sources can be captured by the reduced shear $g_i = \gamma_i/(1-\kappa)$ which can be described by the shear to first order. As the scatter in galaxy shapes is smaller than the scatter in sizes, we are primarily interested in this quantity to extract information about gravitational potential perturbations along the line-of-sight, see Fig. 1.2. In the case of perfect circular sources, Eq. (1.3.8) with the reduced shear tells us that one could obtain a direct estimate of the reduced shear through the axis ratio $b/a = (1-|g|)/(1+|g|)$. In the real Universe, sources also have intrinsic ellipticities of the same order as the shear which mean that we have to extract the lensing effect statistically by local averaging under the assumption that the intrinsic ellipticities are randomly oriented. If $I(\boldsymbol{\theta})$ describes the brightness distribution of an image on the sky, its centre is given by

$$\bar{\boldsymbol{\theta}} = \frac{\int q(I(\boldsymbol{\theta}))\boldsymbol{\theta}\,\mathrm{d}^2\theta}{\int q(I(\boldsymbol{\theta}))\,\mathrm{d}^2\theta}. \tag{1.3.9}$$

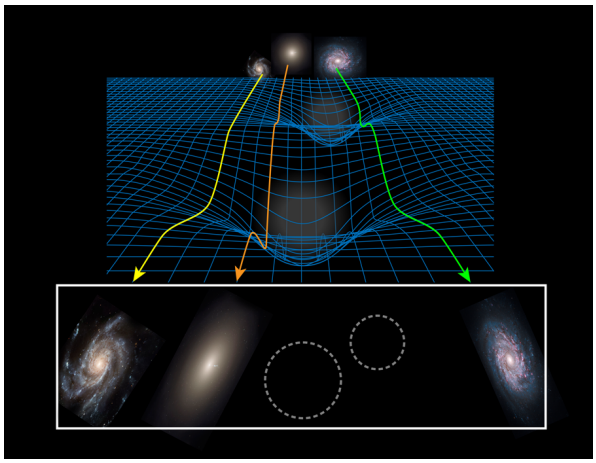

Figure 1.2: Weak gravitational lensing of background galaxies by two foreground dark matter overdensities (dashed lines) with the associated curved spacetime illustrated as a warped grid. The observed images of the galaxies (lower panel) are more elliptical than the fiducial shapes (upper panel). Credit: American Physical Society/Alan Stonebraker with galaxy images from STScI/AURA, NASA, ESA, and the Hubble Heritage Team (Heymans, 2015).

with q as a weight function. The second order brightness moments can then be computed as

$$Q_{ij} = \frac{\int q(I(\boldsymbol{\theta}))\left(\theta_i - \bar{\theta}_i\right)\left(\theta_j - \bar{\theta}_j\right)\mathrm{d}^2\theta}{\int q(I(\boldsymbol{\theta}))\,\mathrm{d}^2\theta}. \tag{1.3.10}$$

Analogously, we can define such second order moments for the un-lensed source

$$Q_{ij}^{(\mathrm{s})} = \frac{\int q\left(I^{(\mathrm{s})}(\boldsymbol{\beta})\right)\left(\beta_i - \bar{\beta}_i\right)\left(\beta_j - \bar{\beta}_j\right)\mathrm{d}^2\beta}{\int q\left(I^{(\mathrm{s})}(\boldsymbol{\beta})\right)\mathrm{d}^2\beta}, \tag{1.3.11}$$

where $\mathrm{d}^2\boldsymbol{\beta} = \det \boldsymbol{A}\,\mathrm{d}^2\boldsymbol{\theta}$ and $\boldsymbol{\beta} - \bar{\boldsymbol{\beta}} = \boldsymbol{A}\left(\boldsymbol{\theta} - \bar{\boldsymbol{\theta}}\right)$ gives that

$$\boldsymbol{Q}^{(\mathrm{s})} = \boldsymbol{A}\boldsymbol{Q}\boldsymbol{A}^{\boldsymbol{T}} = \boldsymbol{A}\boldsymbol{Q}\boldsymbol{A}, \tag{1.3.12}$$

with $\boldsymbol{A} = \boldsymbol{A}(\boldsymbol{\theta})$. Defining two complex ellipticities ζ and ϵ which can easily be converted into one another

$$\zeta \overset{\mathrm{def}}{=} \frac{Q_{11} - Q_{22} + 2\mathrm{i}Q_{12}}{Q_{11} + Q_{22}}, \quad \epsilon \overset{\mathrm{def}}{=} \frac{Q_{11} - Q_{22} + 2\mathrm{i}Q_{12}}{Q_{11} + Q_{22} + 2(Q_{11}Q_{22} - Q_{12}^2)^{1/2}}, \tag{1.3.13}$$

gives the transformation rules

$$\zeta^{(\mathrm{s})} = \frac{\zeta - 2g + g^2\zeta^*}{1 + |g|^2 - 2\mathfrak{Re}\left[g\zeta^*\right]}, \quad \epsilon^{(\mathrm{s})} = \begin{cases} \frac{1-g^*\epsilon}{\epsilon - g}, & |g| \leqslant 1, \\ \frac{\epsilon^* - g^*}{1 - g\epsilon^*}, & |g| \geq 1. \end{cases} \tag{1.3.14}$$

The assumption of random orientation then means

$$\left\langle \zeta^{(\mathrm{s})} \right\rangle = \left\langle \epsilon^{(\mathrm{s})} \right\rangle = 0, \tag{1.3.15}$$

which yields (Schramm & Kayser, 1995; Seitz & Schneider, 1997)

$$\langle \epsilon \rangle = \begin{cases} g, & |g| \leqslant 1 \\ 1/g^*, & |g| \geq 1, \end{cases} \tag{1.3.16}$$

which means that each image ellipticity is an unbiased estimator of the shear field with noise

$$\sigma_\epsilon = \sqrt{\left\langle \epsilon^{(s)} \epsilon^{(s)^*} \right\rangle}, \tag{1.3.17}$$

which can be mitigated by averaging over N images to arrive at a signal-to-noise ratio $\sim \gamma N^{1/2}/\sigma_\epsilon$ above unity. The keys to successful weak lensing measurements are thus a high number density of background galaxies, a large survey area and good shape measurements. An effective number density n_{eff} can be expressed as (Chang et al., 2013)

$$n_{\mathrm{eff}} = \frac{1}{A} \sum_i \frac{\sigma_\epsilon^2}{\sigma_\epsilon^2 + \sigma_{\mathrm{m},\,i}^2}, \tag{1.3.18}$$

where the sum goes over all background galaxies i in survey area A with $\sigma_{\mathrm{m},\,i}$ as the shape measurement error for galaxy i. Variations thereof are used to define the effective number densities in the different weak lensing surveys, depending on the shape measurement pipeline, allowed redshifts and masking used. For the current wide-field lensing surveys[13] such as the Canada-France Hawaii Telescope Lensing Survey (CFHTLenS) the number reads 11 arcmin^{-2} (Heymans et al., 2012), for the source catalogue from the Sloan Digital Sky Survey (SDSS) used in this thesis 1.2 arcmin^{-2} (Reyes et al., 2012), for the sources in the Kilo-Degree Survey (KiDS) also featured in this thesis 5.98 arcmin^{-2} (Kuijken et al., 2015), for the Dark Energy Survey (DES) Y5 10 arcmin^{-2} (The Dark Energy Survey Collaboration, 2005) and lastly for the Hyper Suprime-Cam SSP Survey (HSC) 21.8 arcmin^{-2} (Mandelbaum et al., 2018b), the best in the current generation. In the next decade the corresponding numbers will be 26 arcmin^{-2} for the ground-based Large Synoptic Survey Telescope (LSST) (Ivezić et al., 2008) with expected increase of $\sim 20\,\%$ due to improved modelling (Chang et al., 2013), > 30 arcmin^{-2} for the Euclid satellite (Laureijs et al., 2011), and 45 arcmin^{-2} for the Wide Field Infrared Survey Telescope (WFIRST) satellite (Spergel et al., 2015).

We will not discuss challenges in measuring the shear nor estimating the photometric redshift (photo-z) distributions of background and lens galaxies and direct the interested reader towards (e.g. Kuijken et al., 2015; Hildebrandt et al., 2017; Zuntz et al., 2018; Hoyle et al., 2018; Mandelbaum, 2018) for these most pertinent subjects for observational weak lensing. Recently, it was proposed that biases in the calibration of the photo-z could drive the congruence in cosmological parameters derived from cosmic shear measurements in DES and HSC (Hildebrandt et al., 2018) with CMB observations, mitigating the tension, see Section 1.5.

[13] For instance CFHTLens only covers $\sim$ 154 deg^2, whereas KiDS will cover $\sim$ 1500 deg^2 and DES $\sim$ 5000 deg^2. KiDS (Kuijken et al., 2015; Hildebrandt et al., 2017) offers a slightly better seeing than DES (Troxel & DES Collaboration, 2018; Abbott et al., 2018) ($\sim 0.7''$ vs. $\sim 0.9''$ median r-band point spread function full width at half maximum, PSF FWHM), which determines how accurately galaxy shapes can be measured, making the two surveys comparable at this point in time. The point spread function is the response of an imagining system to a point source. HSC will cover $\sim$ 1400 deg^2 and also has excellent seeing ($\sim 0.6''$ median i-band PSF FWHM) which together with its high background source density makes it the best lensing survey of this generation (Mandelbaum et al., 2018a), although DES will provide the best low redshift cosmological constraints thanks to its large area.

Figure 1.3: Tangential shear of the ellipticity of background source galaxies around foreground matter overdensities, i.e. haloes, (left panel) and underdensities, i.e. voids, (right panel).

The assumption of random orientation breaks down in the presence of *intrinsic alignments* (IA) of galaxy ellipticity orientations (e.g. Hirata & Seljak, 2004; Troxel & Ishak, 2015). These are caused by correlations between the intrinsic ellipticities and the matter field. For instance, luminous red galaxies have been found to preferentially align towards overdense regions, which is the opposite of the shear signal (see Fig. 1.3) which would induce an artificially low signal (e.g. Okumura et al., 2009). The term which is present for galaxy-galaxy lensing is known as the gravitational-intrinsic (GI) term. In the case of galaxy-galaxy lensing, errors in photo-z calculations can mistakenly classify satellite galaxies physically associated with the lens as background sources (e.g. Hirata et al., 2004; Mandelbaum et al., 2005; Blazek et al., 2012), resulting in an IA contamination[14]. In the worst case scenario, this term has been estimated to be at most $\approx 10\,\%$ for $r = 0.1 - 10\,h^{-1}\,\mathrm{Mpc}$ which is below or around the best current statistical uncertainty for the signal, but with conservative photo-z cuts and reasonable IA modelling it may lie on the order of $1-2\,\%$ (Blazek et al., 2012), suggesting that it will not be an insurmountable problem for future surveys. Using currently available data, Blazek et al. (2012); Chisari et al. (2014) find an IA signal consistent with zero. Galaxy-galaxy lensing can also be used to calibrate the GI term for cosmic shear measurements (Blazek et al., 2012). In this thesis we neglect the modelling of such effects as we measure the lensing signal from the shearing of the matter field itself. IA effects are further moderated in the observational signal we use for comparison with spectroscopic redshifts of the lenses and an enforced separation between the redshifts for the peaks of the photometric redshift distributions and these lens redshifts (e.g. Mandelbaum et al., 2005; Dvornik et al., 2017).

1.3.1 Galaxy-galaxy lensing (GGL)

In this Section we discuss galaxy-galaxy lensing (GGL), i.e. the weak gravitational lensing scenario where background galaxies are lensed by individual foreground galaxies where the signal is inferred from stacking, which is the main observational probe of this thesis. Since its first detection by Brainerd et al. (1996), GGL has become well understood in terms of statistical and systematic uncertainties. Recent GGL observations report signal-to-noise ratios ~ 120 (Viola et al., 2015). The available data will increase substantially from ongoing and upcoming surveys such as the DES, KiDS, HSC, LSST, and the Euclid mission. This creates new challenges for GGL theoretical modelling. This Section is primarily based on Marian et al. (2015); Kilbinger (2015) following earlier theory work in Miralda-Escudé (1991); Squires & Kaiser (1996).

[14] GI correlations could also be present among the background source galaxies but they disappear in a stacked signal.

We first express the convergence κ as a projected matter overdensity by substituting the matter overdensity from the Poisson equation Eq. (1.2.27) into the lensing potential Eq. (1.3.7) while adding an extra derivative $\partial^2/\partial^2\chi$ along the line-of-sight, which approximately cancels out in the integration leading to

$$\kappa(\boldsymbol{\theta},\,\chi) = \frac{3H_0^2\Omega_\mathrm{m}}{2c^2}\int_0^\chi \frac{1}{a(\chi')}\frac{f_K(\chi-\chi')f_K(\chi')}{f_K(\chi)}\delta(f_K(\chi')\boldsymbol{\theta},\chi')\,\mathrm{d}\chi'. \tag{1.3.19}$$

We start to show that the constituents of the lensing Jacobian matrix in Eq. (1.3.8) for a circular aperture $\mathcal{C}$ with radius θ and border $\partial\mathcal{C}$ around a matter overdensity can be reduced to an expression for the tangential shear component. Consider the average convergence κ inside this aperture

$$\begin{aligned}\langle\kappa(\leqslant\theta)\rangle_\mathcal{C} &= \frac{1}{\pi\theta^2}\int_{|\boldsymbol{\theta'}|\leqslant\theta}\kappa(\boldsymbol{\theta'})\,\mathrm{d}^2\theta' = \frac{2}{\theta^2}\int_0^\theta \theta'\,\mathrm{d}\theta'\left(\frac{1}{2\pi}\int_0^{2\pi}\kappa(\theta',\,\phi)\,\mathrm{d}\phi\right)\\ &= \frac{2}{\theta^2}\int_0^\theta \theta'\,\langle\kappa(\theta')\rangle_{\partial\mathcal{C}}\,\mathrm{d}\theta'\,.\end{aligned} \tag{1.3.20}$$

Since

$$\begin{aligned}\kappa(\theta',\,\phi) &= \frac{1}{2}\left(\partial_{\theta'}^2+\partial_\phi^2\right)\psi(\theta',\,\phi),\ \gamma_\mathrm{t}(\theta',\,\phi) = \left(\partial_{\theta'}^2-\partial_\phi^2\right)\psi\\ \gamma_\times(\theta',\,\phi) &= \partial_{\theta'}\partial_\phi\psi(\theta',\,\phi),\end{aligned} \tag{1.3.21}$$

in the interior of $\mathcal{C}$ with γ_t and $\gamma_\times$ being the tangential and the cross-component of the shear respectively as illustrated in Fig. 1.3, we can reformulate the expression as

$$\langle\kappa(\leqslant\theta)\rangle_\mathcal{C} = \frac{1}{\theta^2}\int_0^\theta\theta'\,\mathrm{d}\theta'\left(\frac{1}{2\pi}\int_0^{2\pi}\left(\partial_{\theta'}^2+\partial_\phi^2\right)\psi(\theta',\,\phi)\,\mathrm{d}\phi\right). \tag{1.3.22}$$

Using the divergence theorem[15], we can immediately eliminate the term with $\partial_\phi^2\psi$ and partial integration followed by a consecutive application of the divergence theorem on the remaining θ' integral, leads us to deduce that

$$\langle\kappa(\leqslant\theta)\rangle_\mathcal{C} = \frac{1}{2\pi\theta}\int_0^{2\pi}\partial_\theta\psi(\theta,\,\phi)\,\mathrm{d}\phi\,. \tag{1.3.23}$$

Now, multiply this equation with θ and differentiate with respect to θ to acquire the derivative with respect to the radius,

$$\frac{\partial}{\partial\theta}\left[\theta\,\langle\kappa(\leqslant\theta)\rangle_\mathcal{C}\right] = \frac{1}{2\pi}\int_0^{2\pi}\partial_\theta\partial_\theta\psi(\theta,\,\phi)\,\mathrm{d}\phi \overset{Eq.\ (1.3.21)}{=} \langle\kappa(\theta)\rangle_{\partial\mathcal{C}} - \langle\gamma_\mathrm{t}(\theta)\rangle_{\partial\mathcal{C}}\,, \tag{1.3.24}$$

with $\theta'\to\theta$ in Eq. (1.3.21). Likewise, we can perform the same differentiation using the last integral expression in Eq. (1.3.20), yielding

$$\frac{\partial}{\partial\theta}\left[\theta\,\langle\kappa(\leqslant\theta)\rangle_\mathcal{C}\right] = -\langle\kappa(\leqslant\theta)\rangle_\mathcal{C} + 2\,\langle\kappa(\theta)\rangle_{\partial\mathcal{C}}\,, \tag{1.3.25}$$

which allows us to write the averaged tangential shear on the edge of the circle as

$$\langle\gamma_\mathrm{t}(\theta)\rangle_{\partial\mathcal{C}} = \langle\kappa(\leqslant\theta)\rangle_\mathcal{C} - \langle\kappa(\theta)\rangle_{\partial\mathcal{C}}\,, \tag{1.3.26}$$

[15]The equivalence principle guarantees that boundary terms involving ψ and $\partial_\theta\psi$ do not contribute.

which tells us that the tangential shear of background galaxies is a direct measure of the projected mass inside the aperture minus a boundary term. Consider a single lens at angular diameter distance D. For such a setup, we can approximate Eq. (1.3.19) by

$$\kappa(\boldsymbol{\theta}) \approx \frac{4\pi G}{c^2}\frac{D_\mathrm{l} D_\mathrm{ls}}{D_\mathrm{s}} \int_{D-\delta D/2}^{D+\delta D/2} \bar{\rho}\delta(D\boldsymbol{\theta},\, D)\,\mathrm{d}D\,, \tag{1.3.27}$$

with D_s as the angular diameter distance to the source and D_ls the distance between the source and the lens. The prefactor can be combined into a *critical surface mass density* $\Sigma_\mathrm{crit}^{-1} \stackrel{\mathrm{def}}{=} 4\pi G/c^2 D_\mathrm{l} D_\mathrm{ls}/D_\mathrm{s}$ which means that the equation reads $\kappa(\boldsymbol{\theta}) = \Sigma(\boldsymbol{\theta})/\Sigma_\mathrm{crit.}$ and we can define a *differential surface mass density* $\Delta\Sigma$ as

$$\Delta\Sigma(\theta) \stackrel{\mathrm{def}}{=} \Sigma_\mathrm{crit}\,\langle\gamma_\mathrm{t}(\theta)\rangle = \Sigma(\leqslant\theta) - \Sigma(\theta), \tag{1.3.28}$$

which is our primary observable in this thesis (e.g. Miralda-Escudé, 1991; Squires & Kaiser, 1996; Wilson et al., 2001). Now, if we consider a background source galaxy distribution $p(z_\mathrm{s})$, a foreground lens at redshift z_l imprints a tangential shear as

$$\langle\gamma_\mathrm{t}\rangle\,(\boldsymbol{\theta}) = \int_0^\infty p(z_\mathrm{s})\Sigma_\mathrm{crit}^{-1}(z_\mathrm{l},\, z_\mathrm{s})\Delta\Sigma(\boldsymbol{\theta})\,\mathrm{d}z_\mathrm{s}\,, \tag{1.3.29}$$

from which we can define an effective critical density as

$$\Sigma_\mathrm{crit}^{-1} = \frac{4\pi G}{c^2} D_\mathrm{l} \int_{z_\mathrm{l}+\delta}^\infty p(z_\mathrm{s})\frac{D_\mathrm{ls}}{D_\mathrm{s}}\,\mathrm{d}z_\mathrm{s}\,, \tag{1.3.30}$$

to once again arrive at Eq. (1.3.28). We have shifted the integral to only consider background galaxies distinct from the lens. This expression is suitable for the observational surveys quoted in this thesis, SDSS and the Galaxy And Mass Assembly (GAMA) survey (Driver et al., 2011) with KiDS background galaxies where the lenses have spectroscopic redshifts and the sources photometric. Analogously, we can define a similar expression for the case where the lenses as well have photometric redshift distributions suitable for surveys such as CFHTLenS, DES and HSC. Observationally, the azimuthal symmetry mitigates errors associated with shape measurements from PSF uncertainties. The mean cross-component $\langle\gamma_\times\rangle$ illustrated in Fig. 1.3 violates parity and is thus expected to vanish if we stack the signal from foreground galaxies and their surrounding haloes which suppresses potential halo triaxiality contributions. One could also consider stacking the signal around voids to obtain the opposite result which has traditionally been quite challenging until recently with a claim of a $4.4\,\sigma$ detection (Sánchez et al., 2017) but new promising hybrid approaches consider underdense and overdense lines-of-sights as proxies (Gruen et al., 2016; Friedrich & DES Collaboration, 2018; Gruen & DES Collaboration, 2018). Another often used null test for observational systematics is to compute the signal around random points in the foreground sample and around objects such as stars where the tangential shear also should be zero.

As analytical models, we consider NFW lenses (Wright & Brainerd, 2000; Baltz et al., 2009). The lensing expressions are acquired by integrating the NFW density profile Eq. (1.2.42) along the line-of-sight. Expressed in terms of the dimensionless ratio $x = r/r_\mathrm{s}$, the projected surface mass density at a radius x is then acquired through[16]

$$\Sigma(x) = 2r_\mathrm{s}\int_0^\infty \rho_\mathrm{NFW}(\sqrt{l^2+x^2})\,\mathrm{d}l, \tag{1.3.31}$$

[16] We ignore differences between halo density and overdensity profiles, since these do not affect the differential excess surface mass density $\Delta\Sigma$.

whereas $\Delta\Sigma$ is given by Eq. (1.3.28). We restrict the comparison to scales $\lesssim$ the halo virial radii and leave modelling of the large scales for future studies. We do not model the lenses with Einasto profiles as those are similar to NFW lenses (Retana-Montenegro et al., 2012; Sereno et al., 2016).

The lensing signal is different for central, which reside in the centre of the host halo, and satellite galaxies. We denote the central galaxy lensing signal as $\Delta\Sigma_{\rm cent}$, taken to be the same as the halo signal, and $\Delta\Sigma_{\rm sat}$ as the satellite signal. The joint central-satellite signal is calculated as

$$\begin{aligned}\Delta\Sigma_{\rm joint} = f_{\rm sat}(1-f_{\rm red})\Delta\Sigma^{\rm blue}_{\rm sat} + (1-f_{\rm sat})(1-f_{\rm red})\Delta\Sigma^{\rm blue}_{\rm cent} \\ + f_{\rm sat}f_{\rm red}\Delta\Sigma^{\rm red}_{\rm sat} + (1-f_{\rm sat})f_{\rm red}\Delta\Sigma^{\rm red}_{\rm cent},\end{aligned} \tag{1.3.32}$$

where $f_{\rm sat}$ is the satellite fraction for a given stellar mass bin and $f_{\rm red}$ the fraction of red galaxies in that bin. The central signal is effectually the lensing of the host haloes, whereas the satellite signal features a central sharpening from the presence of the subhalo which decreases radially until the contribution from the central host halo kicks in as a central bump. The radial distance between these two features reflects the average projected distance between the satellites and their centrals.

1.4 Galaxy clustering

Having detailed the principles behind galaxy-galaxy lensing, we now proceed with a few notes on the complementary galaxy clustering signal and how we measure it in this thesis.

Under the assumption of statistical isotropy, the spatial two-point correlation functions

$$\xi_{\rm gi}(|\boldsymbol{r}-\boldsymbol{r'}|) = \langle \delta_{\rm g}(\boldsymbol{r})\delta_{\rm i}(\boldsymbol{r'})\rangle\,, \tag{1.4.1}$$

with $\mathrm{i}=\mathrm{g}$ for the galaxy field with itself (galaxy clustering) and $\mathrm{i}=\mathrm{m}$ for the galaxy field with the matter field (galaxy-galaxy lensing) can be inferred from their projections following the arguments in Section 1.2.2, integrated along the line-of-sight $\mathrm{d}l$,

$$\omega_{\rm p}(r) = \int_{-\infty}^{\infty} \xi_{\rm gg}\left(\sqrt{r^2+l^2}\right)\,\mathrm{d}l, \tag{1.4.2}$$

$$\Sigma(r) = \bar{\rho}\int_{-\infty}^{\infty}\left(1+\xi_{\rm gm}\left(\sqrt{r^2+l^2}\right)\right)\,\mathrm{d}l, \tag{1.4.3}$$

with $\bar{\rho}$ as the average matter density, evaluated at the projected radius r with $\omega_{\rm p}(r)$ as the projected clustering correlation function and $\Sigma(r)$ as the projected surface mass density. Observationally, this clustering correlation function was first measured by Baugh et al. (1996), but it really took off around the turn of the millennium with the advent of the Two-degree Field Galaxy Redshift Survey (2dFGRS; Colless et al., 2001) and SDSS (York et al., 2000). Its theoretical potential to constrain the galaxy-halo relation was first discussed in Peebles (1980) and explicitly as a means to constrain halo masses in Bardeen et al. (1986); Mo & White (1996) due to the strong dependence of the signal on the host mass; although other more complicated secondary dependencies might also play a role (e.g. Jenkins et al., 1998), known as assembly bias, see Chapter 2. This is the reason why we are interested in examining the signal in semi-analytical models of galaxy formation and hydrodynamical simulations.

In this thesis in Chapter 4, we estimate the autocorrelation function $\hat{\xi}_{\rm gg}(r)$ using pair counts according to the standard definition as

$$\hat{\xi}_{\rm gg}(r) = \frac{V}{\langle N_{\rm gal}\rangle^2\, V(r)} N_{\rm gal}(r) - 1, \tag{1.4.4}$$

where $N_{\rm gal}$ is the total number of galaxies in the snapshot, V the total volume, and $V(r)$ and $N_{\rm gal}(r)$ the volume and number of galaxies per cylindrical shell with radius r around each galaxy. Effectually, the integration for $\omega_{\rm p}(r)$ in Eq. (1.4.2) is carried out to a maximal distance $l^{\pi}_{\rm max}$ to account for the uncertainty in determining galaxy redshifts. We set $l^{\pi}_{\rm max} = 60\,h^{-1}\,$Mpc following Zu & Mandelbaum (2016). However, this choice primarily affects the clustering 2-halo term. For the lensing signal we integrate along the entire line-of-sight.

1.5 Cosmological and large-scale structure constraints

In this Section we discuss how galaxy-galaxy lensing can be used to constrain four large-scale structure parameters $\Omega_{\rm m}$, σ_8 (cosmological) and $b_{\rm g}$, $r_{(\zeta)}$ (astrophysical).

As implied by Eq. (1.3.19), GGL is sensitive to a combination of the matter fraction $\Omega_{\rm m}$ and amplitude of the fluctuations σ_8. Galaxies are biased tracers of the underlying matter field which on large scales can be described by a constant $b_{\rm g}$, the galaxy bias[17], which depends on the mass of the host haloes, in front of the density field perturbations in Eq. (1.2.22). Thus large-scale galaxy clustering features an expression $b_{\rm g}^2 P_{\rm m}(k)$ where $P_{\rm m}(k)$ is the matter power spectrum and large-scale gravitational lensing $b_{\rm g} r P_{\rm m}(k)$, with r as (Seljak, 2000; Guzik & Seljak, 2001)

$$r^{\rm gm}_{(\zeta)} = \frac{\zeta_{\rm gm}}{\sqrt{\zeta_{\rm gg}\zeta_{\rm mm}}}, \tag{1.5.1}$$

with $\zeta = \xi$ or $\hat{\xi}$ depending on whether we are working in real or in Fourier space as the cross-correlation coefficient between the matter and galaxy field. In Fourier space this parameter captures the stochasticity between the clustering of matter and clustering of galaxies. If we are working in a region where $r \approx 1$ or have a robust prediction for its scale dependence the two probes can be combined to constrain (Baldauf et al., 2010; Mandelbaum et al., 2013)

$$\bar{\rho}^2_{\rm m} \frac{\zeta^2_{\rm gm}}{\zeta_{\rm gg}} = \bar{\rho}^2_{\rm m} r^2_{(\zeta)} \zeta_{\rm mm}, \tag{1.5.2}$$

which on large scales is a product of $\Omega_{\rm m}\sigma_8$ and has a slightly more elaborate dependence $\Omega^{\gamma}_{\rm m}\sigma_8$ with $\gamma \sim 0.6$ with some nonlinear contribution (e.g. Mandelbaum et al., 2013; Wibking et al., 2018). This joint large scale GGL+clustering setup has been used in the current cosmological analyses (Abbott et al., 2017a; van Uitert et al., 2018; Joudaki et al., 2018), see the left panel in Fig. 1.4 for the results from DES, but future surveys and their smaller error bars calls for sophisticated modelling of $r_{(\zeta)}$ and $b_{\rm g}$. At sufficiently large scales, perturbation theory can be used as in Baldauf et al. (2010); Mandelbaum et al. (2013), but on smaller scales one needs to consider the actual population mechanisms of haloes, such as through halo occupation models (e.g. Yoo et al., 2006; van den Bosch et al., 2013) or semi-analytical models (Simon & Hilbert, 2018). Observational measurements (e.g. Dvornik et al., 2018) can also be used to validate

[17] In general $b_{\rm g}(k)$ which can be written as a perturbative expansion (e.g. Desjacques et al., 2018) with nonlinear and stochastic terms appearing on small scales.

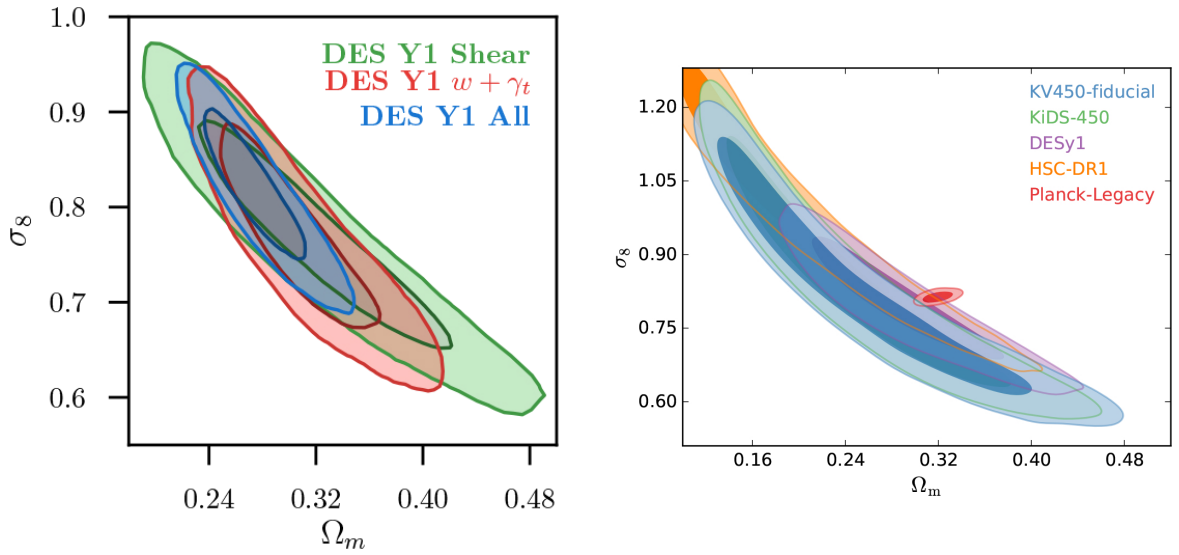

Figure 1.4: Cosmological constraints from weak lensing measurements, from cosmic shear and galaxy-galaxy-lensing with galaxy clustering (left panel) from DES (Abbott et al., 2017a) and constraints from cosmic shear from KiDS including infrared data from the VIKING[18] survey together with previous survey results from KiDS, DES and HSC (right panel) (Hildebrandt et al., 2018).

these models and thus inform on the statistical relationship between the luminous and dark matter fields.

However, these joint probe analyses do not necessitate a combination of GGL+clustering using the same scales. It is also possible to use small-scale lensing information (Seljak et al., 2005; Yoo & Seljak, 2012) to constrain the mean mass of the haloes as M_h is sensitive to $\Omega_m h^2$ and then jointly minimise a data vector with (M_h, Ω_m, σ_8) together with large-scale clustering (Seljak et al., 2005; Yoo & Seljak, 2012), but that also requires recipes on how to populate haloes. In this thesis we do not make any cosmological parameter forecasts, but rather tests these halo occupation recipes for semi-analytical models and hydrodynamical simulations. This is a necessary step to (i) understand how to include the small-scale high signal-to-noise GGL term in these analyses using self-consisted modelling, (ii) push the large-scale lensing signal into the 1-to-2 halo transition regime with a comprehensive treatment of the baryonic feedback.

As shown in Fig. 1.4, the current cosmological constraints on the joint (Ω_m, σ_8) parameter combination from GGL+clustering measurements ($\gamma_t \times w$) are comparable to those from cosmic shear. Yet, the analysis has been restricted to scales $> 8\,h^{-1}\,\mathrm{Mpc}$ (clustering) and $> 12\,h^{-1}\,\mathrm{Mpc}$ (galaxy-galaxy lensing) due to the difficulties to model the nonlinear scales, showing the need of the small-scale analyses performed in this thesis, which will enable us to include such high signal-to-noise signals, enabling tighter constraints than for cosmic shear. As galaxy-galaxy lensing typically (i) has a larger amplitude, (ii) is less sensitive to photo-z uncertainties since the measurement is carried out around specific foreground lenses, (iii) possesses azimuthal symmetry which can be used to mitigate shear measurements errors, (iv) is less prone to systematics such as IA, than cosmic shear, accurate small-scale modelling will bring about a bright future for cosmologists.

[18]The VISTA Kilo-Degree Infrared Galaxy Survey (see e.g. Wright et al., 2018).

In the right panel of Fig. 1.4, we illustrate the current best constraints on these cosmological parameters from cosmic shear from the different surveys previously introduced in this chapter. It is a remarkable feat that all of them arrive at the same conclusion, favouring a combination which is lower than the early Universe constraints from the Planck satellite (Planck Collaboration, 2016a, 2018) from the CMB by about $\sim 2.3\,\sigma$. If this tension persists, it would signal a deviation from the flat ΛCDM model and thus new, exciting physics.

1.6 The galaxy-halo connection

Ending the previous Section on such a positive note, it is now time to start to discuss the challenges of small-scale modelling, i.e. how we populate haloes with galaxies, and how 2-pt correlation functions can be used to inform on these choices. This is known as the *galaxy-halo* connection. We outline the mechanisms behind the collapse and growth of baryonic structures, gas cooling as a prerequisite for star formation and how star formation is regulated through feedback processes to reproduce the observed stellar-to-halo mass relation. More details on the feedback from supermassive blackholes are covered in the subsequent Section.

Inside their host dark matter systems, galaxies are surrounded by a hot gas halo, might feature a cool gas disk[19] and a stellar component which can be decomposed into a disk and a bulge component. For elliptical galaxies there is little to no cool gas left to feed star formation and their morphology is featureless. Galaxies show many correlations between their global properties and such correlations are called scaling relations. The fundamental principles of galaxy formation have been throughly examined in the literature (e.g. White & Rees, 1978; White & Frenk, 1991; Blumenthal et al., 1984) and Mo et al. (2010) and simulations are able to reproduce a range of observables (see e.g. Somerville & Davé, 2015; Naab & Ostriker, 2017, for recent reviews and outstanding theoretical challenges). Major uncertainties still surround the implementation of the feedback processes due to the complex interplay between different effects, which is what we investigate in Chapter 4 using GGL and clustering.

Apart from gravity, baryons also experience pressure forces. This means that they can be stabilised against gravitational collapse. If we use the fluid equations (Euler, Poisson and the continuity equations) for the perturbations, one arrives at the following dispersion relation where c_s is the speed of sound,

$$\omega^2 = \frac{k^2 c_\mathrm{s}^2}{a^2} - 4\pi G\bar{\rho}. \tag{1.6.1}$$

This defines a characteristic *Jeans length* $\lambda_\mathrm{J} \stackrel{\mathrm{def}}{=} 2\pi a/k_\mathrm{J} = c_\mathrm{s}\sqrt{\pi/(\bar{\rho}G)}$ and for $\omega^2 < 0$. Before recombination, the epoch where electrons and protons first became bound to form neutral hydrogen atoms, $c_\mathrm{s} \approx c/\sqrt{3}$. If we define a corresponding Jeans mass M_J within a sphere of radius $\lambda_\mathrm{J}/2$, $M_\mathrm{J} \approx 10^{17} M_\odot$ which is much larger than the mass of a galaxy; i.e. only perturbations of the size of a supercluster could grow prior to recombination. After recombination, the sound speed can be approximated as (Mo et al., 2010)

$$c_\mathrm{s} = \left(\frac{5k_\mathrm{B}T}{3m_\mathrm{p}}\right)^{1/2}, \tag{1.6.2}$$

[19] Except in the case of old massive elliptical galaxies.

with k_B as the Boltzmann constant and m_p as the proton mass, which leads to an $M_\mathrm{J} \sim 10^6\,M_\odot$ which is of the same order as a globular cluster. This means that baryons only collapse on subgalactic scales after recombination, i.e. that they fall into the growing dark matter haloes. In the halo, gas is stabilised by thermal motion.

As the gas falls into the halo it experiences shock heating at the halo boundary, increasing the entropy. A priori the resulting gas temperature T, which can be computed from the virial theorem, is too high to support star formation, which means that there has to be some *cooling* mechanisms. The gas can get rid of the extra energy via radiative exchanges, such as Bremsstrahlung, collisional ionisation followed by recombination and collisional excitation followed by radiative de-excitation, where the dominant mode is determined by the gas temperature. The first is most efficient for $T \simeq 10^7\,\mathrm{K}$ when the gas is fully ionised. For $10^4 < T < 10^7\,\mathrm{K}$, the second mechanism is the most important as atoms can decay into their ground-state and electrons can recombine with ions. Below $10^4\,\mathrm{K}$ cooling manifests itself as collisional excitation and de-excitation of heavy elements (metals) and molecular cooling. As the gas cools it loses pressure support and will gradually be supported by angular momentum. If the cooling time is short with respect to the dynamical time, gas can accrete directly onto the proto-galaxy in a so-called *cold mode accretion* (e.g. White & Frenk, 1991; Birnboim & Dekel, 2003). This primarily happens if the gas flows in along dense filamentary structures (Kereš et al., 2005). If the cooling time is longer, a pressure-supported hot gas halo in pseudo-hydrostatic equilibrium may form where the gas gradually cools known as *hot mode accretion*. Accretion can also happen through galaxy mergers, which allows the creation of larger galaxies than otherwise allowed. Such events are typically associated with increased star formation rates, known as starbursts. In addition mergers can feed the central galactic supermassive black holes (SMBHs), which should exist in all spheroidal galaxies with strong observational evidence (see e.g. Fabian, 2012), which might trigger morphological changes. In this thesis we will study the impact of dynamical friction and how it sets the timescale of galaxy mergers.

Star formation is initiated as soon as gas has collapsed into giant molecular clouds where densities are sufficient to ignite nuclear fusion. Prior to that the gas has become self-gravitating until it eventually collapses under its own gravity which yields a runaway process in the absence of efficient cooling. As the density increases, the cooling becomes more efficient. This is still an area of active research (see e.g. Kennicutt & Evans, 2012, for a recent review with focus on the Milky Way).

What is the peak efficiency of star formation and how does it translate to the galaxy-halo connection? Already the first models of galaxy formation pinpointed the need for feedback processes to prevent all cooled gas from forming stars known as the "overcooling problem" (White & Rees, 1978; Dekel & Silk, 1986; White & Frenk, 1991), with a proposed solution that supernovae could eject gas. Currently, there is a consensus that several different processes connected with massive stars and supernovae contribute to drive gas out of galaxies through large-scale winds and to reduce the efficiency of star formation, such as photo-heating, photo-ionisation and winds (see e.g. Hopkins et al., 2012), although the modelling implementations differ.

Using empirical relations to model the galaxy-halo connection, which we briefly discuss in Chapter 2, one can establish a stellar-to-halo mass relation for central galaxies which is illustrated in Fig. 1.5 at $z = 0.1$. The ratio between the stellar and halo mass is the greatest for haloes with $\sim 10^{12}\,h^{-1}\,M_\odot$ (Milky Way size haloes) and recedes towards lower and higher halo masses. At the low mass end, feedback from supernovae and stellar winds impede the

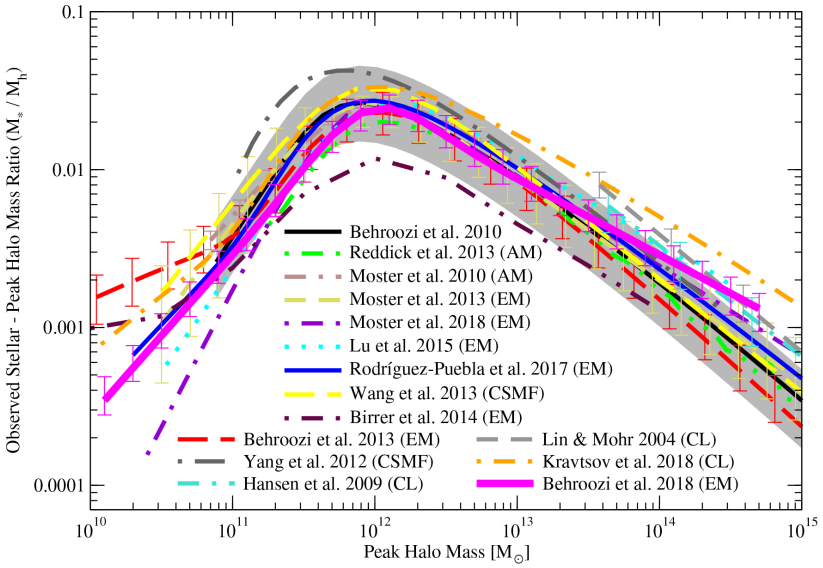

Figure 1.5: Constraints on the stellar-to-halo mass relation for central galaxies from abundance matching (AM), empirical modelling (EM) and conditional stellar mass functions (CSMFs), where more details are provided in Chapter 2. We see that galaxy formation reaches its maximum efficiency for halo masses $\sim 10^{12}\,h^{-1}\,M_\odot$ (Milky Way size haloes). Credit: Peter Behroozi (Behroozi et al., 2018).

formation of stars. Moreover, at the very low mass end, reionization also plays a role as low mass haloes are unable to retain their gas around $z \sim 6$ (see e.g. Bullock et al., 2000).

If one moves on to higher masses, it is believed that feedback from the central SMBHs, from active galactic nuclei (AGN), have had a significant effect[20] on the formation history of the galaxy (Silk & Rees, 1998; Croton et al., 2006). This is thought to be reflected in the observed tight scaling relations between the mass of the SMBH and the bulge mass in low redshift galaxies (e.g. McConnell & Ma, 2013). Indeed, simulations without any sort of AGN feedback or other quenching mechanisms produced inverted colour-magnitude diagrams, i.e. more massive galaxies where more likely to be blue and star forming (e.g. Gabor et al., 2011) inconsistent with observations. We will discuss this feedback process in more detail in the next Section.

So far, we have mostly detailed the star formation quenching scenarios for central galaxies. The situation for satellites is slightly different, where they are influenced by the environment of their host haloes (see e.g. Peng et al., 2012, for observational evidence in SDSS). There are several possible mechanisms to decrease the star formation, such as galaxy harassment, tidal and ram-pressure stripping and strangulation (see descriptions in Mo et al., 2010). In the first case, the galaxy morphology and mass content of a satellite are affected by multiple high speed encounters with other galaxies in a group or cluster. Not only high speed encounters can remove outer material from a satellite; this can also happen in a static configuration which is known as tidal stripping. In high mass clusters, the satellite can experience a drag when traversing the intercluster medium which can remove its cold gas, which fuels the star formation, and this is known as ram-pressure stripping. In the SAM from Henriques et al.

[20]The energy required to grow these massive objects exceeds the binding energy of the host galaxy (Silk & Rees, 1998).

(2015), this effect is restricted to haloes $M_h > 10^{14}\,h^{-1}\,M_\odot$. Strangulation implies a depletion of the gas reservoir surrounding the satellite due to tides or ram-pressure, which leads to a slow decrease in star formation. We will not discuss these processes further, but the results of Chapter 4 indicate that the implementation of these quenching mechanisms in state-of-the-art models require more elaboration to match lensing observations from red satellite galaxies. According to the models, they preferentially reside in high mass haloes, whereas the data suggest otherwise.

1.7 AGN feedback

Feedback from active galactic nuclei (AGN) is generated through the interplay of the energy and radiation from the accretion of material onto the central SMBHs, and the surrounding gas in the host galaxies (see e.g. Fabian, 2012; Kormendy & Ho, 2013, for recent reviews with focus on observational signatures and galactic co-evolution, respectively).

The clearest observational evidence comes from brightest cluster galaxies in cool core galaxy clusters, which without energy input through kinetic feedback would be even more massive and experience giant starbursts.

It is still unclear how the presence of AGNs affects the hosts where multiple effects might be present during galaxy evolution (see e.g. Benson, 2010); they likely heat the gas radiatively in the atmosphere of galaxies preventing the gas to cool. In addition, winds driven by radiation from the broad line region surrounding the black hole, which lies outside the accretion disk, may induce mechanical feedback on the galaxy itself. Moreover, the black hole might produce highly collimated energetic jets in the low accretion state, which can reach far out in the halo.

Two modes of this feedback have been identified, which are separated according to the energy outflow close to the black hole (Fabian, 2012). The first is known as the *radiative* or *quasar* mode which was or is active in a typical bulge when the black hole was or is accreting close to the Eddington limit[21]. Its main effect is to move cold gas around. The second mode is known as *radio* or *maintenance* mode, which typically takes over when the galaxy has a hot gas halo and/or is at the centre of a group or cluster and the accreting black hole produces highly energetic jets. At the current epoch it tends to be present at lower Eddington fractions, in more massive galaxies and in the presence of hot gas.

From the perspective of a computational astrophysicist there are several different ways to implement the feedback (see e.g. Di Matteo et al., 2005; Springel et al., 2005a). In this thesis we are primarily interested in the radio-mode, as the Munich SAM from Henriques et al. (2015) associates the quasar mode with blackhole growth and the radio-mode with the quenching of star formation. For the hydrodynamical simulations we analyse in Chapter 5, we check if there is a better agreement for the predicted lensing mass profiles for massive galaxies in the IllustrisTNG simulation which has an updated, more realistic AGN feedback model with respect to the fiducial Illustris simulation, see the subsequent Chapter 2.

[21] The maximum luminosity an object can achieve as long as there is equilibrium between the radiative and gravitational forces.

Chapter 2 Modelling techniques

In this Chapter we detail the techniques and the simulations[1] used in this thesis for computing lensing and clustering predictions. Modelling the signals at small scales beyond the validity limit of perturbation theory require empirical or computational physics techniques. Empirical schemes, such as halo occupation distribution models and (sub)-halo abundance matching described in Section 2.1, are easier to implement and not as computationally costly. Semi-analytical models (SAMs) and hydrodynamical simulations are examples of the latter, detailed in Section 2.2.3 and Section 2.3, respectively, where subhaloes are populated with galaxies in a self-consistent manner using forward physical modelling. We illustrate these different assignment schemes for the galaxy-halo relation and what is included in each of them in Fig. 2.1 from the recent review by Wechsler & Tinker (2018). In Chapter 4, we will compare predictions from HODs, SAMs and hydrodynamical simulations, but the thesis is primarily directed towards improving and examining the two later methods, which have not been used in cosmological parameter analysis pipelines before.

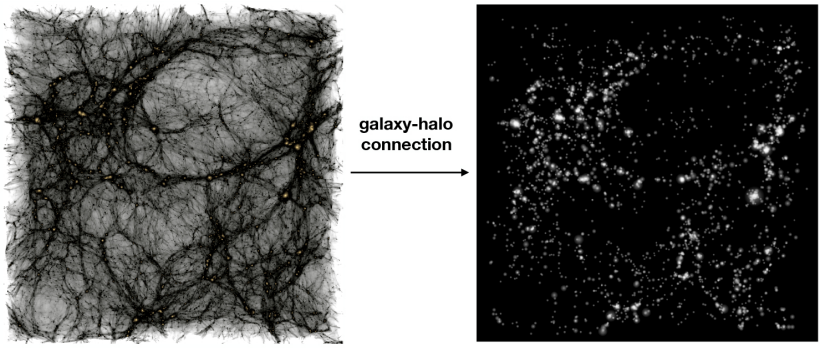

Approaches to modeling the galaxy-halo connection

← physical models — empirical models →

Hydrodynamical Simulations	Semi-analytic Models	Empirical Forward Modeling	Subhalo Abundance Modeling	Halo Occupation Models
Simulate halos & gas; Star formation & feedback recipes	Evolution of density peaks plus recipes for gas cooling, star formation, feedback	Evolution of density peaks plus parameterized star formation rates	Density peaks (halos & subhalos) plus assumptions about galaxy−(sub)halo connection	Collapsed objects (halos) plus model for distribution of galaxy number given host halo properties

Figure 2.1: Different approaches of modelling the connection between the dark cosmic web (left panel) and the observed distribution of galaxies (right panel) listed according to increased modelling complexity with their key assumptions. Credit: Risa Wechsler/Jeremy Tinker from the Annual Review of Astronomy and Astrophysics (Wechsler & Tinker, 2018).

[1] We describe the simulations used to test the cosmological rescaling algorithm separately in Chapter 3.

The Universe which we observe is a static, singular representation where we perceive the evolution by comparing measurements from different redshifts. Performing numerical simulations for cosmological volumes allows us to gain insights into the fast forward action of the physical processes forming galaxies and their interaction with the cosmic web, by varying the model setups and the initial conditions. On cosmological scales, gravity is the dominant force and this describes the success in replicating observations, such as the spatial distribution of galaxies (e.g. Springel et al., 2005b), by the combination of N-body simulations with SAMs or other assignment recipes. It was not until recently that simulations with full hydrodynamical schemes could be run in cosmological volumes (e.g. Vogelsberger et al., 2014a; Dubois et al., 2014; Schaye et al., 2015; Khandai et al., 2015; Pillepich et al., 2018a). The joint analysis of the two is required to capture the small-scale astrophysical behaviour extended to gigaparsec volumes to emulate the statistics of the next generation of large-scale structure surveys.

2.1 Empirical models

Two of the most widely-used frameworks to interpret GGL measurements are halo-occupation distribution (HOD) models (e.g. Peacock & Smith, 2000; Seljak, 2000; Berlind & Weinberg, 2002; Cooray & Sheth, 2002; Leauthaud et al., 2011, 2012; Zu & Mandelbaum, 2015, 2016) and (sub-)halo abundance matching (SHAM) techniques (Kravtsov et al., 2004; Tasitsiomi et al., 2004; Vale & Ostriker, 2006; Conroy et al., 2006; Conroy & Wechsler, 2009; Moster et al., 2010; Behroozi et al., 2010). HODs give the probability distribution of galaxies passing some criteria, such as a stellar mass cut, conditioned on a property, such as the mass, of the host haloes. Classical SHAMs work under the assumption that the most luminous/massive galaxies should reside in the most massive (sub-)haloes, which creates a one-to-one mapping with some scatter that has to be characterised (see e.g. Behroozi et al., 2010). The proxy for the host halo mass could also be other galaxy properties besides stellar mass, and the halo property could also be something else besides mass.

Recent advances have allowed construction of HODs using additional secondary properties such as halo concentration (e.g. decorated HODs, Hearin et al., 2016) as well as boosting their statistical input by consistently accounting for the incompleteness of stellar mass selected samples (e.g. integrated HODs, iHODs, Zu & Mandelbaum, 2015, 2016). However, in general these approaches have trouble to include many secondary parameters and lack the connection between these and the governing physical processes. In addition, there may be aspects poorly understood for certain galaxy samples (Leauthaud et al., 2017). This might be a product of shortcomings of and/or simplifications in these models. For instance, effects such as assembly bias[2], the non-gravitational physics induced by baryons, and the overall dependence on cosmological parameters are difficult to incorporate accurately. Similarly, SHAMs have been improved to act on composite proxies (e.g. Lehmann et al., 2017), which both feature halo mass and concentration, to characterise the dependence. We will analyse iHODs in Chapter 4 but not discuss the other two cases further and instead focus on how these issues could be circumvented through the use of SAMs and hydrodynamical simulations.

[2]The dependency of halo clustering at fixed halo mass on other secondary halo properties such as concentration or formation time (e.g. Gao & White, 2007).

2.2 *N*-body simulations: Gravity-only

The backbone of modern galaxy formation models, N-body simulations deal with solving the collisionless Poisson-Vlasov equation in Newtonian gravity for N point particles representing cold dark matter (e.g. Bertschinger, 1998; Bagla, 2005; Kuhlen et al., 2012). From the first simulation of the Coma cluster with 300 particles (Peebles, 1970), state-of-the art codes are now able to take the first steps at modelling trillions of particles (e.g. Habib et al., 2013; Potter et al., 2017). Initial conditions are typically set a certain time after the end of inflation using that structure evolution during first ~ 100 million years is still in the quasi-linear regime and can thus be subject to an analytical treatment (Zaldarriaga & Seljak, 2000; Lewis & Bridle, 2002; Lewis, 2013). The equations are solved in a comoving frame, usually with periodic boundary conditions, where the expansion rate of the frame is governed by the Friedmann equations in Eq. (1.2.14), although the gravity solvers are Newtonian owing to the negligible impact of relativistic corrections.

Computations are carried out using particle-based, mesh-based or hybrid schemes. A popular particle-based approach is the tree-code (Barnes & Hut, 1986), where the force from remote groups of particles is approximated by multipole moments of the mass distribution of their trees. If we turn to particle mesh (PM)-based algorithms, the method is to compute the potential through Fourier transforms of the gridded density field at the coarsest level, as the Poisson equation has a simple form in Fourier space, and then propagate the effect to the refined levels using a multi-level relaxation scheme. The mesh is often adaptively refined in high-density regions to provide additional resolution. The positions of the particles then evolve along potential gradients (Hockney & Eastwood, 1988). Both frameworks are able to reduce the $\mathcal{O}(N^2)$ complexity of the problem to a computation with an $\mathcal{O}(N \log N)$ scaling[3], although for the PM-based methods N refers to the number of grid cells which typically is set as 2^3 times the number of particles (Kuhlen et al., 2012). Time-wise, PM is considerably faster and automatically accounts for periodic replicas of the volume, whereas particle-based schemes have to resort to less convenient optimisations such as Ewald summation (Hernquist et al., 1991). In tree codes forces can be represented down to a force softening length ϵ, which is introduced to avoid unphysical hard scatterings between particles as they are tracers of the continuous density field (Dyer & Ip, 1993), typically implemented through a Plummer (Plummer, 1911) or cubic spline kernel. For PM-based methods, the resolution is determined by the cell size of the most refined grid.

It is possible to combine the two frameworks into hybrid tree-PM codes, such as GADGET and its successors (Springel et al., 2001a; Springel, 2005), where trees are used to compute short range interactions and a PM for long range forces. These are the codes primarily used for the simulations analysed in this thesis.

2.2.1 Halo finders and merger trees

To identify dark matter structures among the particles, different halo finders can be used on-the-fly (see e.g. Knebe et al., 2011; Muldrew et al., 2011; Onions et al., 2012; Knebe et al., 2013, for reviews and comparisons). This is the first step to construct merger trees between structures in different snapshots of the simulations which can be used by semi-analytical

[3]There are also additional improvements for particle-based methods which can achieve $\mathcal{O}(N)$ scalings such as the Fast Multipole Method (FMM) (Greengard & Rokhlin, 1987), where the force computation is restricted to a couple of tree nodes.

models in post-processing. Substructures were first resolved in N-body simulations twenty years ago (e.g. Ghigna et al., 1998; Klypin et al., 1999) and at present, there exists $\gtrsim 30$ different approaches to identify them, but principally they follow the baseline setup of the first two finders, either through location of spherical overdensities (SO) (Press & Schechter, 1974) or through friends-of-friends (FOF) algorithms (Davis et al., 1985). Generalisations of the former aim to identify peaks in the density field with various methods whereas the latter types connect and link particles by proximity, in physical 3D space (e.g. SUBFIND, Springel et al., 2001b) or in 6D phase-space (e.g. ROCKSTAR, Behroozi et al., 2013a). For the FOF finders, the main hosts are generally identified by particle proximity, but the identification of substructure can differ. Phase-space methods utilise that the velocity distributions of the host and the subhalo often deviate from one another, which allow them to better localise central substructures close to the host and also subhaloes with fewer particles (Knebe et al., 2011). For the 16 different finders in Knebe et al. (2011), the halo mass function at $z = 0$ differed by $\pm 10\,\%$, but this agreement does not necessary apply to higher redshifts (e.g. Klypin et al., 2011). On small scales, the subhalo mass function can be used to discriminate between different models of dark matter (see e.g. Bullock & Boylan-Kolchin, 2017, for a review on small-scale challenges to ΛCDM), as warm dark matter predict significantly fewer substructures (e.g. Knebe et al., 2008; Lovell et al., 2014), although the counts are also influenced by baryonic physics (e.g. Despali & Vegetti, 2017). Still, as substructure finders differ in their proficiency to track objects, they are also susceptible to deficiencies in temporal and spatial resolution (see e.g. Moore et al., 1998; Klypin et al., 1999; Ghigna et al., 2000), with some authors attributing $\sim 80\,\%$ of substructure disruption to numerical artefacts (van den Bosch, 2017) with insufficient force resolution heralded as the main suspect (e.g. van den Bosch et al., 2018).

Having established these structures, one would like to track their evolution through cosmic time with merger trees. The first semi-analytical constructors (e.g. Cole et al., 1994; Kauffmann et al., 1993; Somerville & Primack, 1999) used statistical methods based on excursion sets (Lacey & Cole, 1993) with later editions including empirical corrections to be consistent with simulations (e.g. Parkinson et al., 2008). If one wants to build the trees directly from the snapshots, there are a couple of caveats such as the aforementioned difficulties in finding haloes as well as the unique identification of progenitors as particles in some halo at a given time may end up in other haloes at later times. It has been shown that different tree algorithms produce different results when run on the same simulation (Srisawat et al., 2013). That study also highlights that a successful merger tree algorithm when paired with an accurate halo classifier should keep track of particle ids, be able to handle the temporary disappearance of subhaloes during multiple snapshots due to for instance transits through the host centre and be able to handle and smooth out large, temporary fluctuations in halo mass.

The disruption and loss of subhaloes due to poor resolution translate to fewer satellite galaxies, which can bias clustering measurements. In semi-analytical models, this is compensated through the presence of orphan galaxies (e.g. Springel et al., 2001b; Gao et al., 2004; Guo et al., 2010; Frenk & White, 2012) which continue to exist after the disruption of their host substructures, which are tracked by the most bound particle id of their former hosts. In this thesis we investigate how modifications of the merger criteria for these galaxies affect clustering and lensing measurements. Orphan galaxies can amount to $10-30\,\%$ of all galaxies in a given snapshot (Pujol et al., 2017), which means that their treatment is crucial, and they primarily reside in massive host haloes (Knebe et al., 2015), which has implications for the

lensing signal as we shall see in Chapter 4.

For all simulations used in this thesis, subhaloes are identified using SUBFIND (Springel et al., 2001b) in each FOF group constructed through a halo finder (Davis et al., 1985). For the merger trees for the galaxy formation models, subhaloes with more than twenty bound particles are linked uniquely to descendants in the subsequent snapshots following Springel et al. (2005b) using LHALOTREE, where the details is described in the supplementary material to that publication. The same approach is applied to construct the merger trees in the dark matter-only runs of the IllustrisTNG suite which we use in this study.

2.2.2 Millennium and Millennium-II

We continue to list the specifications of the main simulations used in this thesis. The Millennium (MR) (Springel et al., 2005b) and Millennium-II (MRII) (Boylan-Kolchin et al., 2009) are cold dark matter-only simulations performed using GADGET-2 and GADGET-3 (Springel, 2005), respectively, with 2160^3 particles with masses $8.61\times10^8\,h^{-1}\,M_\odot$ and $6.88\times10^6\,h^{-1}\,M_\odot$, respectively, with a WMAP1 cosmology $\{\Omega_\mathrm{m}, \Omega_\mathrm{b}, \sigma_8, n_\mathrm{s}, h\} = \{0.25, 0.045, 0.90, 1.0, 0.73\}$ (Spergel et al., 2003) with box lengths $500\,h^{-1}$ Mpc and $100\,h^{-1}$ Mpc. The Plummer-equivalent softening lengths ϵ are $5\,h^{-1}$ kpc and $1\,h^{-1}$ kpc, respectively. We primarily use rescaled versions of these simulations with a Planck 2014 cosmology (Planck Collaboration, 2014) using the techniques of Angulo & White (2010); Angulo & Hilbert (2015) with $\{\Omega_\mathrm{m}, \Omega_\mathrm{b}, \sigma_8, n_\mathrm{s}, h\} = \{0.315, 0.049, 0.826, 0.961, 0.673\}$ and box lengths $480.279\,h^{-1}$ Mpc and $96.0558\,h^{-1}$ Mpc and particle masses $9.61\times10^8\,h^{-1}\,M_\odot$ (MRscPlanck) and $7.69\times10^6\,h^{-1}\,M_\odot$ (MRIIscPlanck). Some galaxy formation models as well as the merger trees and halo catalogues are accessible through the Virgo Millennium database (Lemson & Virgo Consortium, 2006).

2.2.3 Semi-analytical models (SAMs)

Together with these gravity-only simulations, one can produce realistic galaxy populations by employing semi-analytical models (SAMs) of galaxy formation (White & Frenk, 1991; Kauffmann et al., 1999; Springel et al., 2001b; Bower et al., 2006; De Lucia & Blaizot, 2007; Guo et al., 2011; Henriques et al., 2013, 2015). In this approach, halo merger trees extracted from N-body simulations are populated with galaxies whose physical processes (see e.g. Benson, 2010; Knebe et al., 2015, for lists of the different physical processes that are implemented in different SAMs), such as cooling, star formation, and feedback, are tracked by a set of coupled differential equations. This allows for self-consistent and physically-motivated predictions for the galaxy population and the respective dark matter, which can then be used to compute the expected weak lensing signal for various lens galaxy samples (e.g. Hayashi & White, 2008; Hilbert et al., 2009; Hilbert & White, 2010; Pastor Mira et al., 2011; Saghiha et al., 2012; Gillis et al., 2013; Schrabback et al., 2015; Wang et al., 2016; Saghiha et al., 2017). SAMs run on top of the merger trees of dark matter-only simulations, and can quickly and cost efficiently produce predictions for galaxy populations in the volumes required for the new surveys. Still, they do not feature a full description of the baryonic physics so the associative effects on the lensing halo profiles have to be calibrated using hydrodynamical simulations which are typically run in smaller volumes. This calibration calls for similar halo occupation distributions in the two frameworks, i.e. that the same types of galaxies populate the same haloes. We describe in details the mechanisms for satellite galaxy mergers and radio-mode AGN feedback in Section 4.4.

2.3 Hydrodynamical simulations: Including gas physics

There is a consensus on how to achieve high-quality results for collisionless dynamics; namely through an accurate gravitational force calculation and time integration, which both can be consistently verified, and with sufficiently many particles for a faithful description of the system and to resolve smaller scales. The situation is more complicated if one seeks to model gas physics (e.g. Springel, 2010a,b; Vogelsberger et al., 2012) due to the relative increased complexity of the hydrodynamical fluid equations. In addition, magnetic and radiation fields demand attention in order to produce realistic populations of galaxies, stars etc. Still, the hydrodynamical scheme cannot be extended to arbitrary small scales, which means that one has to use different subgrid physics prescriptions to track star formation, the evolution of the interstellar medium and so forth. Most codes use either Lagrangian smoothed particle hydrodynamics (SPH) (Gingold & Monaghan, 1977; Lucy, 1977; Monaghan, 1992) which was used in the first hydrodynamical simulations (Efstathiou & Eastwood, 1981; Evrard, 1988; Hernquist & Katz, 1989) or Eulerian mesh-based methods (e.g. Stone & Norman, 1992; Cen & Ostriker, 1992) which may feature adaptive mesh refinement (AMR) (Berger & Colella, 1989). Examples of modern common variants of the former include GADGET-2 (Springel, 2005), which may feature improvements to deal with mixing of fluids (see e.g. Hopkins et al., 2014; Schaller et al., 2015b; Schaye et al., 2015), and the latter RAMSES (Teyssier, 2002).

SPH codes are relatively simple to implement and are able to conserve energy, linear and angular momentum, mass and entropy (in the absence of artificial viscosity) simultaneously (Springel, 2010a). Moreover, due to their Lagrangian nature they track the mass flow and provide additional resolution elements in high density regions, which is suitable for the treatment of merging galaxies or clusters. The drawbacks are that they are less proficient at dealing with shocks, shears and large temperature gradients which appear in some astrophysical problems; some fluid instabilities are suppressed under certain conditions (e.g. Agertz et al., 2007), and the standard implementation cannot properly treat subsonic turbulence (Bauer & Springel, 2012), which occurs in haloes, nor the mixing of phases (e.g. Springel, 2010a). To address the fluid instability suppression issue, the Eagle simulation (Schaye et al., 2015), which is studied in this thesis, uses a modified version of GADGET-3 based on the conservative pressure-entropy formulation of SPH by Hopkins (2013), which is better at treating surface instabilities compared to classical SPH, and also features some other improvements. Yet, as discussed in Schaller et al. (2015b), the differences between this hydrodynamical scheme and the fiducial GADGET-3, which uses entropy-conserving SPH, for cosmological observables are subdominant to reasonable variations of the subgrid physics.

AMR methods do better in this regard, specifically in shock and in mixing problems as the mixing is done intrinsically by averaging the evolved Riemann solutions over the scale of the grid cells at the end of each time step, but can be affected by grid artefacts and numerical diffusion (e.g. Naab & Ostriker, 2017). Particularly, they are sensitive to bulk velocities, which is problematic as galaxies can move with great speed with respect to one another which are typically an order of magnitude larger than the sound speed of the interstellar medium one seeks to trace (e.g. Springel, 2010b), since the truncation errors of Eulerian codes depend on the relative velocity with respect to the grid (e.g. Tasker et al., 2008; Wadsley et al., 2008). Moreover, typical Poisson mesh-based solvers have been shown to provide insufficient force resolution and to produce too few low mass haloes (O'Shea et al., 2005; Heitmann et al., 2008).

New hybrid-methods, such as the moving mesh-code AREPO (Springel, 2010b), attempts

to combine the best of both worlds. Here, the space around particles are subdivided with a Voronoi tessellation and the Riemann problem is solved across all cell faces to obtain the force on the particle. As these particles move, the mesh is re-generated and in this way it is able to trace the mass flow like a Lagrangian code while retaining the benefits of Eulerian schemes in treating contact discontinuities, surface instabilities and shocks, and this without the need for artificial viscosity (which is added in SPH codes to improve the handling of shocks and instabilities). The code still suffers from numerical diffusion, but is able to outperform traditional SPH for mixing problems with high convergence rates (e.g. Sijacki et al., 2012). For the global state of baryons in the simulations, AREPO has been found to cool out more gas than GADGET which affects the late star formation rate of galaxies and also morphologically produce more disk-like structures (Vogelsberger et al., 2012). Due to the complicated topology inherent to the Voronoi tessellation, the code can have difficulties in being massively parallelised for high resolution implementations in very large box sizes, but it is still the basis for the largest, best-resolved hydrodynamical simulation as of yet, the IllustrisTNG TNG300 box (e.g. Pillepich et al., 2018b), for which we analyse lensing and clustering results in this thesis.

We continue by listing the three hydrodynamical simulations which we use for our lensing and clustering studies below.

2.3.1 Eagle

Eagle is a hydrodynamical simulation (Schaye et al., 2015; Crain et al., 2015) carried out with a modified version of the SPH code GADGET-3, in a $(100\,\mathrm{Mpc})^3$ comoving volume with cosmological parameters $\{\Omega_\mathrm{m}, \Omega_\mathrm{b}, \sigma_8, n_\mathrm{s}, h\} = \{0.307, 0.04825, 0.8288, 0.9611, 0.6777\}$ from the Planck 2014 cosmology (Planck Collaboration, 2014). Baryons and dark matter are represented by 2×1504^3 particles with initial mass $m_\mathrm{b} = 1.2 \times 10^6\,M_\odot$ (baryons) and $m_\mathrm{dm} = 9.75 \times 10^6\,M_\odot$ (dark matter), respectively, and the softening length is $\epsilon = 2.66\,\mathrm{kpc}$. The recipes for the AGN feedback[4] are described in Booth & Schaye (2009); Schaye et al. (2015). Model parameters were tuned such that the local SMF and the observed distribution of galaxy sizes were matched (Schaye et al., 2015). The public data releases of the halo catalogues and particle data are detailed in McAlpine et al. (2016); The EAGLE team (2017).

2.3.2 Illustris

Illustris is a hydrodynamical simulation suite (Vogelsberger et al., 2014a,b; Genel et al., 2014; Sijacki et al., 2015) performed with the moving mesh-code AREPO (Springel, 2010b) with the galaxy formation recipes described in Vogelsberger et al. (2013); Torrey et al. (2014) in a cubic comoving $(75\,h^{-1}\,\mathrm{Mpc})^3$ volume with a WMAP9 cosmology (Hinshaw et al., 2013), $\{\Omega_\mathrm{m}, \Omega_\mathrm{b}, \sigma_8, n_\mathrm{s}, h\} = \{0.2726, 0.0456, 0.809, 0.963, 0.704\}$. The highest resolution run features 2×1820^3 resolution elements with Voronoi gas cell masses $m_\mathrm{b} = 1.26 \times 10^6\,M_\odot$ and dark matter particle masses $m_\mathrm{dm} = 4.41 \times 10^6\,h^{-1}\,M_\odot$, with softening lengths $\epsilon_\mathrm{gas} = 0.71\,\mathrm{kpc}$ and $\epsilon_\mathrm{dm} = 1.42\,\mathrm{kpc}$. For the gravity-only run (Illustris-Dark), the particle masses are $m_\mathrm{dm} = 5.29 \times 10^6\,h^{-1}\,M_\odot$. In the low accretion state of the supermassive black holes (radio-mode AGN feedback), hot bubbles are randomly placed around the black hole and the thermal

[4]Eagle does not distinguish between radio and quasar mode for the AGN feedback, but has a joint stochastic thermal mode.

energy injected is directly proportional to the black hole mass growth through thermal coupling and radiative efficiency in the radio mode (Sijacki et al., 2007). This implementation of the AGN feedback is disfavoured[5] by the low gas fractions in galaxy groups and clusters with respect to observations and the too high stellar masses of central galaxies (Genel et al., 2014). Thus, it was replaced in the following IllustrisTNG suite. The parameters in the model were tuned to reproduce the local SMF and the history of the cosmic star formation rate density. The public data release is described in Nelson et al. (2015).

2.3.3 IllustrisTNG

IllustrisTNG is the follow-up project of the Illustris simulation suite which also has been run with the moving mesh-code AREPO. With respect to Illustris, it comes with an updated galaxy formation model (Weinberger et al., 2017; Pillepich et al., 2018a), assuming a Planck 2016 cosmology $\{\Omega_\mathrm{m}, \Omega_\mathrm{b}, \sigma_8, n_\mathrm{s}, h\} = \{0.3089, 0.0486, 0.8159, 0.9667, 0.6774\}$ (Planck Collaboration, 2016a). For the lensing signals, the chief amelioration is a new AGN feedback model for the low accretion state (Weinberger et al., 2017), which sets the stellar-to-halo mass ratio. Box lengths and particle numbers are $75\,h^{-1}\,\mathrm{Mpc}$ with 2×1820^3 particles (TNG100, with the same phases as Illustris in the initial conditions, which enables object-by-object comparisons with the different accessible physical information fields illustrated in Fig. 2.2) and $205\,h^{-1}\,\mathrm{Mpc}$ with 2×2500^3 particles (TNG300) for the highest resolution runs. Particle masses are $m_\mathrm{b} = 9.44 \times 10^5\,h^{-1}\,M_\odot$ and $m_\mathrm{dm} = 5.06 \times 10^6\,h^{-1}\,M_\odot$ (TNG100) and $m_\mathrm{b} = 7.44 \times 10^6\,h^{-1}\,M_\odot$ and $m_\mathrm{dm} = 3.98 \times 10^7\,h^{-1}\,M_\odot$ (TNG300). For the gravity-only runs, the corresponding particle masses are $m_\mathrm{dm} = 6.00 \times 10^6\,h^{-1}\,M_\odot$ (TNG100-DM) and $m_\mathrm{dm} = 4.73 \times 10^7\,h^{-1}\,M_\odot$ (TNG300-DM). The maximum softening lengths are $\epsilon = 0.5\,h^{-1}\,\mathrm{kpc}$ (TNG100) and $\epsilon = 1.0\,h^{-1}\,\mathrm{kpc}$ (TNG300) for the dark matter and stars, with a minimum adaptive gas cell softening of 184 pc (TNG100) and 370 pc (TNG300). Results for the stellar and halo mass functions, galaxy colours, clustering and matter power spectra, magnetic fields and chemical evolution have been presented in Pillepich et al. (2018b); Nelson et al. (2018b); Springel et al. (2018); Marinacci et al. (2018); Naiman et al. (2018), respectively. Details on the latest public data release are published in Nelson et al. (2018a).

[5] To reduce star formation in the centrals would require a higher feedback efficiency and thus expel more gas, which is not a viable solution.

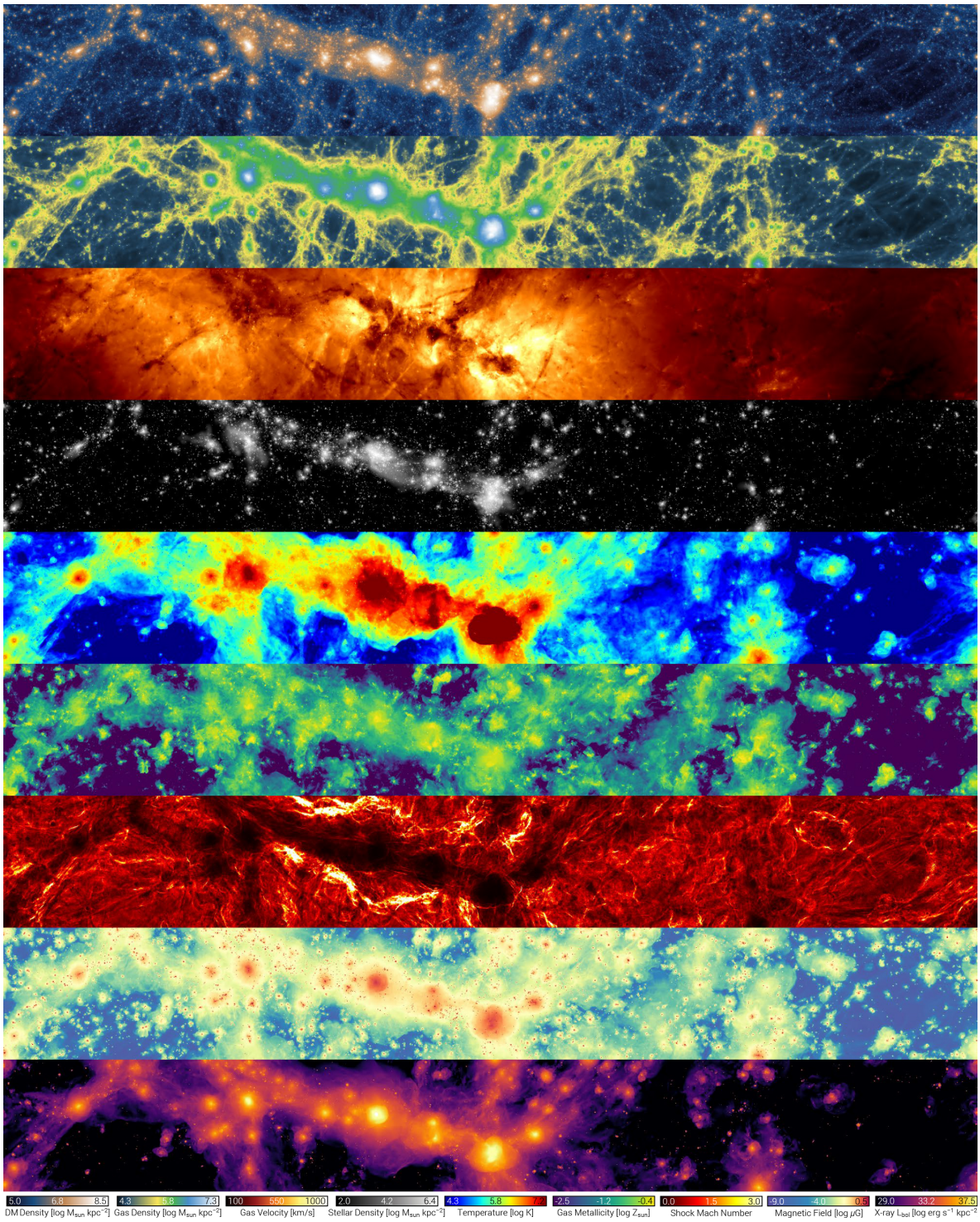

Figure 2.2: A few of the different physical information fields accessible in the IllustrisTNG suite. From top to bottom the following is shown for the same $\sim 110 \times 14 \times 37\,\mathrm{Mpc}$ sub-volume of the highest resolution run of the TNG100 at $z = 0$: dark matter density, gas density, gas velocity field, stellar mass density, gas temperature, gas-phase metallicity, shock mach number, magnetic field strength, and X-ray luminosity. Credit: Dylan Nelson and the IllustrisTNG collaboration from Nelson et al. (2018a).

Chapter 3 Cosmological rescaling

3.1 Prologue

This Chapter appears in Monthly Notices of the Royal Astronomical Society as Renneby et al. (2018) which we reprint here with minor modifications. The first author (me) conducted the work in this analysis with advice from Dr. Stefan Hilbert and Prof. Raúl E. Angulo, PhD.

3.2 Abstract

We investigate 3D density and weak lensing profiles of dark matter haloes predicted by a cosmology-rescaling algorithm for N-body simulations. We extend the rescaling method of Angulo & White (2010) and Angulo & Hilbert (2015) to improve its performance for predicting the inner structure of dark matter haloes by using models for the concentration-mass-redshift relation based on excursion set theory. The accuracy is tested with numerical simulations carried out with different cosmological parameters. We find that predictions for median density profiles are more accurate than $\sim 5\,\%$ for haloes with masses of $10^{12.0} - 10^{14.5} h^{-1}\,M_{\odot}$ for radii $0.05 < r/r_{200\mathrm{m}} < 0.5$, and for cosmologies with $\Omega_{\mathrm{m}} \in [0.15, 0.40]$ and $\sigma_8 \in [0.6, 1.0]$. At larger radii, $0.5 < r/r_{200\mathrm{m}} < 5$, the accuracy degrades to $\sim 20\,\%$, due to inaccurate modelling of the cosmological and redshift dependence of the splashback radius. For feasible changes in cosmology allowed by current data, the residuals decrease to $\lesssim 2\,\%$ up to scales twice the virial radius. We illustrate the usefulness of the method by estimating the mean halo mass of a mock galaxy group sample. We find that the algorithm's accuracy is sufficient for current data. Improvements in the algorithm, particularly in the modelling of baryons, are likely required for interpreting future (dark energy task force stage IV) experiments.

3.3 Introduction

The computationally cost of carrying out numerical simulations over many different cosmological parameters is currently prohibitively expensive. A way to alleviate this challenge is to carry out a small number of high-quality simulations which could then be manipulated to mimic different background cosmologies. This idea was originally brought forth by Angulo & White (2010), henceforth AW10. Their method is to rescale the time and length units such that the variance of the linear matter field in the rescaled fiducial and target simulations match over a range of scales relevant for halo formation. In Angulo & Hilbert (2015), hereafter AH15, an additional requirement on a matched linear growth history was introduced, which improved the accuracy of predictions for shear correlations functions.

Despite the improvements, the rescaling method still produced noticeable biases in the

internal structure of dark matter haloes, owing to different formation times in the fiducial and target cosmologies. In this Chapter, we propose an enhancement to the original algorithm by taking advantage of recent theory developments in predicting the concentration-mass-redshift relation of dark matter haloes by Ludlow et al. (2016), henceforth L16. We then investigate if the updated rescaling algorithm can capture the *small and intermediate scales of the cosmic web* interpretable by galaxy-galaxy lensing.

This Chapter is organised as follows: In Section 3.4, we recap the key ingredients of our rescaling algorithm. Details on the simulations, halo samples, and summary statistics for testing the algorithm are described in Section 3.5. We present the results using the original as well as our updated scaling predictions in Section 3.6. We discuss our results and their implications, e.g. for the estimation of lens masses and predictions for concentration biases, in Section 5.7. We summarise our main findings in Section 5.8.

3.4 Theory

In this section we present the main aspects of our scaling algorithm. We briefly recap the AW10 and AH15 algorithm in Section 3.4.1. In Section 3.4.2 we define halo concentrations from the profiles in Section 1.2.5 and how they transform under rescaling. In Section 3.4.3, we summarise the model of L16, which will be employed later in the Chapter. Throughout the Chapter we use comoving coordinates and densities.

3.4.1 Determining the rescaling coefficients

For the details of the rescaling algorithm, we refer to Section 1.2.6. Here we note that it determines a length rescaling factor α and a redshift z_* in the fiducial cosmology to match to a redshift z'_* in the target cosmology based on (i) the difference in the variance σ of the linear matter field between two smoothing lengths determined by the range of halo masses one would like to emulate and (ii) the difference in growth history. Letting primed symbols denote quantities in the target cosmology, comoving positions $\boldsymbol{x}$ and simulation particle masses m_p in the fiducial simulation are rescaled as

$$\boldsymbol{x}\,[\mathrm{Mpc}/h] \mapsto \boldsymbol{x'}\,[\mathrm{Mpc}/h'] = \alpha \boldsymbol{x}\,[\mathrm{Mpc}/h]\,, \tag{3.4.1}$$

$$\begin{aligned} m_\mathrm{p}\,[M_\odot/h] \mapsto m'_\mathrm{p}\,[M_\odot/h'] &= \alpha^3 \frac{\Omega'_\mathrm{m}}{\Omega_\mathrm{m}} \frac{h'^2}{h^2} m_\mathrm{p}\,[M_\odot/h] \\ &= \beta_\mathrm{m} m_\mathrm{p}\,[M_\odot/h]\,. \end{aligned} \tag{3.4.2}$$

Here, Ω_m denotes the cosmic mean matter density (in units of the critical density) and $H_0 = 100\,h\,\mathrm{km/s/Mpc}$ is the Hubble constant. The comoving matter density ρ_m then transforms as:

$$\rho_\mathrm{m} \mapsto \rho'_\mathrm{m} = \alpha^{-3} \beta_\mathrm{m} \rho_\mathrm{m}. \tag{3.4.3}$$

The simulation box length and redshift change to:

$$L \to L' = \alpha L, \tag{3.4.4}$$

$$z \to z',\ z \leqslant z_*,\ z' \leqslant z'_*, \tag{3.4.5}$$

where higher redshifts are acquired through the linear growth factor relation,

$$D'(z') = D(z)/D(z_*) \cdot D'(z'_*). \tag{3.4.6}$$

The growth constraint from AH15 is implemented through a comparison of a range of scale factors a around the value a_* in the (unscaled) fiducial cosmology corresponding to the best redshift fit z_* of the target simulation at $z = 0$ for a range of proposed scaling options $(\alpha,\, z_*)$ with the growth history[1] of the target simulation. In AW10, the last step of the algorithm involves a large-scale structure correction to account for the differences in the primordial linear power spectrum between the fiducial and target cosmologies, which amounts to moving the particles with respect to one another to reach a better agreement with the positions in the target simulation. Since this analysis focuses on the non-linear regime where this correction translates to an almost uniform displacement, we neglect this correction. As the snapshot output of an N-body simulation usually is discrete in time, the closest match to $(\alpha,\, z_*)$ is selected.

The chief advantage of the algorithm is that all quantities are calculated in the linear regime, wherein we either have explicit predictions or adequate fits for a range of different cosmologies. This allows for a fast evaluation ($\leqslant 5\,\mathrm{s}$ on a contemporary laptop).

3.4.2 Rescaled concentrations

The halo scale radii r_s transform under rescaling as $r_\mathrm{s} \mapsto r'_\mathrm{s} = \alpha r_\mathrm{s}$. NFW halo radii $r_{\Delta\mathrm{m}}$, masses $M_{\Delta\mathrm{m}}$, and concentrations $c_{\Delta\mathrm{m}}$ based on halo overdensities relative to the cosmic mean density also follow simple transformation rules: $r_{\Delta\mathrm{m}} \mapsto r'_{\Delta\mathrm{m}} = \alpha r_{\Delta\mathrm{m}}$, $M_{\Delta\mathrm{m}} \mapsto M'_{\Delta\mathrm{m}} = \beta_\mathrm{m} r_{\Delta\mathrm{m}}$, and $c_{\Delta\mathrm{m}} \mapsto c'_{\Delta\mathrm{m}} = c_{\Delta\mathrm{m}}$.

The rescaling transformation laws for NFW profile quantities based on overdensities relative to the *critical* density are more involved. Applying Eq. (3.4.3) to the NFW profile definition Eq. (1.2.42), we find for the characteristic densities:

$$\delta'_\mathrm{c}\rho'_\mathrm{crit}(z') = \frac{\Omega'_\mathrm{m}}{\Omega_\mathrm{m}}\left(\frac{H'_0}{H_0}\right)^2 \delta_\mathrm{c}\rho_\mathrm{crit}(z). \tag{3.4.7}$$

Thus, the concentration $c_{\Delta\mathrm{c}}$ transforms as

$$c_{\Delta\mathrm{c}} \mapsto c'_{\Delta\mathrm{c}}, \tag{3.4.8}$$

with $c'_{\Delta\mathrm{c}}$ given by the (numerical) solution to

$$\delta'_\mathrm{c}(c'_{\Delta\mathrm{c}}) = \frac{\Omega'_\mathrm{m}}{\Omega_\mathrm{m}}\frac{(1+z')^3}{(1+z)^3}\frac{E(z)^2}{E'(z')^2}\delta_\mathrm{c}(c_{\Delta\mathrm{c}}). \tag{3.4.9}$$

The halo mass $M_{\Delta\mathrm{c}}$ then transforms according to

$$M_{\Delta\mathrm{c}} \mapsto M'_{\Delta\mathrm{c}} = \beta_\mathrm{c} M_{\Delta\mathrm{c}}, \tag{3.4.10}$$

with

$$\beta_\mathrm{c} = \left(\frac{c'_{\Delta\mathrm{c}}}{c_{\Delta\mathrm{c}}}\right)^3 \cdot \alpha^3 \cdot \left(\frac{H'_0}{H_0}\right)^2 \frac{E(z')^2}{E(z)^2}\frac{(1+z)^3}{(1+z')^3}, \tag{3.4.11}$$

and $c'_{\Delta\mathrm{c}}$ as the numerical solution to Eq. (3.4.9). As a range of $c_{\Delta\mathrm{c}}$ values could correspond to a given $M_{\Delta\mathrm{c}}$, this means that the rank order of $M_{\Delta\mathrm{c}}$ is not invariant under rescaling.

[1] The best relative weight on emulating the variance vs. the growth for a given observable is still an open question.

One may also use

$$M_{\Delta\mathrm{m}} = \left(\frac{c_{\Delta\mathrm{m}}}{c_{\Delta\mathrm{c}}}\right)^3 \frac{\Omega_\mathrm{m}(1+z)^3}{E(z)^2} M_{\Delta\mathrm{c}}, \tag{3.4.12}$$

to first convert $M_{\Delta\mathrm{c}}$ to $M_{\Delta\mathrm{m}}$, then rescale $M_{\Delta\mathrm{m}}$ to $M'_{\Delta\mathrm{m}}$, and then convert back to $M'_{\Delta\mathrm{c}}$. We show how to rescale Einasto concentrations in Section 3.12.

3.4.3 Concentration-mass-redshift relation

We focus on what excursion sets (Press & Schechter, 1974; Bond et al., 1991) predict for the concentration of haloes (Lacey & Cole, 1993). One approach for CDM has been to tie the concentration to the mass accretion history of the halo (e.g. Ludlow et al., 2014; Correa et al., 2015). However, this is not suitable for warm dark matter (WDM) models where the concentration-mass relation is non-monotonic despite the different accretion histories of low and high mass haloes. Revisiting the original NFW argument (Navarro et al., 1996, 1997), it was proposed that the characteristic density of the halo δ_c is an imprint of the critical density of the Universe at an appropriate collapse redshift, when progenitors exceeding a fraction f of the final virial halo mass constituted half of this mass. L16 argued that choosing the mean density $\langle\rho_\mathrm{s}\rangle$ inside the scale radius r_s to be proportional to the critical density of the Universe at the collapse redshift (instead of δ_c) and letting the mass inside the scale radius M_s define the characteristic collapsed mass (instead of the virial mass) yields a better agreement for CDM *and* WDM. This relation then takes the form

$$M_\mathrm{s} = \frac{4\pi}{3} r_\mathrm{s}^3 \langle\rho_\mathrm{s}\rangle = \frac{4\pi}{3} r_\mathrm{s}^3 \cdot C \cdot \rho_\mathrm{crit}(z_\mathrm{s}), \tag{3.4.13}$$

where C is a proportionality constant and z_s the collapse redshift. According to excursion sets (Lacey & Cole, 1993), the collapsed mass fraction is given by

$$\frac{M_\mathrm{s}(f,z)}{M_{\Delta\mathrm{c}}} = \mathrm{erfc}\left(\frac{\delta_\mathrm{sc}(z_\mathrm{s}) - \delta_\mathrm{sc}(z_0)}{\sqrt{2}\cdot\sqrt{\sigma^2\left(fM_{\Delta\mathrm{c}}\right) - \sigma^2\left(M_{\Delta\mathrm{c}}\right)}}\right), \tag{3.4.14}$$

where $M_{\Delta\mathrm{c}}$ is the final mass at z_0, $\sigma^2(M)$ the variance of the linear density field on scales equivalent to the mass M, and $\delta_\mathrm{sc}(z)$ a linear barrier height $\delta_\mathrm{sc}(z) = \delta_\mathrm{sc}(z_0)/D(z)$, where the linear growth is normalised such that $D(z_0) = 1$, and the linear density threshold satisfies $\delta_\mathrm{sc}(z_0) = \delta_\mathrm{sc}(z=0) \approx 1.686$ corresponding to spherical collapse at redshift $z = 0$. Combining this with Eq. (3.4.13) and an assumed density profile, this system of three equations yields numerical fits for the $c(M, z)$-relation. The best-fits for the two constants were determined[2] to be $f = 0.02$ and $C = 650$. We neglect the mild cosmological and redshift dependences of $\delta_\mathrm{sc}(z_0)$ in this study.

In L16 this relation was found to fit the median $c(M, z)$-relation estimated with Einasto profiles for relaxed haloes (see Section 3.5.2) for the same simulations that we are using in this Chapter (see Section 3.5.1) with the $M_{\Delta\mathrm{c}}$ mass definition with $\Delta = 200$. We thus calculate the $c(M, z)$-relation with Eq. (3.4.13) and Eq. (3.4.14), assuming an NFW profile Eq. (1.2.42), with $z_0 = z_*$ and z'_* in the fiducial and target simulations, respectively, then adapt the relations for $M_{\Delta\mathrm{m}}$ and $c_{\Delta\mathrm{m}}$.

[2] To achieve internal consistency for a spherical collapse model, $C = 400$ would have been the preferred value, but $C = 650$ produced better fits. This inconsistency primarily affects high mass haloes, which are rare in our simulations. Moreover, we limit the possible length scale factors to $\alpha \in [0.5, 2]$ in Eq. (3.4.1). For the cosmological parameters in this study, this ensures that $\beta_\mathrm{m} M_{\Delta\mathrm{m}}$ remains in the range of validity.

Ω_m	σ_8	L $[h^{-1}\,\mathrm{Mpc}]$	m_p $[10^8 h^{-1}\,M_\odot]$	z_*
0.25	0.90	250.0	8.61	-
0.15	1.00	373.3	17.2	0.32
0.25	0.60	205.3	4.77	0.56
0.29	0.81	224.4	7.22	0.06
0.40	0.70	176.4	4.84	0
0.80	0.40	88.2	1.21	0

Table 3.1: Simulation configurations (fiducial cosmology in the first row) with their values of Ω_m and σ_8 listed. The scale factors α from Eq. (3.4.4) are obtained by dividing the box lengths L with the first column entry. The softening lengths are set as $\alpha \times l_\mathrm{s}$ for the direct simulations with $\alpha = 1$ for the fiducial run. The particle masses m'_p are calculated using Eq. (3.4.2). The rescaling redshifts z_* of the fiducial cosmology's snapshots are listed in the last column.

3.5 Methodology

In this section we present details of our adopted methodology to test the performance of the scaling algorithm. In Section 3.5.1, we describe our fiducial simulation along with five others carried out adopting significantly different cosmologies. We discuss the construction of halo samples in Section 3.5.2. In Section 3.5.3, we define the differential excess surface mass density profiles and provide details about how to measure them, as well as halo concentrations in our simulations.

3.5.1 Numerical simulations

This study is conducted with several N-body simulations employing GADGET-2 (Springel, 2005) with 1080^3 particles which we have previously described in Section 2.2. The fiducial simulation spans a $(250\,h^{-1}\,\mathrm{Mpc})^3$ comoving volume, uses a softening length of $l_\mathrm{s} = 5\,h^{-1}\,\mathrm{kpc}$, and has particle masses $m_\mathrm{p} = 8.61 \times 10^8 h^{-1}\,M_\odot$. It assumes a flat ΛCDM cosmology with a cosmological constant energy density parameter $\Omega_\Lambda = 1 - \Omega_\mathrm{m} = 0.75$, a matter density parameter $\Omega_\mathrm{m} = \Omega_\mathrm{cdm} + \Omega_\mathrm{b} = 0.25$, baryon density parameter $\Omega_\mathrm{b} = 0.045$, Hubble constant $H_0 = 100\,h\,\mathrm{km\,s^{-1}\,Mpc^{-1}}$ with $h = 0.73$, matter power spectrum normalisation $\sigma_8 = 0.90$, and spectral index $n_\mathrm{s} = 1$. The cosmological parameters and force and mass resolution are identical to those of the Millennium simulation (Springel et al., 2005b), see Section 2.2.2.

We rescale the fiducial simulation to cosmologies with different values for Ω_m and σ_8. We then compare these rescaled simulations to simulations carried out directly assuming the target cosmologies. These 'direct' and 'rescaled' simulations have initial conditions with identical phases. The softening lengths, box sizes, and particle masses in these direct simulations have been chosen to match those in the rescaled simulations. Details are provided in Table 3.1 (the other configurations and parameters are the same as in the fiducial run).

Though the rescaling algorithm captures non-linear structure evolution, it cannot arbitrarily adapt to different growth histories. As dark energy becomes more important at lower redshifts, the growth and expansion histories of different ΛCDM cosmologies deviate in different manners from an Einstein-de-Sitter evolution. Thus, we expect the inaccuracy of the scaling to grow with cosmic time. For this reason, we focus on structures at redshift $z = 0$ to obtain a conservative estimate on the accuracy of the scaling method. Finally, note that the rescaling parameters (α, z_*) are identified following AW10 and AH15 for scales corresponding to halo masses in the range $10^8 - 10^{15}\,h^{-1} M_\odot$.

3.5.2 Halo samples

Haloes in the simulations are first identified using a friends-of-friends (FOF) algorithm (Davis et al., 1985) with a linking length of 0.2 times the mean particle separation. The FOF haloes are then processed with SUBFIND (Springel et al., 2001b), employing the same settings as for the MXXL simulation (Angulo et al., 2012), to identify self-bound structures, possibly returning a main subhalo and further self-bound subhaloes.

We will mostly consider halo samples defined by their (rescaled) $M_{200\mathrm{m}}$ mass. However, in some cases we will also consider halo samples that only include matched haloes in direct-rescaled pairs of simulations. Following AW10, we identify as match candidate for each halo in the direct simulation the halo in the rescaled simulation with the most particles with ids matching those of the direct simulation's halo. We repeat the process with the simulations' roles swapped, and consider a haloes matched if they are each others match candidates.

Note that the most accurate rescaling approach would be to transform individual simulation particles and then re-run the group finding algorithm. However, this is computationally expensive, and similarly accurate results can be obtained by directly rescaling the halo catalogue, as shown by Ruiz et al. (2011) (see also Mead & Peacock, 2014a,b), which is the procedure we adopt here; we rescale the position and mass of each snapshot particle but keep the fiducial halo catalogue and rescale it accordingly.

Unrelaxed haloes are poorly described by NFW profiles, and their best fit concentrations tend to be lower than those of relaxed systems (Neto et al., 2007). To test for this in our results, in some cases we will consider samples of haloes that satisfy two criteria. The first criterion is based on the offset between the centre-of-mass $\boldsymbol{r}_{\mathrm{CM}}$ and the gravitational potential minimum $\boldsymbol{r}_{\mathrm{pot}}$ relative to the halo radius r_{200} (Thomas et al., 2001; Macciò et al., 2007; Neto et al., 2007) $d_{\mathrm{off}} = |\boldsymbol{r}_{\mathrm{pot}} - \boldsymbol{r}_{\mathrm{CM}}|/r_{200}$. We consider haloes relaxed if $d_{\mathrm{off}} < 0.1$. The second criterion is a substructure threshold (Neto et al., 2007; Ludlow et al., 2012), $f_{\mathrm{sub}} = M_{\mathrm{sub}}/M_{200} < 0.1$, where M_{sub} is the mass of all bound particles in the subhaloes apart from the main halo identified by the substructure finder.

These criteria lead to similar results as imposing the d_{off} cut and a dynamical age criterion, $t_{50} \geqslant 1.25\, t_{\mathrm{cross}}$ (Jiang & van den Bosch, 2016; Ludlow et al., 2016) curtailing the allowed accretion of the main progenitor w.r.t. its crossing time $t_{\mathrm{cross}} = 2\, r_{200}/V_{200}$, as they exclude recent mergers of structures with similar mass.[3] With the $M_{200\mathrm{m}}$ mass definition[4], the geometric cuts on f_{sub} and d_{off} are trivially invariant under the rescaling mapping[5]. This invariance does not hold for other dynamical relaxation criteria such as bounds on the virial ratio[6] $\eta = 2K/|U|$ (e.g. Cole & Lacey, 1996) or the spin parameter[7] λ (e.g. Bett et al., 2007).

[3] However, a dynamical timescale cut also discriminates against haloes at maximum contraction following a massive merger, which are still present in our subsample.

[4] Given β_{c} in Eq. (3.4.11), the cuts w.r.t. $M_{200\mathrm{c}}$ are not rescaling invariant. Since the measured concentrations are influenced by these cuts (Neto et al., 2007), a recursive rescaling fitting scheme is required to find the passing haloes in the target cosmology.

[5] provided we ignore implicit relations, e.g. redshift evolution which affects f_{sub} (e.g. van den Bosch et al., 2005)

[6] If the simulation's softening length $l_{\mathrm{s}} \mapsto \alpha \mathrm{s}$ and $\alpha_{\mathrm{vel}} \approx \alpha$ for the velocities whose transform is given in AW10 then $\eta \mapsto \eta' \simeq \Omega_{\mathrm{m}}/\Omega'_{\mathrm{m}}(H_0/H'_0)^2\eta$ with the potential U given in Springel et al. (2005b). Since U and T have different transform prefactors, mapping $\lambda \mapsto \lambda'$ is non-trivial.

[7] In AW10, λ was comparable for the haloes in the direct and rescaled simulation snapshots, hinting at similar internal dynamical states, whereas the halo concentrations estimated from velocities displayed a systematic bias.

3.5.3 Halo density and weak-lensing profiles

We measure the spatial cross-correlation between the halo and matter fields in our simulations to obtain mass profiles in 3D and 2D. In 3D, we consider spherically averaged radial matter density profiles for haloes as a function of halo mass. As analytic approximations to these profiles we consider NFW profiles Eq. (1.2.42) and Einasto profiles Eq. (1.2.44).

Operationally, we compute 3D radial halo profiles ρ and projected radial profiles Σ by binning all particles in spherical and cylindrical shells, respectively, around the recorded halo centres given by the positions of their most bound particles. To moderate triaxiality (e.g. Jing & Suto, 2002) and other deviations from azimuthal symmetry, we project the cylinders along the three principal simulation box axes and let the mean signal describe the halo sample, effectively tripling our sample size. For the rescaled simulation, the profiles are computed after applying the adequate rescaling to ensure matching bin boundaries.

In order to assess the errors due to the limited volume, we bootstrap resample (e.g. Efron, 1979) the haloes in each mass bin with 100 realisations to estimate the variance. For $\Delta\Sigma$ we calculate 100 realisations per axis.

We consider halo samples selected by mass with 0.1 dex width above $10^{12}\,h^{-1}\,M_\odot$ to approximately $10^{14.5}\,h^{-1}\,M_\odot$ where we record twenty haloes per bin. For the halo mass function we show the result in 0.05 dex bins. For the 3D profiles, we follow Neto et al. (2007), where the matter density profiles were estimated using 32 log-equidistant bins between $r_{200\mathrm{c}}$ and $\log_{10}(r/r_{200\mathrm{c}}) = -2.5$ where we replace $r_{200\mathrm{c}}$ with $r_{200\mathrm{m}}$. To suppress the impact of outliers on the 3D profile fits, we use the median particle count per spherical shell as input, unless otherwise specified. We then minimise the difference in $\ln\rho$ between the measured median profile and the analytic profile to determine the best fit parameters. We also present concentration estimates for individual haloes from the separate particle counts. To investigate the transition regime between the 1-halo and 2-halo terms, we bin the particles in 64 log-equidistant bins for $0.05\,r_{200\mathrm{m}} < r < 5\,r_{200\mathrm{m}}$.

GGL profiles for each mass-selected halo sample are obtained through Eq. (**??**), with the projected profiles computed by binning the particles in 40 log-equidistant bins in the $30\,h^{-1}\,\mathrm{kpc} - 3\,h^{-1}\,\mathrm{Mpc}$ range. The average GGL profiles are fitted by analytical profiles Eq. (1.3.31) minimising

$$\chi^2 = \sum_{i=1}^{N_r} r_i^2 \left[\Delta\Sigma_{\mathrm{data}}(r_i) - \Delta\Sigma_{\mathrm{NFW}}(r_i; r_{200\mathrm{m}}, c_{200\mathrm{m}})\right]^2 , \tag{3.5.1}$$

w.r.t. $r_{200\mathrm{m}}$ and $c_{200\mathrm{m}}$. The radial weights $\propto r^2$ are observationally motivated, as the shape noise error on the signal scales with the number density of background galaxies, which is proportional to the area of the projected cylinder assuming a constant source density. In observations, masking and blending of background galaxies by foreground galaxies becomes a major systematic as one approaches the central galaxy (Viola et al., 2015), which motivates the lower cutoff.

3.6 Results

In this section we quantify the performance of the scaling algorithm and present alternatives to further improve it. We first focus on the halo mass functions (Section 3.6.1), the 3D density profiles (Section 3.6.2), and the differential excess surface mass density profiles (Section 3.6.3)

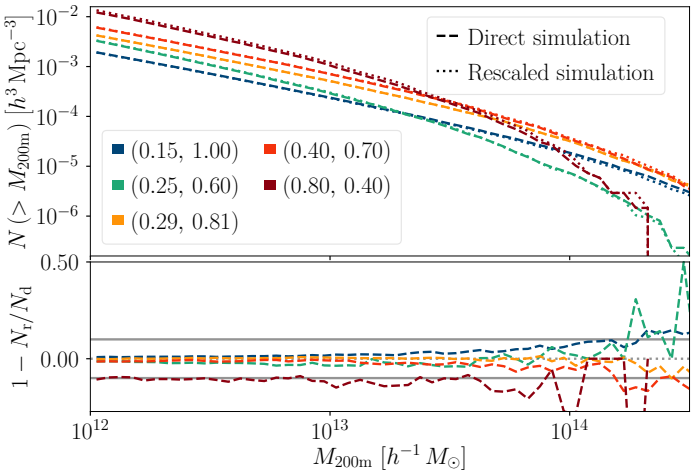

Figure 3.1: Cumulative halo mass function at $z = 0$ (in 0.05 dex bins) for simulations with different values for $(\Omega_\mathrm{m},\, \sigma_8)$ as indicated by the legend. For each cosmology, we display results for direct and rescaled simulations. The fractional differences between these two cases are shown in the bottom panel where solid lines mark $\pm\,10\,\%$.

for the original algorithm. The accuracy of the rescaling for the concentration-mass relation is quantified and compared to the theoretical prediction of L16 in Section 3.6.4. In Section 3.6.5 we use this model to correct the rescaled profiles and show the resulting improvements. Attempts at further ameliorations for the halo outskirts based on models for the position of the splashback radius are discussed in Section 3.6.7. We will focus on representative cases using one of the cosmologies studied where the others manifest similar trends and primarily report on the findings for (0.80, 0.40) in Section 3.10 as these parameters strongly deviate from current observational constraints.

3.6.1 Halo mass function

One of the most basic quantities predicted by simulations is the halo mass function. The cumulative halo mass function (HMF) $N(>M)$ defines the number of haloes above a certain mass M per comoving volume. In AW10, the number densities were properly matched with a bias of order $\lesssim 10\,\%$. To avoid numerical artefacts, we only compare HMFs for haloes with (rescaled) masses exceeding $10^{12}\,h^{-1}M_\odot$ (i.e. objects resolved with > 1000 particles).

In Fig. 3.1, we show $N(>M)$ for all haloes in the direct and rescaled cosmologies with the fractional difference in the bottom panel. In numbers, there are 100 154, 28 427, 47 519, 33 123 and 8 325 haloes with $M_{200\mathrm{m}} > 10^{12}\,h^{-1}M_\odot$ in the direct simulations (listed according to increasing Ω_m), and 97 232, 28 145, 46 620, 32 888 and 8 999 haloes in the rescaled snapshots. As seen in Fig. 3.1, the error in the number counts is in the range $\pm\,10\,\%$ for all simulations except for (0.80, 0.40) and for masses $< 10^{14}\,h^{-1}M_\odot$. At higher masses, Poisson noise is significant. In addition, these clusters are the last structures to have collapsed and thus are most sensitive to changes in the growth rate governed by the background cosmology. Since we opt for a minimisation scheme covering a large range of halo masses, the rescaling parameters are not necessarily the best ones for cluster-size haloes. This could then bias the predicted masses. The best matches are found for the (0.29, 0.81) and (0.40, 0.70) cosmologies, with fractional differences $\lesssim 3\,\%$. Overall, this performance is similar to that stated in AW10.

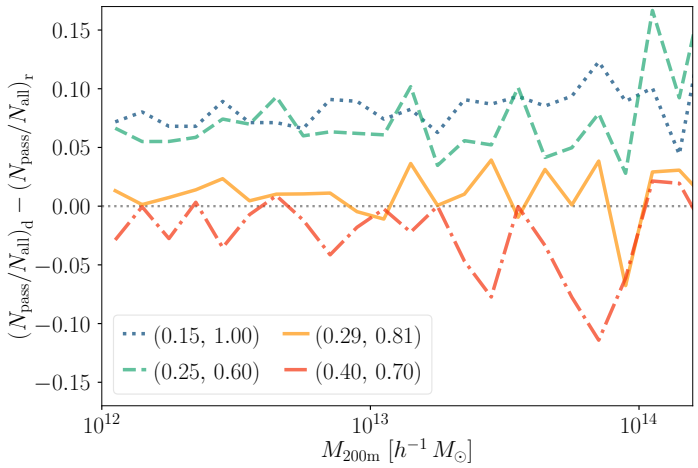

Figure 3.2: Difference in the fraction of relaxed haloes between the direct and rescaled simulations per 0.1 dex mass bin with the $d_{\rm off} + f_{\rm sub}$ cuts enforced (the results are similar if only the $d_{\rm off}$ cut is applied).

Trends for passing the relaxation cuts are similar in the direct and rescaled simulations, with cuts more effective at the high mass end, and peak passing rates between 54 and 73 % for the $10^{12.0} - 10^{12.1} h^{-1}\,M_\odot$ mass bin. As Fig. 3.2 illustrates, there are however some differences between the direct and rescaled simulation in the fraction of haloes per mass bin which satisfy the relaxation criteria. For (0.15, 1.00) and (0.25, 0.60), fewer haloes per mass bin survive the cuts, which may indicate a possible redshift dependence of the cut efficiency, as the rescaled signals come from fiducial snapshots at higher redshifts. This implies that we do not only have a slight scatter in the number of haloes but also in the properties of the haloes which pass the relaxation cuts.

Almost all haloes ($\sim$ 99 %) with $M_{\rm 200m} \geq 10^{12} h^{-1}\,M_\odot$ in the direct simulations have matches in the rescaled simulation (and the few non-matches have no significant impact on the profile statistics considered here). However, properties of matching haloes are usually not identical. The fractional difference in recorded $M_{\rm 200m}$ between the matched haloes in the direct simulation and their matched rescaled counterparts is shown in Fig. 3.3. Both a scatter and a systematic trend with mass and cosmology are discernible. For example, haloes in the rescaled simulation tend to be less massive than their counterparts for (0.15, 1.00). These trends are in part responsible for differences in the halo profiles between the direct and rescaled simulations discussed in the following sections.

3.6.2 3D density profiles

In Fig. 3.4 we plot the median density profiles for five mass bins in the (0.25, 0.60) cosmology in 40 log-equidistant bins between $0.03 - 3\,h^{-1}\,$Mpc. The halo profiles in the direct and rescaled simulations display remarkable agreement, with differences of at most 20 % over two orders of magnitude in density and scale. The differences likely reflect different mass accretion histories and formation times for the direct and rescaled haloes. They are characterised by two features: (i) an underestimation (overestimation) of the density near the halo centre, and (ii) an overestimation (underestimation) of the density near the transition scale between the 1-halo and 2-halo terms for the (0.15, 1.00), (0.25, 0.60) and (0.29, 0.81) cosmologies, with

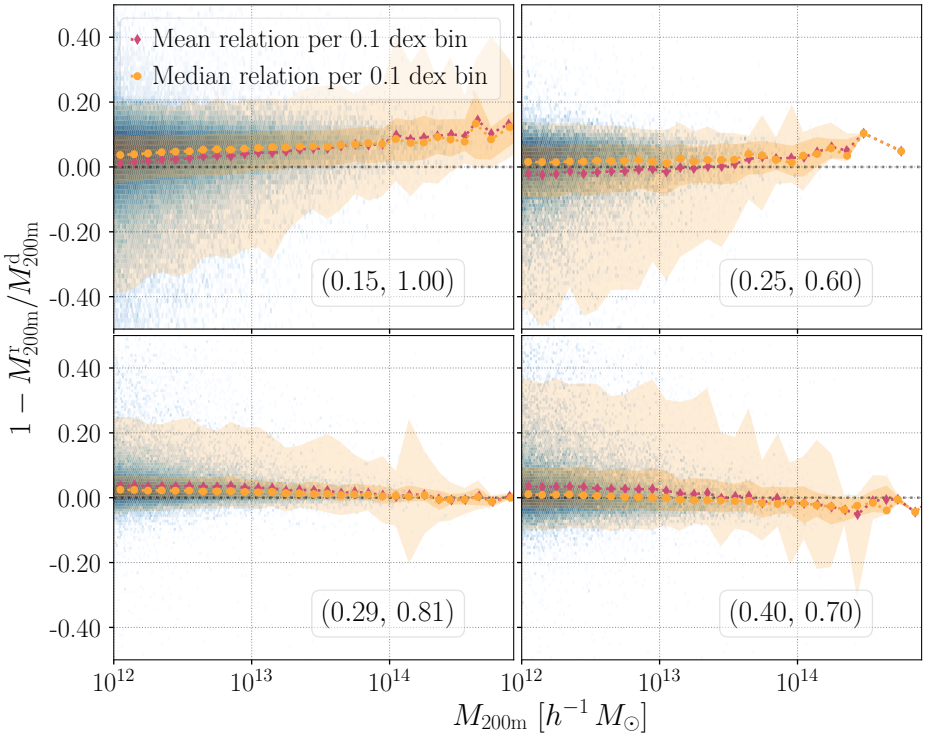

Figure 3.3: Fractional difference in the mass of matched haloes identified in direct and rescaled simulations. Each panel shows results for a different combination of Ω_m and σ_8 indicated in the legend. Contours enclose 68 % and 95 % of the distributions, and symbols mark the mean and median values per mass bin.

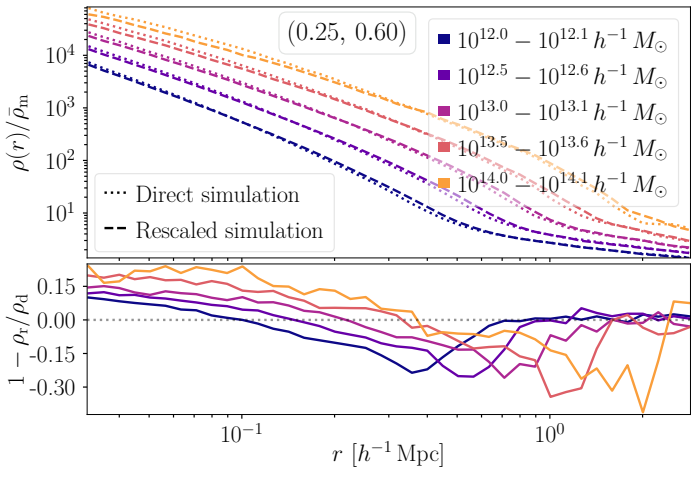

Figure 3.4: 3D comoving matter density profiles $\rho(r)$ in units of the cosmic mean density $\bar{\rho}_\mathrm{m}$ as function of radius r for all haloes in direct and rescaled simulations of the $\Omega_\mathrm{m} = 0.25, \sigma_8 = 0.60$ cosmology for five different mass bins (see legend). Fractional differences between the results from the two simulations are shown in the bottom panel.

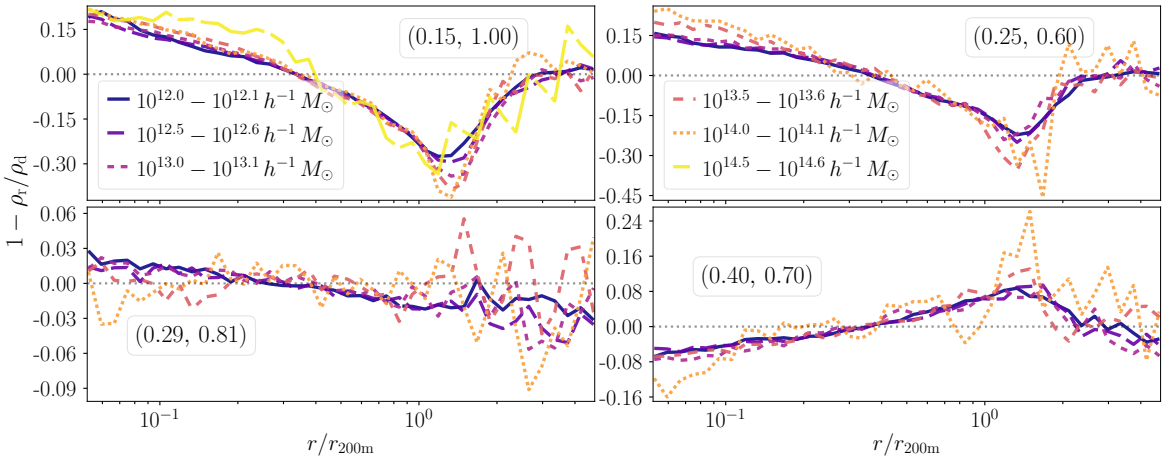

Figure 3.5: Fractional differences in the 3D density profiles of haloes in the direct and rescaled simulation snapshots. Each panel displays results for a different background cosmology and for five to six disjoint halo mass bins, as indicated by the legend. The x-axis is in units of the halo $r_{200\mathrm{m}}$ radius, which highlights that the differences are almost independent of mass.

the opposite signs for (0.40, 0.70) and (0.80, 0.40).

Fig. 3.5 shows the fractional difference for four of our test simulations for haloes in four to six mass bins, where more than twenty haloes have been recorded in the direct and rescaled simulations. The magnitude (though not always the sign) of the differences is similar to that for the (0.25, 0.60) cosmology. From approx. 0.3 to $3\,r_{200\mathrm{m}}$, the rescaled profiles have an outer bias with the opposite sign to the inner ($r \lesssim 0.3\,r_{200\mathrm{m}}$) profile bias, until they reach better agreement at larger scales ($r > 3\,r_{200\mathrm{m}}$). This suggests that the simulations have a similar halo bias. Fewer haloes in the higher mass bins lead to a larger scatter, predominantly in the outskirts where the active evolution takes place. Performing the same tests with just haloes passing the relaxation cuts or matched haloes yield similar results as for the whole population, indicating that the biases are universal features. We show the corresponding fractional differences for matched haloes only in Section 3.11.

3.6.3 Weak lensing profiles

As shown in Fig. 3.6, the small differences in the 3D density profiles propagate to small differences in the weak lensing profiles. The best agreement between the profiles of the rescaled and direct simulations is reached for (0.29, 0.81). The other cosmologies show larger differences, in particular in the inner profiles. In contrast, the outer profile bias is barely discernible except for the low mass bins for (0.25, 0.60), implying that it is washed out by taking the mean and calculating the projection. If we increase the mass bin width to 0.2 dex and recompute the profiles, the outer profile bias almost completely vanishes in 2D but it is still discernible in 3D for median profiles. The transition regime scatter does not necessarily dampen at larger scales[8]. For the total maximum and median values of the residuals below $r_{200\mathrm{m}}$, we refer to Table 3.2.

As for the 3D density profiles, we find negligible differences between all haloes and all

[8]We calculated the large scale $\Delta\Sigma$ for (0.29, 0.81) for the same mass bins for $3 - 30\,h^{-1}$ Mpc and there are small differences at the level of the scatter over this range.

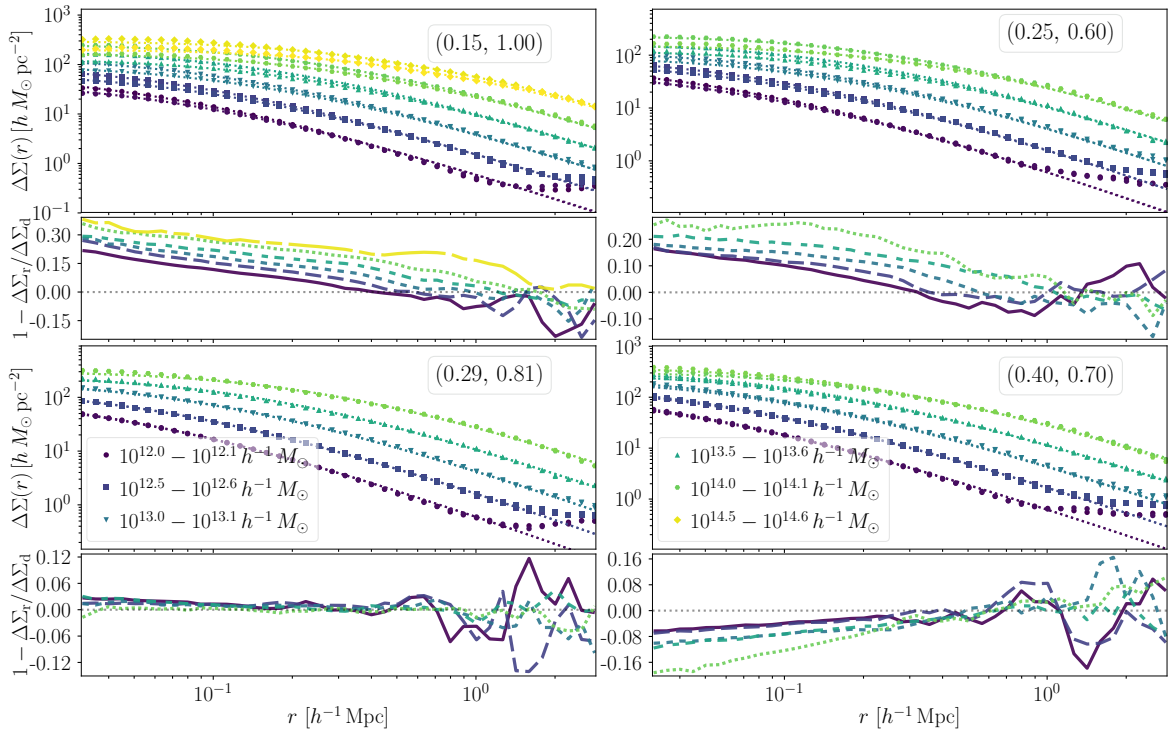

Figure 3.6: Differential excess surface mass density profiles $\Delta\Sigma(r)$ for stacks of haloes in the direct and rescaled simulations. Different colours indicate the different halo mass bins displayed whereas different panels show results for different cosmologies, where the bottom sub-panels show fractional differences with the same mass bin line styles as in Fig. 3.5. In the upper sub-panels, the best fit NFW profiles are indicated by dotted lines. The results for the (0.80, 0.40) cosmology are presented in Section 3.10.

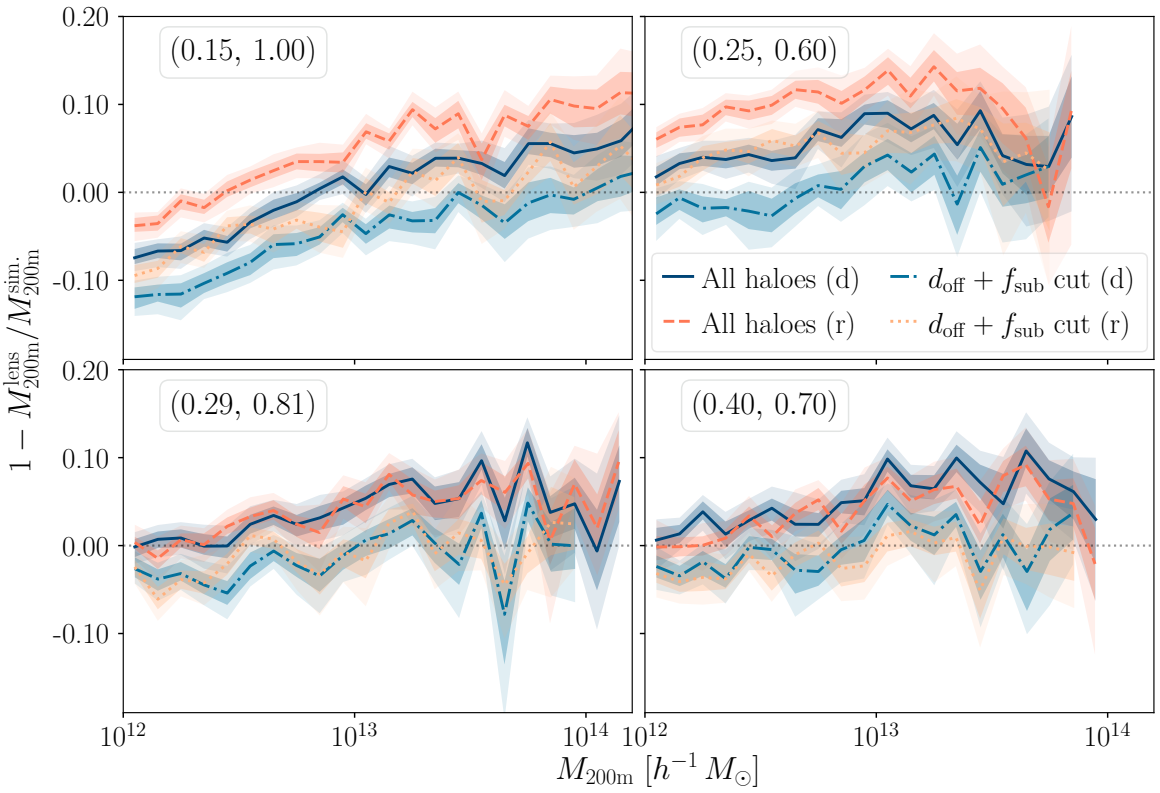

Figure 3.7: Fractional differences between the true mean mass of haloes in our simulations, $M^{\rm sim.}_{\rm 200m}$, and that inferred from their $\Delta\Sigma$ profiles, $M^{\rm lens}_{\rm 200m}$. Each panel focuses on a particular cosmology, and it shows results from the direct and rescaled simulations for all haloes and only for those relaxed according to two different criteria. The coloured regions mark the 68 % and 95 % percentiles, estimated from the bootstrap resample.

matched haloes. However, the scatter in the 2-halo transition regime is dampened, and the inner and outer profile biases are accentuated, especially for (0.29, 0.81). In addition, there are no conspicuous differences between the profiles for all haloes, for those which pass the $d_{\rm off}$ relaxation cut and for those which pass both $d_{\rm off} + f_{\rm sub}$ relaxation cuts.

Fig. 3.6 also illustrates that the $\Delta\Sigma$ profiles for $r \lesssim r_{\rm 200m}$ are well described by NFW lens profiles. We fit the measured mean profiles by minimising Eq. (4.6.1) with both $c_{\rm 200m}$ and $r_{\rm 200m}$ as free parameters. Fig. 3.7 shows the relative difference between the mean $M_{\rm 200m}$ recorded by the halo finder and the value fitted from the $\Delta\Sigma$ profiles. For the simulations with rescaled fiducial snapshots close to $z = 0$, the rescaled and direct simulation mass biases have similar amplitudes and show a similar evolution in mass with additional scatter at the high mass end. Introducing relaxation cuts shifts the amplitude consistently in the direct and rescaled simulation towards zero and for some high mass bins the bias changes signs, presumably due to scatter. The results with only the $d_{\rm off}$ cut enforced are similar to the ones where both cuts are imposed.

The negative bias for low mass haloes, particularly for (0.15, 1.00), is likely due to a lack of spatial resolution, which causes the measured lensing profiles to fall below the analytic profiles in the innermost regions. Moreover, for (0.15, 1.00) and (0.25, 0.60), there is a visible systematic offset between fit masses of the rescaled and direct simulations, which is preserved

with the introduction of cuts. Small but significant cosmology-dependent deviations from the analytic NFW lens profiles even for relaxed haloes might cause this offset. This requires further investigation in future work.

3.6.4 Concentration-mass relations

In Fig. 3.8, we compare the values of the concentration parameter from the 3D and 2D NFW fits to the predictions of the model described in Section 3.4.2. At the low mass end, the finite force resolution of the simulations affects the inner halo profiles and thus the concentrations estimates noticeably, in particular for (0.15, 1.00) due to its larger softening scale. The vertical dotted lines in Fig. 3.8 and 3.9 mark the halo mass above which the scale radius exceeds $r_\mathrm{s} > 6\,l_\mathrm{s}$ for the theory predictions, and thus the concentrations estimates are less affected by the finite force resolution.

In 3D, the model fails to predict the concentration-mass relation within the statistical errors for the general population. Additional cuts remove the tension, as Fig. 3.9 shows for (0.15, 1.00). For low mass haloes, the Einasto fits favour higher c-values than the NFW fits (see Section 3.12) and have the best agreement with the L16 model with the cuts enforced (which is encouraging since the model is supposed to match such relations). We are able to reach a complete agreement with the model with the cuts enforced with the Einasto parameterisation for all cosmologies where we use snapshots close to $z = 0$ in the fiducial run.

Yet, the model cannot describe the measured rescaled $c(M)$-relation for (0.25, 0.60). This is caused by a failure to model the signal at $z = 0.56$ in the fiducial cosmology. We have also computed the unscaled $M_{200\mathrm{c}}$ concentration-mass relations for median Einasto $c(M,\, z)$ relations with the corresponding cuts implemented[9], which yield the highest available concentrations per mass bin. Even in this case, the model predicts higher than observed concentrations. This could be due to the neglect of the redshift evolution of the collapse threshold.

In 2D, the model fits the measured values well at high masses, particularly for the relaxed subpopulations. Due to limited resolution, we cannot discern the expected monotonous $c(M)$-relation in 2D below $\approx 10^{12.7}\,h^{-1}M_\odot$ for (0.15, 1.00). This effect is present in the low mass bins for (0.25, 0.60) as well. The relations in 2D and 3D mainly differ due to different binning choices; in 3D we follow the approach in L16 whereas we opt for an observation conforming choice in 2D. Fewer bins in the inner projected regions of the stacked haloes combined with the down-weighting of these bins result in less sensitivity to the concentration, which explains the flat relations for low mass haloes. On the other hand, the masses are still determined well which is reflected in the small horizontal error bars.

As Fig. 3.10 illustrates, the difference in concentration Δc between the direct and rescaled simulations is approximately constant for haloes in the mass range $10^{12} - 10^{14}\,h^{-1}M_\odot$, and moreover roughly consistent with the model predictions. The deviation for (0.25, 0.60) results in a discrepancy between the model and the measured difference relation, but for (0.29, 0.81), (0.40, 0.70) and partly for (0.15, 1.00) at the high mass end, there is consistency both in 3D and for the lensing profiles. For low mass haloes, resolution effects and the relatively higher amplitude of the (not modelled) 2-halo term obscure the results. At the high mass end, the low number of haloes cause a larger scatter.

[9]Since $M_{\Delta\mathrm{m}} > M_{\Delta\mathrm{c}}$ generally holds, the cuts are more conservative with a $M_{\Delta\mathrm{c}}$ mass definition as neither the centre-of-mass, the position of the most bound particle nor the mass contained in substructure are altered for the same halo.

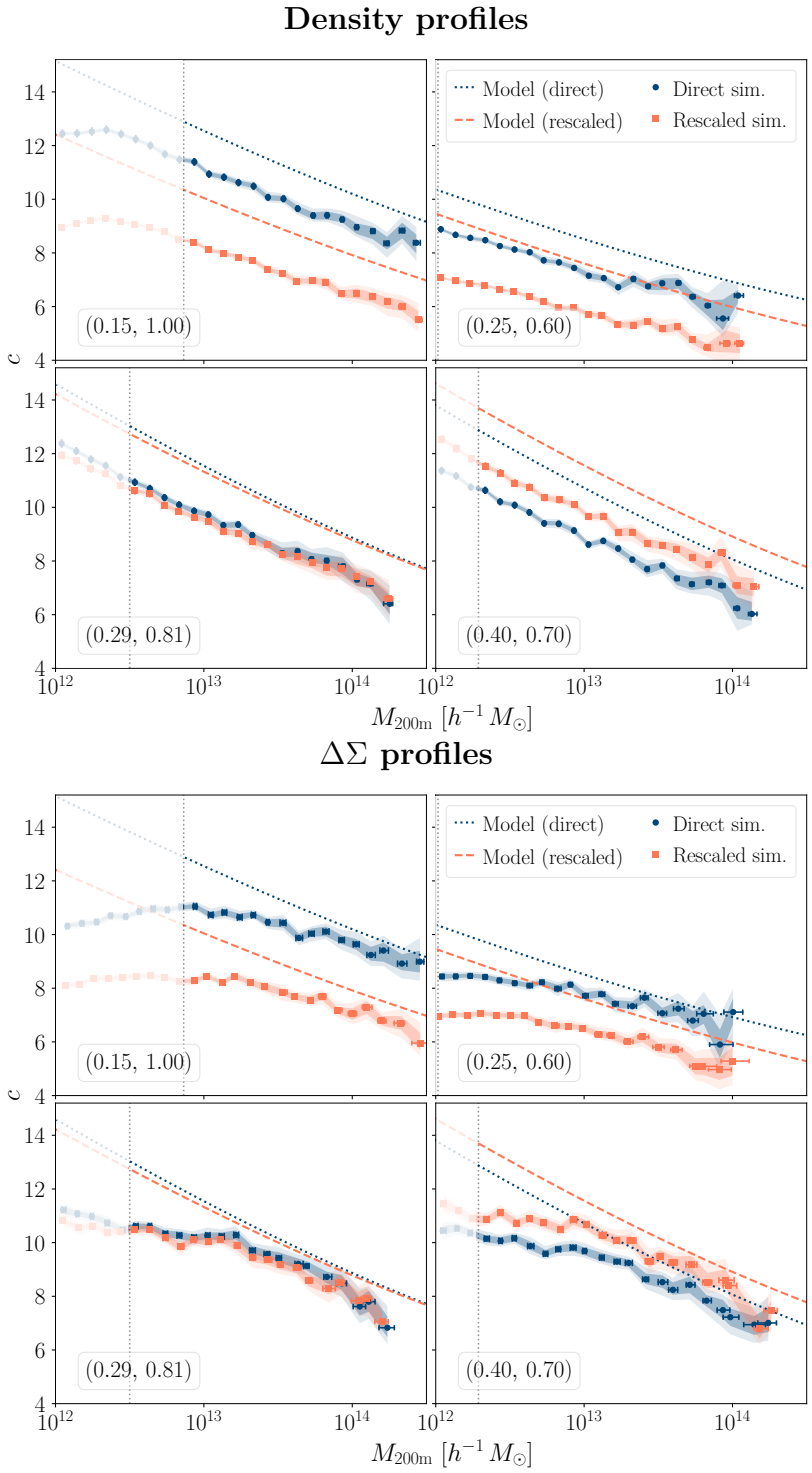

Figure 3.8: The concentration-mass relation of haloes in rescaled and direct simulations. Concentrations were estimated from NFW fits with the halo mass as a free parameter. The left and right plots show results from employing 3D density profiles and $\Delta\Sigma$, respectively, and each sub-panel focuses on a different cosmology. Dotted and dashed lines show the predictions of the model by L16. Symbols mark the mean relations, and shaded regions show the 68 % and 95 % of the distribution at a fixed mass. Horizontal error bars indicate the spread in the fitted M_{200m} masses. The vertical dotted lines denote the mass limit below which the finite force resolution affects the concentration estimates. Note that the disagreement between the model and the measurements originates mostly from unrelaxed haloes (cf. Fig. 3.9). For an analogous plot using concentrations obtained with Einasto profiles, see Section 3.12.

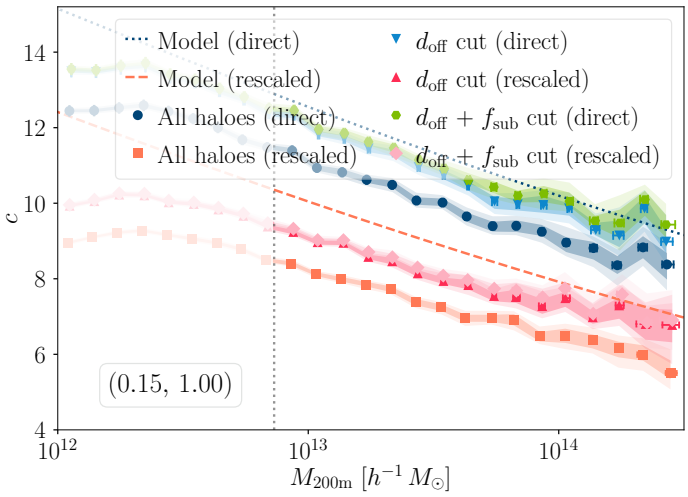

Figure 3.9: The impact of unrelaxed haloes in the concentration-mass relation. Different lines show the results for direct and rescaled halo catalogues after different cuts were applied to eliminate unrelaxed systems. Note that applying relaxation cuts increases the amplitude of the relation and produces a better agreement with the theoretical models.

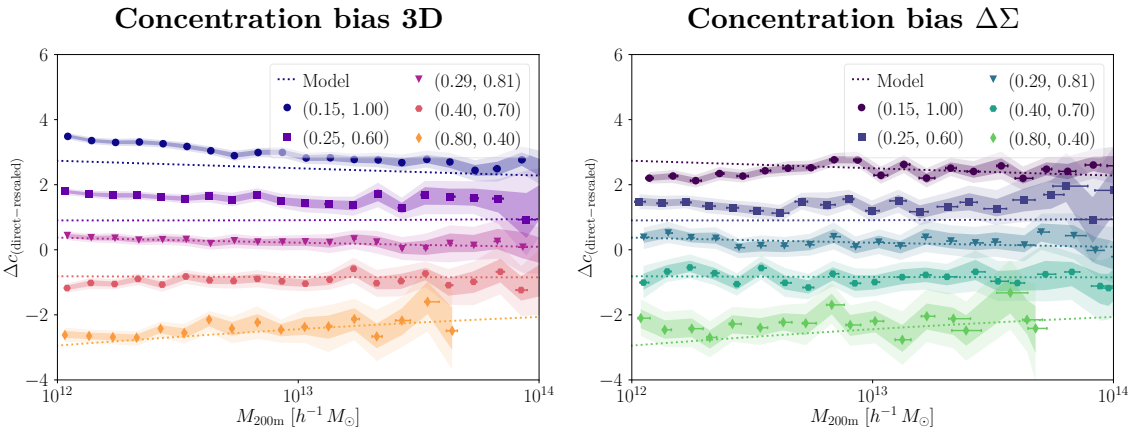

Figure 3.10: The difference in concentrations measured in the direct and rescaled simulations, $\Delta c_{\rm (direct-rescaled)}$, as a function halo mass at $z = 0$. Concentrations were measured by fitting NFW profiles to 3D density profiles (left panel), and to $\Delta\Sigma$ profiles (right panel). Different colours indicate results for different combinations of $(\Omega_{\rm m}, \sigma_8)$. Dotted lines correspond to the predictions for this quantity based on the L16 model. The shaded regions mark the 68 % and 95 % percentiles, and horizontal error bars the range of fitted halo masses.

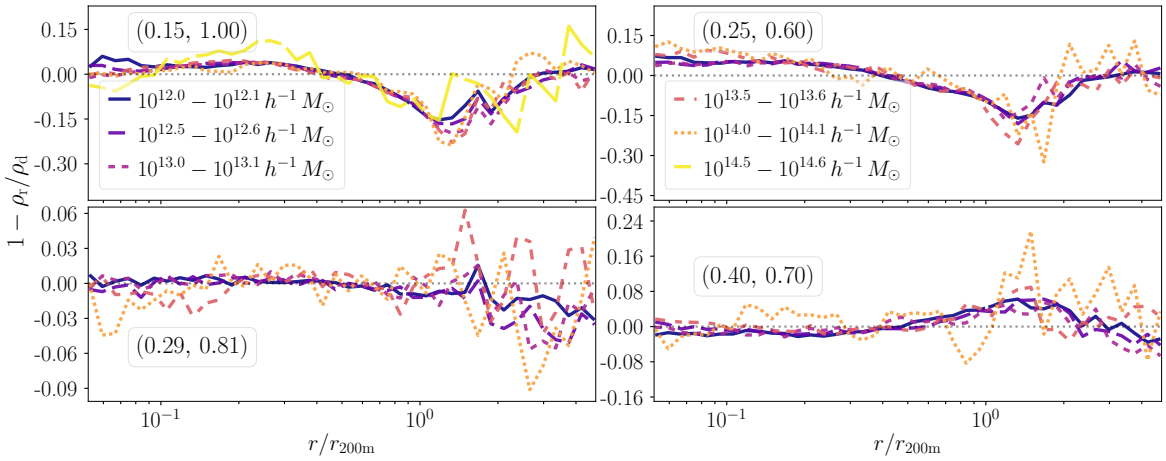

Figure 3.11: Same as Fig. 3.5 but after correcting the inner profiles of rescaled haloes.

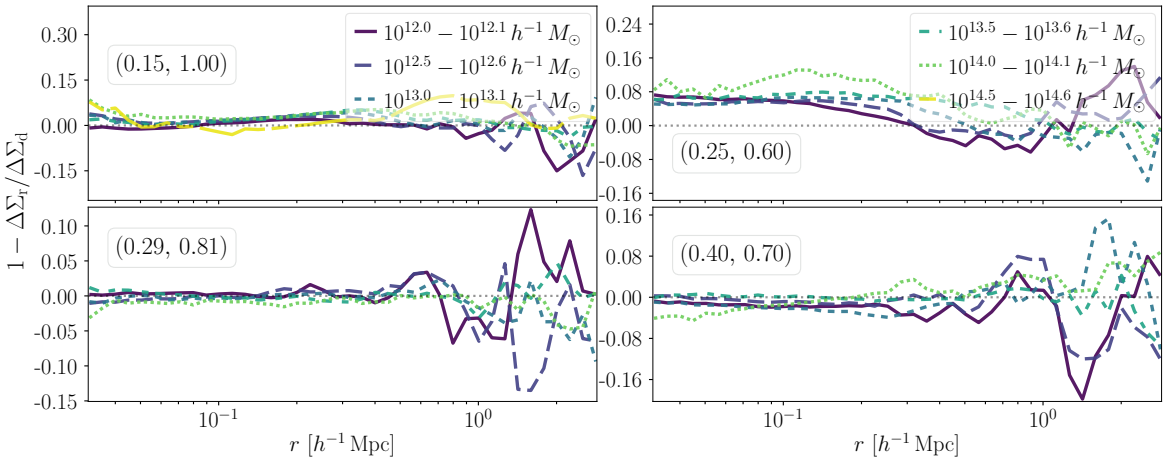

Figure 3.12: Same as Fig. 3.6 but after correcting the inner profiles of rescaled haloes.

The constant Δc relations hold for the relaxed populations as well, especially for $\Delta\Sigma$, though the variance increases. The small changes for the 3D density profiles are quantified by comparing $\Delta c_\mathrm{relaxed}/\Delta c_\mathrm{all\ haloes}$ for haloes with $10^{12} - 10^{14}\,h^{-1}\,M_\odot$ masses and record the median differences in the mass bins where we have more than twenty haloes for each imposed cut. This produces variations of the order of 5 % but there are no consistent trends present for both the NFW and Einasto parameterisations. This means that whereas the L16 model fails to accurately predict the concentration-mass relations for halo samples containing both relaxed and unrelaxed systems, it can predict the difference in this relation between two simulations for such a mixed population very well both for 3D density and $\Delta\Sigma$ profiles. Hence, it is suitable for modern surveys.

3.6.5 Concentration corrected profiles

Motivated by the good agreement in Fig. 3.10, we correct the rescaled profiles by multiplying the measured values with the ratio between the fitted profile to the rescaled simulation data

Residuals:		$\rho(r)$, $30\,h^{-1}\,\mathrm{kpc} < r < r_{200\mathrm{m}}$				$\Delta\Sigma(r)$, $30\,h^{-1}\,\mathrm{kpc} < r < r_{200\mathrm{m}}$			
		Pre-correction		Post-correction		Pre-correction		Post-correction	
Simulation	Halo mass range	Max	Median	Max	Median	Max	Median	Max	Median
(0.15, 1.00)	$10^{12.0} - 10^{14.8} h^{-1}\,M_\odot$	35 %	22 %	−17 %	−9.1 %	39 %	30 %	10 %	5.2 %
(0.25, 0.60)	$10^{12.0} - 10^{14.2} h^{-1}\,M_\odot$	25 %	15 %	−17 %	−7.4 %	36 %	18 %	19 %	7.3 %
(0.29, 0.81)	$10^{12.0} - 10^{14.5} h^{-1}\,M_\odot$	16 %	2.5 %	−16 %	1.3 %	6.1 %	2.4 %	5.1 %	−1.0 %
(0.40, 0.70)	$10^{12.0} - 10^{14.4} h^{-1}\,M_\odot$	25 %	7.4 %	−18 %	3.6 %	−26 %	−9.6 %	−15 %	−2.1 %
(0.80, 0.40)	$10^{12.0} - 10^{13.8} h^{-1}\,M_\odot$	43 %	22 %	11 %	6.5 %	−42 %	−29 %	13 %	−4.3 %

Table 3.2: Total and median maximum deviation between the direct and rescaled simulation, $1 - \rho_\mathrm{r}/\rho_\mathrm{d}$ and $1 - \Delta\Sigma_\mathrm{r}/\Delta\Sigma_\mathrm{d}$, for 3D median and for 2D mean profiles per mass bin for radial bins in the given range before and after the concentration correction.

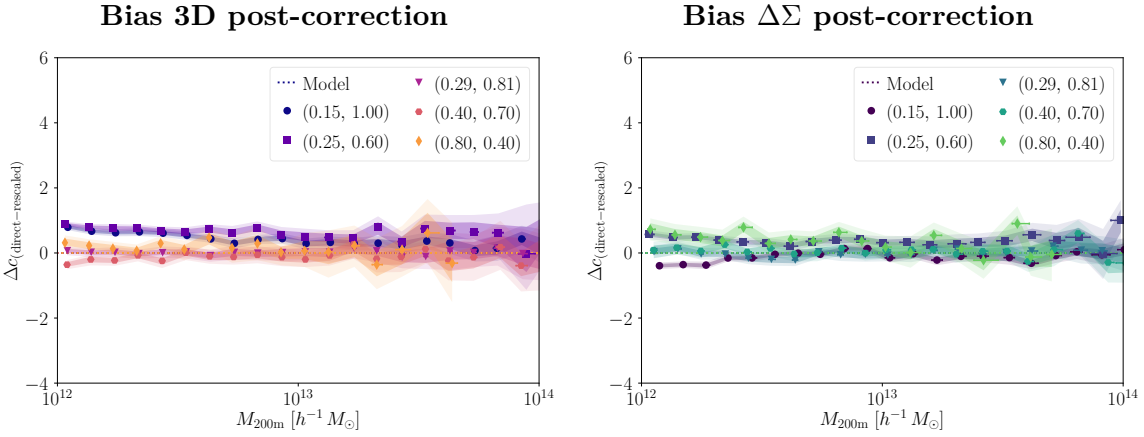

Figure 3.13: Same as Fig. 3.10 but after applying our corrections in Eq. (3.6.1) and Eq. (3.6.2) to the rescaled profiles. The concentration bias for the corrected profiles is reduced considerably.

and a modified profile with the concentration bias from the model, $\Delta c(r_{200\mathrm{m}})$:

$$\rho'(r) \mapsto \frac{\rho_{\mathrm{NFW}}\left(r,\, c + \Delta c\left(r_{200\mathrm{m}}\right),\, r_{200\mathrm{m}}\right)}{\rho_{\mathrm{NFW}}\left(r,\, c,\, r_{200\mathrm{m}}\right)} \rho'(r), \tag{3.6.1}$$

$$\Delta\Sigma'(r) \mapsto \frac{\Delta\Sigma_{\mathrm{NFW}}\left(r,\, c + \Delta c\left(r_{200\mathrm{m}}\right),\, r_{200\mathrm{m}}\right)}{\Delta\Sigma_{\mathrm{NFW}}\left(r,\, c,\, r_{200\mathrm{m}}\right)} \Delta\Sigma'(r), \tag{3.6.2}$$

for all radii $r \lesssim r_{200\mathrm{m}}$. We will refer to these correction factors as $\gamma(r_i)$. The Einasto correction is calculated in the same manner (see Section 3.12). Since $\Delta c(M)$ only weakly depends on M, there are no significant differences between using the fitted $M_{200\mathrm{m}}$ or halo finder value.

Correcting the profiles up to $3\,h^{-1}$ Mpc does not significantly affect the lensing signal, but jeopardises the agreement for the 2-halo term in 3D (see Fig. 3.18). We find that restricting the correction to $r < 1.8\,r_{200\mathrm{m}}$ reduces differences in the 1-to-2-halo transition region without compromising the agreement on larger scales.

The concentration correction could be additive instead of multiplicative. This gives a slightly better performance on scales $r > r_{200\mathrm{m}}$, since the field differences are small, but this correction also induces a small bias and should thus be applied below a cutoff radius. The multiplicative correction preserves the shape of the residual throughout the transition regime slightly better. Otherwise, we have checked that there are no significant differences between the two for all halo mass bins and cosmologies with NFW or Einasto parametrizations for matched haloes, in bootstrapped stacks or individually. Both largely preserve the width and shape of the Δc distribution around the median or the mean concentration, with no obvious advantages, and yield $\Delta c = 0$ if we correct the rescaled profiles with the measured direct concentrations.

The residuals for the corrected 3D density profiles are shown in Fig. 3.11 and for the corrected $\Delta\Sigma$ profiles in Fig. 3.12. The maximum and median pre- and post-correction profile differences are listed in Table 3.2 for the 40 radial bins setup. Typically, the largest differences occur in the most or second most massive halo mass bin. In most cases, the correction reduces the differences by factors of two to five. For (0.25, 0.60), both the residual profiles and residual concentration differences indicate that a larger concentration correction than predicted by the L16 model could improve the agreement between direct and rescaled profiles.

However, when comparing the measured halo concentrations pre- and post-correction, we find significant improvement in the concentration mismatch between rescaled and direct simulations for all considered cosmologies, as Fig. 3.13 illustrates for all haloes (see Section 3.11 for the result for matched populations).

3.6.6 Correcting individual halo profiles

We also examine how the correction in Eq. (3.6.1) affect the concentrations from 3D profile fits to individual haloes. The joint distribution of concentrations for haloes above $10^{12.5}\,h^{-1}M_\odot$ in the (0.40, 0.70)-simulation and their rescaled counterparts is shown in Fig. 3.14. Applying the concentration correction translates the distribution towards the diagonal in a similar manner for high and low concentration haloes. This is a consequence of the modest mass evolution of the concentration bias for the cosmologies in this study. However, the correction cannot account for a slight tilt between the two simulations, with low-c (high-c) haloes having higher

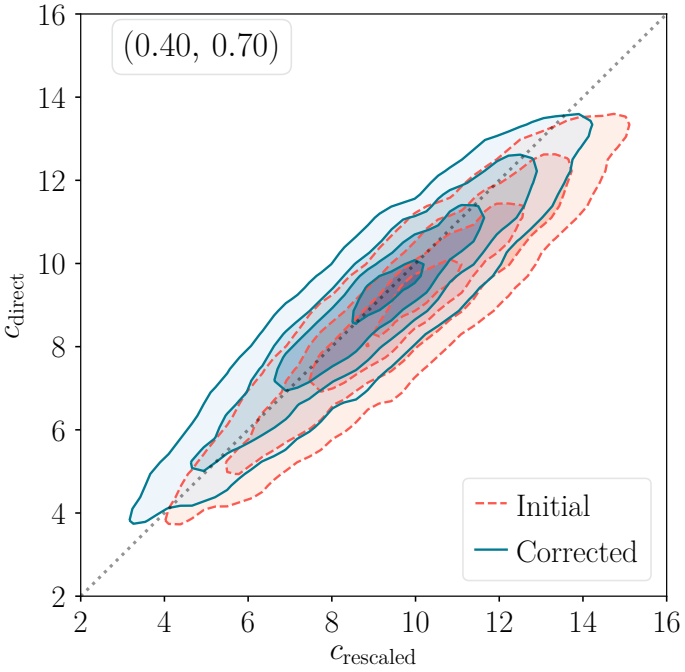

Figure 3.14: Effect of the density field correction on the NFW estimated concentration distribution for individual matched haloes in the direct and rescaled simulation with (0.40, 0.70) where the haloes in the direct simulation have $M_{\rm 200m} > 10^{12.5}\,h^{-1}\,M_\odot$. For smoother contours, the distributions have been convolved with a Gaussian filter with $\sigma = 1$.

(lower) concentrations in the direct simulation than in the rescaled simulation.[10]

The tilt is stronger for cosmologies with $\Delta\Omega_{\rm m} > 0$ away from the fiducial simulation with a clockwise tilt relative to the diagonal (see Section 3.11). For (0.15, 1.00) and (0.25, 0.60), there is a slight counter-clockwise tilt. The results are robust to changes in the fitting scheme.[11] We have checked that there are negligible differences for all cosmologies between the $c(M)$ relations computed from the median profiles and the median $c(M)$ relations from fits to individual haloes, and that the tilt in the distributions persist when one corrects the individual halo concentrations with the median measured relations.

The tilt in the joint distribution is also present for halo samples selected in narrower mass ranges. The asymmetry is partly washed out in the results for the median profiles, as both high c and low c haloes contribute to the effective density field per mass bin. However, this secondary rescaling concentration bias could influence analyses where the halo population is split into different concentration samples at fixed mass, such as assembly bias studies. Further studies with larger simulation volumes are required to accurately quantify this effect.

[10] This tilt persists when relaxation cuts are enforced, regardless of whether $r_{\rm 200m}$ is fixed or a free parameter, and is also present with Einasto parameterisations (Section 3.12).

[11] For all profile fits we use the Levenberg-Marquardt algorithm with ($c = 4$, $r_{\rm 200m} = r_{\rm 200m,\,sim.}$) as a starting point. We have checked that the results are insensitive to the starting point choice for physically viable parameter values. In addition we have computed the parameters with the limited-memory BFGS algorithm with bounds $c \in [1, 30]$ and $r_{200} \in [0.5\,r_{\rm 200m,\,sim.},\ 2\,r_{\rm 200m,\,sim.}]$ and obtain consistent results.

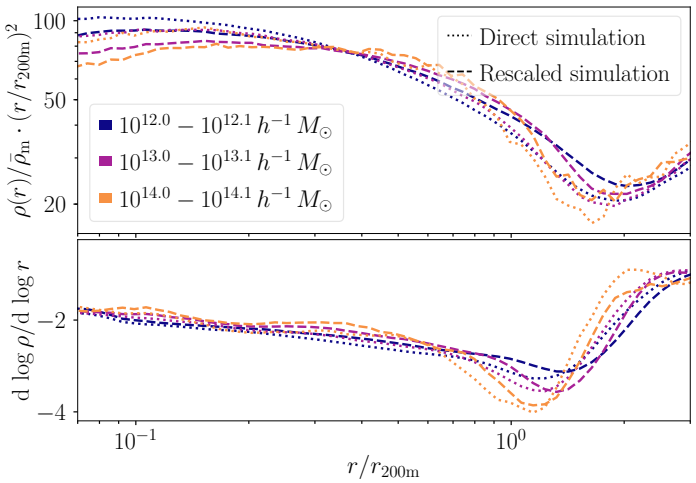

Figure 3.15: Comparison between direct and rescaled profiles and their radial derivatives for matched haloes for (0.25, 0.60) for three mass bins. The concentration bias is visible as an amplitude offset close to the halo centres whereas the outer profile bias corresponds to a radial shift of the profiles at the halo boundaries. This shift is visible in the radial derivatives of the field (computed with a fourth-order Savitzky-Golay filter with a window length of 15 bins) in the lower panel as well, where there are offsets in the positions of the steepest slope between the direct and rescaled profiles.

3.6.7 Halo outskirts

The concentration correction does not fully account for differences in the halo outskirts, as it focuses on rearranging material within the halo. Subsequent outer corrections could redefine the halo boundary and potentially improve agreement in the halo mass function. Fig. 3.15 highlights that the profile bias in the inner halo regions is mostly an amplitude offset, whereas the bias in the halo outskirts is rather a radial offset. Hence, correcting the rescaled profiles by shifting them radially in the outskirts can mitigate the outer profile bias.

In Fig. 3.16, we plot the measured differences in the location of the steepest slope of the density field for matched haloes. We adjust the position of the rescaled profile's steepest slope with $r^{(\mathrm{d})}_{200\mathrm{m}}/r^{(\mathrm{r})}_{200\mathrm{m}}$ to account for the mismatch in halo mass between the matched samples, which has a minor impact on the result. We compare these differences to the expected offset between the splashback radii r_sp, the apocentre of the first orbit of accreted material (e.g. Diemer & Kravtsov, 2014; Adhikari et al., 2014; More et al., 2015; Shi, 2016; Mansfield et al., 2017; Diemer et al., 2017), between the direct and rescaled profiles $\Delta r_\mathrm{sp} = r^{(\mathrm{d})}_\mathrm{sp} - r^{(\mathrm{r})}_\mathrm{sp}$. This radius has been proposed as an alternative, more realistic halo boundary instead of the virial radius, and it may coincide better with the radius at which gas is shock-heated and where in-falling substructures can be stripped of their host subhaloes (e.g. Wechsler & Tinker, 2018). There are claims of detections of the splashback radius in observational data (e.g. More et al., 2016; Baxter et al., 2017; Chang & DES Collaboration, 2018) using projected number density and weak lensing profiles of galaxy clusters. However, these observables are sensitive to the shortcomings of the cluster building algorithm in correctly identifying cluster members in projection, which can bias the result and induce false detections (Busch & White, 2017). In our study, we only focus on rescaling effects on the splashback radii from simulated 3D density profiles and leave the propagation of these errors to projected lensing profiles with realistic cluster finder algorithms for future work.

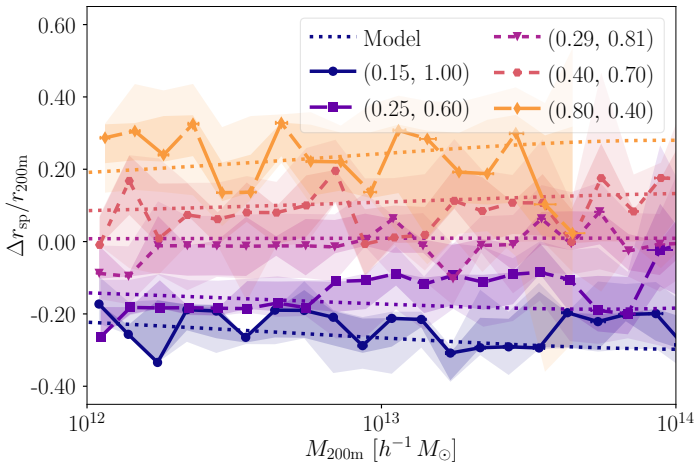

Figure 3.16: Measured differences in the location of the steepest slope of the density field for matched haloes w.r.t. to the Diemer et al. (2017) model, for the 75th percentile. Error regions for 95 % and 68 % are computed from resampled medians from stacks of matched haloes in the direct and rescaled simulation snapshots.

We apply the recent fit provided in Diemer et al. (2017) to simulation results in Diemer (2017) to predict the median splashback radius as a function of halo mass and cosmology. This model has been fitted by tracing billions of particle orbits in haloes spanning from typical cluster to dwarf galaxy host masses in different cosmological simulations up to $z = 8$. Percentiles correspond to the fraction of the first apocenters of the particle orbits contained inside a given radius. Particles which were contained in a subhalo with mass exceeding 1 % of the host halo mass at infall are excluded to minimise bias from dynamical friction. In accordance with previous studies (e.g. Diemer & Kravtsov, 2014; More et al., 2015), the relation between the halo accretion rate Γ and the ratios $r_{\rm sp}/r_{\rm 200m}$ and $M_{\rm sp}/M_{\rm 200m}$ is found to be well described by a functional form $X_{\rm sp} = A + Be^{-\Gamma/C}$ where $X_{\rm sp}$ is either ratio and A, B and C are free parameters where B and C depend on the matter fraction $\Omega_{\rm m}$ and halo peak height $\nu = \delta_{\rm c}/(D(z)\sigma(M_{\rm h}))$ with $M_{\rm h}$ as the halo mass. In addition, the median accretion rate $\Gamma(\nu, z)$ can be well captured by a parameterisation $\Gamma = A'\nu + B'\nu^{3/2}$, where A' and B' are polynomials in z. We use this expression for the median accretion rate to compute the radii.[12] The measurements trace the model prediction, except for (0.80, 0.40) where the scatter is driven by poor statistics due to the small box size.

We also compute the radial shifts that minimise the largest relative difference between the direct and rescaled outer density profiles. Between $0.4 < r/r_{\rm 200m} < 2.0$, we locate the maximum of the $1 - \rho_{\rm r}(r)/\rho_{\rm d}(r)$ residual defining $r = r_{\rm max}$ and then shift the interpolated rescaled profile radially to find the radius $r_{\rm min}$ that minimises $1 - \rho_{\rm r}(r_{\rm min})/\rho_{\rm d}(r_{\rm max})$. The resulting shifts $r_{\rm max} - r_{\rm min}$ are shown in Fig. 3.17 for matched haloes with the $r^{\rm (d)}_{\rm 200m}/r^{\rm (r)}_{\rm 200m}$ correction. This shift is almost constant for haloes, all and matched, with $M_{\rm 200m}$ between $10^{12} - 10^{14}\,h^{-1}\,M_\odot$. For higher masses the result is obscured by scatter. The predicted

[12] As we are probing the median 3D density profiles, we opt for the 75th percentile of the model which was found to best match the median profiles in More et al. (2015), especially at the high mass end. The splashback radius rescales as $r_{\rm sp} \mapsto \alpha r_{\rm sp}$ and the predicted position $r^{\rm (r)}_{\rm sp}$ is hence given as the fitted solution in the fiducial simulation at the fiducial redshift with $\beta_{\rm m}^{-1} M_{\rm 200m}$ determining the peak height and $r_{\rm 200m}$.

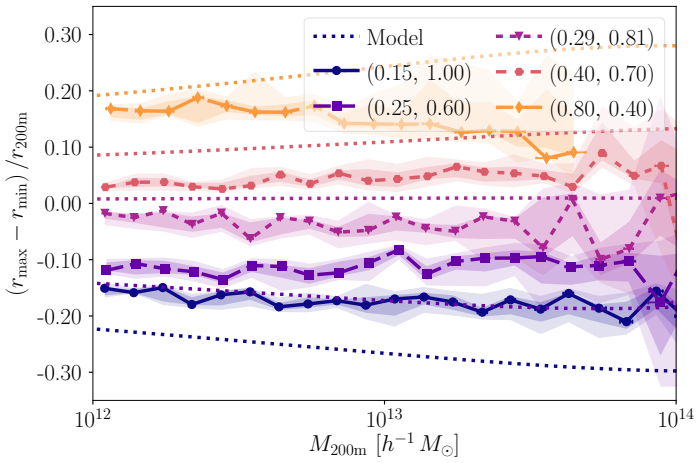

Figure 3.17: Measured density field outer profile bias for matched haloes vs. the predicted $\Delta r_{\rm sp}/r_{\rm 200m}$ bias using the model in Diemer et al. (2017).

splashback bias do not exactly match the required shifts to remove the radial bias[13], but they show similar relative amplitudes, signs and weak mass dependence. A splashback radius model may thus provide a good starting point for further improvements of the rescaled profiles and halo masses (an initial attempt to correct the masses is presented in Section 3.13).

As Fig. 3.18 illustrates the outer profile bias vanishes, if we shift the rescaled density field values radially by $r \mapsto r_{\rm min}/r_{\rm max} \times r$ or $r \mapsto r - \Delta r$ with $\Delta r = r_{\rm max} - r_{\rm min}$. Whereas the multiplicative correction performs better in the halo centre, the additive correction has a better large scale behaviour. To combine the radial shift correction with the concentration correction, we modulate each by a sigmoid function to restrict their actions to their intended radial range:

$$\begin{aligned} \rho \mapsto \rho' = \rho(r - \zeta(r)) + \xi(r),\ \zeta(r) = \frac{1}{1 + e^{-k_0(r-r_0)}}\Delta r, \\ \xi(r) = \frac{1}{1 + e^{-k_1(r_0-r)}} \cdot \left(\rho'_{\rm NFW} - \rho_{\rm NFW}\right), \end{aligned} \tag{3.6.3}$$

where r_0 marks the transition scale, k_0 and k_1 control the sharpness of the onsets of the corrections, and the concentration correction is evaluated at the unshifted radius. Fitting these parameters, r_0 in the vicinity of $r_{\rm 200m}$ seems preferred, but all parameters vary with mass and cosmology when fitting the rescaled simulation to the direct simulation. In Fig. 3.18 we plot one possible solution with $(r_0,\ k_0,\ k_1)$ as $(r_{\rm 200m},\ 9.2,\ 16.4)$, where Δc is obtained from the L16 model and Δr is measured. Future investigations are required to find the best set of parameters.

[13] Moreover, typically $r_{\rm max} \approx 1.3\, r_{\rm 200m}$, which does *not* coincide with the predicted position of the splashback radius for all masses and cosmologies.

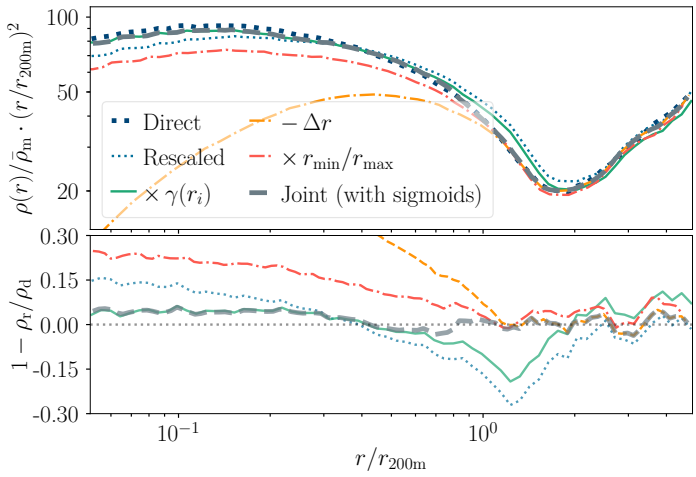

Figure 3.18: Profiles for matched haloes for $(0.25, 0.60)$ for $M_{200\mathrm{m}} \in [10^{13}, 10^{13.1})\,h^{-1}\,M_\odot$ in the direct simulation with different corrections applied (see the text for more detailed descriptions). Although not perfect, the concentration correction '$\times\,\gamma(r_i)$' mitigates the residual in the centre and the shifts remove the outer profile bias. These two corrections can be combined with sigmoids.

3.7 Discussion

The rescaling predictions for the halo matter and lensing profiles are reasonably accurate even before applying the concentration correction. Partly, this is due to the matched initial conditions. This ensures similar peak heights, proto-halo regions, environments, and tidal fields, which leads to similar growth histories, as the growing density perturbations subsequently cross the collapse threshold.

After our additional correction, the predictions become accurate at the 5 % level. In this section, we discuss the expected cosmology dependence of the corrections (Section 3.7.2), the method's accuracy in light of the expected impact of baryons (Section 5.6.4) and large-scale corrections (Section 3.7.4), as well its application for lensing mass estimations (Section 3.7.5).

3.7.1 Comparison to other approaches and further improvements

Our approach differs from the setup in Mead & Peacock (2014a) since it is a nonlocal operation on the density profiles built from the full 3D and 2D rescaled particle distributions whereas their method involve shifting the halo particle positions. They work with a subset of particles randomly sampled from the fiducial distribution to fill up the predicted density profile where information from the tidal tensor helps to account for the asphericity (this produces better agreement in halo morphology but does not take substructure into account which is problematic for satellite galaxies). It is not evident how much this sampling scheme differs from a refined method working on the actual 3D distribution of particles within the halo. A possible way to implement our algorithm as a localised, discrete mapping is to perform a local measurement of the spherically binned density field around each halo, use the correction to find the closest NFW/Einasto profile and shift the particles between the shells accordingly till some convergence criteria has been met. Preferably, this should prioritise displacements between adjacent shells. One could also account for the shape of the tidal tensor, compute Penna-Dines surfaces for accretion responses (cf. Mansfield et al., 2017) and extract addi-

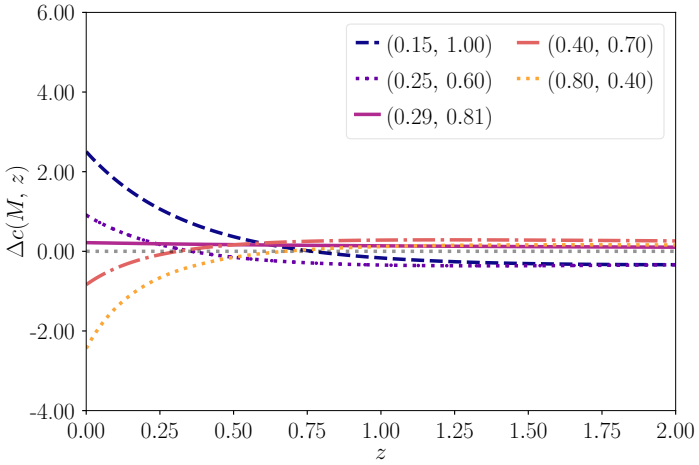

Figure 3.19: Expected bias in the concentration of rescaled haloes based on the L16 model, evaluated as the median bias for haloes with $10^{12} < M_{200\mathrm{m}}/(M_\odot\, h^{-1}) < 10^{14}$, as a function of redshift.

tional phase-space information to preserve the halo shape, composition, stream structure and extension.

3.7.2 Predicting the concentration bias as a function of cosmology

Due to the few simulations in our study, we cannot put strong constraints on a model-independent fitting function for the concentration bias. All cosmologies, with the exception of (0.25, 0.60), trace the $\Omega_\mathrm{m} - \sigma_8$ degeneracy favoured by weak lensing, which means that we have few constraints perpendicular to this line. We thus use the L16 model to predict the rescaled concentration bias for cosmologies and redshifts where we do not have access to a corresponding direct simulation.

Firstly, we investigate the redshift evolution in the cosmologies already covered. We use the linear growth factor relation in Eq. (3.4.6) to calculate the redshifts in the fiducial simulation which correspond to the higher redshifts in the direct simulation. We plot the median concentration bias for haloes with $M_{200\mathrm{m}}$ in $10^{12} - 10^{14}\, h^{-1}\, M_\odot$ as a function of redshift from $z = 0$ to $z = 2$ in the direct simulation in Fig. 3.19. Overall the difference in concentration decreases with redshift and there is a turnover point for all cosmologies expect (0.29, 0.81) where the bias changes sign. This is a consequence of the rescaling parameters being determined by the locally matched growth history. Yet, caution must taken as we have already seen that the model prediction works less well at higher redshifts in Fig. 3.10. To bring about a better agreement with the measurements, the model could be modified to feature a slight redshift dependence which either decreases C and/or raises f since these changes lower the amplitude of the $c(M)-$relation.

In Fig. 3.20, we plot the expected median Δc bias for haloes with masses $M_{200\mathrm{m}}$ in $10^{12} - 10^{14}\, h^{-1}\, M_\odot$ when rescaling the Millennium simulation (Springel et al., 2005b) to match target cosmologies with different Ω_m and σ_8 at $z = 0$, with the target matter power spectra generated by CAMB (Lewis et al., 2000) combined with linear growth factors (e.g. Hamilton, 2001) assuming a constant baryon fraction $\Omega_\mathrm{baryons}/\Omega_\mathrm{m}$. The corresponding contours for the rescaling parameters (α, z^*) are shown in Section 3.14. Rescaling to a lower σ_8 at fixed Ω_m or a lower Ω_m with a higher σ_8 induces a positive Δc, whereas raising Ω_m and lowering σ_8

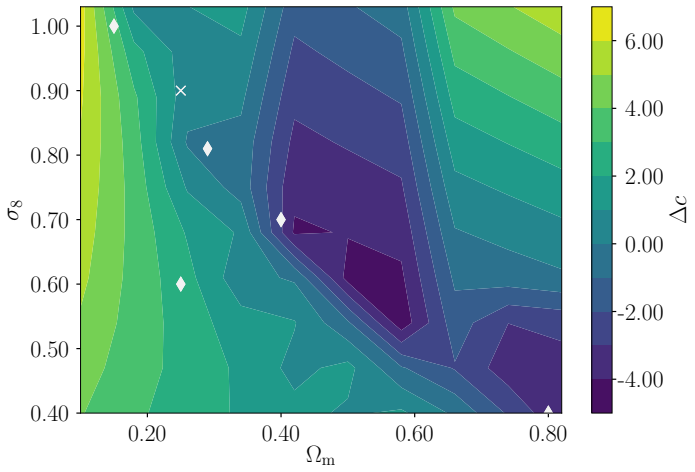

Figure 3.20: Expected bias in the concentration of rescaled haloes at $z = 0$ as a function of the value of Ω_m and σ_8. Our assumed fiducial cosmology is $\Omega_m = 0.25$ and $\sigma_8 = 0.90$ (marked by the white cross). The white diamonds mark the test simulations cosmologies employed in this Chapter.

will produce negative Δc.

If one relaxes the growth history constraint to permit matches in the future, negative redshifts[14] represent the preferred solutions for the $\Delta\Omega_m > 0$, $\Delta\sigma_8 > 0$ quadrant. Such solutions yield $\Delta c < 0$. If we instead restrict our redshift range to $z^* \gtrsim -0.8$, the concentration bias becomes positive again as we move further away from the degeneracy plane. The contours for the predicted Δr_{sp}-bias (see Section 3.14) partly trace the Δc contours with the opposite sign over most of the plane except in the $\Delta\Omega_m > 0$, $\Delta\sigma_8 > 0$ quadrant.

The concentration bias is a smooth function of cosmology, i.e. small changes in the cosmological parameters produce small concentration offsets. A set of well-placed simulations could thus be used together with rescaling to efficiently cover a large region of parameter space accurately.

Lastly, we discuss rescaling to emulate a WMAP7 cosmology (Komatsu et al., 2011) and Planck (2014) cosmology (Planck Collaboration, 2014) at $z = 0$ using the Millennium simulation with SAMs in Guo et al. (2013a) with the AW10 weighting scheme and in Henriques et al. (2015) with the AH15 scheme, respectively. The corresponding (z_*, α) are (0.28, 1.04) and (0.12, 0.96), respectively, which produce $\Delta c(M)$ relations with shallow slopes with median biases $\Delta c = 0.88$ ($\Delta c_{min} = 0.77$, $\Delta c_{max} = 0.97$) and $\Delta c = 0.06$ ($\Delta c_{min} = 0.03$, $\Delta c_{max} = 0.06$) for M_{200m} between $10^{12} - 10^{14}\, h^{-1}\, M_\odot$. This means that the concentration bias for haloes in Henriques et al. (2015) is almost negligible. We plot these relations in Section 3.15 with the predicted redshift evolutions, where the biases also are reduced at earlier times. Hence, we can predict the bias of the measured lensing signal around central SAM galaxies in rescaled simulation snapshots.

3.7.3 Baryonic effects

Our method currently does not account for effects baryonic processes have on halo profiles. The impact of baryonic processes on the matter distribution has been investigated in simula-

[14] An existing N-body simulation can cheaply be evolved into the future (see e.g. Angulo & Hilbert, 2015).

tions (e.g. by van Daalen et al., 2014; Velliscig et al., 2014; Schaller et al., 2015a; Leauthaud et al., 2017; Mummery et al., 2017). Baryon physics affects the matter clustering by $\sim 10\,\%$ on scales $\lesssim 1\,\mathrm{Mpc}$. The impact on $\Delta\Sigma$ is similar. By matching the haloes in Illustris with their counterparts in a dark matter-only run, the baryonic physics has been found to suppress $\Delta\Sigma$ by $\sim 20\,\%$ from $r \gtrsim 0.4\,h^{-1}\,\mathrm{Mpc}$ to $r \leqslant 4\,h^{-1}\,\mathrm{Mpc}$ (Leauthaud et al., 2017).

Even for cosmologies far from the fiducial cosmology, the rescaling predictions without the concentration corrections are at most off by $40\,\%$ in the innermost radial bins, and the disagreement decreases to $\sim 10\,\%$ at $r \approx 1\,h^{-1}\,\mathrm{Mpc}$. The concentration correction substantially improves agreement in the inner region. Moreover, the discrepancies are much smaller for cosmologies closer to the fiducial cosmology. This means that the bias induced by rescaling is subdominant to the baryonic feedback effects below $1\,h^{-1}\,\mathrm{Mpc}$, except for extreme cosmologies.

3.7.4 Large scales

Here, we do not attempt any corrections at very large scales. We have computed the difference between the matter power spectrum in the weakly nonlinear to the nonlinear regime for (0.15, 1.00) with and without the large-scale displacement field correction from AW10 and it was found to be negligible. The large-scale halo-matter correlations do not differ significantly between the rescaled and direct simulations for the halo masses we are investigating in 3D. There appears at most a small offset with surrounding scatter. The connection and coupling between this offset and the detected mass bias, as well as the proper response of the large-scale correlations to the rescaling transform are topics for future studies. In halo models of GGL (e.g. Oguri & Takada, 2011), the large-scale lensing signal (2-halo term) is directly related to the projected linear power spectrum. It should thus be straightforward to compute its response to rescaling. Moreover, the proposed recipe in AW10 to correct the displacement field using the Zel'dovich approximation (Zel'Dovich, 1970) should improve the agreement.

For the linear regime, there already exist fast, accurate large-scale structure solvers, e.g. COLA (Tassev et al., 2013, 2015) and FastPM (Feng et al., 2016). Thus, corrections for exclusive large-scale analyses using the rescaling approach are of limited practical importance. However, the benefits of rescaling the small scales become manifest when successfully coupled to such a large-scale solver, as a wide range of cosmologies can be explored on multiple refinement levels.

3.7.5 Mass estimation forecasts

One application for galaxy-galaxy lensing is halo mass estimation for a selected foreground galaxy sample. We thus examine how the residual statistical and systematic differences in the profiles translate to errors in the measured masses. For simplicity, we focus on the (0.29, 0.81) cosmology, and we choose a series of mass-selected samples in the direct simulation: haloes in mass bins of 0.05 dex or 0.1 dex centred on slightly different masses with bin borders shifted with 0.005 dex w.r.t. one another around $10^{12.5}\,h^{-1}M_\odot$ (i.e. massive galaxy haloes) or $10^{13.5}\,h^{-1}M_\odot$ (galaxy group haloes). The mean $\Delta\Sigma$ profiles for these bins constitute our mock weak lensing observations.

If we fit NFW profiles to these mock lensing observations, we obtain mass estimates that are approx. 5 to $10\,\%$ below the true mean halo masses as recorded by the halo finder (see Fig 3.7). We should be able to bypass this bias if we employ the rescaled simulation's stacked

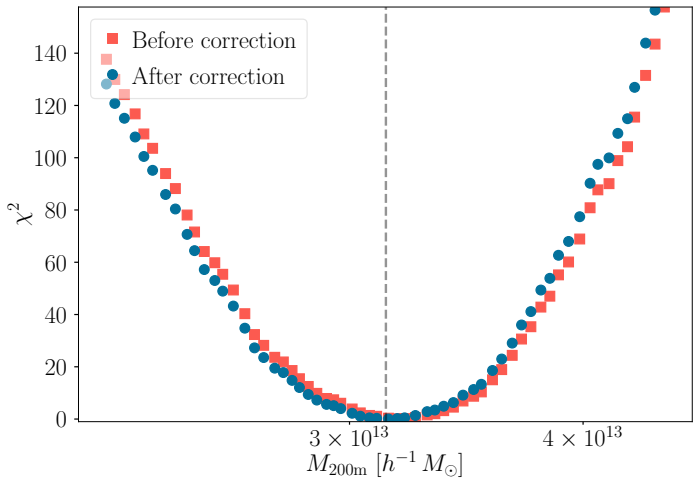

Figure 3.21: χ^2-parabolae for rescaled $\Delta\Sigma$ profiles fitted to a direct $\Delta\Sigma$ profile for a stack of galaxy group-size haloes with mean $M_{200\mathrm{m}}$ marked by the vertical dashed line according to Eq. (3.7.1). The minimum determines the best fit rescaled profile, and the corresponding simulation mass the best fit mass. The concentration correction shifts the parabola to be more symmetric around the direct simulation's mean mass, reducing the difference to the best-fit rescaled mass.

profiles (which should be 'biased' in the same way) as model predictions (instead of analytic NFW profiles) to estimate the mean mass of our mock halo sample. This however requires that the rescaled halo profiles are close enough to the true halo profiles (i.e. the direct simulation's profiles in this exercise), since a mismatch, e.g., in concentration of $\Delta c = 1$ causes an error $\sim 5\,\%$ in the inferred masses (e.g. Applegate et al., 2016; Schrabback et al., 2018). For the considered example, the concentration mismatches are already small before the correction ($\Delta c \sim 0.30$ and $\Delta c \sim 0.15$), and vanish after the correction. Thus, mass errors due to concentration mismatches are well below $1\,\%$ here (this is not necessarily the case for rescaling to the other, more extreme cosmologies).

To fit the rescaled mean profiles (our predictions) to the direct profiles (our mock data), we minimise the figure-of-merit

$$\chi^2 = \sum_i^{N_r} r_i^2 \left[\Delta\Sigma_{\mathrm{direct}}(r_i) - \Delta\Sigma_{\mathrm{rescaled}}(r_i)\right]^2 , \tag{3.7.1}$$

for radial bins $0.05 < r_i/r_{200\mathrm{m}} < 0.8$. Fig. 3.21 illustrates how the figure of merit changes when the mean profile of haloes in the direct simulation in a bin with width 0.1 dex centred on $10^{13.5}\,h^{-1}M_\odot$ is fit with rescaled mean profiles of mass bins with the same width but varying mean mass. The concentration correction shifts the χ^2-parabola to be more symmetric around the direct simulation's mean mass.

The results from the different sweeps are listed in Table 3.3. For smaller halo samples, the χ^2-parabolae feature considerable scatter which cause larger errors for the best-fit mass. As the number of haloes grow, the χ^2-parabolae become smoother and the errors on the best-fit masses decrease. This behaviour is in line with previous work (Becker & Kravtsov, 2011; Hoekstra et al., 2011) where the relative error on the mass was found to be $\sim 30\,\%$ per system for group haloes (and around $20\,\%$ for more massive systems). For example, this yields a relative mass error of ~ 0.01 for stacks of ~ 1000 haloes, and ~ 0.001 for $\sim 10\,000$

Mass range	Bin size	Max error (multi-axial)	Max error (axial)	Corrected max error (multi-axial)	Corrected max error (axial)
Group	0.10 dex	-3.2 %	-4.0 %	-1.1 %	2.5 %
Group	0.05 dex	-6.0 %	-9.4 %	-4.8 %	-7.2 %
Galactic	0.10 dex	-2.4 %	-3.6 %	0.2 %	-1.3 %
Galactic	0.05 dex	-2.4 %	-4.8 %	1.2 %	-3.5 %

Table 3.3: Maximal disagreements in mass between the direct and rescaled profiles for the different sweep ranges and bin widths. 'Group' refers to the $10^{13.45} - 10^{13.55}\,h^{-1}M_\odot$ mass range and 'Galactic' to the $10^{12.45} - 10^{12.55}\,h^{-1}M_\odot$ mass range, respectively. The errors listed are the maximal discrepancies $1 - M^{(\mathrm{r})}_{200\mathrm{m}}/M^{(\mathrm{d})}_{200\mathrm{m}}$ for each of the approximately twenty direct profiles in each sweep range and with 'Corrected' the concentration correction has been applied to the rescaled profiles in Eq. (3.7.1). 'Axial' refers to the largest error for halo profiles compared along a sole projection axis and 'Multi-axial' the largest errors for the average profiles along the three spatial axes.

haloes.

For future dark energy task force stage IV surveys, such as Euclid, statistical errors on mass estimations from $\Delta\Sigma$ profiles are expected to shrink substantially compared to current surveys. We can acquire a rough estimation by scaling corresponding values from CFHTLenS (Velander et al., 2014), which has a similar depth but a smaller survey area of $150\,\mathrm{deg}^2$, to an area of $15\,000\,\mathrm{deg}^2$ for Euclid (Laureijs et al., 2011; Amendola et al., 2013). A hundred times larger survey area roughly translates to a reduction of the statistical errors by a factor of ten. As example, we consider the sample L7 of 344 lenses in Velander et al. (2014) with absolute r-band magnitudes in the range $[-24.0, -23.5]$, average redshift $\bar{z} = 0.3$, fraction of blue galaxies $f_{\mathrm{blue}} = 0.03$. The mean halo mass of these lenses estimated from CFHTLenS is $10^{13.51}\,h^{-1}M_\odot$ with a quoted 20 % error. The statistical error for Euclid would shrink to 2 %. This suggests that our proposed method is accurate enough for current halo weak lensing data, and moreover may be viable for much larger future surveys, once baryonic effects on halo profiles have been properly accounted for.

3.8 Conclusions

We have demonstrated the prowess of a refined rescaling algorithm with growth history constraints in predicting halo 3D and GGL profiles. Residual differences in the inner profiles have been parametrised as concentration biases that can be predicted using linear theory combined with excursion sets. Differences in the profile outskirts can be expressed in terms of a shift in the splashback radius. This enables us to correct the profiles and improve the method's accuracy. This represents an important step towards the reusability of N-body simulations for cosmic structure analyses.

The algorithm's accuracy is satisfactory for current GGL data. However, small remaining discrepancies in the halo profile outskirts and for the lens mass estimates may require further treatment depending on the application. Further studies could clarify, which of these discrepancies are due to systematic biases, and which are due to scatter in, e.g., halo shapes and line-of-sight structure. With possibly improved corrections capturing biases not addressed so far and large N-body simulations to minimise statistical errors, the method may be made suitable for analysing future large (dark energy task force stage IV) surveys.

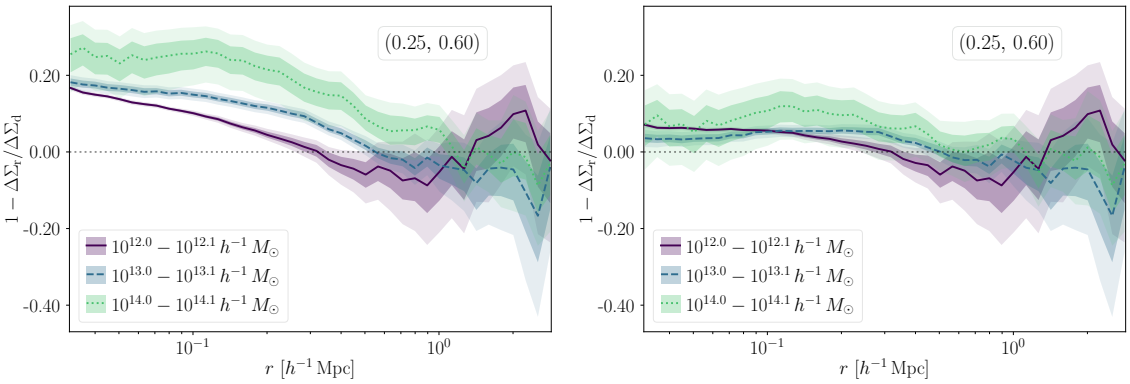

Figure 3.22: Residuals from three different mass bins' $\Delta\Sigma$ profiles for (0.25, 0.60) in the rescaled simulation w.r.t. the direct simulation in panel I and the residuals from concentration corrected profiles for in panel II.

3.9 Impact of radial binning and field residual variances for $\Delta\Sigma$ profiles

The measured differences between direct and rescaled halo profiles presented in Section 3.6 could depend on the radial binning. To investigate the impact of the bin width, we compute $\Delta\Sigma$ profiles with twice as many bins. For $\Delta\Sigma$, the new values for (0.15, 1.00) are 41 % and 32 % (pre-correction) and 15 % and 7.0 % (post-correction), which represent the largest differences owing to the lower resolution of this simulation. For (0.29, 0.81), the differences increase to 7.0 % and 2.6% (pre-correction) and 6.1 % and −1.2 % (post-correction) which implies an increase with 1 % for the total maxima and less than 1 % for the median maximum values. For (0.25, 0.60) and (0.40, 0.70), the resulting changes are below or maximally 1 %. The same is true for (0.80, 0.40), though the median maximum deviation changes signs to −4.2 % post-correction.

Concerning the cosmic variances of these residuals, we plot the residuals from the bootstrapped profiles for (0.25, 0.60) using all haloes in three mass bins in Fig. 3.22, before and after applying concentration correction (the results are qualitatively the same for the other simulations). For galaxy and galaxy group class haloes, the spread in the differences in the inner regions are quite narrow and they widen as one approaches the 1-halo to 2-halo transition regime. For cluster size haloes, there is a larger variance in the inner regions which is both driven by poor statistics and the impact of unrelaxed systems. This is reflected in the spread in concentrations. Overall, the correction preserves the variance with slightly larger error bars for cluster mass haloes as the haloes are not necessarily matched in each bootstrapped stack w.r.t. one another.

3.10 Results for (0.80, 0.40)

The almost Einstein-de Sitter cosmology represents our most extreme sample, and its cosmological parameters deviate strongly from what is favoured by observations. The masses differ substantially between the matched haloes in the direct and rescaled simulation, see Fig. 3.23, with haloes in the rescaled simulation on average more massive. In Fig. 3.24 panel I, we

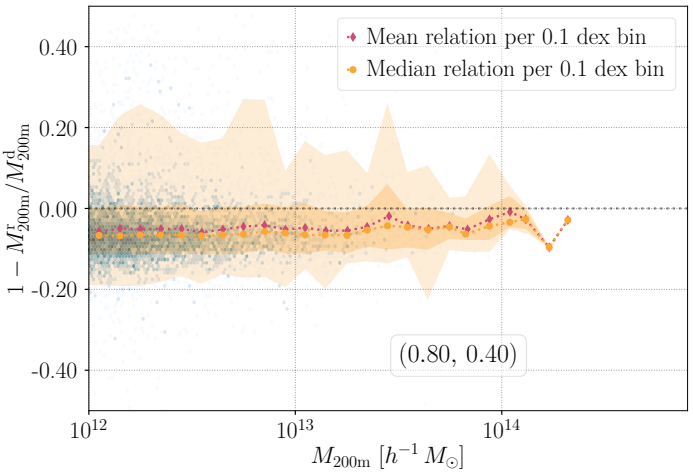

Figure 3.23: Mass bias for matched haloes in the (0.80, 0.40) simulation. The rescaled haloes are consistently more massive than their counterparts in the direct simulation across the whole mass range, with some outliers among galaxy class haloes.

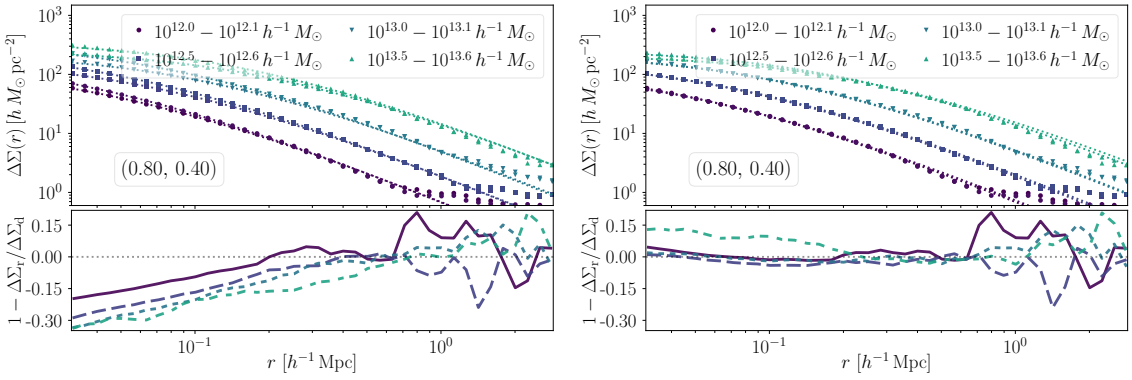

Figure 3.24: $\Delta\Sigma$ profiles for (0.80, 0.40) with the fiducial predictions in panel I and post-concentration correction in panel II.

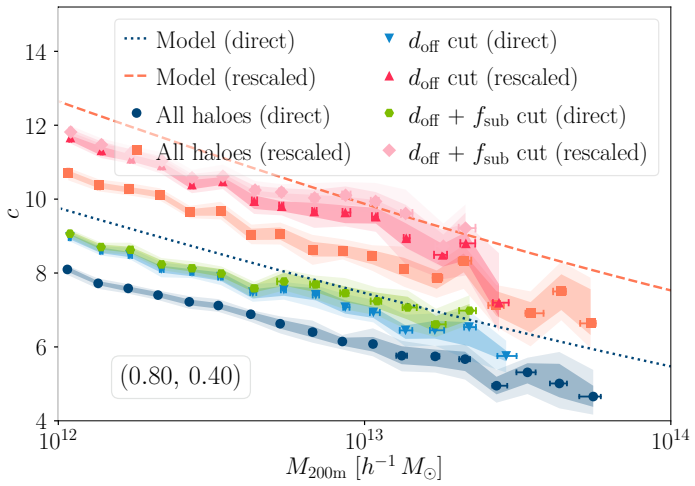

Figure 3.25: NFW $c(M)$-relations for (0.80, 0.40) for all haloes and with different relaxation cuts enforced.

show the measured $\Delta\Sigma$ profiles together with the fitted NFW lens profiles and in panel II the profiles post-correction. Due to the small volume of the simulation as listed in Table 3.1, we do not have any mass bins beyond $10^{14}\,h^{-1}\,M_\odot$ with more than twenty haloes in both the direct and rescaled snapshot. Since the amplitude of the 2-halo term is directly proportional to the matter fraction of the Universe, its influence kicks in at smaller scales than for the other simulations. The inner profile bias is negative and can be quantified as $\Delta c \approx -2$ as seen in Figs. 3.10 and 3.25 where we plot the 3D density profile NFW $c(M)$-relations. The Einasto $c(M)$-relations, see Fig. 3.30, perform slightly better at the low mass end w.r.t. the L16 predictions.

3.11 Matched halo results

In Fig. 3.26 we show the fractional differences in the median density profiles between matched haloes in the direct and rescaled simulations binned according to the mass in the direct run for all test cosmologies. The error regions are calculated from comparing the median differences between the same bootstrapped matched haloes in the direct and rescaled simulations. With respect to the differences shown in Fig. 3.5, the two biases are slightly more discernible, especially the outer profile bias and the (small) concentration bias for (0.29, 0.81). Re-sampling the matched population for each mass bin yields similar results. For all cosmologies and mass bins the profile bias changes signs at $\approx 0.3 - 0.4\,r/r_{\rm 200m}$ which was also observed previously for all haloes. The median Δc-biases for these matched haloes are illustrated in Fig. 3.27 where the error regions are computed from bootstrap resamples of the same matched haloes in the direct and rescaled simulations.

In Fig. 3.28 we plot the individual concentration relations in the direct and rescaled simulation for all cosmologies except for (0.40, 0.70) which was already shown in Fig. 3.14 with the same setup. We only correct the profiles if the fitted $c + \Delta c > 0$. This chiefly affects massive haloes in the (0.80, 0.40) simulation and it has a negligible impact on the shape of the contours. The concentration correction induces a translation towards the diagonal but rotations are required for (0.15, 1.00) and (0.80, 0.40) to bring about agreement. Slight rotational ad-

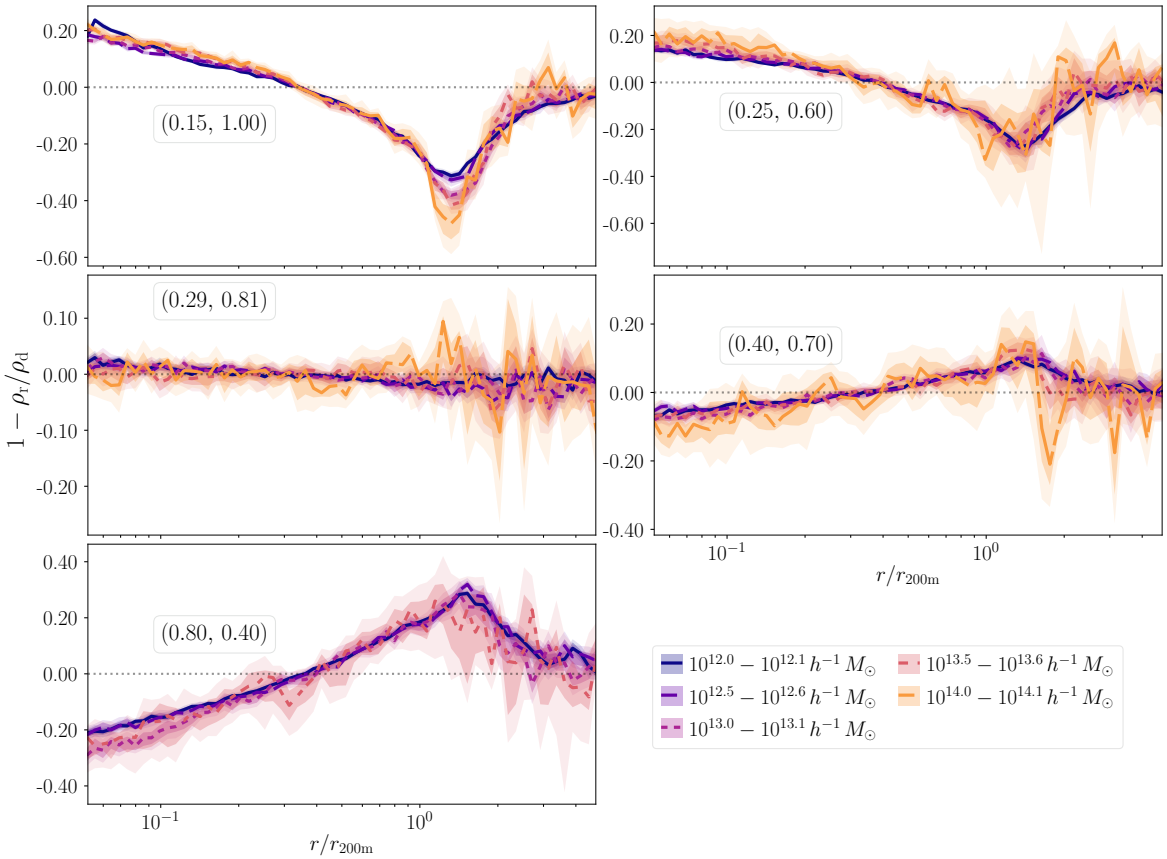

Figure 3.26: Matched halo density field residuals from 64 log-equidistant radial bins with error regions from bootstrapped stacks of matched haloes in each simulation. These error regions trace the median results well.

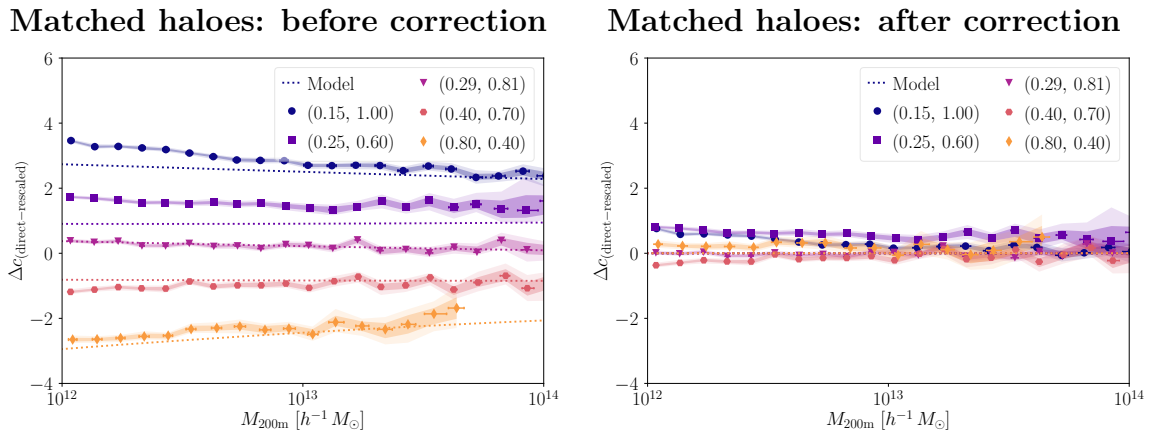

Figure 3.27: Difference in concentration estimated from density profiles (as in the left panel of Fig. 3.10) for matched haloes before and after applying our correction to rescaled haloes.

justments might improve the concordance for (0.25, 0.60) and (0.29, 0.81). For (0.25, 0.60), a larger translation correction is required. Imposing relaxation cuts and demanding that haloes pass them in both simulations does not affect the tilt of the distributions, but removes low concentration haloes as expected.

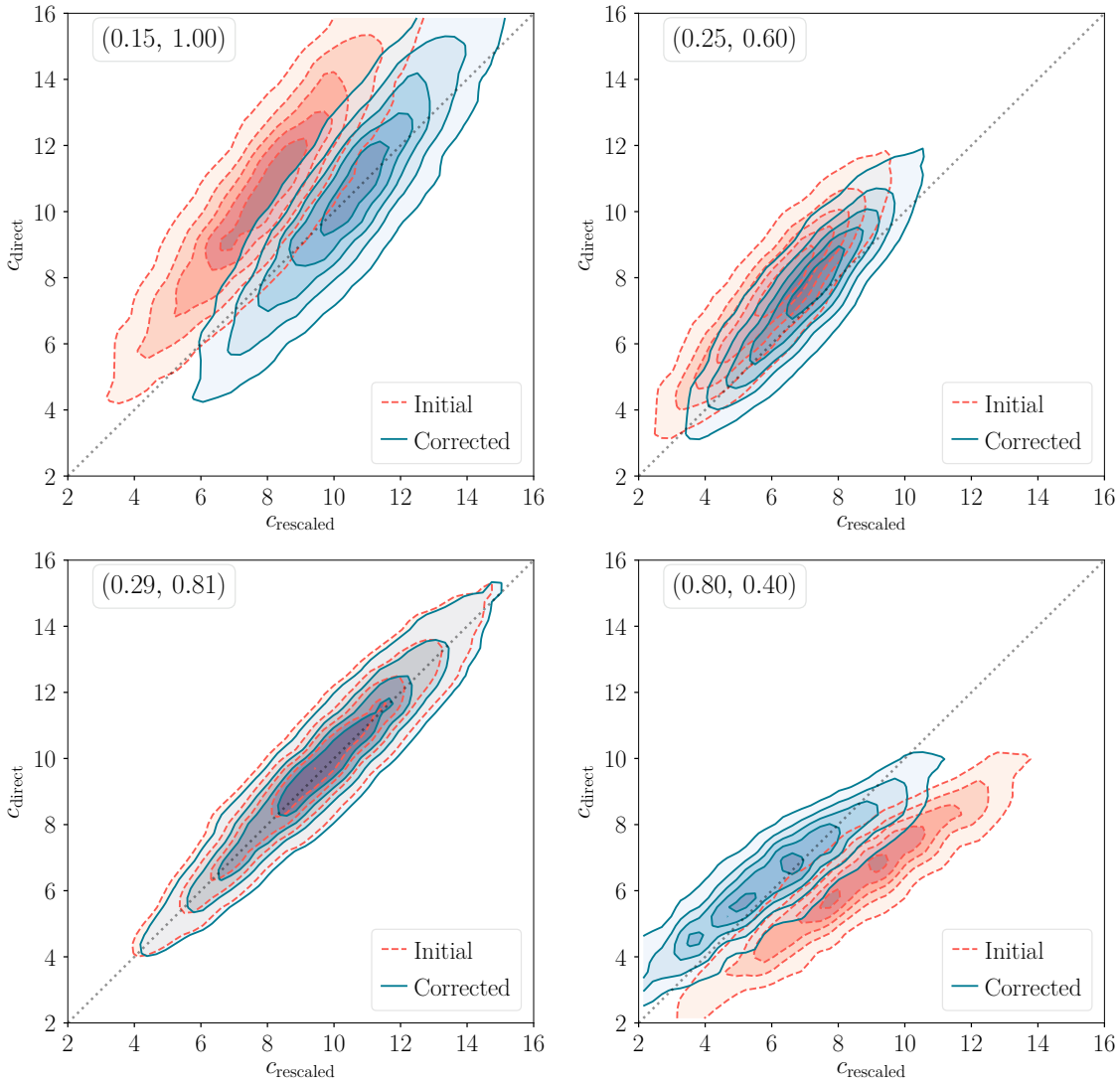

Figure 3.28: Concentration difference for matched haloes quantified with 3D NFW profiles, pre- and post-correction. Note that the lower mass threshold in the direct simulation for (0.15, 1.00) is $M_{\rm 200m} > 10^{12.7}\,h^{-1}\,M_\odot$ instead of $> 10^{12.5}\,h^{-1}\,M_\odot$ for the others to mitigate resolution effects.

3.12 Einasto concentrations

In Figs. 3.29 and 3.30 we plot the measured $c(M)$-relations and relaxation cut impacts for an Einasto parametrisation of the density field, and in Fig. 3.31 the corresponding Δc biases. To compute the rescaling mappings we rephrase the density profile in Eq. (1.2.44) in terms of the average density $\langle\rho_{\rm Einasto}\rangle\,(r)$ for the enclosed mass $M(<r)$:

$$\langle\rho_{\rm Einasto}\rangle\,(r) = \frac{M(<r)}{4\pi/3\,r^3} = \frac{\Delta}{y^3}\frac{\gamma(3/\alpha;\,2/\alpha(yc_\Delta)^\alpha)}{\gamma(3/\alpha;\,2/\alpha c_\Delta^\alpha)}\rho_{\rm crit}(z_0), \tag{3.12.1}$$

where $y = r/r_\Delta$ and $\gamma(a;\,b)$ is the lower incomplete gamma function, readily replace the NFW density profile in Eq. (3.6.1) and calculate the correction accordingly. Evaluating Eq. (3.12.1) at the scale radius, the concentration w.r.t. the mean density $c_{\Delta\rm m}$ is then the solution to

$$\frac{c_{\Delta\rm m}^3}{\gamma(3/\alpha;\,2/\alpha c_{\Delta\rm m}^\alpha)} = \frac{c_{\Delta\rm c}^3}{\gamma(3/\alpha;\,2/\alpha c_{\Delta\rm c}^\alpha)}\frac{E(z)^2}{\Omega_{\rm m}(1+z)^3}. \tag{3.12.2}$$

The masses are rescaled in the same manner as in Section 3.4.2 and the resulting $c(M)$-relations with $\alpha = 0.18$ and $\Delta = 200$ differ negligibly from the NFW curves.

With relaxation cuts enforced, the measured Einasto $c(M)$-relations are close to the L16 model predictions, as Fig. 3.30 shows. Overall the the model predictions better match measured relations for Einasto profiles (see Fig. 3.29) than for NFW profiles (see Fig. 3.8). While the concentration biases are similar to those measured for the NFW relations in Fig. 3.10, we have a slightly larger bias for (0.15, 1.00) and (0.25, 0.60), and for the low mass bins for (0.40, 0.70) in Fig. 3.31. Since the masses are fixed, the small horizontal scatter stems from the different median $M_{200\rm m}$ masses of the bootstrap samples. These values do not deviate significantly from one another until the sparsely populated high mass end for some cosmologies.

Fig. 3.32 shows the Einasto estimated concentration distribution for individual haloes pre- and post-correction for (0.15, 1.00). Compared to the NFW distributions, the Einasto fits favour higher concentrations for low mass haloes which is seen for the median $c(M)-$relations in Fig. 3.29 and also in the shift of the distributions between Fig. 3.32 and the (0.15, 1.00) panel in Fig. 3.28. In addition, the slightly larger mismatch between the L16 model prediction and the measured median concentration relations for (0.15, 1.00) is visible as an offset between the diagonal and the centre of the densest contour in Fig. 3.32 (cf. Figs. 3.28, 3.27 and 3.10). A larger spread of concentrations is also possible, which can be noted by comparing the contours for (0.40, 0.70) in Fig. 3.14 (NFW) to those in Fig. 3.33 (Einasto). Still, the tilt is preserved by the two parameterisations for all cosmologies. The results in general are qualitatively quite similar.

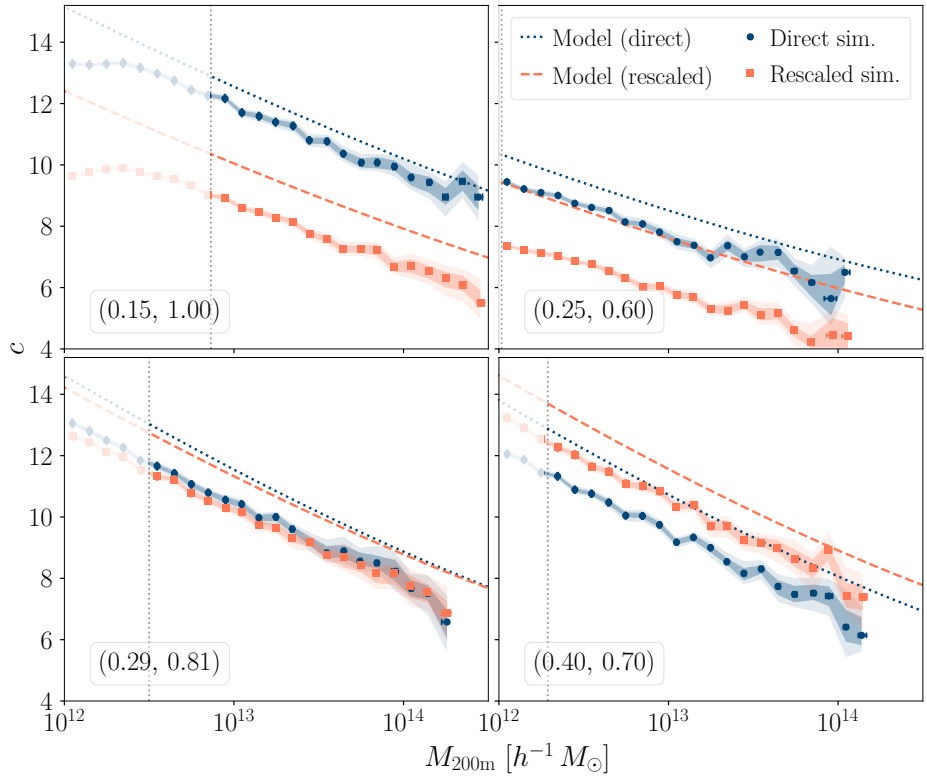

Figure 3.29: Concentration-mass relations for Einasto fits with $\alpha = 0.18$ for direct and rescaled simulations w.r.t. the L16 model predictions.

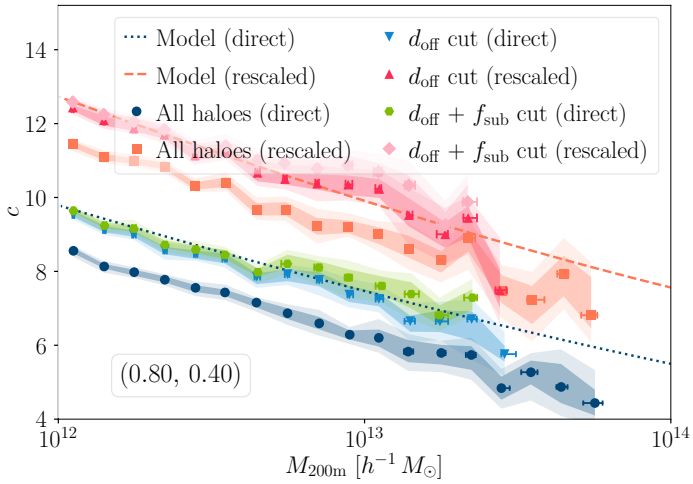

Figure 3.30: Einasto $c(M)$-relations for (0.80, 0.40) for all haloes and with different relaxation cuts enforced. The corresponding NFW relations are similar though the Einasto measurements correspond better to the theory values at the low mass end.

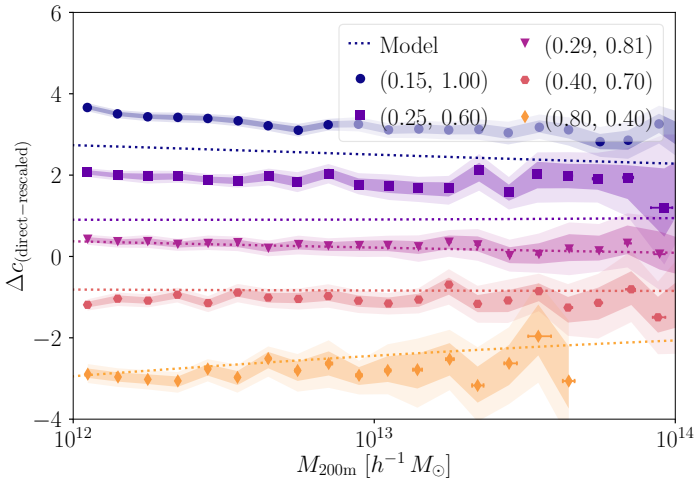

Figure 3.31: The measured differences for Einasto concentrations with $\alpha = 0.18$ and r_s and ρ_s free.

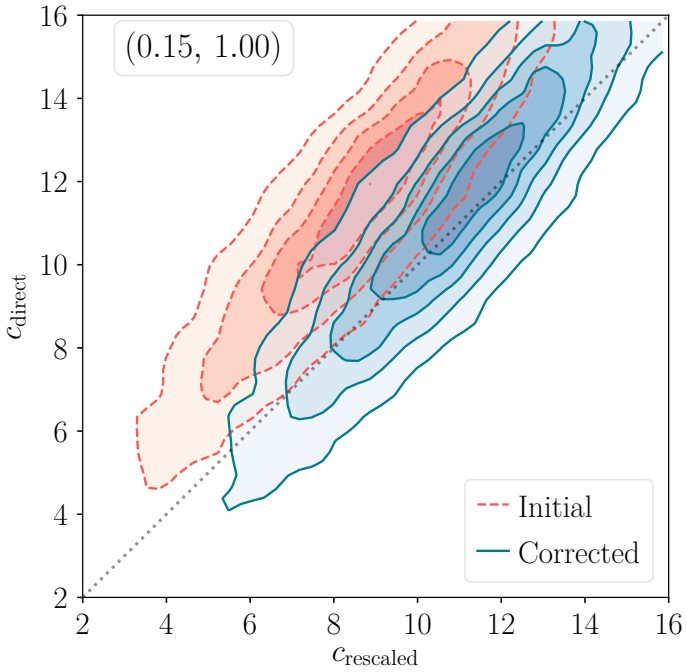

Figure 3.32: Einasto estimated concentrations for matched haloes in the direct and rescaled simulation with $M_{200\mathrm{m}} > 10^{12.7}\,h^{-1}\,M_\odot$ for haloes in the direct simulation.

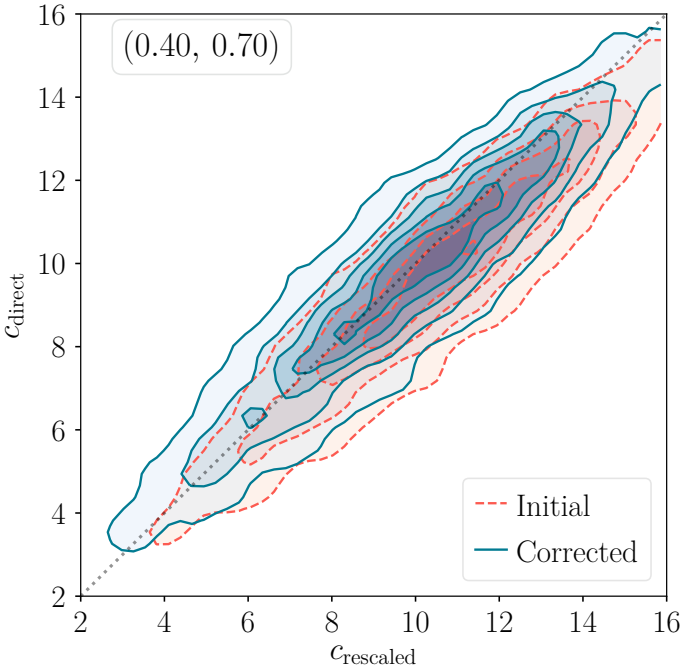

Figure 3.33: Einasto estimated concentrations for matched haloes in the direct and rescaled simulation with $M_{\rm 200m} > 10^{12.5}\,h^{-1}\,M_\odot$ for haloes in the direct simulation.

3.13 Splashback mass correction

The outer profile correction can be used to build a naïve mass correction, if we redefine the $M_{\rm 200m}$ masses in the rescaled simulation as masses within the perturbed $r'_{\rm 200m}$, which is set such that $r_{\rm sp}^{\rm (d)}/r_{\rm 200m}^{\rm (d)} = r_{\rm sp}^{\rm (r)}/r'_{\rm 200m}$. Assuming that the density field just beyond $r_{\rm 200m}$ is dominated by the 1-halo term which is well captured by an NFW profile, one could extend the integration to $r'_{\rm 200m} = (1+\delta)r_{\rm 200m}$ where $1+\delta = 1/(1+\Delta r_{\rm sp})$. This simplifies to the following expression for the mass correction:

$$\frac{M_{\rm 200m}^{\rm eff.}}{M_{\rm 200m}} = \frac{1 - 1/(1+c/(1+\Delta r_{\rm sp})) - \ln\left(1+c/(1+\Delta r_{\rm sp})\right)}{1 - 1/(1+c) - \ln\left(1+c\right)}, \tag{3.13.1}$$

where $c = c(M)$, and $\Delta r_{\rm sp}$ could be predicted with the L16 and Diemer et al. (2017) model fits, respectively. The weak mass evolution of this correction factor for the different cosmologies is plotted in Fig. 3.34 for the uncorrected and corrected rescaled density field. The concentration correction affects the relation marginally. Due to the mismatch between the detected outer profile bias for (0.15, 1.00), (0.25, 0.60) and (0.40, 0.70) and the model prediction in Fig. 3.17, as well as the mismatch between the L16 model and the measured $c(M)$-relations, the correction is too large. This is reflected in the cumulative halo mass function in Fig. 3.35 for matched haloes pre- and post-mass correction, where the agreement is worse. For (0.15, 1.00) and (0.80, 0.40), however, the bias changes signs at the low mass end, and for (0.80, 0.40), the situation improves somewhat at the low mass end.

We can interpret these results in light of the discrepancies in mass between the matched direct and rescaled haloes in Fig. 3.3, where the median relations for these two simulations are off (see appendix 3.10 for (0.80, 0.40)) and the mass correction shifts these median levels

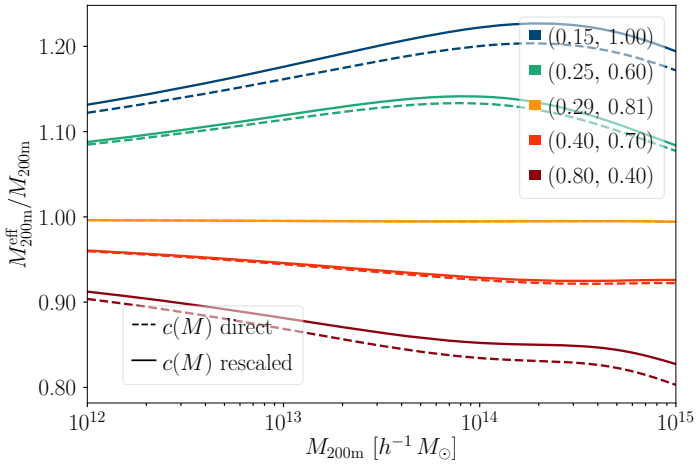

Figure 3.34: Effective mass correction with the NFW density field correction before and after the concentrations are corrected.

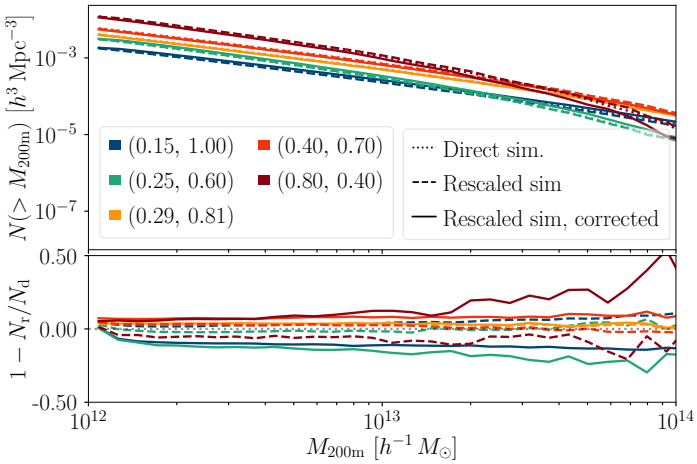

Figure 3.35: Halo mass function before and after the mass correction.

in the right direction. Still, there is a mass evolution of the discrepancy between the direct and rescaled haloes which must be modelled by a more elaborate correction. For the other simulations, this tilt dominates over the wrong offset level, and for (0.29, 0.81) there is a very small predicted shift.

3.14 Cosmological contour plots for the rescaling parameters

In Fig. 3.36 the predicted offsets computed with the Diemer et al. (2017) model in the position of the splashback radius w.r.t. $r_{200\mathrm{m}}$ for matched halo samples in different target cosmologies is shown. In large sections of the parameter plane, $\Delta r_{\mathrm{sp}}/r_{200\mathrm{m}}$ has the opposite sign as Δc although this is not necessarily true for small changes from the fiducial run nor for the $\Delta\Omega_{\mathrm{m}} > 0$, $\Delta\sigma_8 > 0$ quadrant. We plot the (α, z_*) pairs to emulate these different cosmologies in Fig. 3.37. They are smooth functions depending on $\Delta\Omega_{\mathrm{m}}$ and $\Delta\sigma_8$ to the fiducial cosmology. Shrinking the simulation box is preferable to emulate a cosmology with a higher matter fraction, and expanding the box for lower matter fractions. Similarly intuitively, going to a higher redshift in the fiducial simulation could be used to match a cosmology with a lower σ_8, i.e. with a lower amplitude of the fluctuations of the matter field. This puts the Millennium simulation in a suitable position for rescaling as the WMAP1 $\sigma_8 = 0.9$ is comparably high to the current best fit matter power spectrum amplitudes.

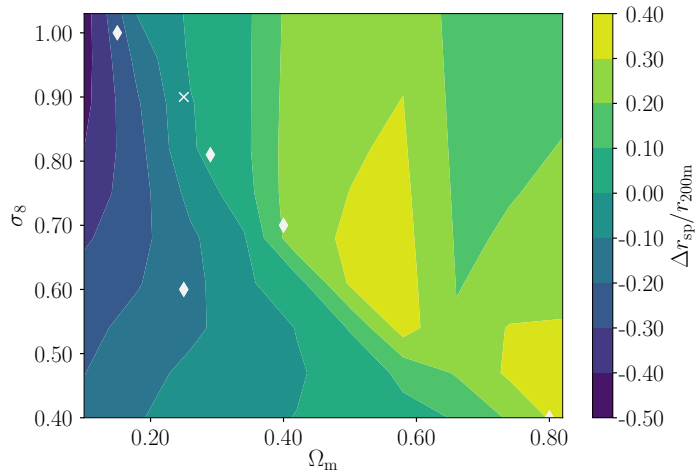

Figure 3.36: Predicted offset in splashback radius for matched haloes in a direct and rescaled fiducial simulation with WMAP1 parameters from the Diemer et al. (2017) model (75th percentile).

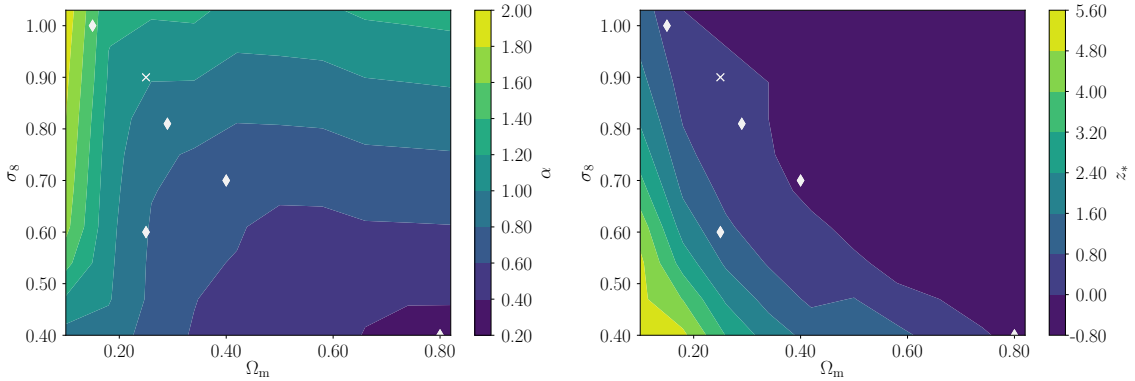

Figure 3.37: The length scale parameter α as a function of $\Delta\Omega_m$ and $\Delta\sigma_8$ w.r.t. a fiducial simulation with WMAP1 parameters in panel I. In panel II we show the time scale parameter z_* as a function of $\Delta\Omega_m$ and $\Delta\sigma_8$.

3.15 Biases for a rescaled Millennium simulation to WMAP and Planck cosmologies

In Fig. 3.38, we illustrate the predicted concentration biases for the Millennium simulation (Springel et al., 2005b) with its WMAP1 parameters (Spergel et al., 2003) rescaled to a range of cosmologies (WMAP3, WMAP5, WMAP7, WMAP9, Planck 2014) (Spergel et al., 2007; Komatsu et al., 2009, 2011; Hinshaw et al., 2013; Planck Collaboration, 2014) at $z = 0$ according to the parameters in Henriques et al. (2015) and Guo et al. (2013a). For the cosmologies where there is a mass evolution of the concentration bias in Fig. 3.38, the slope decreases at higher redshift. The predicted concentration bias for haloes with a Millennium simulation rescaled to Planck 2014 with the parameters in Henriques et al. (2015) is very small and decreases for higher redshifts, which is fortuitous for future lensing analyses.

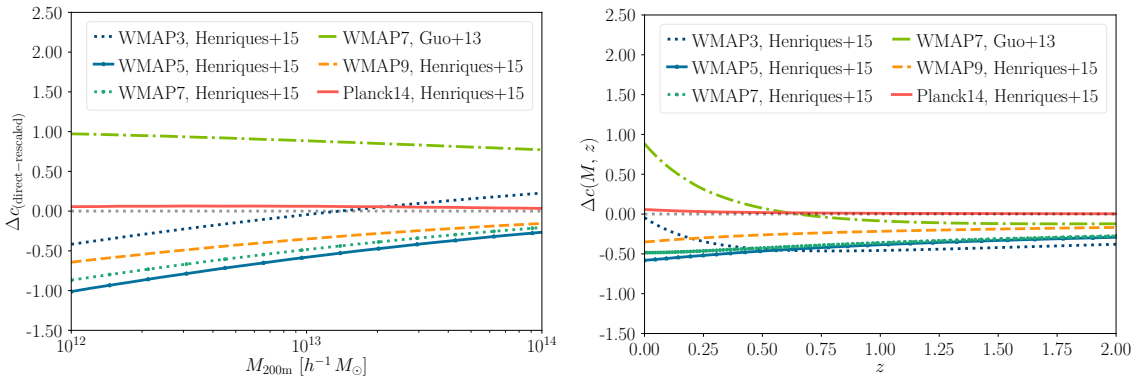

Figure 3.38: In panel I the predicted concentration biases for haloes rescaled using the parameters in Henriques et al. (2015) and Guo et al. (2013a) are illustrated. The corresponding redshift evolutions of the biases are displayed in panel II.

Chapter 4 Joint 2-pt statistics constraints on galaxy formation

4.1 Prologue

This Chapter will shortly be published in Monthly Notices of the Royal Astronomical Society, to which we rescind all copyrights, as Renneby et al. (prepa). As for the division of labor, the first author (me) conducted the work in this analysis with advice from Dr. Stefan Hilbert and Bruno Henriques, PhD, and Prof. Raúl E. Angulo, PhD, as well as Dylan Nelson, PhD, and Dr. Mark Vogelsberger. The final publication will have additional contributions from Prof. Dr. Volker Springel and Prof. Lars Hernquist, PhD, and a slightly modified structure.

4.2 Abstract

We compare predictions for galaxy-galaxy lensing profiles and galaxy clustering from the latest public version of the Munich semi-analytical model of galaxy formation and the IllustrisTNG suite with observational measurements from the KiDS+GAMA equatorial overlap and SDSS. Using four different selection functions for the lens samples (stellar mass, stellar mass and group membership, stellar mass and isolation criteria, stellar mass and colour) we find that this version of the SAM is disfavoured by current data for stellar masses $M_* > 10^{11}\,M_\odot$. By decreasing the time which dictates how fast satellite galaxies merge with their centrals as well as reducing the AGN accretion efficiency in radio-mode in the SAM, we are able to mitigate the discrepancies and obtain a better agreement both for the lensing and the corresponding clustering signal. We use the lens signals from the GAMA group catalogue presented in Velliscig et al. (2017) as a test sample and show that the new model is consistent with the observed signal for central galaxies. However, this modification induces a slight deviation for the galaxy clustering signal for low mass galaxies away from previous observational constraints from SDSS. This suggests that a refined quenching model for satellite galaxies in galaxy groups is required. In addition, such modifications produce discrepancies in the stellar mass function at the high mass end, but these are subdominant to the current allowed errors. We show the implications of an insufficient dust model for the lensing and clustering signals for samples selected according to colour and stellar mass as well as abundance corrections for our results. Turning to the hydrodynamical simulation, the IllustrisTNG produces excellent lensing predictions, both for stellar-mass only, superior to the SAM, and LBG samples, equally well as the SAM. With added dust corrections to the colours it matches the SDSS clustering signal well for red low mass galaxies. We find that both the SAMs and the IllustrisTNG fail to reproduce the lensing signal for intermediate mass red galaxies below $< 10^{11}\,M_\odot$, caused by difficulties to match the satellite signals, highlighting the need for further developments.

4.3 Introduction

Thanks to the fast implementation of semi-analytical models, see Section 2.2.3, it is possible to explore the parameter space of the underlying physical models using Monte Carlo Markov chains (MCMC) (Henriques et al., 2009, 2013, 2015) with observational constraints such as the stellar mass function (SMF) and red fraction of galaxies ($f_{\rm red}$) (1-pt functions). In van Daalen et al. (2016) it was shown that the introduction of galaxy clustering constraints (2-pt functions) in the sampling gave additional insights into the formation physics. In this Chapter, we explore how the latest version of the Munich semi-analytical model L-Galaxies (Henriques et al., 2015), henceforth H15, for a Planck 2014 cosmology (Planck Collaboration, 2014) and a set of derivative models close to the fiducial run fare with respect to current lensing and clustering observations with different selection functions. In Wang et al. (2016) this model was found to overpredict the lensing signal around Sloan Digital Sky Survey (SDSS)-Planck 2013 locally brightest galaxies, LBGs, (Planck Collaboration, 2013; Anderson et al., 2015). By enforcing a stellar mass correction based on abundance matching to SDSS via the fitting function in Li & White (2009), a better agreement was reached. The version with the smallest necessary abundance correction was the Guo et al. (2011) model, henceforth G11, adapted for the Planck 2014 cosmology, owing to the MCMC tuning to low redshift observations. This model also passed a more stringent test in Mandelbaum et al. (2016) with a separation of the lensing signal for red and blue LBGs. Still, due to the low redshift tuning, this version has difficulties to produce predictions for future deep surveys, for instance the Hyper Suprime-Cam SSP Survey (HSC) (Aihara et al., 2018) and the Euclid mission, where the signal will be measured for lens systems beyond $z = 1$. In addition, it does not feature later developments to improve the modelling of low mass galaxies, where H15 has reduced the over-abundance of $8.0 < \log M_*/M_\odot < 9.5$ systems at $z \geqslant 1$ as well as the excessive fraction of red dwarf galaxies at low redshift. Hence, we investigate if moderate changes to the free parameters governing the stellar-to-halo mass relation as well as the fraction of satellites in H15 can be chosen to better fit local lensing observations while retaining the agreement at higher redshifts.

We also compare these predictions with results from the IllustrisTNG suite, described in Section 2.3.3, which are a set of state-of-the-art hydrodynamical simulations. Primarily we use the TNG300 simulation which has a box length of $205\,h^{-1}\,$Mpc which allows for similar statistics as for the SAMs run on large gravity-only simulations.

We focus on selections based on stellar mass, joint stellar mass and colour and joint stellar mass and isolation/group membership criteria. The latter is especially important for upcoming group and cluster finders, where lensing can be used to validate models of feedback from active galactic nuclei (AGN) (e.g. McCarthy et al., 2010; Viola et al., 2015). Colour bimodality can inform on quenching mechanisms for star formation and their relations to the host halo mass (e.g. Zu & Mandelbaum, 2016; Mandelbaum et al., 2016). With respect to Wang et al. (2016); Mandelbaum et al. (2016), we also go beyond the locally brightest galaxies to the full galaxy distribution and include constraints on the satellite fractions which sets us on a path to modify the merger criteria. Moreover, we discuss the incorporation of observationally motivated errors on the stellar masses, abundance corrections and colour definitions.

The purpose of this study is thus two-fold, (i) Investigate if L-Galaxies fits current observational constraints from galaxy-galaxy lensing and galaxy clustering. (ii) Examine if modest changes to a few model parameters can bring about a better agreement. (iii) Assess

the agreement of the IllustrisTNG hydrodynamical simulation with observations and explore interesting differences with respect to the SAM.

For lensing, we consider a deeper field from the equatorial overlap of the Kilo-Degree and Galaxy And Mass Assembly (KiDS+GAMA) surveys (Liske et al., 2015; Kuijken et al., 2015) with data from van Uitert et al. (2016) and Velliscig et al. (2017) and a shallow field (SDSS-DR7) (Wang et al., 2016; Mandelbaum et al., 2016; Zu & Mandelbaum, 2016) to illustrate how different surveys and redshifts affect the lens sample. We also compare predictions from HOD models from Zu & Mandelbaum (iHODS, 2016) and hydrodynamical simulations (IllustrisTNG, Weinberger et al., 2017; Pillepich et al., 2018a) to illustrate how well the different frameworks with increasing granular level of model sophistication can capture the signal. For the SAM, we use the LBG and stellar mass only sample to constrain the model parameters and then use the group lens samples from Velliscig et al. (2017) as test cases for the new models.

This Chapter is organised as follows: We review the physical recipes of the feedback processes in the SAM and compare the stellar mass functions in Section 4.4 and Section 4.5, respectively, and present our methodology in Section 4.6. We previously detailed our simulations in Chapter 2, with the Millennium suite described in Section 2.2.2 and IllustrisTNG in Section 2.3.3. The different datasets we use to gauge the performance of the models, as well as their colour distributions, are given in Section 4.7. In Section 4.8, we show our results for the modified galaxy formation models for the stellar mass functions (Section 4.8.1), stellar mass selected lenses (Section 4.8.2) followed by the implications of various systematics, stellar mass and colour selection (Section 4.8.6), LBGs (Section 4.8.7) and galaxy clustering (Section 4.8.8). Finally, we conclude with computing the predictions for a few of our models for the KiDS+GAMA group lens sample in Section 4.9.

4.4 Modified galaxy formation models

We modify the existing H15 model[1] by changing the values of three parameters, $k_{\rm AGN}$, $\epsilon_{\rm reheat}$ and $\alpha_{\rm dyn}$, governing the stellar-to-halo mass relation and the satellite fraction. Here we review the parts of the model where those parameters occur.

From the peak of star formation efficiency for Milky Way class galaxies, the lower mass end is impeded by supernovae (SN) and galactic wind feedback and the high mass end by AGN feedback (see abundance matching results in e.g. Moster et al., 2010; Behroozi et al., 2010). Hence, these two processes are a natural starting point for modifications. Since the lensing signal for H15 in Wang et al. (2016) was too high, it means that one could lower each or both efficiencies for these processes to increase the stellar-to-halo mass ratio for the galaxies. In H15, AGN feedback is implemented with a radio mode accretion model (Croton et al., 2006) normalised to the expansion rate of the Universe,

$$\dot{M}_{\rm BH} = k_{\rm AGN} \left(\frac{M_{\rm hot}}{10^{11} M_{\odot}} \right) \left(\frac{M_{\rm BH}}{10^{8} M_{\odot}} \right), \tag{4.4.1}$$

with $\dot{M}_{\rm BH}$ as the accretion rate, $k_{\rm AGN}$ as a free parameter which regulates the efficiency, $M_{\rm hot}$ and $M_{\rm BH}$ the masses of the hot gas halo and the supermassive black hole (SMBH), respectively. This accretion then impedes the cooling flow onto the cold disc as it is accompanied by

[1]Public release available at: http://galformod.mpa-garching.mpg.de/public/LGalaxies/index.html.

relativistic jets which deposits additional energy into the hot gas halo. With respect to previous versions of the model, $k_{\rm AGN}$ is assumed to be fixed across all redshifts.

For SN feedback, H15 has two chief efficiencies, where one adjusts the fraction of energy available for long-term alterations of the thermodynamic state of the gas components of the galaxy. The other sets the fraction of this energy for the reheating of cold gas and the subsequent injection into the hot gas atmosphere. For the latter, the mass of cold gas reheated due to star formation $\Delta M_{\rm reheat}$ is set to be proportional to the amount of stars formed (see e.g. Martin, 1999)

$$\Delta M_{\rm reheat} = \epsilon_{\rm disc} M_{\rm disc}, \tag{4.4.2}$$

where $M_{\rm disc}$ is the mass of stars in the galaxy disc and $\epsilon_{\rm disc}$ is

$$\epsilon_{\rm disc} = \epsilon_{\rm reheat} \left(0.5 + \left(\frac{V_{\rm max}}{V_{\rm reheat}} \right)^{-\beta} \right), \tag{4.4.3}$$

where $\epsilon_{\rm reheat}$ is the efficiency, $V_{\rm max}$ the maximum circular velocity and $V_{\rm reheat}$ and β parameters determining the normalisation and slope of the feedback, respectively. In this study we keep these two parameters fixed to the fiducial H15 values.

Another way to increase the stellar masses is to modify processes governing the merging of systems. In SAMs, the subhaloes of satellite galaxies can be disrupted and the satellite shortly lives on as an orphan galaxy before falling into the central galaxy due to dynamical friction. The time between disruption and accretion, $t_{\rm friction}$, is fixed by a merging clock following Binney & Tremaine (1987) as

$$t_{\rm friction} = \alpha_{\rm dyn} \frac{V_{\rm 200c} r_{\rm sat}^2}{G M_{\rm sat} \ln(1 + M_{\rm sat}/M_{\rm 200c})}, \tag{4.4.4}$$

where $M_{\rm sat}$ as the total mass of the satellite, $r_{\rm sat}$ the radius of the satellite orbit, $M_{\rm 200c}$ and $V_{\rm 200c}$ the mass and circular velocity of the friends-of-friends host halo, G the gravitational constant and $\alpha_{\rm dyn}$ a merger time multiplier. This value was set to $\alpha_{\rm dyn} = 2.4$ by De Lucia & Blaizot (2007) to conform with the bright end of the luminosity function at $z = 0$. This choice was later found to be consistent with direct numerical simulation inferences (Boylan-Kolchin et al., 2008; De Lucia et al., 2010). Intuitively decreasing $\alpha_{\rm dyn}$ lowers $f_{\rm sat}$ and boosts the stellar mass of central galaxies which dominate the high mass end of the SMF as mergers are associated with starbursts. However, a short merger timescale implies that one overall ends up with fewer massive systems. Hence, one can decrease the efficiency of the feedback process to increase this number, which means that these two simultaneous modifications produce indistinguishable SMFs.

We list the fiducial values of these parameters in Table 4.1 and the derivative values in Table 4.2. In the G11 version of the model, $\alpha_{\rm dyn}$ has a slightly lower value and in van Daalen et al. (2016), a 40 % to 50 % lower value was required to match clustering observations. Hence we are focusing on derivative models with a lower $\alpha_{\rm dyn}$ and lower $k_{\rm AGN}$ than in the fiducial H15 model. H15 also found that boosting $V_{\rm reheat}$ was necessary for a better clustering agreement. In the H15 this value is already fixed to a much higher value so we just modify the normalisation. With respect to observations, this SN mass loading factor was found to be a bit large in H15 and this motivates the decrease.

Model	$\mathbf{k_{AGN}}$	$\epsilon_{\mathbf{reheat}}$	$\alpha_{\mathbf{dyn.}}$
G11	1.5×10^{-3}	6.5	2.0
H15	5.3×10^{-3}	2.6	2.5

Table 4.1: The fiducial SAM model parameters. Note that G11 has a different implementation of the AGN feedback, neglecting the normalisation with $H(z)$.

$\mathbf{k_{AGN}}/\mathbf{k_{AGN}^{fid.}}$	$\epsilon_{\mathbf{reheat}}/\epsilon_{\mathbf{reheat}}^{\mathbf{fid.}}$	$\alpha_{\mathbf{dyn.}}/\alpha_{\mathbf{dyn.}}^{\mathbf{fid}}$
0.1	1	1
1	0.1	1
1	1	0.1
0.1	1	0.1
0.1	1	0.1
0.5	1	0.1
0.1	1	0.3
0.2	1	0.3
0.3	1	0.3
0.1	1	0.4
0.2	1	0.4
0.3	1	0.4
0.1	1	0.5
0.2	1	0.5
0.3	1	0.5
0.4	1	0.5
0.5	1	0.5
0.5	0.5	0.5
0.5	1.5	0.5

Table 4.2: The different SAM configurations compared in this Chapter, derivatives of the H15 model. 'fid' refers to the values in the H15 model.

4.5 Impact of cosmology, rescaling and hydrodynamics

Apart from differences in galaxy formation, the galaxy-galaxy lensing and clustering signals are also influenced by cosmological parameters. To illustrate this we also compute the SAM predictions for lensing for the fiducial H15 model in a WMAP1 cosmology, which has a lower matter fraction $\Omega_{\rm m}$ and greater σ_8 than the Planck 2014 cosmology. The difference between these two cosmologies should lie in the most extreme allowed range for flat ΛCDM universes. In Renneby et al. (2018) it was shown that the rescaling concentration bias for the lensing signal around centrals was negligible for a rescaled Millennium simulation (MR) to a Planck 2014 cosmology, which means that we mainly refrain from comparisons to direct simulations with different cosmological parameters as already carried out in Wang et al. (2016). We have run the SAMs on the gravity only versions of IllustrisTNG, (Weinberger et al., 2017; Pillepich et al., 2018a), for the TNG100 and TNG300 boxes. In these simulations, the background cosmology, Planck 2016 (Planck Collaboration, 2016a), is close to the assumed Planck 2014 cosmology, which means that the model parameters chosen should be fairly optimal. We find consistent results with the models run on the rescaled Millennium simulation, see Section 4.15, also for mixed lens samples.

We have compared the halo mass functions, which are what the rescaling algorithm is set out to match, for the central galaxies for the H15 model run on top of the rescaled MR and Millennium-II (MRII) runs as well as the gravity only runs of the TNG100 and TNG300 and note negligible differences. This however, does not necessarily translate to a good agreement in the SMFs, as illustrated in Fig. 4.1, for the rescaled MRII whose SMF deviates from the TNG100 results above $10^{10.2}\,h^{-2}\,M_\odot$. Hence, we only plot results for that simulation below this transition mass. We attribute this mass bias to small number statistics and potential biases in how the SAM assigns galaxies to the rescaled merger trees. Because of this issue, and in order to conform with the number of objects in the Velliscig et al. (2017) study, we carry out the group lensing comparison with the SAM derivatives run on the merger trees of the gravity-only TNG100 simulation.

Compared to the full physics TNG SMFs, the SAM predictions are lower beyond the knee, as seen in Fig. 4.1. As those curves also are consistent with observations, it means that we have room to modify the SMF with a similar amount. Here we have enforced the resolution correction from Pillepich et al. (2018b) for the TNG300, called the rTNG300, and we work with 30 pkpc (physical kpc) aperture masses. In this Chapter, we will refer to the rTNG300 as TNG300 unless explicitly specified in plots where we compare predictions from the two.

As we have seen, running a semi-analytical model on top of dark matter merger trees does not necessary result in the same population of galaxies as in a full hydrodynamical treatment. We can also illustrate it as a shift in host halo masses. In Fig. 4.2 we show the host halo mass distributions for $M_{200\rm c}$ for central and satellite galaxies for three different stellar mass bins using the IllustrisTNG simulation suite compared with the L-Galaxies SAM model. For the TNG300 stellar masses we have applied a resolution correction scheme (Pillepich et al., 2018b) to make them conform with the TNG100 stellar masses. Whereas the satellite host halo mass distribution is similar for all models, stellar masses and simulation volumes, L-Galaxies preferentially populate high mass haloes with centrals, which can be seen in the extended lognormal tail. We will investigate this discrepancy in this Chapter.

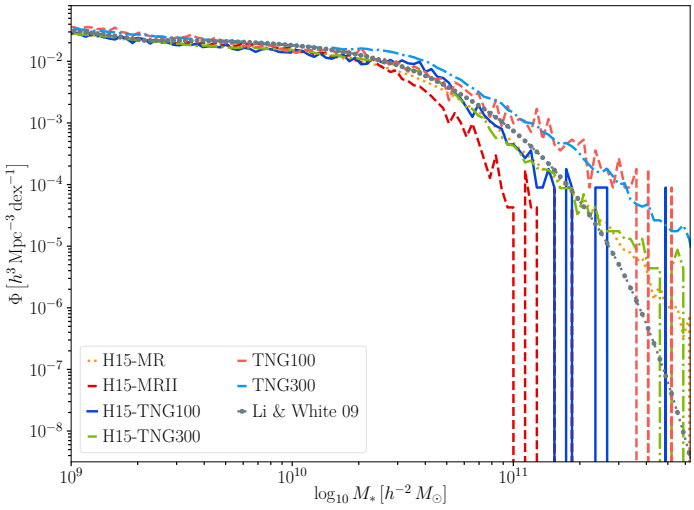

Figure 4.1: The stellar mass function at $z = 0.11$ for the H15 model run on top of the rescaled MR and MRII runs as well as the gravity only runs of the TNG100 and TNG300 compared to hydrodynamical results from the baryonic runs for TNG100 and TNG300 and the SDSS fit from Li & White (2009). We note that the SMFs for the SAM on top of TNG100 and TNG300 results are similar to the rescaled MR, whereas the rescaled MRII starts to deviate from the TNG100 above $10^{10.2}\,h^{-2}\,M_\odot$. These simulations have comparable size and similar cosmologies which leads us to deduce that the rescaling for this simulation volume is accurate up to this transition mass. The hydrodynamical TNG curves lie above the SAM curves above the knee of the SMF.

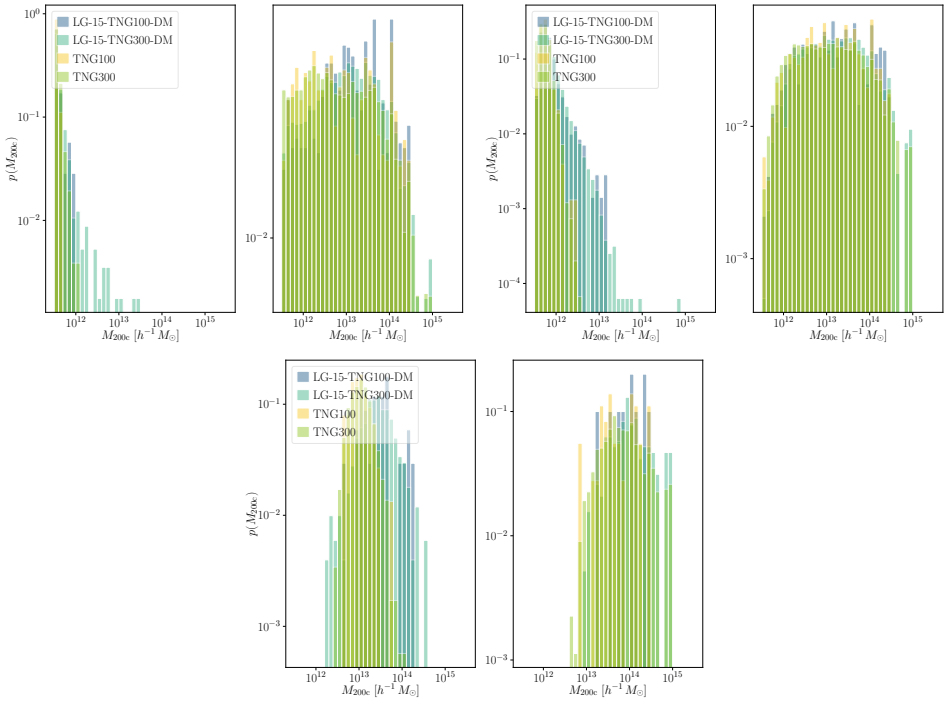

Figure 4.2: Host halo mass distributions at $z = 0.1$ for central (*left panels*) and satellite galaxies (*right panels*), respectively, for $\log M_* = 9,\, 10,\, 11 \pm 0.1\,\mathrm{dex}\left[h^{-2}\,M_\odot\right]$. For low stellar masses the central host halo distribution is narrowly concentrated with a lognormal tail whereas the distribution is Gaussian for high stellar masses. In the hydrodynamical runs we measure stellar masses in 30 pkpc apertures, which is the standard choice for SAM and observational comparisons.

4.6 Methodology

For the van Uitert et al. (2016) comparison, we measure the signal[2] at $z = 0.31$ in the rescaled MR and MRII runs. We also show the corresponding predictions from the TNG300 simulation at $z = 0.30$.

We select the mock LBGs following Wang et al. (2016); Mandelbaum et al. (2016) by matching the observational criteria as defined by Planck Collaboration (2013). We define a cylinder with radius 1 Mpc in physical coordinates spanning $\pm 1000\,\mathrm{km/s}$ in redshift around each galaxy and if the galaxy has the brightest absolute $r-$band magnitude with dust extinction it is considered an LBG. We project the full particle distribution of the box along each spatial axis to maximise the statistical signal with all LBG candidates per axis, which not necessarily are the same. Since there is only a slight redshift evolution of the satellite fraction at low redshifts, we use a single snapshot with the closest z to mock the observational selection. In the SAM the stellar mass is given as the combined mass in stars in the bulge and disk. We neglect the intracluster light (ICL) component which primarily affects the high mass end. In addition, we assume that the stellar masses given by the model correspond to the observed stellar masses, although we quantify errors induced on the lensing profiles by observational misclassification by convolving the model masses with a Gaussian in $\log M_*$ with width $0.08 \times (1 + z)$ following H15. We refer to H15 for a motivation of this choice in an observational context. At $z = 0.11$ this only has a minor impact on the result, but as we move to higher redshifts this becomes important. As only a few percent of the simulated galaxies satisfy the LBG criteria, we use the rescaled MR run and TNG300 to compute the predictions. In this Chapter we use the $z = 0.$ snapshot for the TNG300 to boost the statistical signal and the $z = 0.11$ snapshot for the MR run, but we have checked that there are negligible differences at such low redshifts.

At the high mass end, completion rates for LBGs exceed 90 % for central galaxies, i.e. the fraction of central galaxies which are also LBGs, but less luminous red galaxies are excluded to a higher extent than blue centrals since red centrals live in denser and thus more clustered environments, see Section 4.14, although this effect is of the order of $5 - 10\,\%$.

Galaxies in the SAMs are classified as centrals, satellites or orphans in their host haloes depending on whether their associated subhaloes are central, satellite or stripped. In IllustrisTNG there are only central and satellite subhalo hosts. We use the simulation specific h values to convert between stellar masses. We are primarily interested in looking at predictions from the largest boxes, which limit the lowest allowed stellar masses due to resolution effects. Hence we consider only galaxies with $M_* > 10^{9.39}\,h^{-2}\,M_\odot$ in accordance with Henriques et al. (2017). This limits the stellar mass only clustering data from Henriques et al. (2017) to masses above $M_* > 10^{9.50}\,h^{-2}\,M_\odot$, which in total amounts to four bins.

All distances quoted are in comoving units, except for the LBG selection cylinder with a radius in physical Mpc.

The separation of galaxies into red and blue can be affected by the dust model used, especially while considering dusty star-forming galaxies. This in turn can influence the predicted clustering and lensing signals. To illustrate this we perform the analysis with and without dust extinction for the derivative H15 models as well as the IllustrisTNG suite. The main

[2]For the low stellar mass bins, the median redshift is closer to $z = 0.18$, but we have performed the same analysis at $z = 0.11$ for a few of the models and note negligible differences. Hence we use the same snapshot for all mass bins.

difference in the dust treatment between the G11 and H15 versions is a stronger scaling with redshift in the latter for the extinction by the interstellar medium in galactic discs[3]. This should have a minor impact on the result since we only probe colours at $z = 0.11$.

For the IllustrisTNG, we use model C from Nelson et al. (2018b), which we refer to for the technical details, with resolved dust attenuation following the simulated distribution of neutral gas and metals. This model depends on the viewing angle and we use the median magnitudes of the twelve angles provided. For the uncorrected colours we sum the magnitudes of the individual bound star particles per subhalo. Colours are assigned using the Bruzual & Charlot (2003) stellar synthesis models assuming a Chabrier IMF.

We quantify the best models through a figure-of-merit:

$$\chi^2 = \frac{1}{N} \sum_i \frac{1}{\sigma^2} \left(\xi_{\rm model}(r) - \xi_{\rm data}(r)\right)^2 , \tag{4.6.1}$$

where i goes over all overlapping data points N where we linearly interpolate the model between the bins and σ is the reported variance of the observations. For the clustering data points without error bars, we use conservative $\pm 15\,\%$ estimates for the variance which correspond to the smallest quoted errors. Theoretical error bars for the lensing are computed using a hundred bootstrap samplings of the signal with replacements with the $95\,\%$ percentiles shown.

For the galaxy clustering signal we measure the signal in 40 log-equidistant bins between $20\,h^{-1}\,$kpc and $20\,h^{-1}\,$Mpc and for the lensing 40 log-equidistant bins between $20\,h^{-1}\,$kpc and $2\,h^{-1}\,$Mpc (KiDS+GAMA) and $30\,h^{-1}\,$kpc and $3\,h^{-1}\,$Mpc (SDSS-DR7). Hence we probe the 1-halo and 2-halo terms for the clustering and mainly the 1-halo term for galaxy-galaxy lensing.

For the galaxy group lensing sample from Velliscig et al. (2017), we show predictions from the different SAMs run on the TNG100 at $z = 0.18$. We have also carried out the same analysis at $z = 0.18$ and $z = 0.11$ for the fiducial H15 model using the rescaled Millennium simulation. The corresponding results for the full physics TNG100 and TNG300 runs appear in Chapter 5 on baryonic effects. In the SAMs we introduce a minimal stellar mass $M_*^{\rm lim}$ following Velliscig et al. (2017) from which we start counting group members. This mass is set such that the satellite fraction for galaxies in the GAMA fields is matched for a given stellar mass bin. Increasing this mass leads to an almost monotonous increase in $f_{\rm sat}$, depending on the sample size, as the number of group central galaxies decreases whereas the number of satellite galaxies is almost constant for a given stellar mass bin.

4.7 Data

In this Section we list the different lensing and clustering datasets used in this study and in Section 4.7.5 we define our colour cuts.

4.7.1 KiDS+GAMA: Stellar mass

We compare the predicted lensing signals to observational results from the KiDS shear catalogues and GAMA foreground lens sample in the equatorial regions (field G09, G12 and

[3]The total dust model is separated into an ISM treatment and one for the molecular birth clouds of stars following De Lucia & Blaizot (2007).

G15) using the published data in van Uitert et al. (2016) for the partly overlapping region (75.1 deg^2) with an effective source density of 5.98 arcmin^{-2} (Kuijken et al., 2015). For the sample, we consider all galaxies which satisfy the stellar mass criteria (based on the stellar mass information in Taylor et al. (2011)). Error bars incorporate the effect of cosmic variance.

4.7.2 KiDS+GAMA: Group environment

We make use of observations presented in Velliscig et al. (2017) which were compared to the Eagle hydrodynamical simulation with satisfactory agreement. This study considered measurements which satisfy the stellar mass criteria and are constituents of galaxy groups with at least five members ($N_{\rm FOF} \geqslant 5$) from the GAMA group catalogue G3Cv7 (Robotham et al., 2011). Galaxies in this group catalogue are linked via friends-of-friends based on their line-of-sight and projected distances and the catalogue has been calibrated against the Millennium simulation with SAMs (Bower et al., 2006). For groups with more than five members, galaxies are reliably classified as centrals/satellites above the completeness limit of GAMA which is $\sim \log(M_*/M_\odot) = 8$. The field overlap is 180 deg^2.

4.7.3 SDSS: LBGs

For LBGs, we use the lensing measurements in Wang et al. (2016) (all) and in Mandelbaum et al. (2016) (red and blue). The source catalogue is described in Reyes et al. (2012) and the effective source density is 1.2 arcmin^{-2}. The colour cut is described in Section 4.7.5.

4.7.4 SDSS: Clustering

For the stellar mass only clustering, we use the observations from G11, which have appeared for comparisons with H15 in Henriques et al. (2017) and with TNG100 and TNG300 in Springel et al. (2018).

4.7.5 SDSS: Colour bimodality

We use the SDSS DR7 (Abazajian et al., 2009) lens and clustering sample from Zu & Mandelbaum (2016) as well as the all main SDSS lensing sample from Mandelbaum et al. (2016). We address the difficulties in mocking the former sample in Section 4.12.

Red and blue galaxies are separated according to the following ${}^{0.1}(g-r)$ colour (with filter magnitudes computed in rest-frame wavebands blueshifted to $z = 0.1$),

$$ {}^{0.1}(g-r)_{\rm cut} = 0.8 \left(\frac{\log M_*}{10.5} \right)^{0.6} . \tag{4.7.1} $$

For the SDSS LBGs in Mandelbaum et al. (2016), we separate red and blue according to

$$ {}^{0.1}(g-r)_{\rm cut} = 0.8. \tag{4.7.2} $$

We first K-correct our magnitudes and convert this cut into a separation for magnitudes in rest-frame wavebands at $z = 0$ using the empirical filter conversion formulae by Blanton & Roweis (2007). Transformed to the ${}^{0}(g-r)$ filters, this cut is similar as the one used by Springel et al. (2018) and Henriques et al. (2017) and it reasonably follows the depth of the green valley in L-Galaxies as well as in TNG300, see Fig. 4.3 where we show the colour

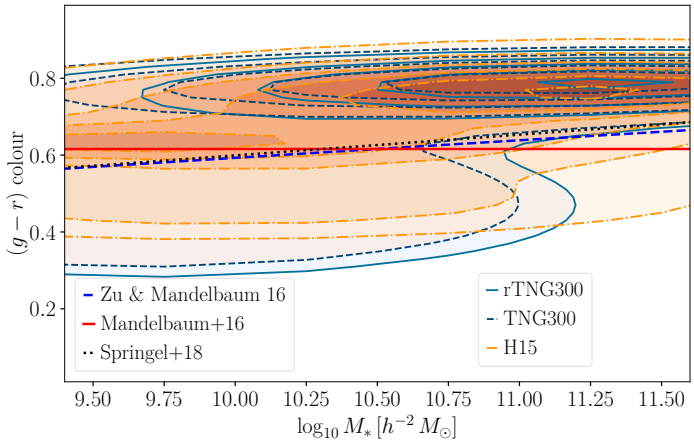

Figure 4.3: Spread in rest-frame $g-r$ colours with dust corrections for H15 and TNG300 with and without resolution corrections. H15 has a flatter red sequence and an additional locus at low stellar masses close to the separation cut. The resolution correction shifts the colour distribution towards the blue for low stellar masses for TNG300.

distribution with dust corrections. We see negligible differences in the colour distributions at the high mass end between the ${}^0(g-r)$ colours with and without dust extinction added, but there is a shift for low mass galaxies around $10^{9.5} \, h^{-2} \, M_\odot$ with blue galaxies being misclassified as red which leads to a slight blurring of the green valley. In SDSS (Schawinski et al., 2014; Nelson et al., 2018b), the effect of dust mostly translates to a shift in the green valley. The Pillepich et al. (2018b) stellar mass resolution correction for the TNG300 does not take into account the differences in the colour distributions between the TNG100 and TNG300, which primarily affects galaxies with $9.0 < \log M_* \, [M_\odot] < 10.5$ in the range of stellar masses we are probing. This means that the red sequence is shifted into the blue by about 0.1 mag for $9.5 < \log M_* \, [M_\odot] < 10.0$, and a slightly smaller shift for higher masses. We note that the fiducial colour distributions for the TNG100 and TNG300 trace each other well.

4.8 Results

In this Section we list our results for the different datasets, starting with the SMFs and the predictions for the different galaxy-galaxy lensing datasets, followed by the galaxy clustering results and lastly by the galaxy group lensing test case.

4.8.1 SMFs and abundance corrections for the SAMs

The nineteen free parameters in L-Galaxies has been calibrated against the stellar mass function (SMF) at $z = 0$, 0.4, 1, 2, 3 and red fraction of galaxies $z = 0$, 0.4, 1, 2. Hence the parameters chosen do not necessarily best match the SMF for low redshifts. We quantify the deviation from the local SMF by computing the necessary stellar mass correction to bring about agreement in abundances with the Li & White (2009) fitting formula for SDSS following Wang et al. (2016). In Fig. 4.4 we start by showing the obtained SMFs at $z = 0.11$ compared to the fitting function in Li & White (2009) for a few of the different $k_{\rm AGN}$ SAMs at fixed $\alpha_{\rm dyn}$ and the two fiducial models, as well as the effect of the most extreme parameter choices

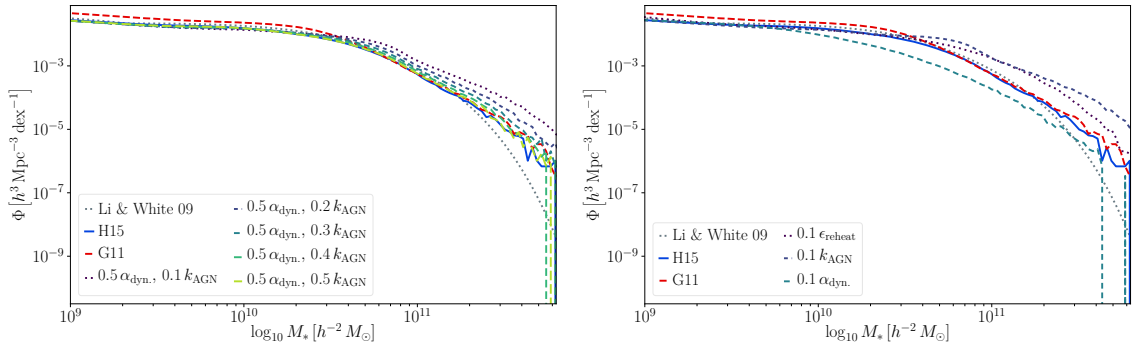

Figure 4.4: Stellar mass functions at $z = 0.11$ for the H15 and G11 fiducial models and model derivatives with different strength of the AGN feedback (panel I). The ($0.5\,\alpha_{\rm dyn}$,$0.5\,k_{\rm AGN}$) model traces the fiducial H15 solution and the different AGN feedback strengths become noticeable above the knee of the SMF. In panel II with illustrate the same situation with the fiducial models compared to the three most extreme parameter choices. Similarly as for the TNG100 and TNG300, the weak feedback models $0.1\,k_{\rm AGN}$ and $0.1\,\epsilon_{\rm reheat}$ predict an excessive number of galaxies beyond the knee of the SMF. The $0.1\,\alpha_{\rm dyn}$ model on the other hand has very few massive galaxies and the change of the SMF is opposite to the direction allowed by observations, leading us to discard this solution.

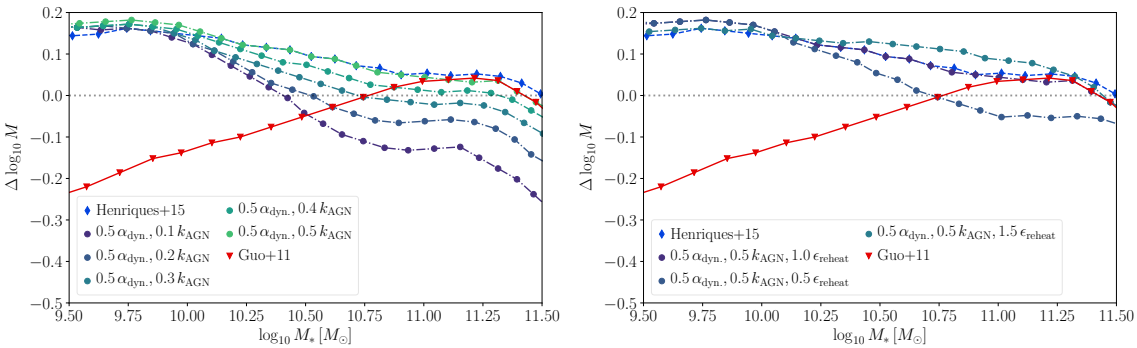

Figure 4.5: Abundance corrections for models with the same $\alpha_{\rm dyn}$, but different $k_{\rm AGN}$. The ($0.5\,\alpha_{\rm dyn}$, $0.5\,k_{\rm AGN}$) model is almost degenerate with the fiducial H15 model, and the ($0.5\,\alpha_{\rm dyn}$, $0.4\,k_{\rm AGN}$) and ($0.5\,\alpha_{\rm dyn}$, $0.3\,k_{\rm AGN}$) solutions have the smallest correction factors around the turnover point of the SMF at $10^{11}\,M_\odot$. Panel II is analogous to panel I but for models with the same $k_{\rm AGN}$ and $\alpha_{\rm dyn}$ but different $\epsilon_{\rm reheat}$ compared to the fiducial choices. Simultaneously decreasing $k_{\rm AGN}$ and $\epsilon_{\rm reheat}$ produces a smoother transition around the knee than solely decreasing the AGN feedback efficiency.

Stellar mass lensing	Fiducial	Abundance corrected
First	$0.1\,k_{\rm AGN}$	H15
Second	$(0.5\,\alpha_{\rm dyn},\,0.1\,k_{\rm AGN})$	$0.1\,\epsilon_{\rm reheat}$
Third	$(0.4\,\alpha_{\rm dyn},\,0.1\,k_{\rm AGN})$	$(0.5\,\alpha_{\rm dyn},\,0.5\,k_{\rm AGN},\,0.5\,\epsilon_{\rm reheat})$

Table 4.3: The best fit models according to stellar mass only lensing without and with abundance corrected masses. Lensing prefers models with weaker AGN feedback and the H15 does a good job once the stellar masses have been altered to comply with SDSS abundances.

from Table 4.2 in panel II. Here we have not convolved the masses with the observational error estimate but this has a minor effect below $10^{11.2}\,h^{-2}\,M_\odot$ and only affects the massive end. We observe that the SMF of the $(0.5\,\alpha_{\rm dyn},\,0.5\,k_{\rm AGN})$ model closely resembles the H15 result, indicating that reducing the dynamical friction time while simultaneously reducing the AGN efficiency indeed trace a degeneracy. The more extreme AGN feedback choices produce deviations away from the fitting function starting at $10^{10.4}\,h^{-2}\,M_\odot$. Yet, measurements of the stellar masses at the high mass end are highly uncertain due to difficulties in properly integrating the sizes of the galaxies, as well as accounting for the ICL, and flux corrections can modify these masses by 0.3 dex (D'Souza et al., 2015). Hence, we determine that these modifications are allowed by the observational constraints. The $0.1\,\epsilon_{\rm reheat}$ and $0.1\,k_{\rm AGN}$ models lie on the extreme end of what is allowed whereas the $0.1\,\alpha_{\rm dyn}$ model is ruled out. Compared to the TNG suite predictions in Fig. 4.1, these model derivatives look more similar to those results above $10^{10.2}\,h^{-2}\,M_\odot$.

The abundance corrections are illustrated in Fig. 4.5 with the mass correction in dex on the $y-$axis for a given stellar mass on the $x-$axis. All derivative models of H15 has a positive correction for low stellar masses whereas it is negative for the G11 model with approximately the same magnitude. These two models have a similar correction for stellar masses around $10^{11}\,M_\odot$. The model with reduced $\alpha_{\rm dyn}$ and AGN feedback efficiency $k_{\rm AGN}$, $(0.5\,\alpha_{\rm dyn},\,0.5\,k_{\rm AGN})$, needs a very similar correction as H15 as seen in Fig. 4.5. At fixed $\alpha_{\rm dyn}$, altering $k_{\rm AGN}$ has the net effect of gradually decreasing the correction for high stellar masses, but the effect is small for dwarf galaxies with a congruence towards the fiducial solution. As we shall see in the following sections, the $(0.5\,\alpha_{\rm dyn},\,0.2\,k_{\rm AGN})$ model will give the best LBG and clustering results, and we see that it comes with a small correction. Fixing $k_{\rm AGN}$ and changing $\alpha_{\rm dyn}$ gradually offsets the solution similarly across the whole range of stellar masses, although the effect is slightly larger around $10^{10.5}\,M_\odot$. Lastly, varying the SN feedback in panel II of Fig. 4.5 produces concave and convex curves around the fiducial valued $\epsilon_{\rm reheat}$ model, with a congruence at $10^{10}\,M_\odot$. The extreme solutions with 10 % of the fiducial H15 values for the AGN feedback and SN feedback are similar to the low $k_{\rm AGN}$ solutions, where the $0.1\,\epsilon_{\rm reheat}$ model lacks the plateau feature around $10^{11.25}\,M_\odot$ which the $0.1\,k_{\rm AGN}$ and H15 have. The $0.1\,\alpha_{\rm dyn}$ solution is ruled out and remains positive across the whole mass range. If lensing does not offer any additional constraining power w.r.t. the stellar mass function, changing the stellar masses in the samples to conform with the SMF will bring the signal into agreement.

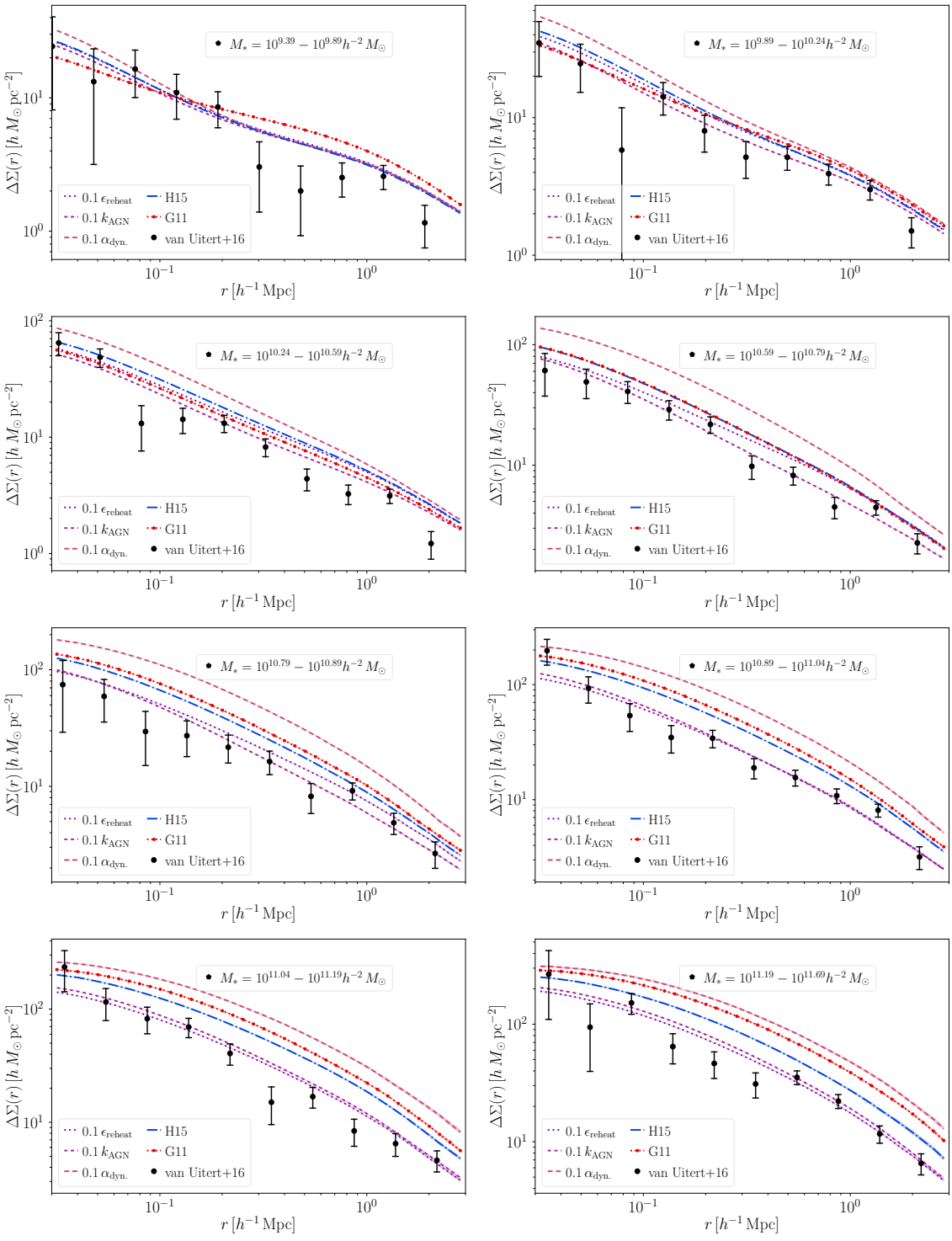

Figure 4.6: Lensing signals for galaxies selected according to stellar mass at $z = 0.31$ compared to measurements from van Uitert et al. (2016). Predictions from the G11 model exceed the H15 model for the lowest mass bin and for mass bins $M_* > 10^{10.79}\,h^{-2}\,M_\odot$. From this mass onwards, the two extreme SAMs with $0.1\,k_{\rm AGN}$ and $0.1\,\epsilon_{\rm reheat}$ have the best performance.

4.8.2 Stellar mass selection: KiDS+GAMA

If we only select galaxies by stellar mass for the overlapping KiDS+GAMA fields at $z = 0.31$ for the van Uitert et al. (2016) observations, the SAMs, both the H15 and G11 models, predict an excessive signal around all galaxies for masses $M_* > 10^{10.79}\,h^{-2}\,M_\odot$. This is apparent in Figs. 4.6 and 4.7, where we illustrate the fiducial model predictions together with the results for the extreme models (Fig. 4.6) and the models with fixed $0.5\,\alpha_{\rm dyn}$ and different strength of the AGN feedback (Fig. 4.7). The H15 predicts a lower lensing signal than G11 from this mass onwards. For the least massive bins, the G11 model yields a smaller signal in the centre, but more pronounced central bumps owing to its high satellite fractions, see Fig. 4.8. Such a signal is disfavoured by the observations, leading us to conclude that the H15 model has the best fiducial performance. This shift in preference could both be attributed to the higher satellite fractions as well as the shift to $z = 0.31$ since the H15 model has a better agreement with the observed SMFs across a wider redshift range.

In the lowest mass bin we have roughly 1 million galaxies in the fiducial H15 model and its derivatives and ~ 1.5 million for the G11 model, which means that we are analysing a very general average. For these low masses, all models perform approximately equally well, but the more extreme choices with low supernovae and/or low AGN efficiency are able to capture the signal across the whole mass range. As visible in Fig. 4.6, these two extremes produce equivalent predictions for $M_* > 10^{10.89}\,h^{-2}\,M_\odot$, but at lower masses the $0.1\,k_{\rm AGN}$ model suggests a lower lensing signal from $r \sim 100\,h^{-1}$ kpc outwards for $10.59 < \log M_*\,[h^{-1}\,M_\odot] < 10.89$ and starting already at the centre for lower mass bins. This difference could be driven by the stronger relative strength of the AGN feedback modification for the SMF and also the higher satellite fraction of the $0.1\,\epsilon_{\rm reheat}$ model as shown in Fig. 4.8. The satellite fraction for this model is higher as the lower SN feedback boosts star formation in centrals and satellites alike, whereas the AGN feedback modification mainly concerns the centrals[4].

In Fig. 4.7 we show the effect of gradually lowering the AGN feedback efficiency. At the high mass end, predictions for the $(0.5\,\alpha_{\rm dyn},\, 0.1\,k_{\rm AGN})$ model are similar to the $0.1\,k_{\rm AGN}$ results. It is the favoured solution from $M_* > 10^{10.79}\,h^{-2}\,M_\odot$ upwards, and the intermediate models do better for the $9.89 < \log M_*\,[h^{-1}\,M_\odot] < 10.24$ and $10.59 < \log M_*\,[h^{-1}\,M_\odot] < 10.79$ mass bins. Decreasing the feedback efficiency lowers the signal step-by-step, except for the least massive bin where there are only small differences between the models, which we could also infer from the convergence of the abundance corrections in Fig. 4.5. We also plot the results for the H15 model run on MRII to investigate simulation volume and resolution effects for the two least massive bins. These curves lie slightly above the MR results which we attribute to smaller statistics. Thanks to the increased resolution, there are fewer orphan galaxies in this simulation, and thus the mismatch with the observations should partly be attributed to the general treatment of the satellites in this mass range. In Section 4.15, we see that this statement is supported by the model run on the TNG100, where we also predict excessive signals for the massive stellar mass bins, demanding model modifications. As suggested by Fig. 4.6, we can lower either or both of the AGN or supernovae efficiencies to obtain a better agreement with data. In Fig. 4.9, we show the result for moderate changes in

[4]Observationally, the accretion or quasar mode of AGN feedback is more prominent among in-falling satellites into a massive cluster environment than for the centrals themselves, which can be attributed to mechanisms such as ram-pressure stripping preventing accretion onto the centrals (e.g. Gordon et al., 2018). There are no to minor differences for low mass groups. However, the radio-mode feedback is mainly restricted to the centrals.

$\epsilon_{\rm reheat}$, where simultaneously lowering $k_{\rm AGN}$ and $\epsilon_{\rm reheat}$ and $\alpha_{\rm dyn}$ help to mitigate the tension with observations. This model performs well except in the two most massive stellar mass bins, and as shown in Fig. 4.5 comes with a smaller discrepancy for the SMF at the high mass end than models with lower $k_{\rm AGN}$ only. For small variations in $\alpha_{\rm dyn}$ while $k_{\rm AGN}$ is fixed, the resulting lensing profiles only change marginally.

However, these signals feature degenerate effects from the host halo masses and the satellite fractions $f_{\rm sat}$, which encumbers the modelling interpretations. Still, the discrepancies shown are too large to be a product of these factors alone for the SAMs. In Fig. 4.8 we show the predicted satellite fractions for the different mass bins and they lie within the allowed range from the lensing observations and trace the GAMA group $N_{\rm FOF} > 2$ results well. Intuitively, the satellite fractions are lower for the models with low $\alpha_{\rm dyn}$ as satellite galaxies merge faster. Most models trace a degenerate solution close to the fiducial H15 model and the G11 model predicts more low mass satellites. Although the two extreme feedback models $0.1\,k_{\rm AGN}$ and $0.1\,\epsilon_{\rm reheat}$ predict similar lensing signals in Fig. 4.6, especially at the high mass end, the $0.1\,\epsilon_{\rm reheat}$ model predicts more satellites. We shall see in Section 4.8.8 that this affects the clustering signal at $z = 0.11$. The resolution corrected TNG300 satellite fractions are excessive around the knee of the SMF, where there is a corresponding excess in the stellar mass function. If we switch the selection to the fiducial simulation without the correction, the satellite fractions trace the TNG100 solution.

In Table 4.3, we list the SAMs which perform best according to the mean figure-of-merit from all lensing mass bins with and without abundance corrected stellar masses. The lensing data favour a low AGN feedback, with a preference for the fiducial dynamical friction parameter or large fractions of it. If we perform the same test post-abundance corrections, the fiducial H15 model comes out on top followed by the low SN feedback efficiency models. Hence, while these models also come with large abundance corrections, the result does not change much. It is interesting that the corrected H15 profiles lie closer to the data than the corrected and (uncorrected) G11 model predictions.

4.8.3 Abundance and stellar mass error impacts

As we already saw in Section 4.8.1, the predicted abundances from the SAMs differ from the observed SMF at $z = 0.11$. If we account for these deviations, how much are the lensing profiles altered? In Wang et al. (2016), such corrections were able to reconcile the discrepancies for the H15 model for LBG lenses. In this section we investigate if these modifications are potent enough to mitigate the large deviations observed in Fig. 4.6 for a more general lens sample. Since we do not have a fitting function for the SMF at $z = 0.31$, we perform the corrections and measurements for the $z = 0.11$ sample and we assume that the GAMA SMF is similar to the SDSS SMF which has been shown to be the case (e.g. Weigel et al., 2016). The result for the H15 model is illustrated in Fig. 4.10. While the correction serve to mitigate the tension, it is not enough to solve it. Intuitively, we observe the opposite effect for the extreme models in e.g. Fig. 4.6, where the abundance correction serves to bring the profiles away from the data points as seen in panel II of Fig. 4.10 for the best fit $0.1\,k_{\rm AGN}$ model. This serves to caution that a well-matched SMF does not necessary imply observationally consistent lensing profiles and vice versa.

In addition, we convolve the stellar masses with a Gaussian in $\log M_*$. We have performed this comparison at $z = 0.31$ and $z = 0.11$ and note that the effect is slightly more pronounced at the higher redshift due to the redshift dependence of the convolution. In Fig. 4.11, we show

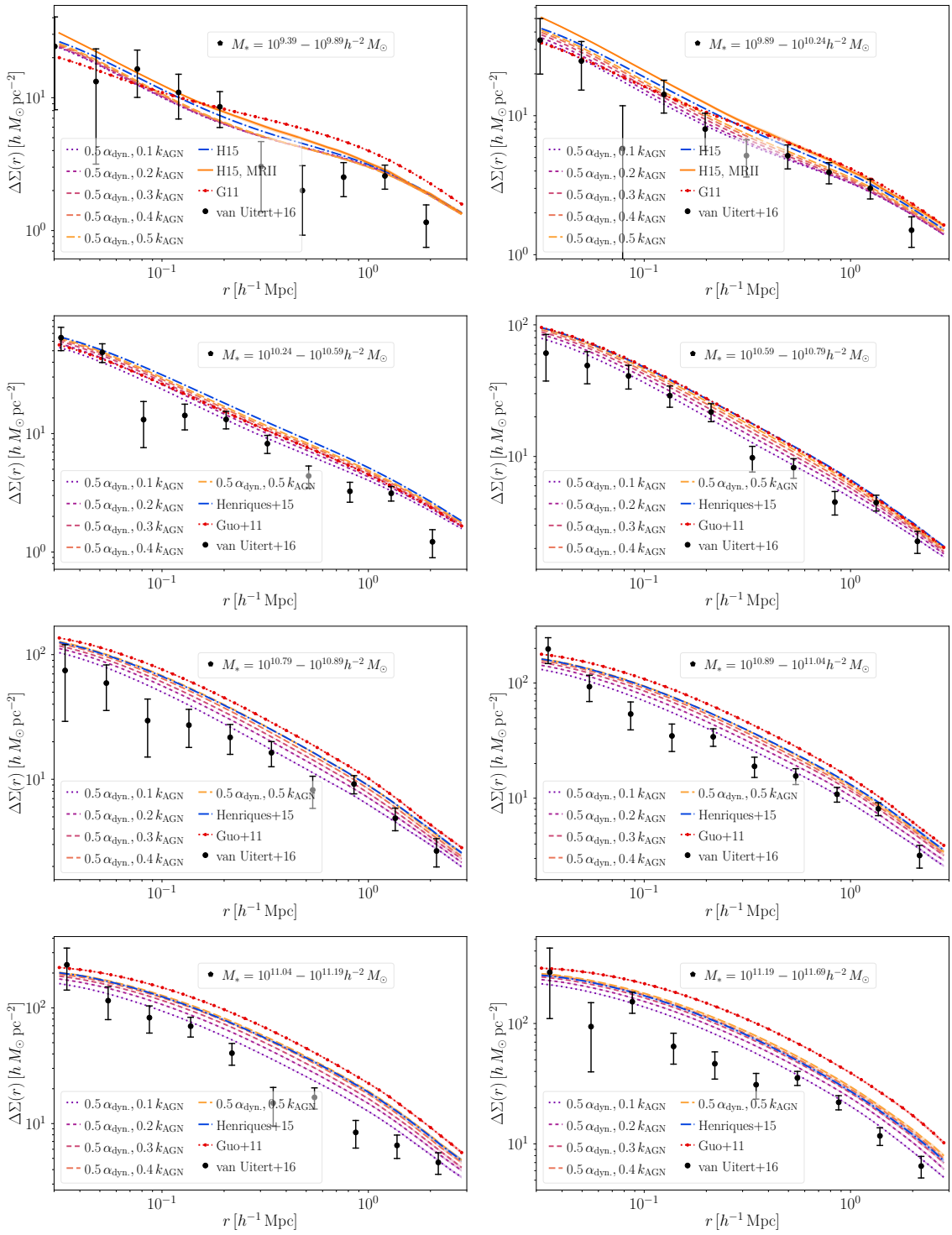

Figure 4.7: Similarly as Fig. 4.6 but for models with varying strength of the AGN feedback, compared to the two fiducial models. Here we have also included the MRII predictions from H15 for the two least massive bins. As hinted by the shape of the SMF in Fig. 4.1, the lensing signals for the rescaled MR and MRII simulations compare to one another below $10^{10.2}\,h^{-2}\,M_\odot$. Except for the two least massive bins where the effect is not apparent, the data favours a SAM with a weaker AGN feedback, also with shorter merger times, with a gradual decrease of the signal as the feedback efficiency drops.

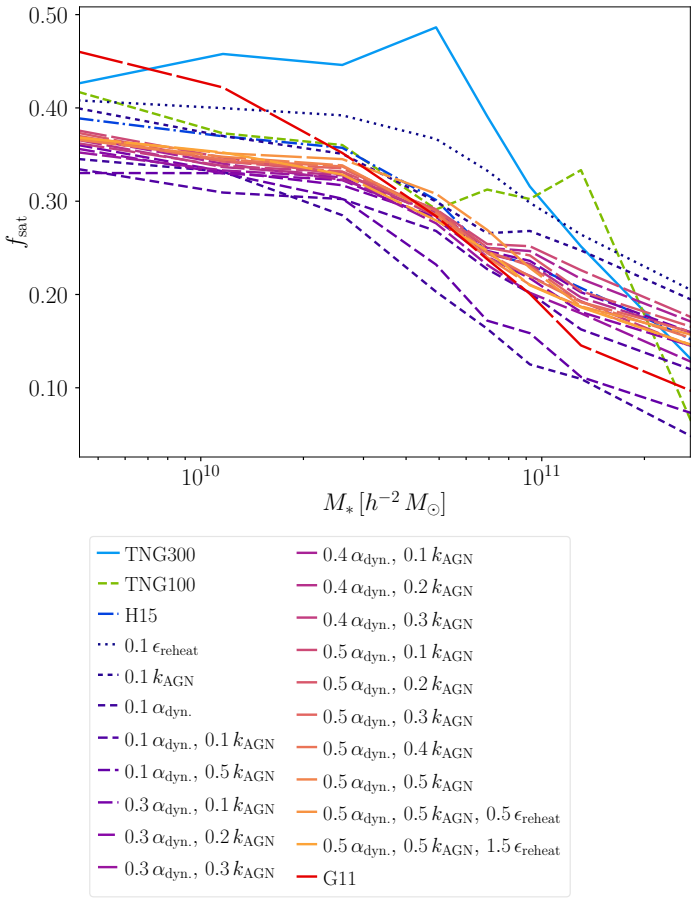

Figure 4.8: Satellite fractions for the mass bins in the van Uitert et al. (2016) comparison for the different SAMs and the TNG suite.

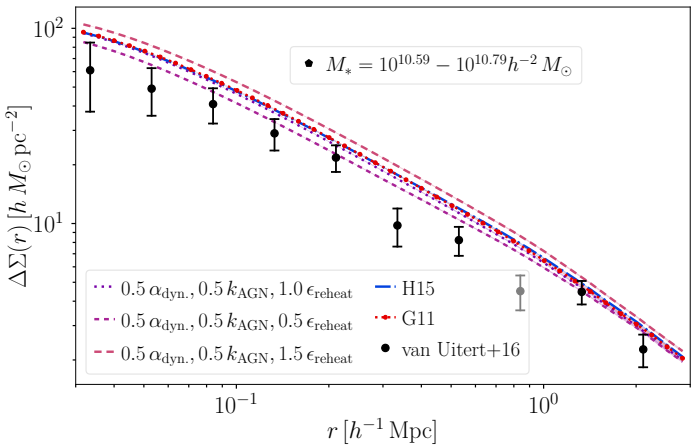

Figure 4.9: Lensing profiles from SAMs with varying $\epsilon_{\rm reheat}$. As implied by the results in Fig. 4.6, the data can equally well be accommodated by a weaker SN feedback together with a weaker AGN feedback.

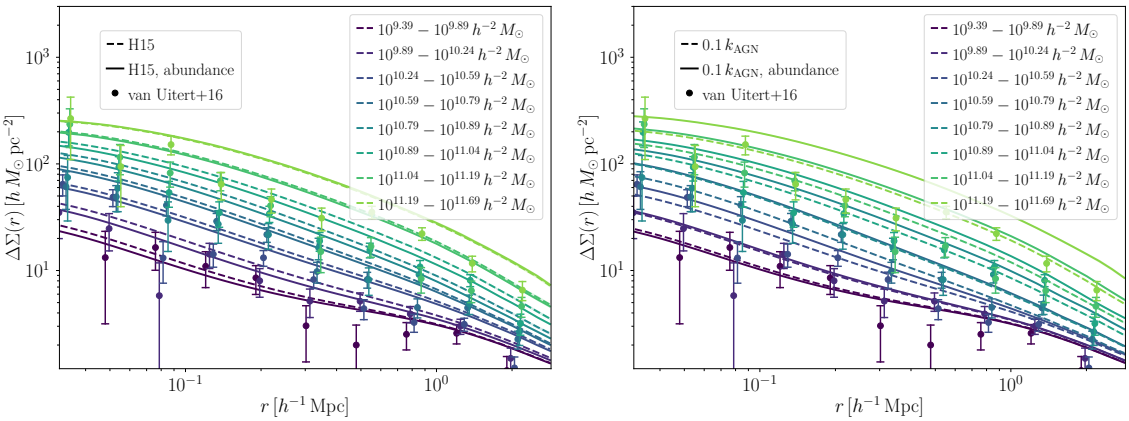

Figure 4.10: In panel I, we show the abundance corrected lensing signals for the H15 model with respect to the fiducial predictions. While the correction shifts the profiles in the right direction, it is not sufficient to fully reconcile the tension. Lensing predictions from the best-fit $0.1\,k_\mathrm{AGN}$ model, with and without corrections, are displayed in panel II. Here the stellar mass correction worsens the agreement with data.

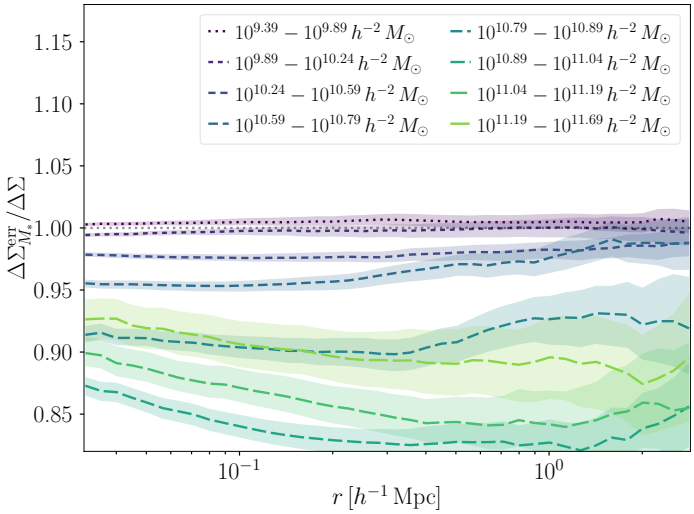

Figure 4.11: Impact of Gaussian errors on the stellar masses for the lensing profiles for the H15 model. We see that the stellar mass errors do not influence the low mass signal, but can lower the high mass signal for the $10^{10.89} - 10^{11.04}\,h^{-2}\,M_\odot$ mass bin by $15 - 20\,\%$. The effect is roughly homogeneous across the whole radial range with a slightly smaller effect in the centres.

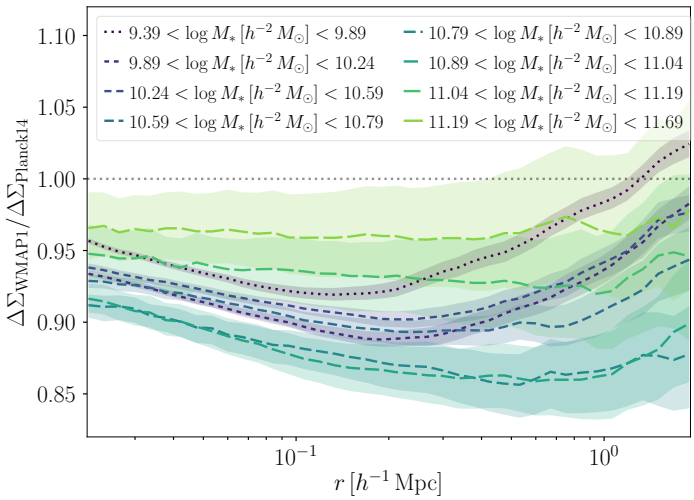

Figure 4.12: Residuals for the H15 model run on top of the fiducial Millennium run w.r.t. the rescaled simulation at $z = 0.31$. The signal is suppressed by approximately 10 % with the largest differences recorded around the knee of the SMF.

the result for the H15 model and find that the effect is negligible for the low mass signal, but can amount to $\sim 15\,\%$ at the high mass end, peaking at the knee of the SMF. The impact is model specific, with $\sim 5\,\%$ effects for the $0.1\,\epsilon_{\rm reheat}$ and $0.1\,k_{\rm AGN}$ derivatives, whereas the result for the G11 model is similar to H15. These errors lower the lensing signal as abundant lower stellar mass galaxies, generally residing in less massive host haloes, are upscattered to a more massive bin. As we shall see in the coming subsections, this effect is of the same order of magnitude as the abundance correction, cosmological and baryonic impacts. Alone, it is not enough to explain the discrepancy. Moreover, the observational error bars should already account for these stellar mass errors, which means that this is a conservative estimate.

4.8.4 Cosmological impact

We also plot the predictions for H15 run on top of the unscaled Millennium simulation. We see in Fig. 4.12 that the predictions are slightly lower by about $\sim 10\,\%$ than for the Planck cosmology but not sufficient to explain the observational difference. This suppression has a flat evolution with radius for the highest mass bins which are central dominated, whereas there is a difference for the satellite population which dominates the lowest mass bins. The largest effect is recorded around the knee of the SMF, which is to be expected since it is most subject to calibration. A more fair comparison from the perspective of the galaxy formation model, would be with a retuning of a few model parameters to account for this change, which leads us to conclude that the results in Fig. 4.12 are upper conservative estimates of the cosmological impact. In Wang et al. (2016), predictions from the G11 model were compared across three different cosmologies (WMAP1, WMAP7 and Planck 2014) for LBG profiles and the WMAP1 curves were notably higher for the two most massive bins w.r.t. the other cosmologies, which means that one cannot draw a general conclusion on the sign of the impact as a function of background cosmology for all formation models.

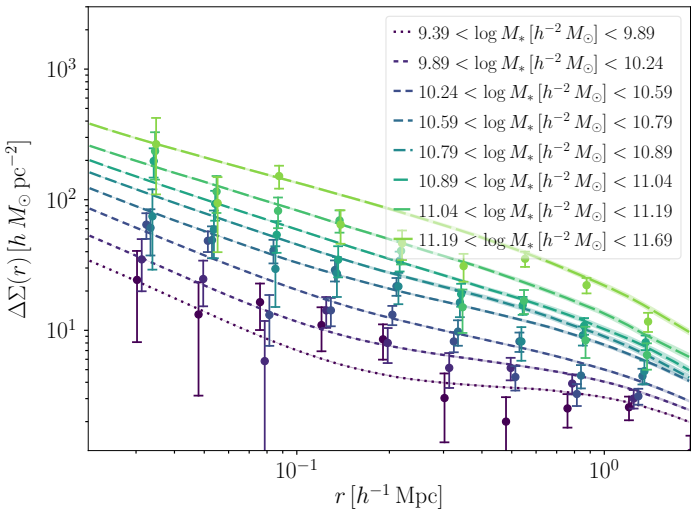

Figure 4.13: Measurements for the TNG300 at $z = 0.30$ for the full physics run compared to observations with the resolution correction from Pillepich et al. (2018b) applied for the selection. If one computes the same profiles using bound masses, the amplitude of the two lowest mass bins increases and the two highest mass bins drops with smaller effects in between. The TNG300 is able to reach comparable agreement with the data as the SAMs with better performance than the fiducial G11 and H15 models at the high mass end.

4.8.5 Baryonic impact

In Fig. 4.13, we show the predictions from the TNG300 simulation at $z = 0.30$ with respect to the van Uitert et al. (2016) observations. Compared to the two fiducial SAM models, the curves do not persistently lie above the data points, with a similar excellent performance as the $0.1\,k_{\mathrm{AGN}}$ model in panel II of Fig. 4.10 for the most massive stellar mass bins, and the results are overall more consistent across the whole stellar mass range.

By matching subhaloes in the baryonic runs with their dark matter only counterparts with their particle ids, we can obtain an estimate of the impact of baryonic feedback processes on the profiles. This works particularly well for central galaxies and we will use this matched central galaxy signal to estimate the baryonic deformation of the profiles here using the TNG300 simulation. The result for the *central* galaxies satisfying the stellar mass criteria of van Uitert et al. (2016) is given in Fig. 4.14. As already found in the literature (e.g. Schaller et al., 2015a; Leauthaud et al., 2017), the baryons enhance the profiles close to the central galaxy due to the presence of additional cooling from the stellar component and the associated adiabatic contraction of the dark matter, a suppression from $r \sim 100\,h^{-1}\,\mathrm{kpc}$ to $r \sim 1\,h^{-1}\,\mathrm{Mpc}$ and then convergence at larger scales since the same projected mass is contained inside the aperture. This is what we observe in Fig. 4.14 where the suppression increases with increasing stellar mass till $M_* > 10^{10.6}\,h^{-2}\,M_\odot$ and is self-similar for the four subsequent mass bins with deviations for the most massive bin. Note that the satellite fraction is high for the lower stellar mass bins which means that the baryonic effect measured here is not a good proxy for the observational signal. The maximum suppression amounts to $\sim 15\,\%$ attained at $r \sim 200\,h^{-1}\,\mathrm{kpc}$ and the central enhancement is roughly $\sim 20 - 40\,\%$ depending on the stellar mass and radial bin. Except for the two least massive bins, a good convergence is reached at $r \sim 2 - 3\,h^{-1}\,\mathrm{Mpc}$ with the dark matter-only run. However, these effects are

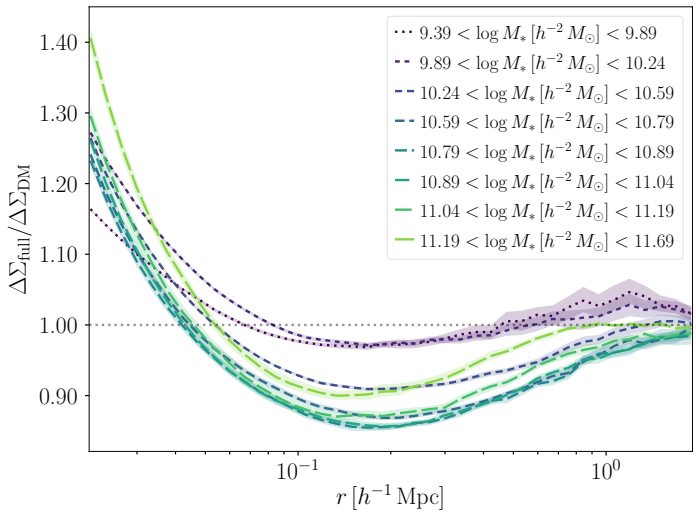

Figure 4.14: Residuals for TNG300 at $z = 0.30$ between the full physics run and the dark matter only run for matched centrals, here with the resolution correction from Pillepich et al. (2018b) applied for the selection. The result using bound stellar masses differs negligibly, except for the most massive bin where the central enhancement is $\sim 5\,\%$ lower than what is plotted here. The baryonic imprint is characterised by three features; a central enhancement, an intermediate scale suppression and a residual enhancement/suppression around $r \sim 1\,h^{-1}\,{\rm Mpc}$, depending on the stellar mass of the bin.

smaller than the measured deviations for the SAMs in e.g. Fig. 4.7, implying that a better assignment scheme between galaxies and subhaloes is required.

4.8.6 Stellar mass selection - SDSS colour

In this section we show a few comparisons between the lensing signal separated according to colour and observations from SDSS, with the Zu & Mandelbaum (2016) imposed and without for all main SDSS galaxies Mandelbaum et al. (2016). For low mass galaxies, the SAMs and the TNG300 outperform the iHODs slightly for red galaxies, see Fig. 4.15, whereas the predictions for the blue signal is comparable, although the SAMs and the TNG300 suggest a steeper central profile. Weakening the AGN feedback has the net effect of increasing the amplitude of the central bump on scales $r \sim 700\,h^{-1}\,{\rm kpc}$, which means that the red lensing signal can be used to constrain this combination, although it is sensitive to the colour assignment scheme and dust corrections as we describe in Section 4.16.

Switching to a higher mass bin around the knee of the SMF in Fig. 4.16, here with the extreme models shown, we find that the SAMs and the TNG300 systematically overpredict the red lensing signal for $M_* \lesssim 10^{11.2}\,M_\odot$ for the all main sample. We note that the data points for the Zu & Mandelbaum (2016) sample lie slightly lower beyond the knee of the SMF which induces a tension with our best fit models. For more massive bins for the all main sample, the weak feedback models and the TNG300 are once again in agreement with observations, reflecting the results in Section 4.8.2. This statement holds true for all SAMs and none of the model variations listed in Table 4.2 produce acceptable solutions for this intermediate mass range. However, this can be caused by problems matching the stellar masses in SDSS and enforcing the proper colour separation, as we compare to Fig. 4.6 for the M_*-only sample from KiDS+GAMA where both the $0.1\,k_{\rm AGN}$ and the $0.1\,\epsilon_{\rm reheat}$ models are

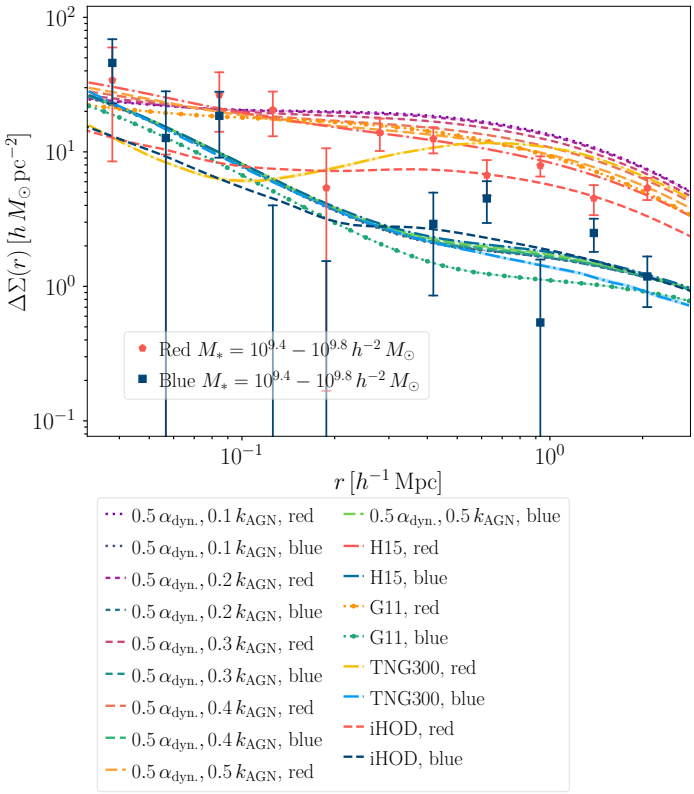

Figure 4.15: Lensing predictions for red and blue galaxies with $9.4 < \log M_* \left[h^{-2}\,M_\odot\right] < 9.8$ in SDSS using the Zu & Mandelbaum (2016) datasets and iHODs compared to the different SAMs and the TNG300. For this mass range, the predictions for the red lensing signal from the SAMs and TNG300 are in slightly better agreement with the data than the iHODs, whereas there are no major differences for the blue signal.

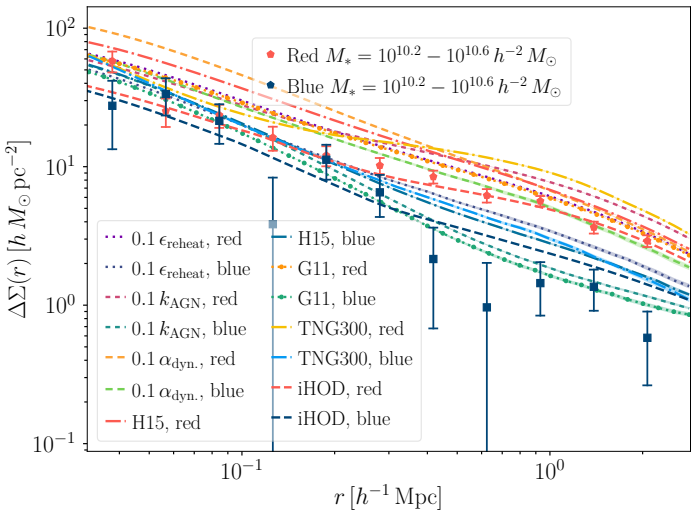

Figure 4.16: Same as in Fig. 4.15, but for galaxies with $10.2 < \log M_* \left[h^{-2}\,M_\odot\right] < 10.6$ and with the most extreme SAMs shown. Here, the iHODs agree with observations for the red lensing signal whereas all SAMs and the TNG300 predict excessive signals. For the blue galaxies, the G11 and the $0.1\,k_{\rm AGN}$ model produces the best results, especially for scales around $r \sim 1\,h^{-1}\,{\rm Mpc}$.

Model	$f_{\rm sat}^{\rm red}$	$f_{\rm sat}^{\rm blue}$	$f_{\rm orphan}^{\rm red}$	$f_{\rm orphan}^{\rm blue}$
G11	0.36	0.18	0.11	0.00
H15	0.38	0.24	0.12	0.01
$0.1\,\epsilon_{\rm reheat}$	0.40	0.31	0.14	0.02
$0.1\,k_{\rm AGN}$	0.47	0.19	0.15	0.00
$0.1\,\alpha_{\rm dyn}$	0.28	0.32	0.03	0.01

Table 4.4: The satellite and orphan fractions for red and blue galaxies separated according to Eq. (4.7.2) for galaxies with $10.7 < M_*\,[M_\odot] < 11.0$. Similarly as for the TNG300 in Fig. 4.8, the $0.1\,k_{\rm AGN}$ model predicts an excessive satellite fraction, which can be culled by reducing $\alpha_{\rm dyn}$. Removing the red orphan galaxies reduces the overall satellite fractions by about 10 %, except for the $0.1\,\alpha_{\rm dyn}$ model which do not have that many orphans.

able to match the lensing signal at the high mass end. With respect to the quoted satellite fractions for the samples listed in Zu & Mandelbaum (2015), the two fiducial SAMs are only a few percent off[5]. In addition, the average host halo masses only differ by about 0.1 dex. These differences are too small to drive the large biases we observe.

An alternative explanation is offered in Figs. 4.17 and 4.18, where we plot the predicted signals from the SAMs and the TNG300 without orphan galaxies and without unmatched subhaloes, respectively, w.r.t. lensing observations from the all main SDSS-DR7 with the same colour cut as for the LBGs. As implied by the illustrated cuts in Fig. 4.3 and the arguments brought forth in Section 4.12, there are only minor differences between these observations and those of Zu & Mandelbaum (2016). By removing the orphan galaxies, the

[5]For the $10.2 < \log M_* \left[h^{-2}\,M_\odot\right] < 10.6$, the quoted $f_{\rm sat} = 0.37 \pm 0.02$ and we measure $f_{\rm sat} = 0.33$ and $f_{\rm sat} = 0.34$ for the G11 and H15 models. The reported average host halo mass is $\langle \log M_{\rm h} \rangle = 12.15(+0.03)(-0.04)\left[h^{-1}\,M_\odot\right]$ and we record 12.16 and 12.29, respectively. In Zu & Mandelbaum (2016), a red fraction $f_{\rm red} = 0.71$ for this mass bin is given, whereas we note $f_{\rm red} = 0.87$ and $f_{\rm red} = 0.77$. Hence, we have more red galaxies but for the H15 model the difference should be negligible.

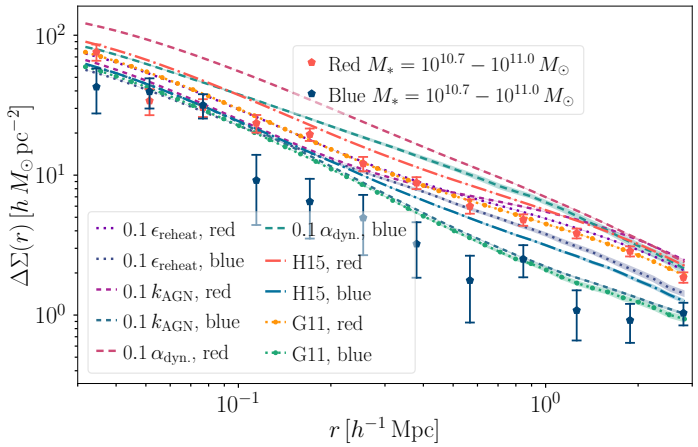

Figure 4.17: Lensing predictions for all main SDSS red and blue galaxies with the same colour cut as for the LBGs without orphan galaxies. If we consider the whole signal from SDSS there little to no tension w.r.t. the Zu & Mandelbaum (2016) dataset for this mass range. Removing the orphan galaxies produce a better agreement for the red lensing signal with the new and old satellite fractions listed in Table 4.4.

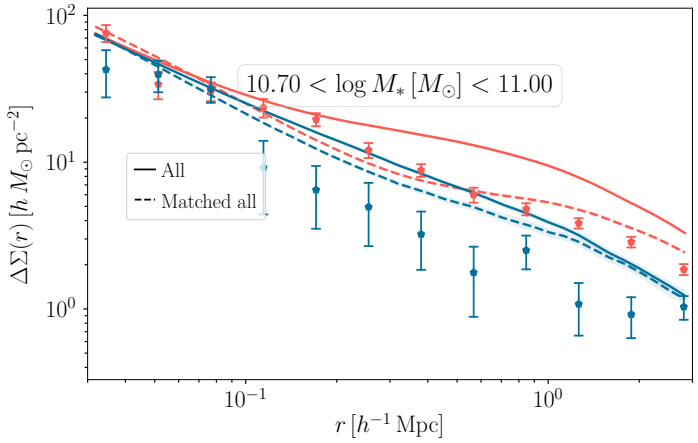

Figure 4.18: Lensing profiles from the TNG300 for blue and red galaxies in SDSS with the matched and total signal highlighted. If we restrict ourselves to matched subhaloes, the tension with respect to the red lensing signal drops. The red satellite fraction also drops from $f_{\rm sat} = 0.51$ to 0.35 with a central galaxy matching rate of 0.999 (red). The blue satellite lensing fraction also drops a corresponding amount from 0.52 to 0.35 with a similar matching rate 0.999, but the effect on the lensing signal is much more modest.

tension between the SAMs and the data points is reduced and the corresponding satellite fraction drops, see the listed values in Table 4.4, except for the $0.1\,\alpha_{\rm dyn}$ model which have only a few orphans. If we just examine the orphan galaxy signal, we find that it is similar to a massive central term as the orphans reside close to the halo centres. At lower masses the large abundance of low mass haloes hosting central galaxies offsets the imprint of this signal and produces an agreement with observations.

In Section 4.16, we show conservative estimates on much the dust extinction affects the signal amplitude for the two fiducial SAMs for the Zu & Mandelbaum (2016) selection function. At the high mass end for $M_* > 10^{11}\,h^{-2}\,M_\odot$ for the G11 model there are only small differences for the red signal with and without dust whereas the dusty red signal is suppressed for all masses for H15 with at most $\sim 15\,\%$ for the $10.6 < \log M_*\,[h^{-2}\,M_\odot] < 11.0$ mass bin, closely followed by the effects for the $10.2 < \log M_*\,[h^{-2}\,M_\odot] < 10.6$ mass bin. Not surprisingly, the dust correction thus work in the opposite direction to reconcile the tension for the red lensing signal. For the blue signal, the dust extinction boosts the predictions by about a factor of 2 and 1.5 for the most massive bins where there are many red galaxies and few blue, with smaller effects for lower masses. For low mass systems below $10^{10.2}\,h^{-2}\,M_\odot$ in the H15 model, there is a suppression for the central bump by about $\sim 15\,\%$ in the dust extinct signal. We attribute this effect to dusty blue galaxies residing in less massive haloes, which are able to keep more dust than their massive counterparts (e.g. Bekki, 2013), and thus a lower central signal.

In Fig. 4.18, we highlight a corresponding effect for the TNG300 for the same observations where we remove all subhaloes which lack a match in the gravity-only run and compare the lensing signal to the full physics predictions. If we restrict ourselves to matched substructures, a much better agreement with data is reached. We note that the satellite fractions are comparable for the red and blue signals, implying that the colour of a satellite galaxy is not a good predictor for the likelihood of its host substructure to still be present in the dark matter-only run. Restricting the signal to matched substructures has thus the effect of reducing the satellite fraction by a similar amount for the blue and the red signal, although the impact on the red lensing signal is more considerable as the amplitude of the central host halo term drops for the satellite signal. This can be caused by substructures merging and getting disrupted more quickly in more massive host haloes, where galaxies on average are redder, which are excluded by the matching criterium. If we look at more massive red galaxies, the TNG300 is in agreement with observations for $M_* > 10^{11.4}\,[M_\odot]$, also for scales around $r \sim 1\,h^{-1}$Mpc. For these masses the signal is dominated by centrals, which we are well-matched as we shall see in the following Section.

4.8.7 LBG lensing signals

By limiting our selection to LBGs, the predicted lensing signals drop and are more compatible with the data for all models. In Figs. 4.19 and 4.20, we show the results for an assorted model collection with M_* and $M_* + (g - r)$ selection functions, respectively. By selecting according to stellar mass only we have $\sim 300\,000$ galaxies in the least massive bin per axis for the SAMs run on the rescaled MR and a couple of hundred systems in the TNG300. Contrary to Wang et al. (2016), we find that the predictions from the H15 model tend to agree better with observations than the G11 curves, especially for $M_* > 10^{11.2} M_\odot$, as seen in panels II-IV in Fig. 4.19. This tension can origin from small number statistics from the few systems at the massive end of the SMF and from the fact that we are using only one snapshot instead of a

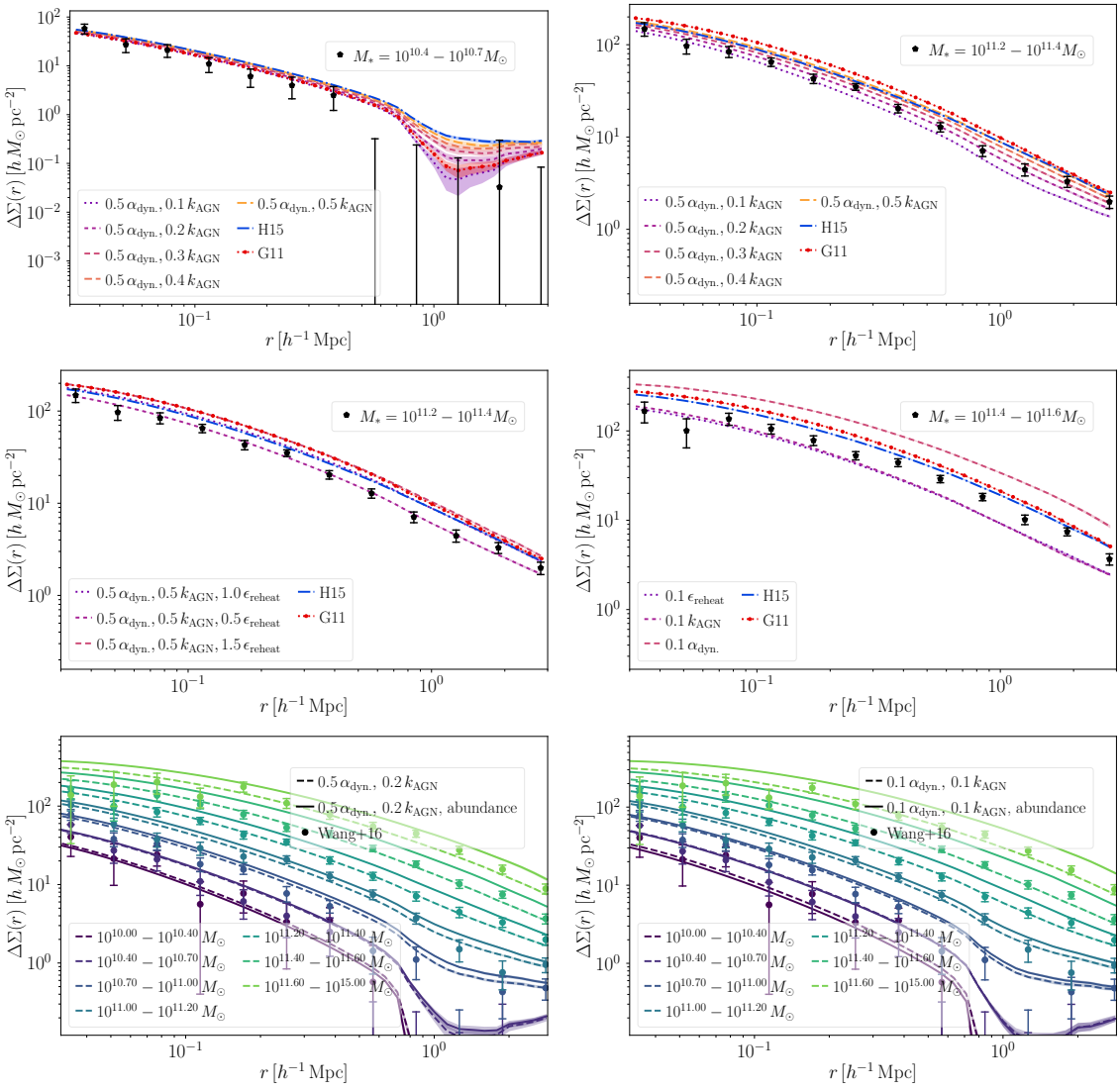

Figure 4.19: Predicted GGL signals compared to observations from SDSS LBGs with data from Wang et al. (2016). In panel I and panel II (top), we show the effect of changing the strength of $k_{\rm AGN}$, where the effect is modest to none for intermediate masses and where it starts to have an effect on high mass systems. In general the fiducial H15 model produces equivalent predictions as the G11 model, with better performance at the high mass end from $M_* > 10^{11.4} M_\odot$. We are also able to produce reasonable agreements by reducing $\epsilon_{\rm reheat}$ and $k_{\rm AGN}$ at the same time as illustrated in panel III. The predictions from the extreme models are ruled out by the LBG signal at the high mass end, as shown in panel IV. In the two last panels, we show the two models with the lowest figure-of-merits and we discern that they are in excellent agreement with observations.

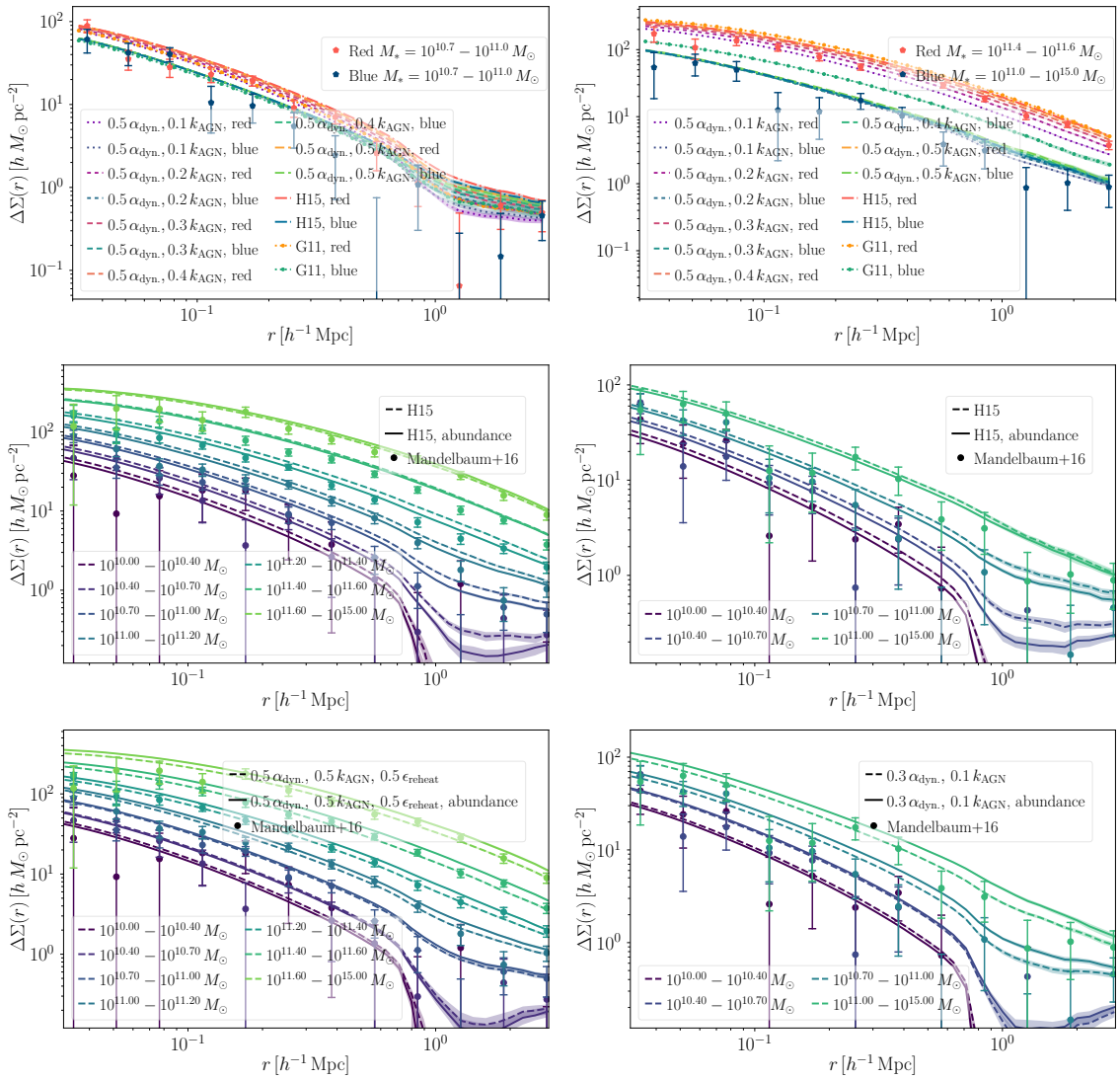

Figure 4.20: Similarly as Fig. 4.19 but for LBGs separated according to colour and compared to the Mandelbaum et al. (2016) observations. In the first two panels, we show how low $k_{\rm AGN}$ values act to reduce the host halo bimodality (panel I) where the effect becomes more apparent as we increase the stellar masses (panel II). There is little to no effect on the corresponding blue signal. We also observe that the H15 model predicts a stronger bimodality than G11. In the two subsequent panels, we explicitly show the predictions for the H15 for all mass bins for red (panel III) and blue (panel IV) LBGs. The predicted signal for red galaxies is excessive for masses $10^{11}\,M_\odot$, but the abundance correction mitigates the tension and the signal for blue galaxies conform with observations. In the bottom row we plot the predictions for the best fit models for red and blue LBGs, respectively, for comparison. The biggest improvement can be discerned for the signal around massive red LBGs.

LBG lensing (fiducial)	**All**	**Red**	**Blue**
First	$(0.5\,\alpha_{\rm dyn.},\,0.2\,k_{\rm AGN})$	$(0.5\,\alpha_{\rm dyn.},\,0.5\,k_{\rm AGN},\,0.5\,\epsilon_{\rm reheat})$	$(0.3\,\alpha_{\rm dyn.},\,0.1\,k_{\rm AGN})$
Second	$(0.1\,\alpha_{\rm dyn.},\,0.1\,k_{\rm AGN})$	$(0.5\,\alpha_{\rm dyn.},\,0.2\,k_{\rm AGN})$	$(0.5\,\alpha_{\rm dyn.},\,0.1\,k_{\rm AGN})$
Third	$(0.4\,\alpha_{\rm dyn.},\,0.2\,k_{\rm AGN})$	$(0.4\,\alpha_{\rm dyn.},\,0.2\,k_{\rm AGN})$	$(0.4\,\alpha_{\rm dyn.},\,0.1\,k_{\rm AGN})$
LBG lensing (abundance)	**All**	**Red**	**Blue**
First	H15	$0.1\,\epsilon_{\rm reheat}$	$(0.5\,k_{\rm AGN},\,0.5\,\alpha_{\rm dyn},\,1.5\,\epsilon_{\rm reheat})$
Second	$(0.5\,k_{\rm AGN},\,0.5\,\alpha_{\rm dyn},\,0.5\,\epsilon_{\rm reheat})$	H15	$(0.5\,k_{\rm AGN},\,0.5\,\alpha_{\rm dyn})$
Third	$0.1\,\epsilon_{\rm reheat}$	$(0.5\,k_{\rm AGN},\,0.5\,\alpha_{\rm dyn},\,0.5\,\epsilon_{\rm reheat})$	H15

Table 4.5: The best fit models according to stellar mass only lensing without and with abundance corrected masses. For the total LBG signal, the $(0.5\,\alpha_{\rm dyn.},\,0.2\,k_{\rm AGN})$ model is the best and it also does reasonably well for the red signal. Performing the analysis with abundance corrections favours the H15 and $(0.5\,k_{\rm AGN},\,0.5\,\alpha_{\rm dyn},\,0.5\,\epsilon_{\rm reheat})$ models.

mock lightcone. Still, we are able to reproduce their results by running the H15 model with the G11 parameter inputs which corresponds to the fixed model (not listed in Table 4.2), but not exactly the version published in G11.

For intermediate stellar masses, fixing $\alpha_{\rm dyn}$ and playing with $k_{\rm AGN}$ has no to little effect on the profiles, see panel I in Fig. 4.19, except for the transition regime between the 1-halo and 2-halo terms where a weaker $k_{\rm AGN}$ yields a lower signal. Still, the variance of the observations is quite large for these scales for low stellar masses. If we move to higher stellar masses beyond the knee, the different feedback prescriptions start to have an effect as visible in panel II in Fig. 4.19, where the $(0.5\,\alpha_{\rm dyn},\,0.1\,k_{\rm AGN})$ model produces a too low prediction. These differences are driven by the different physical recipes and not by differences in the contamination from satellites and orphan galaxies as discerned from the central purity of the signals presented in Section 4.14. The situation is similar if we split the sample into red and blue lenses.

For the stellar mass only selection, setting $k_{\rm AGN} = 0.1\,k_{\rm AGN}^{\rm fid.}$ and $0.1\,\epsilon_{\rm reheat}$, solves the tension for group scale lenses, although the produced signals are too low for $M_* > 10^{11}\,M_\odot$ systems, see panel IV of Figs. 4.19. For intermediate and high masses, simultaneously reducing $k_{\rm AGN}$ and $\epsilon_{\rm reheat}$ improves the agreement as see in panel III, although there is still tension for LBGs with $M_* < 10^{11}\,M_\odot$. Hence, this model class is disfavoured by these lensing observations as we use all stellar mass bins to construct our model ranking.

In Table 4.5, we list the best ranked models for the LBG sample with and without abundance matching stellar mass corrections. Similarly as for the M_*-only sample, the lensing data prefer a low AGN feedback efficiency, although here the intermediate $(0.5\,\alpha_{\rm dyn.},\,0.2\,k_{\rm AGN})$ model is the best. We deem that this shift is caused by the investigation of the signals from centrals only, where the $(0.5\,\alpha_{\rm dyn.},\,0.2\,k_{\rm AGN})$ model produces fewer galaxies, but they are also more isolated due to the shorter merger timescale. On second place, we find the $(0.1\,\alpha_{\rm dyn.},\,0.1\,k_{\rm AGN})$ model, which also has more isolated centrals due to the low $\alpha_{\rm dyn.}$, where the signal is too high beyond $10^{10.79}\,h^{-2}\,M_\odot$ for the stellar mass only selection. This is also true for the previous model. For the van Uitert et al. (2016) comparison these two models are ranked seven and six, respectively. The result post-abundance corrections is similar to the whole stellar mass comparison with the fiducial H15 model with the best performance followed by the low SN feedback efficiencies. We show the results for the two best models in

panels V-VI in Fig. 4.19 where it is difficult to distinguish between them, although the latter comes with larger abundance corrections.

Separating the signal into red and blue according to Eq. (4.7.2) for the Mandelbaum et al. (2016) dataset comparison, the $0.1\,k_{\rm AGN}$ and $0.1\,\epsilon_{\rm reheat}$ solutions are again ruled out by the signal from systems with $M_* > 10^{11.2}\,M_\odot$, which constitute the bulk of the whole signal for this mass range. We plot the result for a few of the SAMs in Fig. 4.20, where we observe that weakening the AGN feedback efficiency reduces the host halo bimodality as the red LBG lensing signal drops in panel I. In addition, we note that the H15 model in general predicts a stronger bimodality than the G11 model, and that the former is not plagued by a tension with data for the blue LBG lensing signal at the high mass end, see panel II. In addition, this holds true for the red signal but to a smaller extent, also apparent in this panel. Similarly as for the total signal, the $(0.5\,\alpha_{\rm dyn.},\,0.2\,k_{\rm AGN})$ model does a good job. In panels III-IV, we plot the results for the H15 model with and without abundance corrections. We note a mild excess in the red signal starting at $\sim 10^{11}\,M_\odot$, but the correction bring the signal into agreement for intermediate mass systems. The blue LBG lensing predictions appear to more or less concur with the observational data in panel IV.

Also in Table 4.5 we list the best fit models for red and blue LBGs with and without abundance corrected masses. The $(0.5\,\alpha_{\rm dyn.},\,0.5\,k_{\rm AGN},\,0.5\,\epsilon_{\rm reheat})$ model now nabs the first place, followed by the $(0.5\,\alpha_{\rm dyn.},\,0.2\,k_{\rm AGN})$ model, where the improved agreement originates from the two most massive bins, although it is hard to perceive by visual inspection. For the total LBG signal, this model finishes on fourth place, so there is reasonable concordance. Again, post-abundance corrections the $0.1\,\epsilon_{\rm reheat}$ and the fiducial H15 do well. If we switch to the blue signal, we see a shift in preference towards models with short $\alpha_{\rm dyn.}$ and weak $k_{\rm AGN}$, with the biggest gains on scales $r \sim 400\,h^{-1}\,$kpc and outwards for stellar masses $M_* > 10^{10.7}\,M_\odot$ w.r.t. the $(0.5\,\alpha_{\rm dyn.},\,0.2\,k_{\rm AGN})$ model, which is the sixth best. Still, the uncertainties in this signal region are quite large, and there are only a few blue LBGs in this mass range, meaning that we have more confidence in the red signal.

In Section 4.16, we illustrate how removing the dust correction on the colours impact the lensing signal for the two fiducial models with the LBG selection[6]. Compared to the previous figure-of-merits, we note no major shifts by removing the dust extinction, except for the blue lensing signal post-abundance corrections, and the signals are suppressed (boosted) by about $\sim 10\,\%$ for the two fiducial models for red (blue) LBG lensing for the two fiducial models depending on the mass bin as shown in Section 4.16.

In the last two panels (V-VI) in Fig. 4.20, we show the two best fit predictions for our top SAM models for the red and blue LBG lensing, respectively, with excellent agreement with data.

Moving on to the hydrodynamical predictions, we plot in Figs. 4.21 and 4.22 the LBG lensing predictions for all, red and blue LBGs from the TNG300 with the resolution correction enforced. Similarly, as in Fig. 4.13, this mass choice induces a drop in the signal from the least massive bins and increases the most massive signals from the fiducial bound mass predictions, but both cases are in agreement with observations. We see that this statement holds for red and blue galaxies in Fig. 4.22, where we do not plot the most massive blue signal due to poor statistics. If we do not enforce the resolution correction, the predicted signals for the two most massive bins for red galaxies are too high. The effect of baryons is mostly noticeable in

[6]Note that we still select the LBGs according to their $r-$band magnitude with dust extinction. This should have a negligible impact on the results.

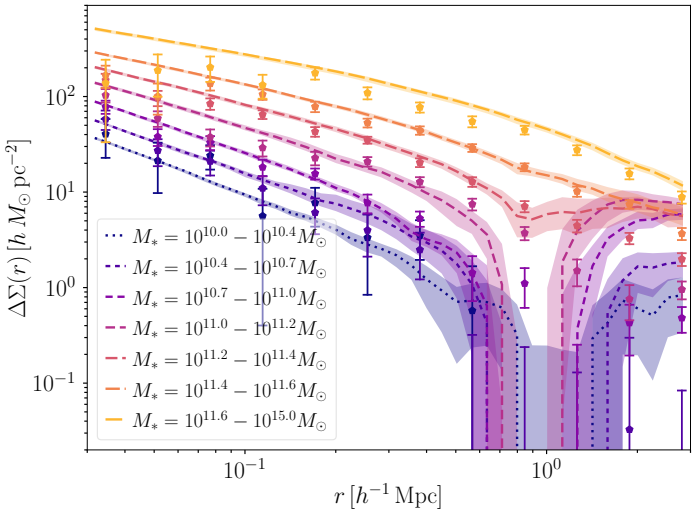

Figure 4.21: LBG lensing signal from the TNG300 with resolution corrected stellar masses compared to measurements from Wang et al. (2016). The central signal is a bit low for the $10^{11} < M_*\,[M_\odot] < 11.2$ mass bin and slightly excessive for the most massive bin, but overall the agreement is excellent.

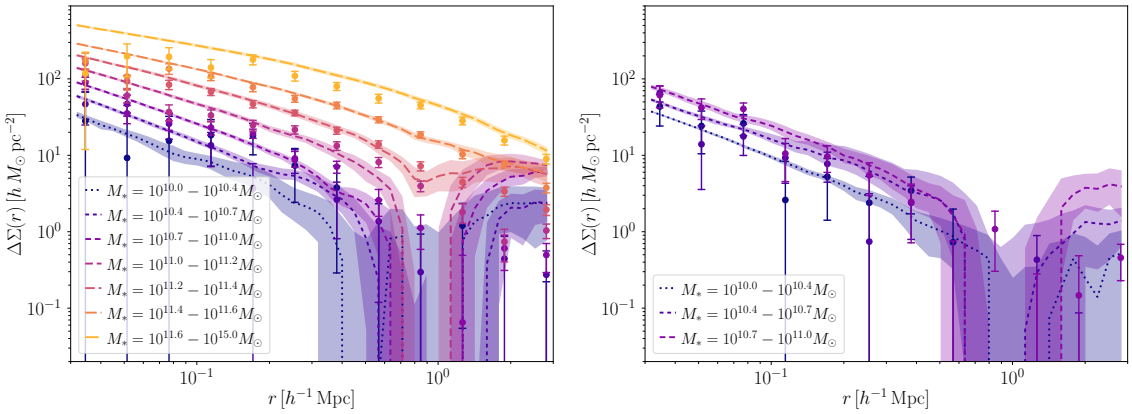

Figure 4.22: Same as Fig. 4.21 but for the signal split into red (panel I) and blue (panel II) LBGs from the TNG300 with resolution corrected stellar masses and dust extinction compared to measurements from Mandelbaum et al. (2016). The simulation predictions are in good agreement with the observations.

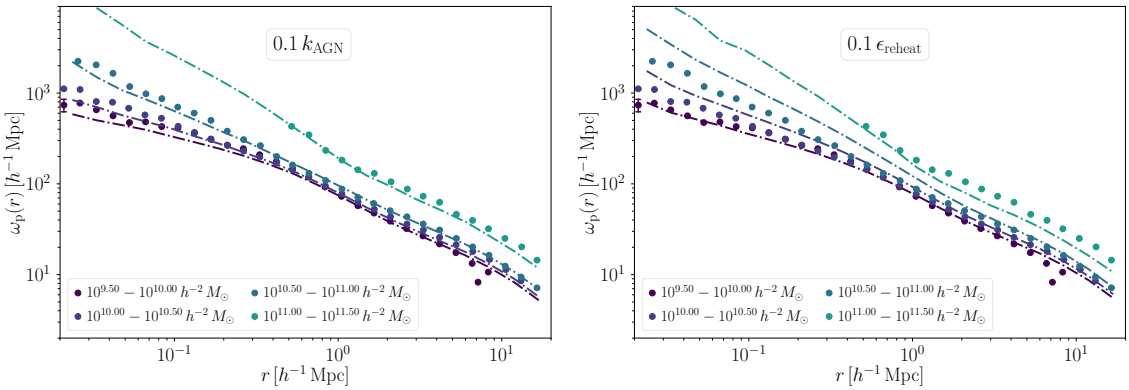

Figure 4.23: Clustering predictions for galaxies in the best fit $0.1\,k_{\rm AGN}$ model (panel I) and for galaxies in the $0.1\,\epsilon_{\rm reheat}$ model (panel II) w.r.t. SDSS observations from G11. By comparing the two, we realise that the data favours a weaker AGN feedback and not weaker SN feedback.

Clustering (fiducial)	**All**	**Red**	**Blue**
First	$0.1\,k_{\rm AGN}$	$(0.3\,\alpha_{\rm dyn},\ 0.2\,k_{\rm AGN})$	$(0.3\,\alpha_{\rm dyn},\ 0.1\,k_{\rm AGN})$
Second	$(0.5\,\alpha_{\rm dyn},\ 0.2\,k_{\rm AGN})$	$(0.4\,\alpha_{\rm dyn},\ 0.2\,k_{\rm AGN})$	$(0.4\,\alpha_{\rm dyn},\ 0.1\,k_{\rm AGN})$
Third	$(0.5\,\alpha_{\rm dyn},\ 0.1\,k_{\rm AGN})$	$(0.5\,\alpha_{\rm dyn},\ 0.3\,k_{\rm AGN})$	$(0.5\,\alpha_{\rm dyn},\ 0.1\,k_{\rm AGN})$

Table 4.6: The best fit models according to galaxy clustering. Our best LBG lensing model $(0.5\,\alpha_{\rm dyn},\ 0.2\,k_{\rm AGN})$ is a runner up on the fourth place for the red clustering.

the innermost bin due to the presence of the stellar term, which produce an excessive signal for the two most massive bins for the total and red LBG signal compared to the SAMs, but otherwise the result conforms well with what we previously shown. The least massive red predictions are slightly low with respect to the data, but this could be partly caused by the shift in the colour distribution illustrated in Fig. 4.3 induced by the resolution correction. Still, they are within the error bars of the data points. With respect to our best fit LBG SAM $(0.5\,\alpha_{\rm dyn.},\ 0.2\,k_{\rm AGN})$ which slightly under-predict the most massive red LBG lensing signal, it is moderately increased for the TNG300 as seen in Fig. 4.21 and panel I of Fig. 4.22. We thus conclude that the TNG suite is not only able to reproduce stellar mass only signals with a higher precision than the SAMs but is also equally good at producing predictions for LBGs.

4.8.8 Clustering

Having determined the best fit models from lensing only, we also examine whether these models hold up with respect to galaxy clustering observations to produce accurate joint 2-pt statistics predictions necessary for the next generation of large-scale structure surveys. Here, we do not change the stellar masses to match abundances but only focus on the baseline model predictions.

For the stellar mass only clustering, we determine the best fit models through Eq. (4.6.1) by the mean values for all four clustering bins with the results given in Table 4.6. We find that both 2-pt statistics point towards a consistent picture with the lowest, best fit values reached

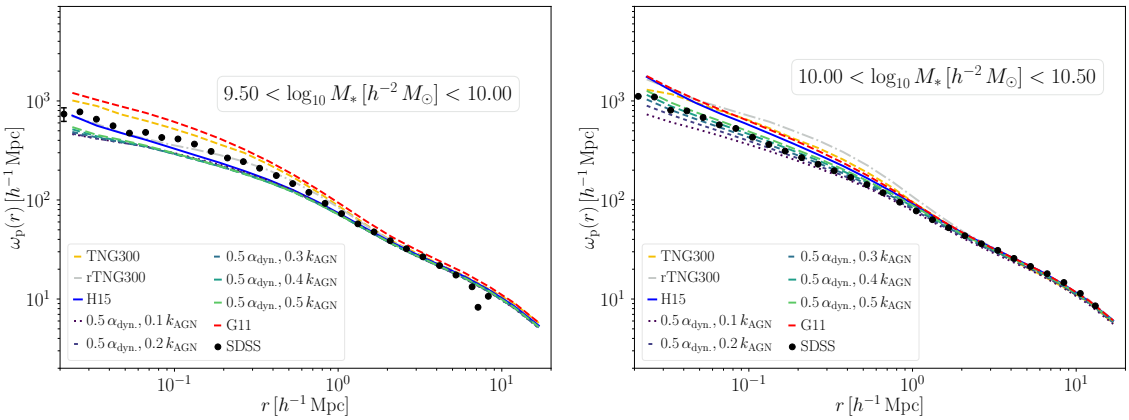

Figure 4.24: Clustering predictions for all galaxies with $9.5 < \log M_* \left[h^{-2} \, M_\odot\right] < 10.0$ (panel I) and $10.0 < \log M_* \left[h^{-2} \, M_\odot\right] < 10.5$ (panel II), respectively. There is little to no difference between predictions from the derivative H15 models with different k_AGN in this mass range, although they predict a slightly lower clustering signal than the fiducial model, in tension with the observations. In panel II one starts to notice deviations between the different k_AGN models for the clustering 1-halo term.

for the weak AGN feedback models. In Table 4.6 we see that the best agreement is reached for the $0.1 \, k_\mathrm{AGN}$ model, plotted in Fig. 4.23, which also gave the best stellar mass only lensing predictions in Table 4.3 and that the $(0.5 \, \alpha_\mathrm{dyn}, \, 0.2 \, k_\mathrm{AGN})$ is number two, which was the best for LBG stellar mass only lensing in Table 4.5. The latter model predictions are very similar to the former and thus we refrain from showing them. In the case of lensing, both all and for LBGs only, it was not apparent at the high mass end whether the weak AGN feedback models or the weak SN feedback models were to prefer, but if we compare the results in Fig. 4.23, we recognise that the $0.1 \, \epsilon_\mathrm{reheat}$ model is disfavoured by the massive clustering signals. However, it produces a better prediction for the least massive $9.5 < \log M_* \left[h^{-2} \, M_\odot\right] < 10.0$ bin, where we see in Fig. 4.24 that there is a tradeoff in accuracy by reducing the strength of the AGN feedback. We note that the signals for the fiducial H15 model are slightly higher than reported in Henriques et al. (2017), and this could be due to the imposed limits on the line-of-sight integration suppressing the spurious clustering contribution.

In Fig. 4.24, we show results for the models with reduced α_dyn and k_AGN for the two lowest mass bins compared to H15 and G11 as well as the TNG300 with and without resolution corrections. As previously mentioned, reducing the strength of the AGN feedback and shortening the dynamical friction timescale produces a discrepancy in panel I of Fig. 4.24, but helps to mitigate the tension for the subsequent mass bin. This issue is a topic for further improvements. The G11 model produces excessive clustering signals in both cases, whereas the resolution corrected TNG300 model and the H15 model do well for the lowest mass bin.

We compare the projected red and blue clustering signal to SDSS DR7 data from Zu & Mandelbaum (2016) in Figs. 4.25 and 4.26. We focus on these low masses as it where the different model prescriptions are most apparent. For the fixed α_dyn models with varying k_AGN, there are only small differences in the predictions for all low mass systems, see Fig. 4.24, but the differences between the H15 and G11 models are substantial due to the overproduction of red galaxies in the G11 model which are more clustered. For low mass systems, the AGN feedback strength has a significant effect on the amplitude of the 1-halo term for red galaxies

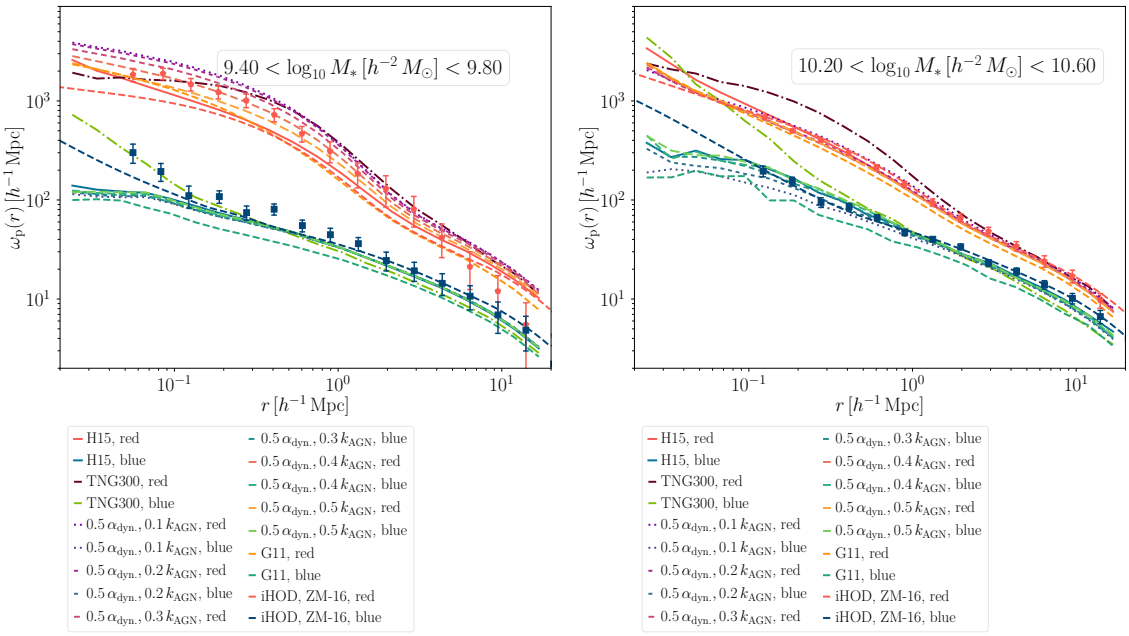

Figure 4.25: Clustering predictions for red and blue galaxies with $9.4 < \log M_* \left[h^{-2}\, M_\odot\right] < 9.8$ (panel I) and $10.2 < \log M_* \left[h^{-2}\, M_\odot\right] < 10.6$ (panel II) with dust extinction. Whereas there is little change in the blue signal between the models, reducing $k_{\rm AGN}$ boosts the 1-halo term for red galaxies in panel I. As suggested by Fig. 4.24, the different $k_{\rm AGN}$ models start to deviate from one another for blue galaxies from this mass bin in panel II onwards.

as seen in Fig. 4.25 in panel I. The TNG300 results are tangential to the lowest feedback model predictions, although the signal drops towards the centre. For higher masses, the effect is not as noticeable as shown in panel II of Fig. 4.25 which is representative for higher stellar masses as well. As we show in Section 4.16, the effect of the dust model on the red clustering signal can amount to $\sim 40\,\%$ for low mass systems, meaning that it is premature to use the results in Fig. 4.25 to constrain the AGN feedback strength.

Fixing the AGN feedback and varying $\alpha_{\rm dyn}$ changes the offset of the predictions w.r.t. the fiducial model, although it is most easily noticeable for systems with $M_* < 10^{10}\, h^{-2}\, M_\odot$. For the extreme solutions, the $0.1\,\epsilon_{\rm reheat}$ model predictions are very similar to the H15 model for $M_* < 10^{11}\, h^{-2}\, M_\odot$ and it is only in the most massive bin differences become significant. The largest effects are present for the $0.1\,k_{\rm AGN}$ model for stellar masses $M_* > 10^{10}\, h^{-2}\, M_\odot$ and the $0.1\,\alpha_{\rm dyn}$ model lowers the clustering below $0.1\,h^{-1}$Mpc and gives it a slight boost on larger scales. For the different SN feedback models, there is only a small difference in the offset for the 1-halo term for masses $M_* < 10^{10.5}\, h^{-2}\, M_\odot$ and the $(0.5\,k_{\rm AGN},\, 0.5\,\alpha_{\rm dyn},\, 1.5\,\epsilon_{\rm reheat})$ is degenerate with the fiducial model for $0.1 < r\ \left[h^{-1}{\rm Mpc}\right] < 1$ for $10.5 < \log M_* \left[h^{-2}\, M_\odot\right] < 11.0$. Differences are most noticeable beyond $M_* > 10^{11}\, h^{-2}\, M_\odot$.

Again in Table 4.6 we highlight the best models for red and blue clustering. If we compare the two, the red clustering favours a longer $\alpha_{\rm dyn}$ and both prefer weaker AGN feedback. Our best model for the LBG lensing finishes on fourth place for the red clustering although the top three is dominated by its close siblings in parameter space. It is interesting to note that the top blue clustering models in Table 4.6 closely resemble the top models in Table 4.5 for blue LBG lenses. If we neglect dust extinction, our best fit lensing model is also the best blue

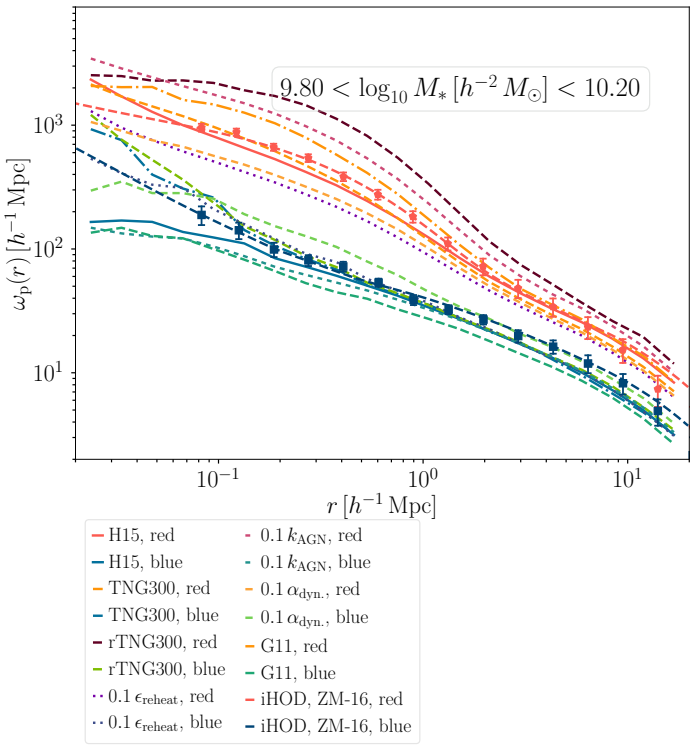

Figure 4.26: Same as Fig. 4.25 for galaxies with $9.8 < \log M_* \left[h^{-2} \, M_\odot\right] < 10.2$ and with the extreme SAM models. Here we also compare the clustering predictions for the TNG300 with and without resolution corrections with dust extinction.

clustering model as shown in Section 4.16.

In Fig. 4.26, we also illustrate how the Pillepich et al. (2018b) resolution correction together with dust extinction affects the predicted clustering signal for red and blue galaxies in the TNG300. As previously reported in Springel et al. (2018), there was a tension for the predicted clustering signal for red galaxies with $9.5 < \log M_* \left[h^{-2} \, M_\odot\right] < 10.0$ without dust extinction w.r.t. SDSS observations. If we use dust corrected colours the signal decreases and the tension is mitigated as discerned in Fig. 4.26 as less clustered blue galaxies are classified as blue. The changes in the amplitude due to dust extinction is strongest in this low mass range since there are only a few red galaxies present and there is a rapid transition between red and blue. Still, if we apply the additional resolution correction, the tension is re-introduced as the red sequence is artificially shifted into the blue, leaving the most clustered galaxies. If we restrict ourselves to the stellar mass only clustering, we see in panel I of Fig. 4.24 that the resolution correction brings about a better agreement with the observations, whereas the opposite is true in panel II. As hinted by the different satellite fraction at the knee of the SMF in Fig. 4.8, the resolution correction induces a similarly large tension for galaxies with $10.5 < \log M_* \left[h^{-2} \, M_\odot\right] < 11$ w.r.t. data, as the one highlighted in Springel et al. (2018). Hence, whereas this correction brings about a slightly better lensing signal, the corresponding clustering signal does not necessarily improve. Further work has to be undertaken to clarify which corrections are necessary for which observable and to quantify the magnitude of the induced biases.

We also show results for our extreme SAMs in Fig. 4.26, where we spot a clear tension

between the $0.1\,\epsilon_{\rm reheat}$ model and the observations. This is the reason the low SN feedback models do not feature among our best. However, if we consider a scenario without dust extinction with the best fit models presented in Section 4.16, the ($0.5\,\alpha_{\rm dyn.}$, $0.5\,k_{\rm AGN}$, $0.5\,\epsilon_{\rm reheat}$) model claims the top spot. The $0.1\,k_{\rm AGN}$ model is not as extreme as the resolution corrected TNG300 in Fig. 4.26 for red galaxies, which holds true for more massive systems, and it traces the ($0.5\,\alpha_{\rm dyn}$, $0.1\,k_{\rm AGN}$) solution for the least massive bin. As for the $0.1\,\alpha_{\rm dyn}$ model, it produces an excessive blue clustering signal, although it is in agreement with data for the least massive bin, and a too low red signal.

As shown in previous studies (e.g. Henriques et al., 2017; Springel et al., 2018), SAMs and hydrodynamical simulations in cosmological volumes are able to produce very accurate clustering predictions and it is nice to see the concordance between the iHODs and these two other frameworks.

4.9 Group criteria

In this comparison, we are using our constrained measurements from the LBG and clustering samples to produce predictions to be tested against an independent survey, in this case the KiDS+GAMA equatorial overlap for galaxy groups. Here we focus on a few models from Table 4.2, and especially our best fit ($0.5\,\alpha_{\rm dyn}$, $0.2\,k_{\rm AGN}$) model run on the gravity-only TNG100. We also list the corresponding host halo masses and other properties for the rescaled MR to show that they are consistent across simulation volumes.

Compared to the quoted values in Velliscig et al. (2017) listed in Table 4.7 for the hydrodynamical Eagle simulation (Schaye et al., 2015; Crain et al., 2015), we see that the limiting stellar masses $M_*^{\rm lim}$ are quite different in the SAMs and this also applies to the host halo masses in Tables 4.8, 4.9, 4.10, 4.11, 4.12 to satisfy the $f_{\rm sat}$ criteria. By comparing the values in Table 4.7 and 4.8, we observe that they are consistent with one another, although the rescaled MR has better statistics. In general, a more massive stellar mass bin requires a higher $M_*^{\rm lim}$ for the group membership criteria, although this is not necessarily true for the derivative H15 models from $10^{10.9}\,M_\odot$, cf. Table 4.11. One may argue that the results are dependent on the value $M_*^{\rm lim}$. It is true that $f_{\rm sat}$ only evolves slowly with an increased $M_*^{\rm lim}$ for the lowest group mass bins due to the large number of satellites, see Fig. 4.28, which allows for a larger range of viable $M_*^{\rm lim}$. We discern in Fig. 4.28 that the average host halo mass for centrals is robust to moderate variations of $M_*^{\rm lim}$ with only $\pm\,0.1$ dex changes. Fixing the host halo mass distribution for the most massive bins is given a higher priority due to the

$M_*[\log_{10} M_\odot]$	$\bar{d}_{\rm LG}$	$\bar{d}_{\rm E}$	$M_{\rm 200c}^{\rm cen.,\,LG}$	$M_{\rm 200c}^{\rm sat.,\,LG}$	$M_{\rm 200c}^{\rm cen.,\,E}$	$M_{\rm 200c}^{\rm sat.,\,E}$	$N_{\rm gal}^{\rm LG}$	$N_{\rm gal}^{\rm E}$	$M_*^{\rm lim,\,LG}$	$M_*^{\rm lim,\,E}$	$f_{\rm sat}$
10.3 – 10.6	0.686	0.590	13.19	13.61	12.29	13.78	95 467	354	9.98	9.46	0.98
10.6 – 10.9	0.728	0.725	13.45	13.74	12.75	13.92	60 289	150	10.22	9.91	0.95
10.9 – 11.2	0.763	0.902	13.64	13.83	12.96	13.97	26 387	68	10.26	9.96	0.81
11.2 – 11.5	0.859	1.151	13.89	14.08	13.22	14.02	6 698	22	10.36	10.33	0.50
11.5 – 11.8	0.976	1.877	14.05	14.30	13.52	14.07	1 908	29	9.86	-	0.21

Table 4.7: Velliscig et al. (2017) comparison simulation sample properties (LG = L-Galaxies 15, E = Eagle) with all mean halo masses $M_{\rm 200c}$ of the samples (host FOF groups) in units of $\log_{10} h^{-1}\,M_\odot$ and all stellar masses in units of $\log_{10} M_\odot$. The satellite fractions $f_{\rm sat}$ match the ones in the GAMA group catalogue. $\bar{d}$ is the average 3D distance between the satellite galaxies and their centrals and $N_{\rm gal}$ the total number of galaxies.

$M_*[\log_{10} M_\odot]$	$\bar{d}_{\rm LG}$	$M_{\rm 200c}^{\rm cen.,\ LG}$	$M_{\rm 200c}^{\rm sat.,\ LG}$	$N_{\rm gal}^{\rm LG}$	$M_*^{\rm lim,\ LG}[\log_{10} M_\odot]$
$10.3 - 10.6$	0.732	13.12	13.80	400	9.87
$10.6 - 10.9$	0.757	13.23	13.83	324	10.13
$10.9 - 11.2$	0.937	13.60	13.92	157	10.39
$11.2 - 11.5$	0.766	13.93	14.08	24	10.75
$11.5 - 11.8$	0.818	13.80	14.31	6	-

Table 4.8: Average host halo masses, 3D distances between the satellite galaxies and the central galaxy in each FOF group in units of h^{-1} Mpc and number counts for H15 on the gravity only TNG100. If we compare these values with those quoted in Table 4.7, they are consistent with one another. For the average satellite distances, the H15 predicts more coherent values across the whole mass range w.r.t. Eagle.

$M_*[\log_{10} M_\odot]$	$\bar{d}_{\rm LG}$	$M_{\rm 200c}^{\rm cen.,\ LG}$	$M_{\rm 200c}^{\rm sat.,\ LG}$	$N_{\rm gal}^{\rm LG}$	$M_*^{\rm lim,\ LG}[\log_{10} M_\odot]$
$10.3 - 10.6$	0.691	13.01	13.78	683	10.03
$10.6 - 10.9$	0.753	13.41	13.84	417	10.35
$10.9 - 11.2$	0.887	13.58	13.91	185	10.43
$11.2 - 11.5$	0.855	13.82	14.13	26	10.65
$11.5 - 11.8$	-	13.91	-	4	-

Table 4.9: The same properties as in Table 4.8 for G11 on TNG100-DM. The values are very similar to those of H15 listed in Table 4.8, which means that we do not expect large differences in the lensing signal.

$M_*[\log_{10} M_\odot]$	$\bar{d}_{\rm LG}$	$M_{\rm 200c}^{\rm cen.,\ LG}$	$M_{\rm 200c}^{\rm sat.,\ LG}$	$N_{\rm gal}^{\rm LG}$	$M_*^{\rm lim,\ LG}[\log_{10} M_\odot]$
$10.3 - 10.6$	0.772	13.20	13.82	417	10.09
$10.6 - 10.9$	0.830	13.59	13.88	319	10.45
$10.9 - 11.2$	0.801	13.55	14.02	88	10.52
$11.2 - 11.5$	0.375	14.01	14.11	12	10.83
$11.5 - 11.8$	1.192	14.10	14.35	4	-

Table 4.10: Equivalent as Table 4.8 but for H15 with $2\,\alpha_{\rm dyn}$ and $2\,k_{\rm AGN}$ on TNG100-DM. We note that mean host halo masses for the two most massive bins are higher than for the fiducial H15 model listed in Table 4.8.

$M_*[\log_{10} M_\odot]$	$\bar{d}_{\rm LG}$	$M_{\rm 200c}^{\rm cen.,\ LG}$	$M_{\rm 200c}^{\rm sat.,\ LG}$	$N_{\rm gal}^{\rm LG}$	$M_*^{\rm lim,\ LG}[\log_{10} M_\odot]$
$10.3 - 10.6$	0.751	13.13	13.81	355	9.83
$10.6 - 10.9$	0.789	13.46	13.88	247	10.27
$10.9 - 11.2$	0.818	13.39	13.82	253	9.60
$11.2 - 11.5$	1.312	13.70	14.03	39	10.56
$11.5 - 11.8$	0.635	13.64	14.18	13	-

Table 4.11: Same properties as in Table 4.8 for H15 with $0.5\,\alpha_{\rm dyn}$ and $0.5\,k_{\rm AGN}$ on TNG100-DM. Here the host halo masses for the centrals from the third bin onwards are reduced w.r.t. the fiducial setup.

$M_*[\log_{10} M_\odot]$	$\bar{d}_{\rm LG}$	$M_{\rm 200c}^{\rm cen.,\ LG}$	$M_{\rm 200c}^{\rm sat.,\ LG}$	$N_{\rm gal}^{\rm LG}$	$M_*^{\rm lim,\ LG}[\log_{10} M_\odot]$
$10.3 - 10.6$	0.751	13.08	13.80	345	9.83
$10.6 - 10.9$	0.759	12.97	13.87	238	10.24
$10.9 - 11.2$	0.808	13.16	13.79	275	9.49
$11.2 - 11.5$	0.964	13.52	13.87	108	9.95
$11.5 - 11.8$	0.925	13.48	14.13	46	-

Table 4.12: Table 4.8 for our best fit $0.5\,\alpha_{\rm dyn}$ and $0.2\,k_{\rm AGN}$ model on TNG100-DM. Compared with Table 4.11, the central host halo masses are reduced further and we have more galaxies in the two most massive bins. There is little to no effect on the average host halo masses for the satellites.

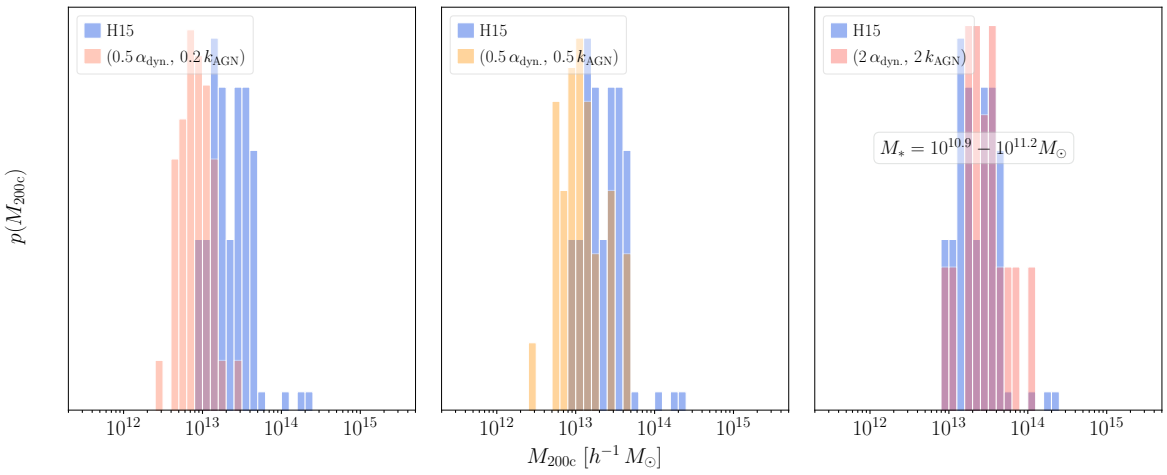

Figure 4.27: Host halo masses for central galaxies in the $10.9 < \log M_*\,[M_\odot] < 11.2$ mass bin for the Velliscig et al. (2017) selection, for $(0.2\,k_{\rm AGN}, 0.5\,\alpha_{\rm dyn})$, $(0.5\,k_{\rm AGN}, 0.5\,\alpha_{\rm dyn})$, the fiducial H15 model and $(2\,k_{\rm AGN}, 2\,\alpha_{\rm dyn})$ run on TNG100-DM. Reducing the dynamical friction parameter as well as the AGN feedback efficiency brings about a better agreement with the observational constraints, as already indicated by the LBG lensing.

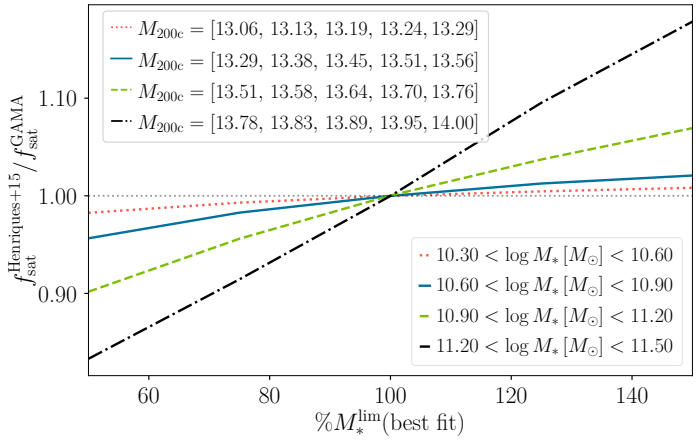

Figure 4.28: The satellite fraction dependency of $M_*^{\rm lim}$ for the H15 model run on the rescaled Millennium simulation normalised to the measured GAMA values, see Table 4.7, and the average host halo masses for centrals in $\log M_\odot$ with quoted values at 50, 75, 100, 125, 150 % of the best fit mass. For the low stellar mass bins, there is only a slowly evolving relation with increasing $M_*^{\rm lim}$ whereas larger deviations from the best fit values are produced for the more massive bins, suggesting stronger constraints.

increasing strength of the matching $f_{\rm sat}$ constraint.

We perceive that the host halo masses for the lowest mass bin differ by about 1 dex between Eagle and the SAMs, but if we look at the predicted lensing signal for central galaxies in Fig. 4.29 in panel I, we discern that the SAMs are still consistent with observations. The low host halo masses for the least massive bins hold across the examined SAM parameter range in this examination. For the central signal in Fig. 4.29, all models are in agreement with data, especially below $10^{10.9}\,M_\odot$. If we start to modify the SAMs to achieve a better agreement, changing $\alpha_{\rm dyn}$ and $k_{\rm AGN}$ as seen in Tables 4.10, 4.11 and 4.12, can affect the signal and average host halo masses. If we reduce $\alpha_{\rm dyn}$ and $k_{\rm AGN}$ we are able to obtain more consistent values with the central galaxy signals for $10.6 < \log M_* [M_\odot] < 11.5$. This is especially notable for stellar masses exceeding $10^{10.9}\,M_\odot$ where we illustrate the shift in the host halo mass distribution in Fig. 4.27 compared to that of the reference H15 model. Increasing $\alpha_{\rm dyn}$ and $k_{\rm AGN}$ produces a similar SMF, but causes a shift in the host halo mass distribution away from the observational data points. The best fit LBG model ($0.5\,\alpha_{\rm dyn}$, $0.2\,k_{\rm AGN}$) give the lowest mass distribution and the best central lensing signal for $10.6 < \log M_* [M_\odot] < 11.5$. When it comes to the satellite signal, however, the model does not do equally well as the fiducial models for $10.9 < \log M_* [M_\odot] < 11.5$ as illustrated in panels II-III in Fig. 4.30. This error then propagates into the joint signal as seen in panels III-V in Fig. 4.31. Hence, while it is the best model for LBG lensing and for most of the central galaxy signals in Velliscig et al. (2017), it still needs refinements to conform with the satellite lensing signal. In conclusion, we see that our best constraint model ($0.5\,\alpha_{\rm dyn}$, $0.2\,k_{\rm AGN}$) conforms reasonably well with the new dataset for centrals, validating our approach.

If we consider the two fiducial models H15 and G11, they give similar predictions, especially for the satellite lensing signals in Fig. 4.30. For the central galaxies, the G11 model predicts a lower signal for the $10.3 < \log M_* [M_\odot] < 10.6$ and is greater by an almost equal amount for $10.6 < \log M_* [M_\odot] < 10.9$ and the two are equal for $10.9 < \log M_* [M_\odot] < 11.2$

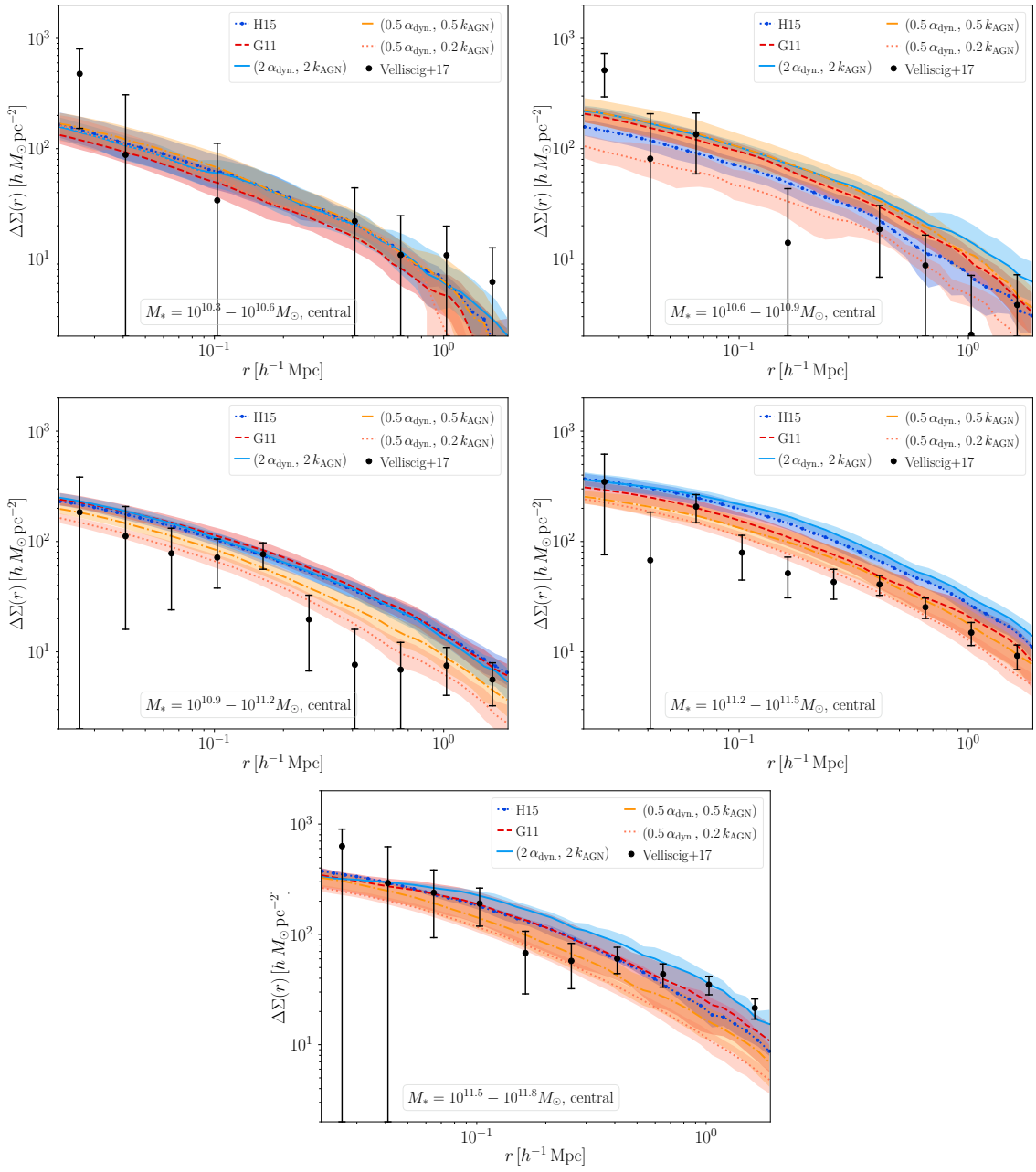

Figure 4.29: GGL signals for central galaxies w.r.t. data from Velliscig et al. (2017). We see that the best fit $(0.5\,\alpha_{\rm dyn}, 0.2\,k_{\rm AGN})$ model produces accurate predictions across the whole mass range, particularly evident in panels II-IV, although the signal around $1\,h^{-1}$ Mpc in panel V for the most massive bin is somewhat low. For this bin the best agreement is reached for the $(2\,\alpha_{\rm dyn}, 2, k_{\rm AGN})$ model, but we attribute the tension to small number statistics.

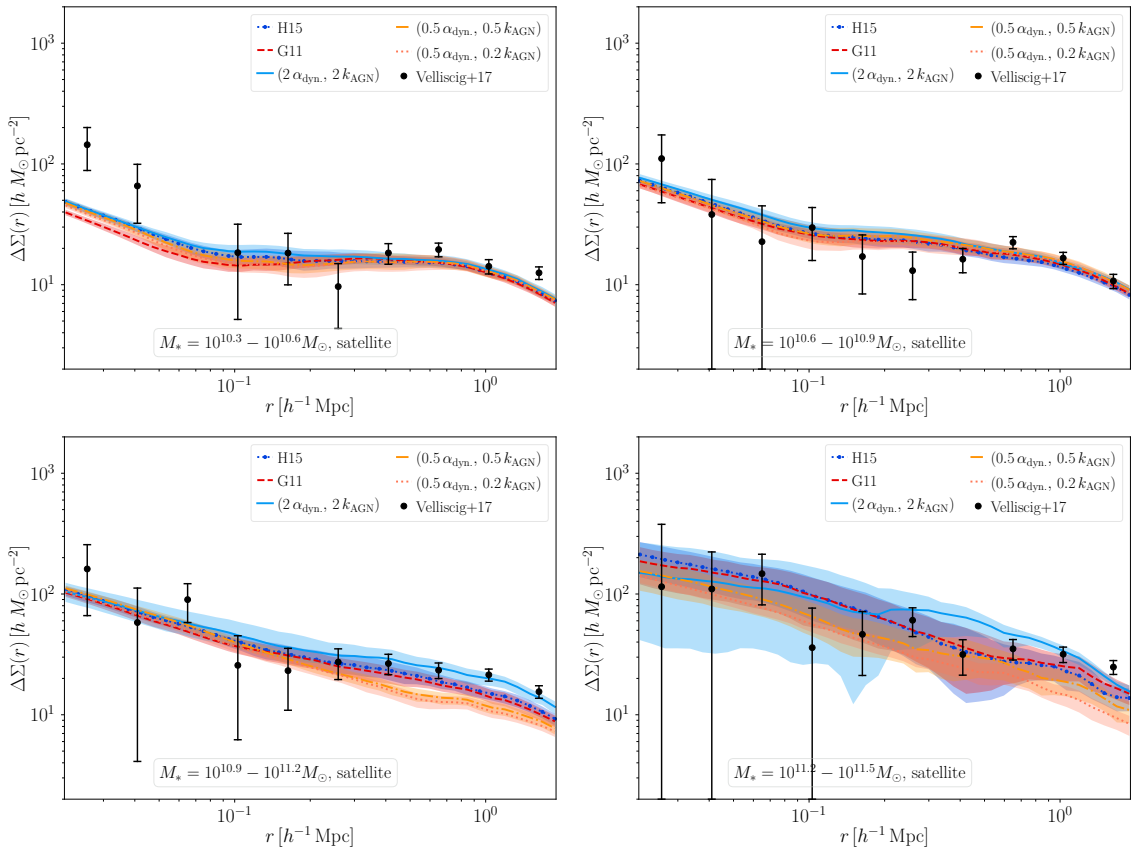

Figure 4.30: Same as Fig. 4.29 for satellite galaxies w.r.t. data from Velliscig et al. (2017). We have omitted the most massive bin as one of our models lack satellite galaxies for those stellar masses. For the two least massive bins in panels I-II, all models produce accurate predictions and the $(2\,\alpha_{\rm dyn},\,2\,k_{\rm AGN})$, the H15 and G11 yield the best results for the two subsequent bins in panels III-IV, especially on scales $r \sim 1\,h^{-1}\,{\rm Mpc}$ around and beyond the central bump. The low signal for the $(0.5\,\alpha_{\rm dyn},\,0.2\,k_{\rm AGN})$ model for these bins suggests that we should have more satellites in massive host haloes. We only have six galaxies in panel IV for the $(2\,\alpha_{\rm dyn},\,2\,k_{\rm AGN})$ model which causes the large scatter.

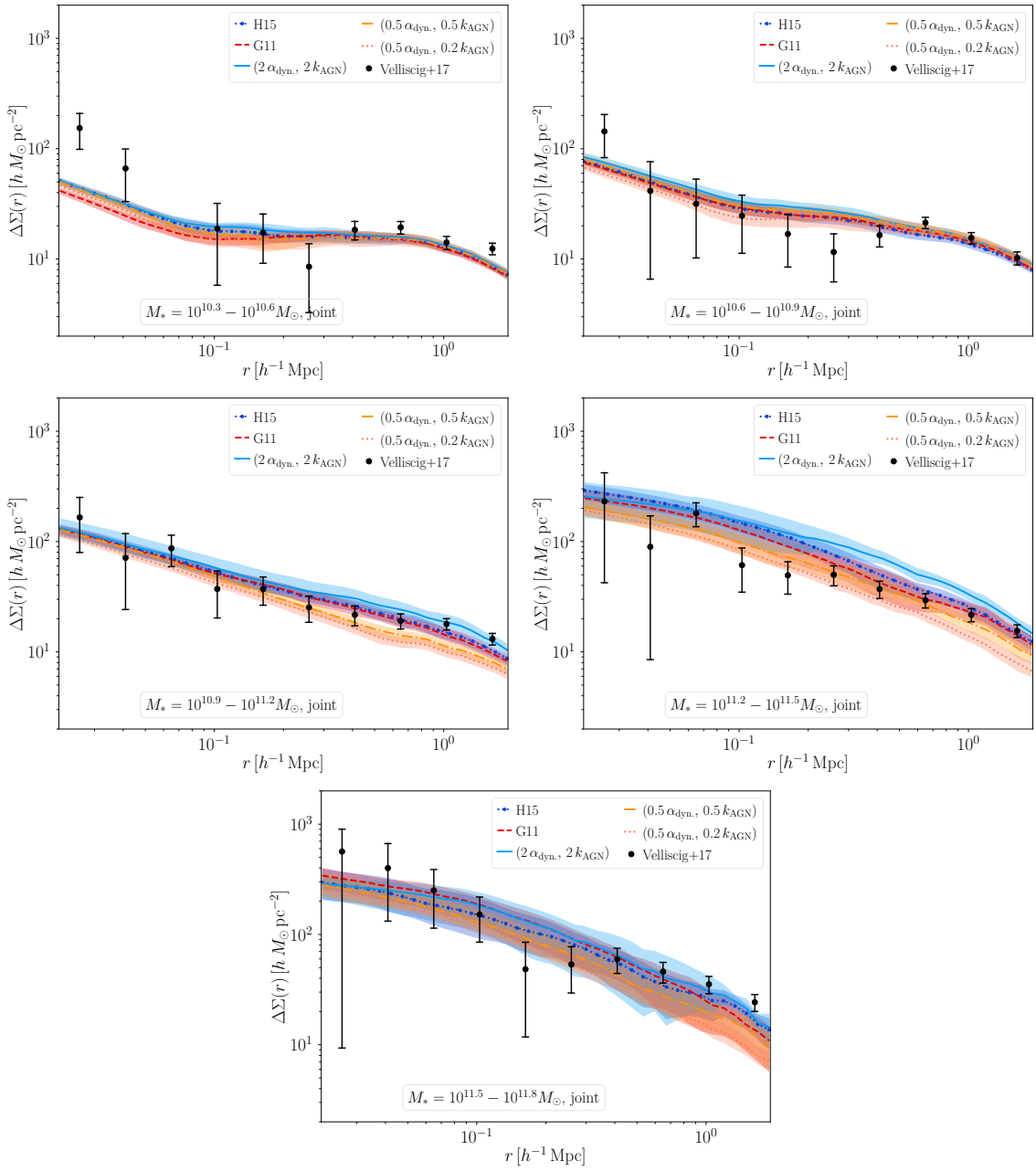

Figure 4.31: Joint GGL signals for central and satellite galaxies w.r.t. data from Velliscig et al. (2017). Here we see that the matched satellite fractions ensure an agreement with observations, compared to the van Uitert et al. (2016) comparison. Originating from their problems to match the large scale ($r \sim 1\,h^{-1}\,{\rm Mpc}$) satellite lensing signal and the most massive central signal in panel V of Fig. 4.29, the $(0.5\,\alpha_{\rm dyn},\,0.5\,k_{\rm AGN})$ and $(0.5\,\alpha_{\rm dyn},\,0.2\,k_{\rm AGN})$ models do not conform well with the joint signal data points for the three most massive bins in panels III-V in this radial range.

and $11.5 < \log M_* \, [M_\odot] < 11.8$. Thus this dataset cannot be used to discriminate them against each other.

Compared to the stellar mass only selection, we are able to conform to the joint and satellite lensing measurements in Figs. 4.30 and 4.31 with all SAM models in the comparison, highlighting the need for isolation and group membership information from future surveys. We also obtain better agreement for the satellite lensing signal than Eagle, which had a suppressed amplitude of the central bump. They argued that this was caused by the small simulation volume, but as we see for the SAMs on the TNG100 this does not necessarily have to be an issue, although we have very few galaxies in our most massive bins. If we compare the lensing signal for the H15 model run on the rescaled MR, we find that the signal amplitude is slightly higher due to the presence of more massive haloes, specifically for the $10.6 < \log M_* \, [M_\odot] < 10.9$, $10.9 < \log M_* \, [M_\odot] < 11.2$ and the $11.5 < \log M_* \, [M_\odot] < 11.8$ bins (the rescaled MR actually gives a slightly lower lensing signal for the $11.2 < \log M_* \, [M_\odot] < 11.5$ bin). For the satellite lensing signal the central bumps are less prominent due to the large statistics and spread in the average distances between the satellites and their centrals, which induces a smoothing between the central subhalo lensing signal and its host central. We have to wait for larger observational datasets to see if this applies to such surveys.

We show the corresponding IllustrisTNG predictions in Chapter 5 for this dataset.

4.10 Discussion

We have carried out a comparison between different SAMs as well as the IllustrisTNG for different galaxy-galaxy lensing and galaxy clustering datasets and found satisfactory agreement across several of them. The greatest challenge seems to be the proper modelling of the red satellite lensing signals as seen in Section 4.8.6, where we cannot reach a sufficient conformance even for extreme model parameter variations. This will probably require major work on the quenching of satellite galaxies. Traditionally, a way to boost the galaxy clustering has been to populate massive galaxies with more satellite galaxies and we see that this has alarming consequences for the lensing. For intermediate stellar masses, the TNG300 has the same issues as the SAMs highlighting that including baryonic physics do not solve the tension. If we compare to the iHODs from Mandelbaum et al. (2016), they have no trouble getting the red lensing signal right, although we are able to produce equally well or slightly superior predictions at the extreme low mass end. We have also checked the halo occupation distributions for our SAMs compared to those shown in Zu & Mandelbaum (2015) for the iHOD setup for stellar masses at $\log M_* = 10 \pm 0.1 \, [M_\odot]$ and $\log M_* = 11 \pm 0.1 \, [M_\odot]$, and we find an adequate agreement for the central galaxies, but for satellites the distribution have tails of the order of 0.5 dex towards lower and higher masses. If we remove the orphans these two tails disappear, and it is mostly the massive tail which dominates the lensing signal. Hence, we deduce that the satellite treatment much be improved.

Our best fit $(0.5\,\alpha_{\rm dyn}, 0.2\,k_{\rm AGN})$ model does a good job in producing predictions for the Velliscig et al. (2017) central galaxy signals. In Section 4.17, we show its SMF up to $z = 3$ and its predicted red galaxy fractions with respect to the fiducial H15 model. As already pointed out in Section 4.8.1, the SMF is slightly too high above the knee at $z = 0.11$ and this also applies to $z = 1$ but given the large uncertainties this is still consistent. We are thus able to retain the good agreement to the SMF to $z = 4$, meaning that this simplified study is compatible with the fiducial MCMC constraints used to tune H15. This bodes well for SAMs

to produce predictions for future deep lensing surveys such as HSC, given the possibility to introduce isolation and group membership criteria. Yet, if we examine the red fractions, we see that the new model shifts the distribution away from the observational data points. Still, the division is very sensitive to the actual shape of the colour distribution, especially for stellar masses between $9.5 < \log M_* \left[h^{-2}\, M_\odot\right] < 10.5$ where the transition between blue and red is rapid. Thus, we do not put equal weight on matching the colour cuts. For $z = 3$ we are in excellent agreement with H15. Future endeavours should focus on the incorporation of these lensing constraints into the MCMC chains themselves for the model selection, but as we have shown, the modification of a few pertinent parameters is sufficient to produce an acceptable improvement.

In Wang et al. (2016) it was argued that abundance corrections could be used to bring the signal into agreement. We also find that this is the case, but the effects are the largest at the high mass end where the uncertainties are considerable. Thus it should not be a method of choice, even though the SMF agreement at low redshift can be compromised by including higher redshift constraints in the MCMC analysis. Moreover, as pointed out in Section 4.8.7, we have difficulties to achieve the exquisite agreement for the LBG lensing signal for the G11 model when we run the SAM with the proper model switch, but are in perfect agreement when we run it as the H15 model with G11 parameters. This model combination also outperforms the others for a few of the datasets we have considered, highlighting the need to explore the parameter space further. Still, the agreement with the SMF for $z \geqslant 1$ is poor which makes us discard this model.

Finally, while modifying the free parameters of the SAM can lead to better predicted power, it is not necessarily true that the underlying physical model is sound. In addition, the approaching the era of precision cosmology requires a more profound understanding of systematic effects such as the influence of baryons. With the baryonic feedback prescriptions offered by the TNG300 detailed in Section 5.6.4, we comprehend that we are still safe from their impact for the current datasets by restricting the analyses to scales $r > 30\,h^{-1}\,\mathrm{kpc}$ to avoid the impact of the stellar term. Still, future progress should be directed towards understanding the amplitude and scope of the suppression on intermediate radial scales, which is specifically important for group scale systems where the effect of the AGN feedback is the strongest. We will show and quantify the deformation effects for the IllustrisTNG and the Illustris suite in Chapter 5.

Further developments could also to be made to include additional 2-pt statistics in the analysis, such as cosmic shear which has been shown to offer interesting galaxy formation constraints (e.g. Foreman et al., 2016).

4.11 Conclusions

In this Chapter we have shown predictions from different semi-analytical models of galaxy formation and hydrodynamical simulations for various observational datasets and we have found two major biases related to the satellite fractions (for the SAMs) and red satellite lensing signal (for the SAMs and the IllustrisTNG). To remedy the former, one can adjust the merger times and AGN feedback parameters of the SAMs to bring about agreement at the high mass end. For the latter, major work is required to model the stripped subhalo satellite lensing signal in both hydrodynamical simulations as well as in SAMs.

By combining lensing data across different stellar masses and by adding clustering in-

formation, we arrive at a few viable parameter combinations for the central galaxy signal which we have verified to also be consistent with the external group membership datasets from Velliscig et al. (2017). Our best fit model suggests a weaker AGN feedback and shorter dynamical friction merger time multiplier than the fiducial H15 model, and it retains the good agreement with the SMF at $z = 0$ up to $z = 3$, making it suitable for future lensing and clustering surveys. Thus we conclude that joint 2-pt statistics analyses are interesting, promising approaches to constrain galaxy formation.

Acknowledgements

We would like to thank Edo van Uitert, Wenting Wang, Ying Zu and Rachel Mandelbaum for sharing their data.

4.12 Mixing limit

The samples in Zu & Mandelbaum (2016) and Zu & Mandelbaum (2015) are approximately volume complete until an imposed limit in stellar mass M_*^{mix} which gives the maximum redshift a galaxy with a given stellar mass could be observed at as

$$z_{\mathrm{max}}^{\mathrm{mix}} = \left[\frac{\log(M_*^{\mathrm{mix}}/h^{-2}\,M_\odot) - 8.0}{5.4}\right]^{1./0.33} + 0.025. \tag{4.12.1}$$

This sensitivity function can be incorporated into differential comoving volume element $\mathrm{d}V(z)$, which can be used to set the relative weight of the different simulation snapshots for each stellar mass bin i. Such a setup effectively down-weights the contribution from the highest redshift snapshots. Below the mass limit M_*^{mix}, the sensitivity is considered to be full and we use the ordinary differential comoving volume element to define that volume. Each individual stellar mass lensing sample is thus constructed from the list of available snapshots with individual weights set by their fractional contribution to the total comoving volume, and since we have different bin borders

$$\omega_{ij}^{\mathrm{red,\ blue}} = \left(\sum_j V_{ij}\right)^{-1} \int_{z_{\mathrm{min}}}^{z_{\mathrm{max}}^{\mathrm{mix}}} \mathrm{d}V_{ij}(z), \tag{4.12.2}$$

where j marks the available snapshots. We have checked that there are negligible differences in the host halo masses for centrals and satellites for samples defined using this technique with respect to using a single snapshot at $z = 0.11$ to define the sample, although the satellite fraction changes on the order of $\sim 1\,\%$ for the H15 model. Hence, we use the $z = 0.11$ snapshot for our mocks.

4.13 Abundance correction residuals

In Fig. 4.32, we show the residuals for the corrected profiles. Since the high mass signal is dominated by centrals, the abundance correction results in a homogeneous shift of the signal with radius, whereas the impact on the low mass satellite signal is more extreme with a suppression (H15) and boost (G11), respectively.

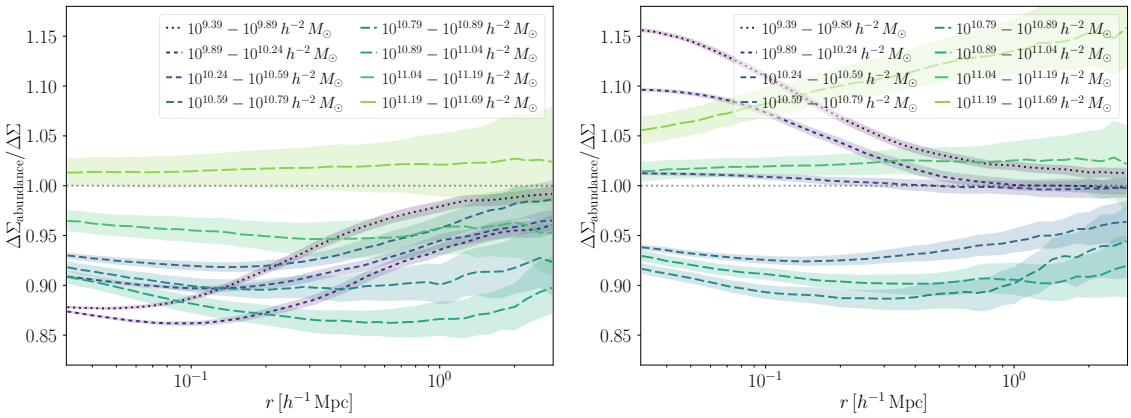

Figure 4.32: In panel I, we show the abundance corrections residuals for the H15 model. While the correction is almost homogeneous across all radii at high masses due to the central signal dominance, the effect is different for the low mass signal with a stronger suppression of the satellite lensing signal visible in the centre. In panel II we show the corrections for the G11 model. The trend for the low mass signal is inverted here, with a boost of the satellite lensing term. Although the G11 correction for the SMF is slightly smaller than for H15, the impact on the lensing signal is comparable.

4.14 LBG central fractions

In Fig. 4.33, we show the fraction of central galaxies in a few of the SAMs with the G11 and the H15 models as well as the different $k_{\rm AGN}$ models with fixed $\alpha_{\rm dyn} = 0.5$ which are classified as LBGs for all galaxies and separated according to colour in panels I-II. For intermediate mass galaxies, we are only able to capture $50\,\% - 60\,\%$ of the centrals with the isolation criterium, but for higher masses above $10^{11.5}\,M_\odot \geqslant 10$, $\geqslant 90\,\%$ of the centrals are LBGs. If we separate the signal into red and blue, virtually all blue massive galaxies are LBGs whereas some of the red massive galaxies are excluded, owing to them residing in more clustered environments. Also for less massive systems the discrepancy is apparent; at $10^{10.4}\,M_\odot$ only $\sim 40\,\%$ of the red centrals are LBGs compared to $\sim 60\,\% - 70\,\%$ of the blue centrals. There is only a small variation depending on the galaxy formation model, although the massive red central galaxies in the G11 model are more likely to pass the criterium. It is not obvious from the massive clustering signal for G11 for red galaxies why this is the case.

We turn the argument around in panels III-IV, quantifying how many of the LBGs which are actually central galaxies, determining the purity of the sample. This peaks for the lowest mass bins, with $\sim 95\,\%$ of the LBGs being centrals independent of model and colour, which gradually drops to $85\,\% - 90\,\%$ around $10^{11}\,M_\odot$ and then increases anew for red galaxies. We see that reducing the strength of the AGN feedback yields slightly more central LBGs and that all derivative H15 models lie above the fiducial curve. Verifying the picture shown in the previous plots, the G11 LBGs are slightly more likely to be centrals than the LBGs from H15. Looking at the colour separation in panel IV, the weak AGN feedback models produce LBGs which are less likely to be centrals for the most massive bin for blue galaxies, and the result for red galaxies is similar to the curves in panel III, i.e. elevated w.r.t. the fiducial model.

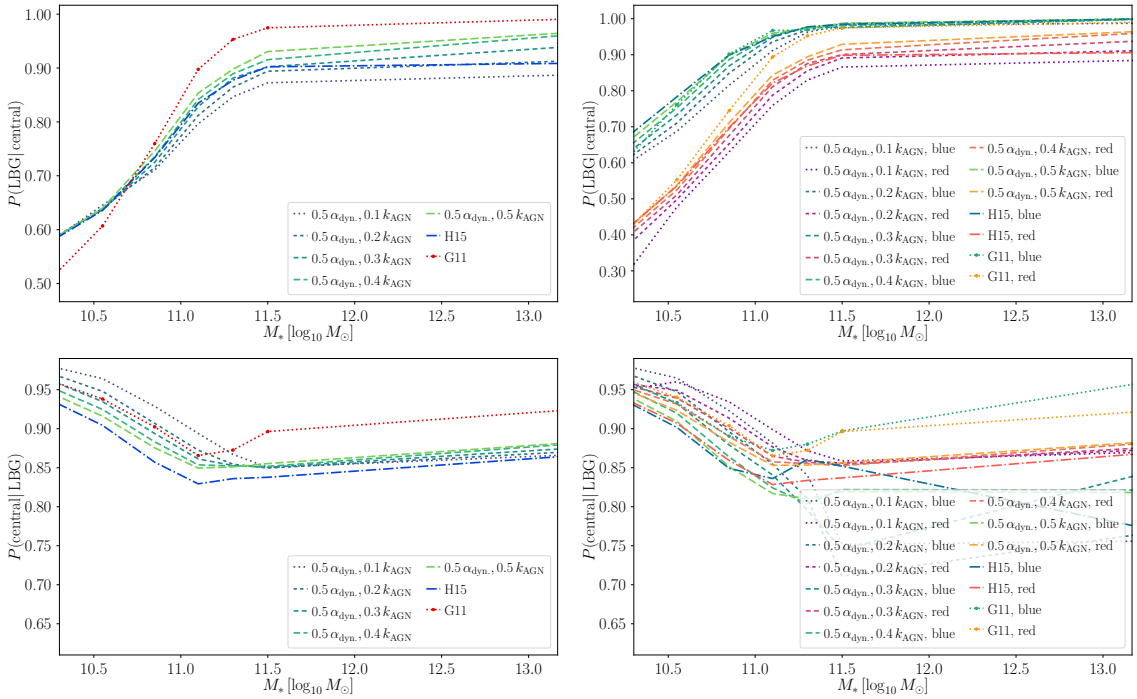

Figure 4.33: Fraction of centrals which are also classified as LBGs (panels I-II) and central purity for the LBG sample for different mock catalogues (panels III-IV). The fraction increases with stellar mass and the G11 LBGs are most likely to be centrals. In panel II we split the result for red and blue galaxies. As central blue galaxies, in general, reside in less clustered environments they are more likely to be LBGs than their red counterparts. For the G11 model, the most massive red centrals are as likely as the blue galaxies to be LBGs. Switching to the purity of the sample in panels III-IV, the G11 lenses are 2-5 % more central than in the H15 model, but the difference is too small to influence the signal dramatically. There is only a large difference in the most massive bin, but here the two models yield similar predictions. Lenses from the derivative models with different $k_{\rm AGN}$ strength are equally pure. Panel IV shows the result for red and blue LBGs. Up to $M_* = 10^{11}\,M_\odot$ there are only small differences between the different model predictions with a large scatter at the high mass end for the blue LBGs produced by the poor statistics.

4.15 Stellar-mass only lensing predictions on TNG100

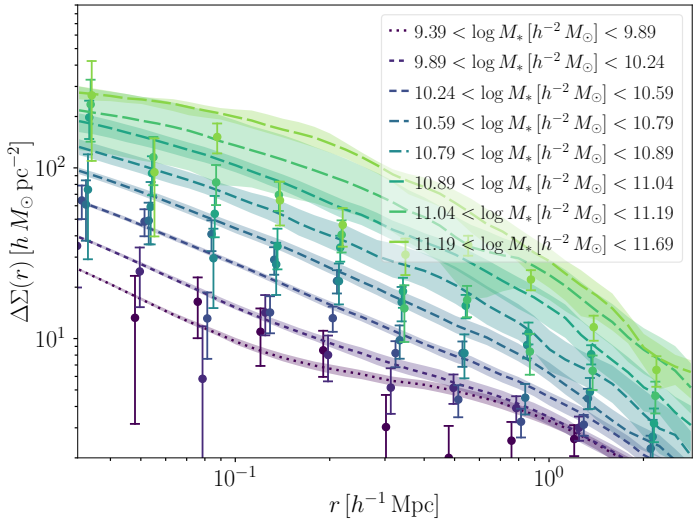

Figure 4.34: Lensing predictions from the H15 model run on the gravity-only TNG100. Similarly as for the MR simulation, the high stellar mass lensing signal is significantly over-predicted with this SAM.

In Fig. 4.34, we illustrate the predictions for the H15 model run on top of the direct Planck16 cosmology of the gravity-only TNG100 for the van Uitert et al. (2016) dataset. The result is very similar to the MR result in Fig. 4.6, although the variance is larger at the high mass end due to the small volume, which means that we can neglect any rescaling biases also for mixed central and satellite samples.

4.16 Dust extinction

Fig. 4.25 suggests that one could use the coloured clustering signal to determine the strength of the AGN feedback efficiency. However, this is sensitive to the model for dust extinction used, see Fig. 4.35. In this plot we provide a conservative upper limit of the dust impact on the clustering signal, given that we do not modify the colour cut. For stellar masses $< 11\,h^{-2}\,M_\odot$, there is a clear smooth suppression of the signal for red galaxies, as more dusty star-forming blue galaxies which are on average less clustered are counted as red. This primarily affects the 1-halo term and the effect can amount to $30-40\,\%$ whereas the effect for the 2-halo term is $\sim 10-20\,\%$ depending on the galaxy formation model. This effect is greater for the G11 model due to its many low mass red galaxies, and it is greater for lower masses since most galaxies in that range are blue. For blue galaxies the situation is less clear; we observe a mild suppression for the two lowest mass bins for the H15 model, but the result at higher masses contains a lot of scatter.

If we switch to the lensing predictions for the G11 and H15 models, we illustrate the residuals with and without dust extinction in Figs. 4.36 and 4.37 for all galaxies using the Zu & Mandelbaum (2016) selection and colour separation and for LBGs according to Mandelbaum et al. (2016), respectively. By comparing the effect with the results in Section 5.6.4, we see that the dust model can change the predictions by as much as the presence of baryons,

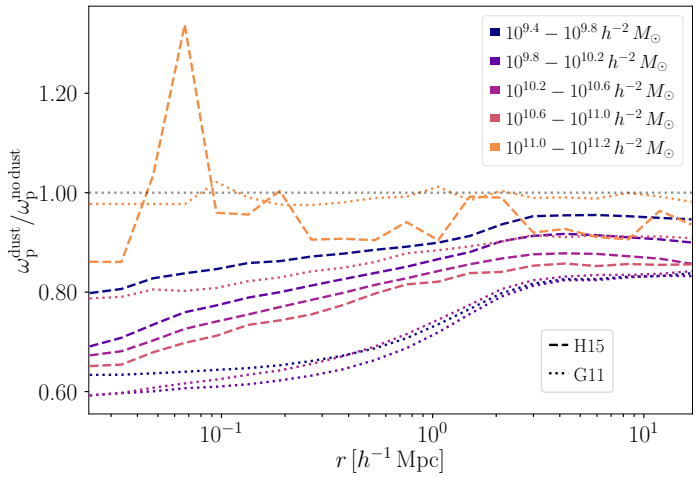

Figure 4.35: Clustering residuals for red galaxies for the G11 and the H15 models with and without dust extinction for the Zu & Mandelbaum (2016) observational criteria. Including dust suppresses the clustering signal with $30 - 40\,\%$ for the lowest mass bins for the 1-halo term. At higher masses, this effect goes towards unity with a lot of scatter.

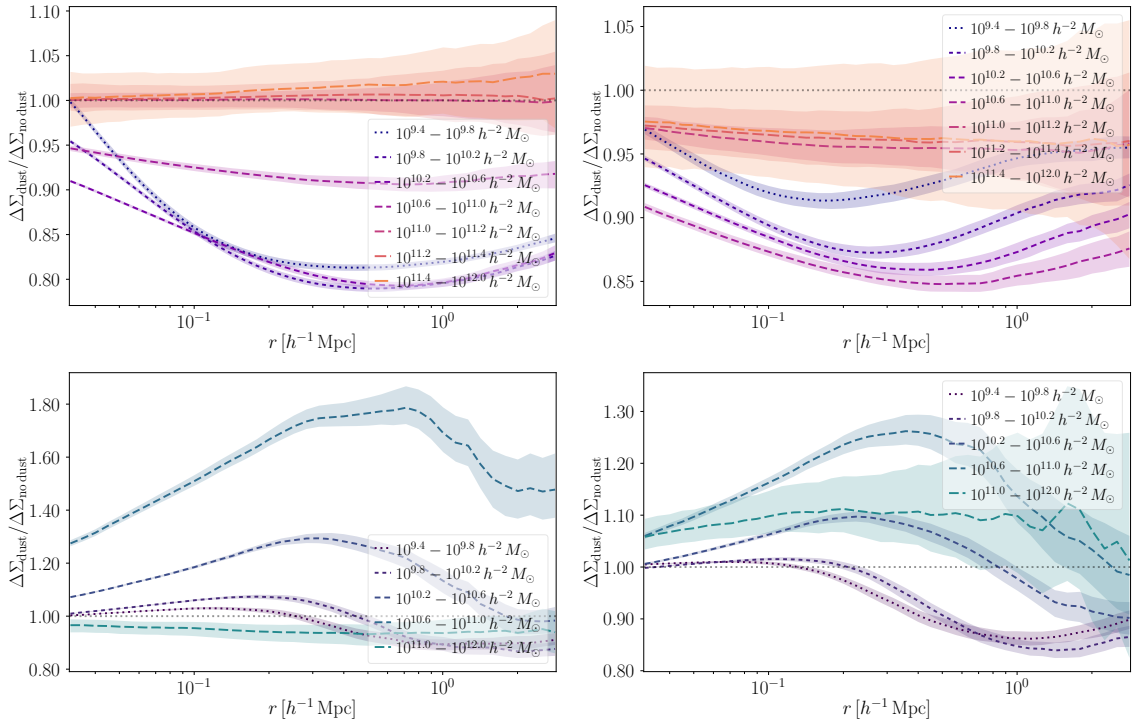

Figure 4.36: The impact of dust extinction on the colour selection on $\Delta\Sigma$ profiles for the Zu & Mandelbaum (2016) observational criteria with the Eq. (4.7.1) colour cut, assuming the same colour and stellar mass cuts. Predictions from the G11 model (left panels) and the H15 model (right panels) with the signal for red (top) and blue galaxies (bottom) are susceptible to the implemented dust model to a similar degree as the cosmological and baryonic effects. For the most massive red galaxies, the profiles for the G11 model are enhanced in the dust extinction case, whereas the H15 profiles are suppressed at all masses.

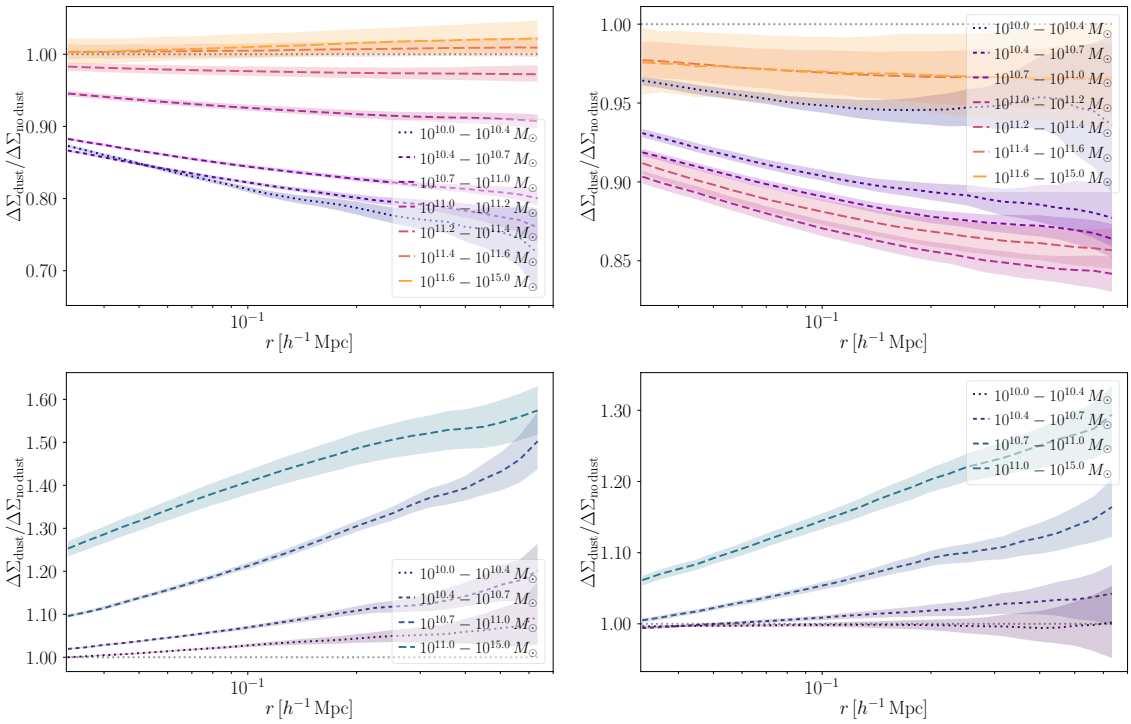

Figure 4.37: Dust extinction errors for the colour selection with the Eq. (4.7.2) cut for LBG $\Delta\Sigma$ profiles for the Mandelbaum et al. (2016) observations with the same model and red and blue separation as in Fig. 4.36. With respect to those results, the two models now showcase a similar behaviour. We only illustrate results below $r \sim 0.7\,h^{-1}\,{\rm Mpc}$ to avoid the scatter in the 1-halo to 2-halo transition regime.

Clustering (without dust)	Red	Blue
First	$(0.5\,\alpha_{\mathrm{dyn.}},\, 0.5\,k_{\mathrm{AGN}},\, 0.5\,\epsilon_{\mathrm{reheat}})$	$(0.5\,\alpha_{\mathrm{dyn.}},\, 0.2\,k_{\mathrm{AGN}})$
Second	$(0.3\,\alpha_{\mathrm{dyn.}},\, 0.3\,k_{\mathrm{AGN}})$	$0.1\,k_{\mathrm{AGN}}$
Third	$0.1\,\epsilon_{\mathrm{reheat}}$	H15

Table 4.13: The best fit models according to red and blue clustering without dust.

especially for $10.6 < \log M_* \,[h^{-2}\,M_\odot] < 11.0$ blue galaxies and $11.0 < \log M_* \,[M_\odot] < 15.0$ blue LBGs. The effect is more prominent in this mass range as there are only a few massive blue galaxies, and those susceptible to the dust extinction implementation live in low mass haloes which have retained more of the dust. These low mass objects are then shifted into the red, but as there are relatively many red galaxies, the impact on the red lensing signal is modest. The boost for the blue signal is more apparent in the G11 model, but we see the same qualitative trends for H15. For massive red galaxies, there are only small differences between the signal with and without dust extinction for the G11 model whereas there is still a $\sim 3\,\%$ for the H15 model.

Examining the results for LBGs in Fig. 4.37 which we show up to $r \sim 0.7\,h^{-1}\,\mathrm{Mpc}$, one sees that similar trends are reproduced, although the effect is smoother across the radial range since the signal is central dominated. There is a mild increase in the dust modelling impact as we move to larger scales away from the galaxy centres, which can amount to as much as $\sim 15\,\%$ for the H15 model for $11 < \log M_* \,[M_\odot] < 11.2$ red LBGs and around $10\,\%$ in the centres.

We also present the figure-of-merit rankings for the lensing and clustering predictions where we have neglected dust extinctions in Table 4.13 for red and blue clustering and in Table 4.14 for red and blue LBG lenses, respectively. Analogously as for the case with dust extinction, the two colours do not agree on a single model, but we note that the $(0.5\,\alpha_{\mathrm{dyn.}},\, 0.5\,k_{\mathrm{AGN}},\, 0.5\,\epsilon_{\mathrm{reheat}})$ fits best for red clustering and also red LBG lensing as seen in Table 4.14. This model is still the best if we account for abundance corrections to the masses. The second best $(0.1\,\alpha_{\mathrm{dyn.}},\, 0.1\,k_{\mathrm{AGN}})$ model for the total LBG lensing signal now finishes on second place. The listings in Table 4.14 for blue LBG lensing without dust is similar to the ranking of the models for blue galaxy clustering with dust in Table 4.6. As for the LBG lensing for all galaxies and red galaxies only with abundance corrected masses, the H15 model does a good job for the red lensing LBG signal without dust extinction and with abundance corrected masses, but it is overtaken by the G11 model for blue LBGs without dust and with abundance corrected masses.

LBG lensing (without dust, fiducial)	**Red**	**Blue**
First	$(0.5\,\alpha_{\rm dyn.},\ 0.5\,k_{\rm AGN},\ 0.5\,\epsilon_{\rm reheat})$	$(0.3\,\alpha_{\rm dyn.},\ 0.1\,k_{\rm AGN})$
Second	$(0.1\,\alpha_{\rm dyn.},\ 0.1\,k_{\rm AGN})$	$(0.4\,\alpha_{\rm dyn.},\ 0.1\,k_{\rm AGN})$
Third	$(0.3\,\alpha_{\rm dyn.},\ 0.1\,k_{\rm AGN})$	$(0.1\,\alpha_{\rm dyn.},\ 0.1\,k_{\rm AGN})$
LBG lensing (without dust, abundance)	**Red**	**Blue**
First	$(0.5\,k_{\rm AGN},\ 0.5\,\alpha_{\rm dyn},\ 0.5\,\epsilon_{\rm reheat})$	$(0.5\,k_{\rm AGN},\ 0.1\,\alpha_{\rm dyn})$
Second	H15	G11
Third	$0.1\,\epsilon_{\rm reheat}$	$0.1\,\alpha_{\rm dyn.}$

Table 4.14: The best fit models according to red and blue LBG lensing without dust.

4.17 SMFs and red fractions for our best fit model

In Fig. 4.38, we show the predicted SMFs with respect to the observational constraints used in the MCMC analysis in the H15 paper for our best fit $(0.5\,\alpha_{\rm dyn},\ 0.2\,k_{\rm AGN})$ model compared to the fiducial H15 results. We see that we are able to retain the good SMF agreement[7] of the H15 model at higher redshifts, showing that the parameter choices are valid. The curve at $z = 3$ also lies above the H15 prediction for low mass systems and not only above the knee of the SMF as seen at $z = 0$ and $z = 1$. Still, we do not have observations for this mass range and the small tension is well within the quoted error bars of the other measurements.

We move on to the red fraction of galaxies in Fig. 4.39. At $z = 0$, this corresponds to a split in $g - r$ with dust extinction and for the higher redshift bins we refer the reader to H15 for the exact definition. We see that the $(0.5\,\alpha_{\rm dyn},\ 0.2\,k_{\rm AGN})$ model produces fewer red galaxies than the fiducial H15, moving away from the observational constraints. Yet, this is not a dramatic shift and could be accommodated by changing the colour cut. Still, we have already seen that the $(0.5\,\alpha_{\rm dyn},\ 0.2\,k_{\rm AGN})$ model not finishes first for the red LBG lensing and red clustering, which could be a related effect to the colour distribution being slightly off.

[7] Apart from the observables quoted here, we have also checked that no new discrepancies arise for the star formation rates and the bulge mass-black hole mass relations.

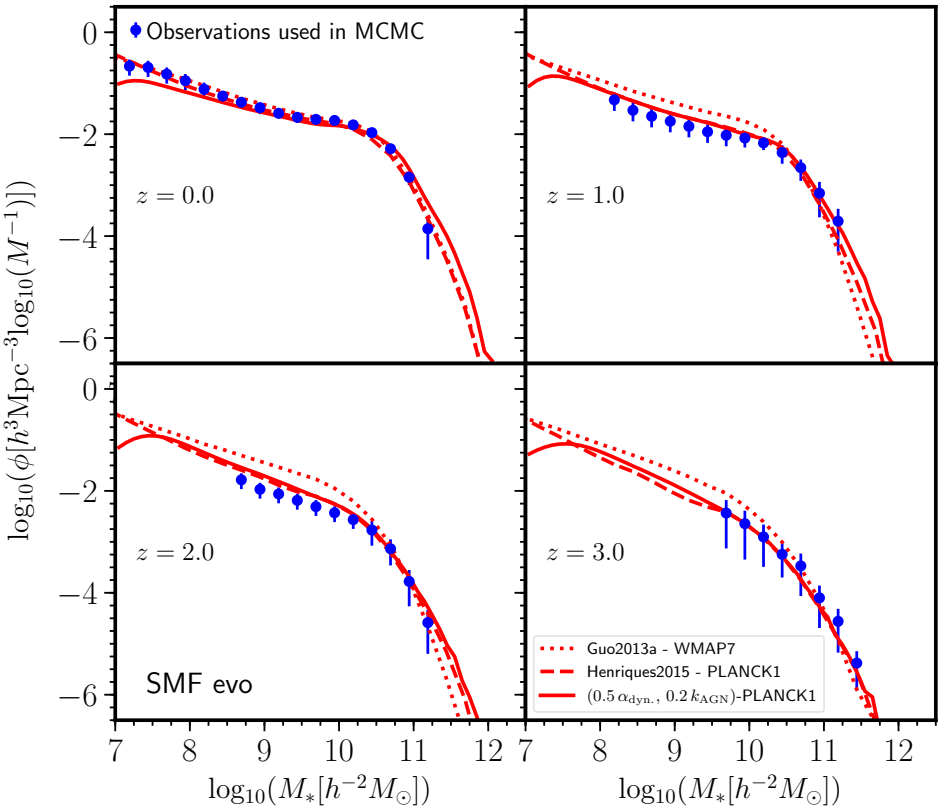

Figure 4.38: SMFs at different redshifts from our best fit $(0.5\,\alpha_{\rm dyn},\,0.2\,k_{\rm AGN})$ model compared to the H15 model and the galaxy formation model from Guo et al. (2013b) on the MR run rescaled to a WMAP7 cosmology (Komatsu et al., 2011). We see the largest differences at $z = 0.$ and at $z = 1$ beyond the knee at the high mass end, but we are still in agreement with observations.

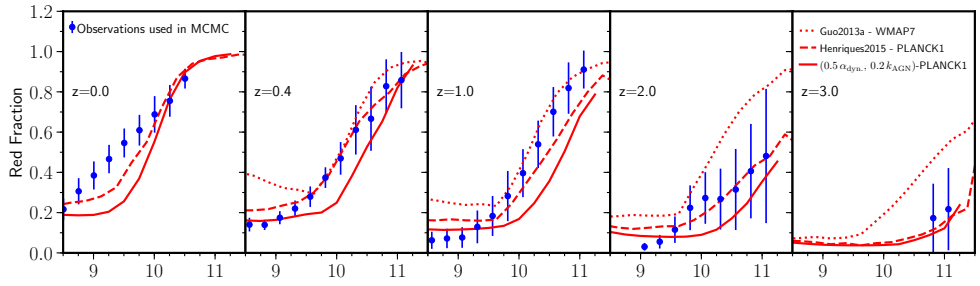

Figure 4.39: Red fractions with dust extinction at different redshifts with stellar masses in $\log M_*\,\left[h^{-2}\,M_\odot\right]$ on the x-axis from our best fit $(0.5\,\alpha_{\rm dyn},\,0.2\,k_{\rm AGN})$ model compared to the H15 model and the Guo et al. (2013b) model. The new red fractions deviate from the MCMC constraints, but we also have to take into account the shift of the colour distribution and the quoted uncertainties are still quite large.

Chapter 5 Baryonic effects

5.1 Prologue

The results from this Chapter will shortly be published in Monthly Notices of the Royal Astronomical Society, to which we rescind all copyrights, within Renneby et al. (prepb). The first author (me) conducted the work in this analysis with advice from Dr. Stefan Hilbert, but the final publication will feature additional contributions from other co-authors not listed here.

5.2 Abstract

We use the Illustris, IllustrisTNG and Eagle simulation suites to predict galaxy-galaxy lensing profiles for various lens samples adapted for observational data from KiDS+GAMA and SDSS-DR7. We examine selections based on stellar mass only, the separation of the signal according to colour, and group membership. We find that the IllustrisTNG and Eagle produce accurate predictions for the observations, although they cannot capture the most massive central galaxy group signals. By matching the subhaloes with their counterparts in the gravity only runs we investigate the impact of baryonic physics on the 1-halo term as well as on the transition regime between the 1-halo and 2-halo terms. Mass convergence between the two runs is achieved at $r \sim 5 - 6\,h^{-1}\,\mathrm{Mpc}$ for Illustris and at $r \sim 1 - 2\,h^{-1}\,\mathrm{Mpc}$ for IllustrisTNG, reflecting the different strength of the AGN feedback. The baryonic imprint on central galaxies and central dominated samples can be captured by a smooth function with small scatter, dependent on the feedback prescriptions. For satellite dominated samples, the suppression around $r \sim 1\,h^{-1}\,\mathrm{Mpc}$ has more scatter due to the differences in the projected distance to the central subhalo and host halo mass between the two runs. We examine whether this well-behaved central signal can be encapsulated by a semi-analytical prescription using the parameterisation of Schneider & Teyssier (2015) for galaxy groups and clusters in the TNG300. The parameterisation is able to capture the general trends but further tuning is required for it to serve as a basis for profile-by-profile deformation. The differences in the predictions between Illustris and TNG100 are of the same order as between TNG100 and TNG300, although the two volumes display similar trends. To conclude, we produce mock signals for HSC galaxy groups and clusters and investigate the impact of baryons on the signal from $z = 1.1$ to today. We find that the stellar parameterisation is more important for higher redshifts, affecting the innermost radial bins in a lensing survey, and also setting the scale where the baryonic suppression takes hold. However we note no major developments for the halo outskirts, meaning that one should keep the same conservative radial cuts for the new deeper surveys if one wants to mitigate the impact of baryons.

5.3 Introduction

As we enter the era of precision cosmology, significant gains in information extraction can be achieved by including smaller scales from 2-pt statistics measurements in the analysis pipelines, which offer better signal-to-noise ratios. Still, the tradeoff is that one has to pay more attention to systematics from astrophysical and nonlinear processes, as one leaves the validity regime of perturbative treatments. The latter can be modelled using numerical N-body simulations together with e.g. SAMs, see Section 2.2.3, or as a basis for pure emulators for the matter power spectrum (e.g. Heitmann et al., 2014; Lawrence et al., 2017), but the former requires hydrodynamical simulations where the implementation of the baryonic feedback processes can differ. So far cosmological analyses have taken a conservative approach, either excluding these scales completely (e.g. Abbott et al., 2017a) to ensure that survey statistical errors exceed systematics from nonlinear effects (Krause et al., 2017), or attempting to capture the main trends using simplified fitting formula (e.g. Mead et al., 2015, 2016) calibrated against hydrodynamical simulations (e.g. van Daalen et al., 2011) to mock the amplitude of the baryonic feedback (e.g. van Uitert et al., 2018; Joudaki et al., 2018). To push deeper into the nonlinear regime requires more elaborate recipes.

It is well known that baryons affect the power spectrum starting at $k \sim 1\,h\,\mathrm{Mpc}^{-1}$, where the less dense gas distribution with respect to dark matter suppresses structure compared to gravity-only simulations. At $k \approx 10\,h\,\mathrm{Mpc}^{-1}$ the additional cooling due to the presence of baryons produces an enhanced matter clustering signal up to the halo centres (e.g. Jing et al., 2006; Rudd et al., 2008; Semboloni et al., 2011). These effects propagate into uncertainties on the weak lensing signal, i.e. for the galaxy-matter cross-correlations. They also influence the galaxy clustering, i.e. the autocorrelation of the galaxy field, and both of these effects have been investigated in the literature in terms of amplitude changes of cross-power spectra (e.g. Semboloni et al., 2013; van Daalen et al., 2014; Mohammed et al., 2014; Schneider & Teyssier, 2015; Harnois-Déraps et al., 2015; Osato et al., 2015; Schneider et al., 2018) for cosmological surveys. Finally, they can also affect the shape of the halo mass function (e.g. Bocquet et al., 2016) inducing errors for cosmological constraints from cluster counts.

We can also investigate the effect for the real-space correlation functions by examining the deformations of the lensing profiles, previously briefly performed in Leauthaud et al. (2017). To avoid projection effects, more studies have been carried out on 3D density profiles (e.g. Duffy et al., 2010; Schaller et al., 2015a; Dutton et al., 2016; Peirani et al., 2017; Mummery et al., 2017; Lovell et al., 2018; Chua et al., 2018; Wang et al., 2018). Specific focus has been directed towards galaxy clusters (e.g. Henson et al., 2017; Shirasaki et al., 2018) although the chief directives have been to classify biases for concentration and mass estimates.

So far, these analyses have focused on one or a small set of simulations to measure the effects, though recent advances have allowed baryonic deformations from different cosmological hydrodynamical simulations to be quantified in terms of parameterised principal components for matter and lensing power spectra (e.g. Zentner et al., 2013; Eifler et al., 2015; Kitching et al., 2016; Mohammed & Gnedin, 2018; Huang et al., 2018). Comparisons for the baryonic impact on the matter power spectrum have been carried out by Chisari et al. (2018); Springel et al. (2018) and for the galaxy clustering 1-halo term in Artale et al. (2017).

In this Chapter, we would like to extend the enquiry to predictions for galaxy-galaxy lensing profiles using the Eagle (Schaye et al., 2015; Crain et al., 2015), Illustris (Vogelsberger et al., 2014a,b; Genel et al., 2014) and IllustrisTNG (Weinberger et al., 2017; Pillepich et al., 2018a) for observational criteria from the Kilo-Degree and Galaxy And Mass Assembly

(KiDS+GAMA) surveys (Liske et al., 2015; Kuijken et al., 2015) presented in van Uitert et al. (2016); Velliscig et al. (2017) for GAMA lenses selected by stellar mass and stellar mass and group membership, respectively. By comparing the lensing signal with the predictions from the corresponding objects in the gravity-only runs, we are able to extend the 3D density profile deformations to projected profiles, which are what we observe in the real Universe. These two selection functions represent the simplest classes for future surveys and the most interesting for galaxy groups and clusters, which can inform on the strength and deformation properties of the feedback from active galactic nuclei (AGN) (e.g. McCarthy et al., 2010; Viola et al., 2015). We restrict ourselves to evaluations using the highest resolution runs of Illustris and the two large simulation boxes from the IllustrisTNG suite, TNG100 and TNG300.

Moreover, we are interested in the differences in the imprint for additional classification criteria, such as colour. It has already been established that the other great systematic plaguing weak lensing analyses, namely intrinsic alignments, is different for red and blue galaxies modelled through different couplings to the tidal field (e.g. Hirata et al., 2007). In addition, some lensing surveys such as the Dark Energy Survey (DES) currently restrict their galaxy-galaxy lensing observations to red galaxies due to uncertainties in photometric redshifts for blue galaxies (Prat & DES Collaboration, 2018). This calls for an investigation on how the baryonic deformation of host haloes differ between red and blue galaxies, which can affect the observed host halo bimodality (e.g. Mandelbaum et al., 2016; Zu & Mandelbaum, 2016), which we examine using the TNG300 with mocks for SDSS-DR7 (Abazajian et al., 2009).

In addition, new and upcoming large-scale structure surveys such as the Hyper Suprime-Cam SSP Survey (HSC) (Aihara et al., 2018), the Euclid satellite (Laureijs et al., 2011) and the Large Synoptic Survey Telescope (LSST) (Ivezić et al., 2008) will allow us to probe the galaxy-galaxy lensing out to systems with $z \simeq 1$, allowing us to constrain the galaxy-halo relation over cosmic time. Baryonic effects do not necessarily take the same form at these different redshifts. Observationally, AGN activity is assumed to peak around cosmic noon at $z = 2$ (e.g. Hopkins et al., 2007). Although there is a significant build-up of supermassive black holes between $z = 1$ and $z = 0$, which are traced by the AGN, this is simultaneously accompanied by an increase in star formation rate and thus stellar mass (e.g. Shankar et al., 2009) and a corresponding increase in halo mass, where the deeper potential wells are better at retaining gas, which have led previous studies (e.g. Schneider & Teyssier, 2015), henceforth ST15, to neglect redshift evolution in their parameterisation. Here we quantify the baryonic impact on group and cluster-scale host haloes in the TNG300 up to $z = 1.1$ appropriate for the new surveys and attempt to express it with the ST15 model. This is crucial for the next generation of surveys which will span volumes inaccessible by current cosmological hydrodynamical simulations, where parameterised forms could be incorporated in a suitable SAM framework.

The aim of this Chapter is thus to answer the following questions: (i) Can hydrodynamical simulations produce accurate galaxy-galaxy lensing predictions for the 1-halo term? (ii) How large are the effects of baryons on galaxy-galaxy lensing profiles, and at which scales? (iii) Is there a difference in the ejected radius of gas due to the strength of the AGN feedback? (iv) Is there a redshift evolution of the effects? (v) Can we adapt profiles for gravity-only runs with semi-analytical models of galaxy formation to mimic hydrodynamics for future surveys?

This Chapter is organised as follows: In Section 5.4 we describe the baryonic correction model which we use to modify the gravity-only profiles and in Section 5.5 our methodology. We previously described our simulations in 2.3. We present our results starting with the stellar mass only selection at $z = 0.31$ in Section 5.6.1, the group lenses at $z = 0.18$ in Section 5.6.2

and the colour lenses at $z = 0.11$ in Section 5.6.3. Next we proceed to modify the gravity-only 3D profiles in Section 5.6.4 and compare them with their full physics counterparts, and conclude with producing mock group and cluster lensing predictions for HSC in Section 5.6.5.

5.4 Baryonic correction model

The baryonic correction model (BCM) proposed in ST15 features a hot gas component in hydrostatic equilibrium, ejected gas from feedback processes, a central galaxy stellar component and adiabatically relaxed dark matter. These form a density profile

$$\begin{aligned}\rho_{\rm BCM}(r) = f_{\rm rdm}y_{\rm rdm}(r) + f_{\rm cgal}(M_{\rm h})y_{\rm cgal}(r) \\ + f_{\rm bgas}(M_{\rm h})y_{\rm bgas}(r) + f_{\rm egas}(M_{\rm h})y_{\rm egas}(r) + \bar{\rho}_{\rm bg},\end{aligned} \tag{5.4.1}$$

with $\bar{\rho}_{\rm bg}$ as a constant background term of non-collapsed matter which has the same amplitude in the gravity only and the full physics runs, with $M_{\rm h}$ as the total halo mass. The different components y_χ satisfy

$$Y_\chi(r) = 4\pi \int_0^r r'^2 y_\chi\left(r'\right) {\rm d}r',\ Y_\chi(r=\infty) = M_{\rm h}. \tag{5.4.2}$$

The fiducial density profile $\rho(r)$ is captured by a truncated NFW profile (Navarro et al., 1996, 1997) for $x = r/r_{\rm s}$ with $r_{\rm s}$ as the scale radius

$$\rho_{\rm NFW}(x) = \frac{\rho_0}{x(1+x)^2}\frac{1}{(1+(x/\tau)^2)^2}, \tag{5.4.3}$$

to ensure mass conservation with truncation radius $\tau = 8c$ with the halo concentration $c = r_{\rm 200c}/r_{\rm s}$ plus the background term. This profile can be integrated analytically (Baltz et al., 2009), which allows us to convert halo masses from catalogued $M_{\rm 200c}$ values to total $M_{\rm h}$ through

$$M_{\rm h} = M_{\rm 200c} \times \frac{m_{\rm NFW}(\infty,\,\tau)}{m_{\rm NFW}(c,\,\tau)}, \tag{5.4.4}$$

with

$$\begin{aligned}m_{\rm NFW}(x,\,\tau) = \frac{\tau^2}{2\left(\tau^2+1\right)^3}\times \\ \left[\tau^2\left(\tau^2-3\right)\ln\frac{\tau^2(x+1)^2}{\tau^2+x^2} + \tau\left(6\tau^2-2\right)\tan^{-1}\frac{x}{\tau} + \right. \\ \left.\frac{x\left(-2\tau^6+\tau^4(1-3x)x+2\tau^2\left(-x^2+x+1\right)+x^2+x\right)}{(x+1)\left(\tau^2+x^2\right)}\right],\end{aligned} \tag{5.4.5}$$

which requires an estimate of the halo concentration. We wish to examine whether

$$\rho(r) \to \rho'(r) = \rho_{N\text{-body}} + \left(\rho_{\rm BCM}(r) - \rho_{\rm NFW}(r) - \bar{\rho}_{\rm bg}\right), \tag{5.4.6}$$

can be a reasonable proxy[1] of the density profiles measured in the full physics run, where we assume that the large scale 2-halo term is the same in the two runs.

[1]The BCM model gives a recipe on how to move particles around between the different shells whereas we interpolate the new profile values and adjust the density amplitude of each shell accordingly.

Recently, an updated simplified BCM model was introduced in Schneider et al. (2018). We have checked that the shape of the gas profiles differs negligible in the two approaches, although the updated model features a joint profile for the bound and ejected gas with a degeneracy for the amplitude of the inner profile for the ejection radius and bound gas slope index. The BCM profile is constructed to account for the intermediate scale suppression of the profiles due to gas ejection and the small-scale enhancement due to presence of the stellar component. For the suppression of the power spectrum this can be captured by a fitting function with three free parameters, M_c, the mass scale of the clusters below which the suppression happens, η_b, a dimensionless quantity which relates the radius of the ejected gas and the virial radius, and k_s, the scale below which the stellar component enhances the spectrum. In the fiducial setup these are assumed to be redshift independent, but Chisari et al. (2018) found an anti-correlation of the best-fit values for η_b and k_s for $0 < z < 1$ whereas M_c was found to be mostly constant. Intuitively this makes sense as the AGN feedback enters maintenance mode and manifests little evolution at this stage whereas subhaloes with higher concentration gradually grow more massive and gas cannot be ejected as far due to the deepening potential wells. If we switch to the profiles themselves, M_c and the normalisation of the slope[2] β are set by fitting the hot bound gas fractions inside $r_{500\mathrm{c}}$,

$$f_\mathrm{bgas}(M_h) = \frac{\Omega_\mathrm{b}/\Omega_\mathrm{m}}{1 + (M_\mathrm{c}/M_\mathrm{h})^\beta}, \tag{5.4.7}$$

where Ω_b and Ω_m are the baryon and total matter fraction, respectively. The bound gas profile $y_\mathrm{bgas}(x)$ assumes hydrostatic equilibrium as well as a polytropic form for the gas pressure $P = T\rho \propto \rho^\gamma$ (Komatsu & Seljak, 2001; Suto et al., 1998; Martizzi et al., 2013) leading to

$$y_\mathrm{bgas}(x) = y_0 \left[\frac{\ln(1+x)}{x}\right]^{\Gamma_\mathrm{eff.}}, \Gamma_\mathrm{eff.} = \frac{1}{\Gamma - 1} \tag{5.4.8}$$

with the polytropic index Γ (Komatsu & Seljak, 2001) set such that the slope of the NFW profile is matched at $r = r_{200}/\sqrt{5}$, capturing that the gas in the outskirts acts as a collisionless fluid,

$$\Gamma = 1 + \frac{((1+x_\mathrm{eq})\ln(1+x_\mathrm{eq}) - x_\mathrm{eq})}{((1+3x_\mathrm{eq})\ln(1+x_\mathrm{eq})}, x_\mathrm{eq} = \frac{c}{\sqrt{5}}. \tag{5.4.9}$$

The gas ejection parameter η is set by equating the fraction of ejected gas,

$$f_\mathrm{egas}(M_\mathrm{h}) = \Omega_\mathrm{b}/\Omega_\mathrm{m} - f_\mathrm{bgas}(M_h) - f_\mathrm{cgal}(M_h), \tag{5.4.10}$$

with the integrated Maxwell-Boltzmann distribution for gas particles receiving kicks from the AGN from the ejected gas profile

$$y_\mathrm{egas}(r) = \frac{M_\mathrm{h}}{(2\pi r_\mathrm{ej}^2)^{3/2}} \exp\left[-\frac{r^2}{2r_\mathrm{ej}^2}\right], \tag{5.4.11}$$

which determines the ejection radius r_ej as the numerical solution to

$$1.0 - \mathrm{Erf}\left[\frac{\eta r_\mathrm{esc.}}{\sqrt{2}r_\mathrm{rej}}\right] + \sqrt{\frac{2}{\pi}}\frac{\eta r_\mathrm{esc.}}{r_\mathrm{ej}} \exp\left[-\frac{\eta^2 r_\mathrm{esc.}^2}{2r_\mathrm{ej}^2}\right] = \frac{\Omega_\mathrm{m}}{\Omega_\mathrm{b}} f_\mathrm{egas}(M_\mathrm{h}), \tag{5.4.12}$$

[2]This parameter has a negligible impact on the power spectrum suppression for moderate variations of M_c around its fiducial best-fit value so it is ignored in such analyses.

where the escape radius is estimated as $r_{\rm esc.} \sim 0.5\sqrt{\Delta_{200}} r_{\rm 200c}$ where the typical time-scale is half the Hubble time. The uncertainty of both these radii are then encapsulated in η. We can fix η by computing the gas fractions within different radial shells from the halo centre up to a few $r_{\rm 200c}$ for galaxy clusters where $r_{\rm ej.}$ is of the order of $r_{\rm 200c}$.

The shape of the dark matter component in the baryonic run differs from that in the dark matter only run due to the cooling from the presence of baryons which yield a central adiabatic contraction (Blumenthal et al., 1986) and a back-reaction in the halo outskirts due to missing gas. These two effects (Gnedin et al., 2004; Abadi et al., 2010; Teyssier et al., 2011) can be captured by a displacement of the initial positions r_i to final positions r_f given by

$$\frac{r_f}{r_i} - 1 = a\left(\frac{M_i}{M_f} - 1\right), \; a = 0.68, \tag{5.4.13}$$

with masses

$$\begin{aligned} M_i &= M_{\rm NFW}(r_i) \\ M_f &= f_{\rm rdm}(M_{\rm h}) M_{\rm NFW}(r_i) + f_{\rm cgal}(M_{\rm h}) Y_{\rm cgal}(r_f) \\ &\quad + f_{\rm bgas}(M_{\rm h}) Y_{\rm bgas}(r_f) + f_{\rm egas}(M_{\rm h}) Y_{\rm egas}(r_f). \end{aligned} \tag{5.4.14}$$

The stellar component is assumed to follow a power law in the centre and to drop exponentially beyond twice the half-light radius, estimated as $R_{1/2} = 0.015\, r_{\rm 200c}$ (Mohammed et al., 2014)

$$y_{\rm cgal}(r) = \frac{M_{\rm h}}{4\pi^{3/2} R_{1/2} r^2} \exp\left[-\left(\frac{r}{2R_{1/2}}\right)^2\right], \tag{5.4.15}$$

and the total stellar fraction $f_{\rm cgal}(M_h)$ is set by abundance matching techniques using the model in Kravtsov et al. (2018) based on fits in Behroozi et al. (2013b). This profile, however, does not account for the stellar components of the satellites in the halo and intra-cluster light, and might be too steep. The stellar density profile for central galaxies in hydrodynamical simulations (Remus et al., 2017) has previously been successfully described by Einasto profiles (Einasto, 1965), which we fit as

$$y_{\rm cgal}(r) = y_{-2} \exp\left[\frac{2}{\alpha}\left(\left(\frac{r}{r_{-2}}\right)^{\alpha} - 1\right)\right], \tag{5.4.16}$$

where we set the characteristic radius as $r_{-2} = R_{1/2}$. This allows for a shallower continuation to larger scales. We also fit a simpler power law $y_{\rm cgal}(r) = Ar^b$ to allow for an even flatter evolution. Nevertheless, the stellar term is only the third most massive component in the outskirts of the halo which means that its contribution to the total profile is almost negligible.

5.5 Methodology

For the hydrodynamical simulations we consider both the bound mass in substructure and contained in 30 pkpc (physical kpc) apertures, where the former was used for the KiDS+GAMA and Eagle comparison in Velliscig et al. (2017). This latter stellar mass is the preferred choice to equate predictions from SAMs and hydrodynamical simulations (Guo et al., 2016; Mitchell et al., 2018) as well as with observational data for the stellar mass function (e.g. Pillepich et al., 2018b). For low mass galaxies, this aperture covers all bound star particles.

We project the full particle distribution along each spatial axis and compute the differential excess surface mass density profiles for each individual lens in 40 log-equidistant cylindrical shells for projected radii which we later stack. This object-by-object lensing enables us to find each corresponding system in the gravity-only runs using the particle ids. To examine the validity of the BCM parameterisation, we switch to 3D density profiles where we also consider the whole adjacent particle distribution to each halo.

Conforming to Velliscig et al. (2017), we use a single simulation snapshot for each set of predictions, corresponding to $z = 0.30$ for the van Uitert et al. (2016) datasets, $z = 0.18 - 0.19$ for the Velliscig et al. (2017) observations and $z = 0$ for SDSS-DR7. For the redshift evolution and the BCM model parameterisation, we have measured the lensing signal for eleven snapshots equally spread between $z = 1.1$ and $z = 0.02$. We show results for six of them, where the intermediate redshift results lie as interpolating curves between them.

The underlying cosmologies for the different hydrodynamical simulations differ slightly, and this propagates into discrepancies for the halo and stellar mass functions, but we expect these small deviations to have negligible impact for the comparison at hand as the different feedback prescriptions dominate.

5.6 Results

5.6.1 KiDS+GAMA: stellar mass only

In Fig. 5.1, we show the predictions from our simulations for two stellar mass bins, which are representative of the adjacent bins, for the comparison with the van Uitert et al. (2016) datasets. Here we show the result for the bound mass definition, as we find that the predictions for the Eagle simulation differ substantially between the two mass definitions at the high mass end, see Section 5.9, perhaps because the apertures are not optimally defined for the massive end. We also show the predictions for all mass bins for Eagle (Fig. 5.3) and Illustris and TNG100 (Fig. 5.4). All simulations produce results which do not deviate far from the observations, although the Illustris simulation lies a bit too low starting at approximately $10^{10.59}\,h^{-2}\,M_\odot$. Eagle and TNG100/TNG300 yield equivalent signals, despite their different galaxy formation recipes, and their superiority to Illustris is most apparent at the high mass end. This is partly a result of a well-matched stellar-to-halo mass relation for Eagle (Schaye et al., 2015; Matthee et al., 2017) and IllustrisTNG (Pillepich et al., 2018b) to abundance matching and more refined empirical model results (e.g. Moster et al., 2013; Behroozi et al., 2013b; Rodríguez-Puebla et al., 2017; Moster et al., 2018), but nevertheless heralds a landmark concordance. This is remarkable as the models also differ in the predicted satellite fractions, which we show in Fig. 5.2 with the corresponding plot for the bound mass definition in Section 5.9. Until $10^{10.5}\,h^{-2}\,M_\odot$ the curves for TNG100 and the SAM trace one another with Illustris and TNG300 giving a lower and higher ratio, respectively. At the high mass end, all models predict fewer satellites, in line with the observational constraints from KiDS+GAMA in van Uitert et al. (2016), but the exact numbers differ. Since the 2σ error regions are quite broad for the $N_{\rm FOF} \geqslant 2$ GAMA group sample in van Uitert et al. (2016), the observationally inferred satellite fractions cannot be used to distinguish between the different simulations, and it is hard to tell from the lensing signals which model is preferable.

The fact that TNG100 and TNG300 produce different predictions in panel II of Fig. 5.1, where the trend starts at $M_* \sim 10^{10.24}\,h^{-2}\,M_\odot$, indicates that it is not straightforward to conclude that certain galaxy formation recipes are successful in describing the lensing signal

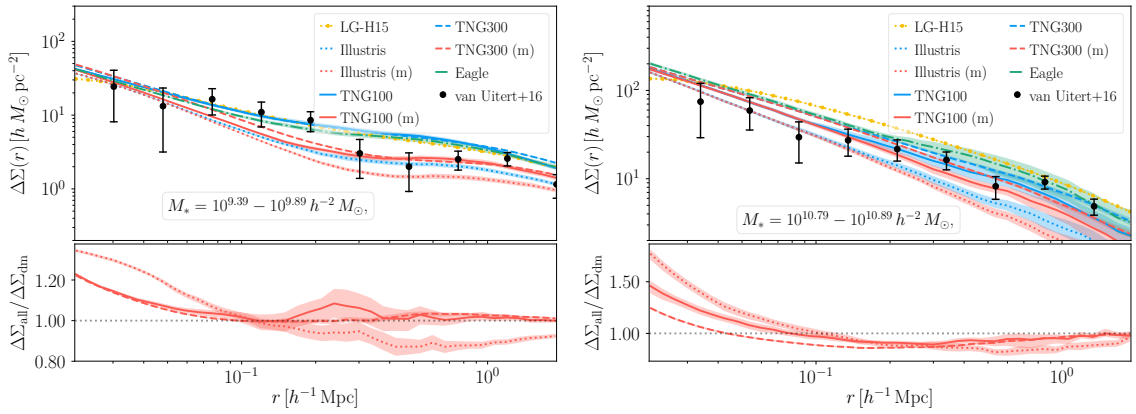

Figure 5.1: Lensing predictions from the different simulations w.r.t. observations from van Uitert et al. (2016). For Illustris and IllustrisTNG (TNG100 and TNG300) we plot the signals from the full physics run (blue) and for those subhaloes in the full physics run which have matches in the gravity-only run (red) with the residuals plotted in the lower panel. We can see significant departures between the matched and full physics signals, most apparent at scales $r \sim 100\,h^{-1}\,\mathrm{kpc}$ for Illustris and already from $r \sim 20\,h^{-1}\,\mathrm{kpc}$ for the TNG suite. The Illustris simulation is the best choice for the halo outskirts, whereas all the other simulations do equal well on intermediate scales and in the halo centres. In panel II we show the result for galaxies with $10.79 < \log M_* \left[h^{-2}\,M_\odot\right] < 10.89$. We see that the Illustris simulation has the best performance for the innermost radial bins, with the TNG100 is most successful in the outskirts. In the lower panel, we observe a shift in the enhancement of the profiles between Illustris (largest), TNG100 and TNG300 (smallest) and the baryonic imprint for TNG100 and TNG300 converges around $r \sim 0.5\,h^{-1}\,\mathrm{Mpc}$.

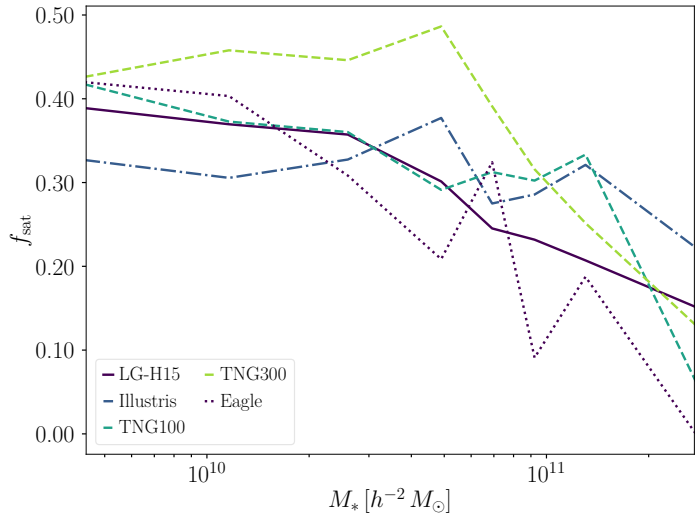

Figure 5.2: Satellite fractions for the different hydrodynamical simulations depending on the stellar mass bin. All simulations produce values in line with the observational uncertainties quoted in van Uitert et al. (2016). The TNG100 and TNG300 do not agree on the satellite fractions, although the tension is alleviated for $M_* < 10^{10.2}\,h^{-2}\,M_\odot$ using the bound mass definition in Section 5.9.

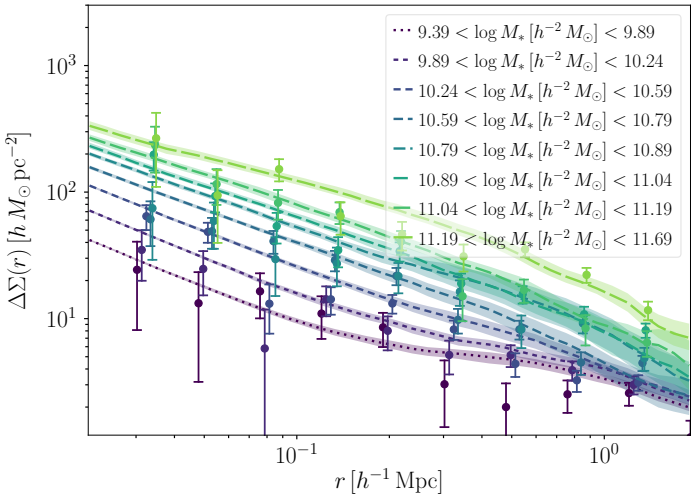

Figure 5.3: Lensing predictions from the Eagle simulation with bound masses compared to van Uitert et al. (2016) observations.

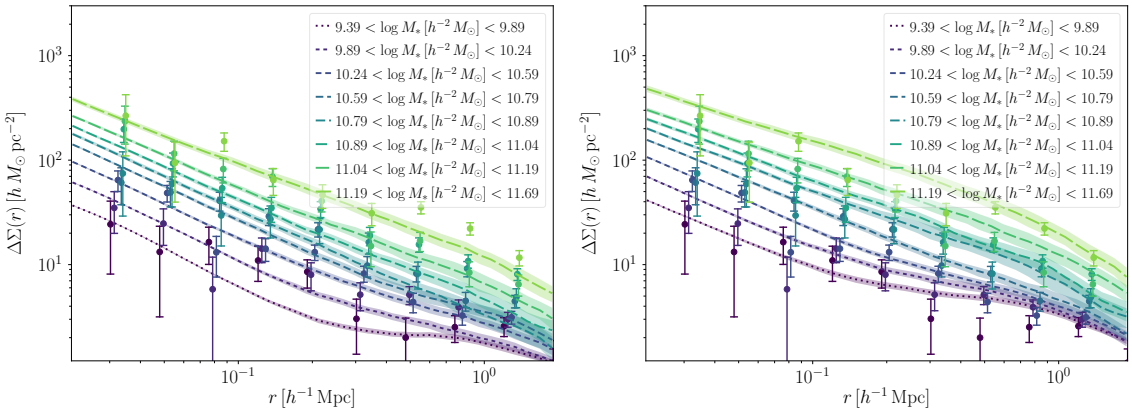

Figure 5.4: Analogously as in Fig. 5.3 for the Illustris simulation (panel I) with 30 pkpc masses (there are no major differences for bound masses, except for the most massive bins) and for TNG100 (panel II). The most significant improvements for the latter includes a boost of the satellite central bump, visible for the low mass bins, and a larger signal for the high mass end of the SMF.

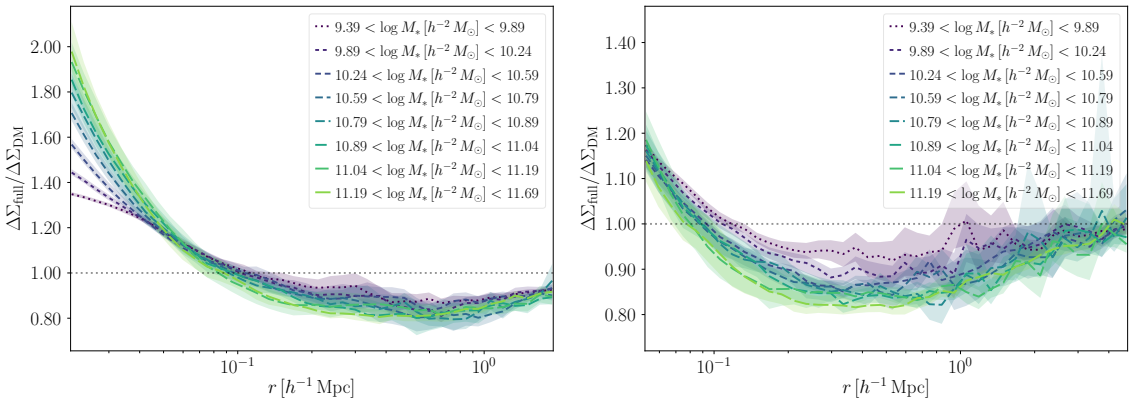

Figure 5.5: Baryonic effects on the full lensing profiles from the Illustris simulation using all matched subhaloes with 30 pkpc aperture masses. Panel II is similar but now only for matched centrals, extending the radial range to $5\,h^{-1}$ Mpc. Here, at the largest scales, we start to see a mass convergence between the two runs.

without volume comparisons. Running a model in a larger volume primarily affects the magnitude of the central bump of the signal, as more massive haloes are included in the large box. It so happens that the baryonic impact for the TNG100 and TNG300 coincide in the halo centres as seen in the lower panel in panel I of Fig. 5.1. If we compare the residuals in Figs. 5.6 and Figs. 5.7 using the 30 pkpc apertures, we already see small differences in this low mass bin. This extends to the lower panel of panel II in Fig. 5.1, where the difference in the baryonic impact for the stellar term is similar between Illustris and the TNG100, as to the difference between TNG100 and TNG300.

We show the residuals for the whole matched samples in Figs. 5.5 (Illustris), 5.6 (TNG100) and 5.7 (TNG300). In Fig. 5.5, we also provide the signal for matched centrals for Illustris to $r \sim 5\,h^{-1}$ Mpc. We discern that the maximum suppression of about $\sim 20\,\%$ persists between the two selections. Compared to TNG100 and TNG300, we do not see any peak in the suppression for intermediate stellar masses obtained for the $10.79 < \log M_*\,[h^{-2}\,M_\odot] < 10.89$ (TNG100) and $10.89 < \log M_*\,[h^{-2}\,M_\odot] < 11.04$ (TNG300) mass bins, but the maximum impact is reached for the most massive stellar mass bin. Mass convergence between the two runs is attained around $r \sim 5 - 6\,h^{-1}$ Mpc, far beyond the average virial radii of the host halo masses. One could argue that convergence is reached slightly earlier for the low mass bins, but the scatter in 1-halo-to-2-halo transition regime makes it hard to draw any definite conclusions. As already found for the power spectra (Chisari et al., 2018; Springel et al., 2018), the different simulations predict different baryonic imprints, both for the stellar enhancement and intermediate scale suppression in terms of amplitude and shape. Illustris predicts the highest stellar term, with a boost of the signal by a factor of two for the most massive stellar mass bin, followed by the TNG100 and lastly TNG300, where more massive hosts contribute to a slightly deeper suppression and also a smaller enhancement in the centre. For TNG100 and TNG300, convergence is already assured around $r \sim 1-2\,h^{-1}$ Mpc. The baryonic suppression of the signal lies in the range of $\sim 15-20\,\%$ for Illustris from $r = 0.1-1\,h^{-1}$ Mpc, $\sim 10-15\,\%$ for TNG100 for $r = 0.1 - 0.4\,h^{-1}$ Mpc and $\sim 15\,\%$ for TNG300 for $r = 0.1 - 0.4\,h^{-1}$ Mpc.

If we compare the residuals for the matched centrals to the whole matched joint sample, there are only minor differences for the TNG300 with a slightly wider suppression for the

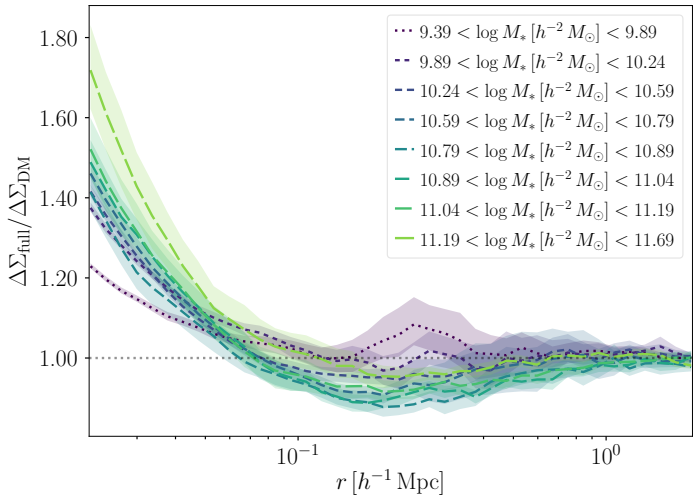

Figure 5.6: Same as in Fig. 5.5 but for TNG100. The stellar enhancement is not as pronounced as for Illustris and scatter from the satellite displacements produce enhancements for the low mass bins on intermediate radial scales.

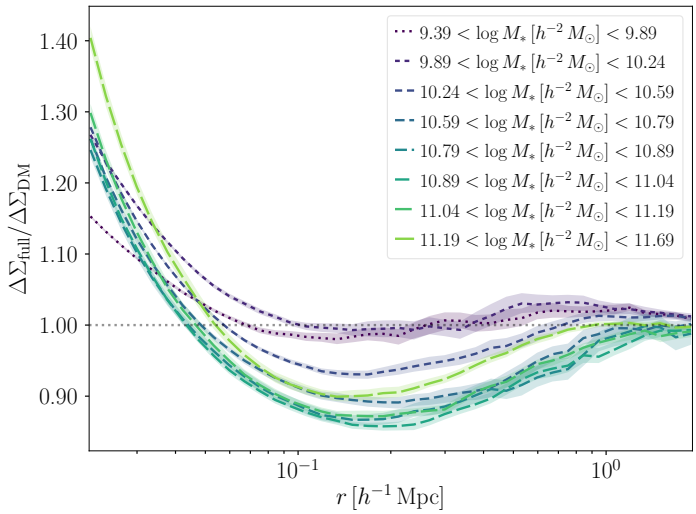

Figure 5.7: Similarly as Fig. 5.5 for TNG300. For the most massive bin, the TNG100 in Fig. 5.6 predicts a stronger stellar imprint, but otherwise there is little difference, except for the least massive bins where the intermediate scale boost in the signal is shifted to larger radii.

$M_*[\log_{10} M_\odot]$	$\bar{d}_{\rm I}^{\rm all}$	$\bar{d}_{\rm I\text{-}Dark}$	$\bar{d}_{\rm I}^{\rm matched}$	$\bar{d}_{\rm I\text{-}Dark}^{\rm matched}$	$M_{\rm 200c}^{\rm cen.,\ I}$	$M_{\rm 200c}^{\rm sat.,\ I}$	$M_{\rm 200c}^{\rm cen.,\ I\text{-}Dark}$	$M_{\rm 200c}^{\rm sat.,\ I\text{-}Dark}$	$N_{\rm gal}^{\rm I}$	$M_*^{\rm lim}[\log_{10} M_\odot]$
$10.3 - 10.6$	0.661	0.729	0.760	0.729	12.15	13.52	12.10	13.59	406 (282)	9.34
$10.6 - 10.9$	0.728	0.866	0.926	0.871	12.56	13.57	12.67	13.66	280 (186)	9.68
$10.9 - 11.2$	0.680	0.785	0.835	0.784	12.71	13.56	12.83	13.65	213 (148)	9.69
$11.2 - 11.5$	0.882	1.115	1.084	1.119	12.94	13.72	13.09	13.78	157 (130)	9.62
$11.5 - 11.8$	1.498	1.279	1.594	1.172	13.30	13.74	13.41	13.79	80 (78)	

Table 5.1: Host halo masses $M_{\rm 200c}$ for central and satellite galaxies in units of $h^{-1}\,M_\odot$ for the full physics runs and the gravity-only runs (dark), average 3D distance d between the satellite galaxies and the central galaxy in each FOF group in units of $h^{-1}\,$Mpc and for matched subhaloes, number of objects $N_{\rm gal}$ for 30 pkpc stellar masses for Illustris with the corresponding gravity-only numbers in parentheses. In the last column, we list the limiting stellar masses from which we start counting group members.

$M_*[\log_{10} M_\odot]$	$\bar{d}_{\rm I}^{\rm all}$	$\bar{d}_{\rm I\text{-}Dark}$	$\bar{d}_{\rm I}^{\rm matched}$	$\bar{d}_{\rm I\text{-}Dark}^{\rm matched}$	$M_{\rm 200c}^{\rm cen.,\ I}$	$M_{\rm 200c}^{\rm sat.,\ I}$	$M_{\rm 200c}^{\rm cen.,\ I\text{-}Dark}$	$M_{\rm 200c}^{\rm sat.,\ I\text{-}Dark}$	$N_{\rm gal}^{\rm I}$	$M_*^{\rm lim}[\log_{10} M_\odot]$
$10.3 - 10.6$	0.510	0.695	0.639	0.696	12.43	13.67	12.23	13.64	600 (365)	9.06
$10.6 - 10.9$	0.660	0.813	0.781	0.815	12.69	13.74	12.65	13.71	395 (284)	9.62
$10.9 - 11.2$	0.720	0.955	0.889	0.948	13.11	13.80	13.13	13.81	188 (137)	10.03
$11.2 - 11.5$	1.078	1.266	1.171	1.182	13.33	13.93	13.36	13.92	84 (75)	10.09
$11.5 - 11.8$	1.111	1.258	1.111	1.142	13.57	14.08	13.58	14.02	41 (41)	

Table 5.2: Same as in Table 5.1 but for the TNG100 simulation. Due to the increased efficiency of the new AGN feedback model to quench star formation, we end up with roughly half as many galaxies as Illustris at the massive end of the stellar mass function seen in the last rows.

centrals exceeding $r > 1\,h^{-1}\,$Mpc and also a radial shift in the low mass signal boost from $0.5\,h^{-1}\,$Mpc (joint) to $1 - 2\,h^{-1}\,$Mpc (central). At the high mass end there are only small changes since the signal is central-dominated. The radial shift also occurs for the TNG100, albeit from $0.2 - 0.3\,h^{-1}\,$Mpc to $1 - 2\,h^{-1}\,$Mpc, implying that low mass galaxies are slightly more clustered in the full physics runs. Here, we also observe that the suppression is wider for the centrals up to similar radial scales as TNG300, but also that the central enhancement is lowered by $3 - 4\,\%$ with respect to the joint signal for the intermediate stellar mass bins. To conclude, we also see the same trends for Illustris with a wider, smoother suppression beyond $r > 2\,h^{-1}\,$Mpc in Fig. 5.5 where the depth of the suppression is governed by the stellar mass, and correspondingly the average host halo mass, of the bin.

5.6.2 KiDS+GAMA: Lensing signals for group membership

Having investigated a stellar mass only selection, we now move on the lensing signals for members in galaxy groups for the Velliscig et al. (2017) comparison. We do not show results for the Eagle simulation as they were already published in Velliscig et al. (2017), and we are able to reproduce their results by projecting the entire simulation particle volume across the three spatial axes, whereas they restricted their analysis to particles in a projected sphere around each lens. Hence, the line-of-sight contribution is not significant, unless percent-level precision is required.

In Tables 5.1, 5.2 and 5.3 we list the host halo masses, limiting M_* values for group membership and average 3D distances between the satellite galaxies and their centrals in the full physics run. Compared to the full physics run, we end up with fewer subhaloes in the dark matter only run, starting with $50\,\%$ to $\sim 2/3$ of the number counts, which gradually increases to an almost $100\,\%$ matching rate for the most massive stellar mass bin. We note

$M_*[\log_{10} M_\odot]$	$\bar{d}_{\rm I}^{\rm all}$	$\bar{d}_{\rm I\text{-}Dark}$	$\bar{d}_{\rm I}^{\rm matched}$	$\bar{d}_{\rm I\text{-}Dark}^{\rm matched}$	$M_{\rm 200c}^{\rm cen.,\,I}$	$M_{\rm 200c}^{\rm sat.,\,I}$	$M_{\rm 200c}^{\rm cen.,\,I\text{-}Dark}$	$M_{\rm 200c}^{\rm sat.,\,I\text{-}Dark}$	$N_{\rm gal}^{\rm I}$	$M_*^{\rm lim}[\log_{10} M_\odot]$
$10.3 - 10.6$	0.541	0.726	0.657	0.725	12.20	13.78	12.06	13.78	15875 (9205)	9.04
$10.6 - 10.9$	0.577	0.798	0.735	0.798	12.57	13.86	12.57	13.85	14064 (8306)	9.60
$10.9 - 11.2$	0.545	0.857	0.805	0.854	12.86	13.93	12.91	13.92	8970 (4767)	9.77
$11.2 - 11.5$	0.749	1.207	1.112	1.195	13.29	14.10	13.32	14.03	2368 (1713)	10.32
$11.5 - 11.8$	1.131	2.242	1.562	2.073	13.69	14.30	13.70	14.26	786 (731)	

Table 5.3: Analogously as Table 5.1 for the TNG300 simulation with the resolution correction of Pillepich et al. (2018b). Compared to the less voluminous TNG100, central galaxies tend to live in less massive host haloes by about $0.1 - 0.2$ dex for the least massive bins, whereas satellites reside in more massive haloes with $0.1 - 0.2$ dex. For the two lowest mass bins, the limiting stellar masses are comparable but they differ for the two subsequent ones.

that the matching rate for the TNG300 is artificially low at the high mass end due to the resolution correction which renders less massive galaxies more massive, and that the numbers are more consistent with the TNG100 if we switch to the bound mass definition. Concerning halo masses, central $M_{\rm 200c}$ in the least massive stellar mass bin for all simulations are lower in the gravity-only run, but this does not pertain in the more massive bins, where there are only small differences between the gravity-only and full physics $M_{\rm 200c}$ masses. For Illustris, reflecting the large scale mass convergence in Fig. 5.5, the average full physics host halo masses are lower by ~ 0.1 dex compared to the gravity-only run.

Regarding the average 3D distances between the satellites and their centrals, the TNG100 and TNG300 do not paint a consistent picture with differences which could be as large as $0.3\,h^{-1}$ Mpc for the $11.2 < \log M_* \,[M_\odot] < 11.5$ mass bin. In Illustris and TNG100 (as well as in Eagle not listed here), there is a clear trend where more massive satellites reside further away from their centrals, where we instead note a dip for the $10.9 < \log M_* \,[M_\odot] < 11.2$ mass bin for the TNG300 with the resolution correction (for bound masses it has the same behaviour as the others, although there are still residual differences w.r.t. TNG100). In the third column, we list the distances in the gravity-only run for all satellite subhaloes, and in column five we restrict the selection to the matched subhaloes which are satellites in both runs. There are no major differences between them, except that distances are slightly greater for the most massive bin if we consider all dark objects. Compared to their matched counterparts in the full physics run, the dark satellites reside further away from their centrals, and the matched subhaloes in the full physics run are on average further away than the satellites selected without matching conditions. This makes sense as satellites close to their host centrals are more likely to be disrupted. Baryons affect the orbital structure of haloes significantly (e.g. Valluri et al., 2010; Zhu et al., 2017), and subhaloes are more likely to be disrupted if they have a high number of pericentric passages (e.g. Nadler et al., 2018). Compared to gravity-only runs, full physics simulations predict fewer surviving low-mass substructures (e.g. Wetzel et al., 2016; Zhu et al., 2016; Garrison-Kimmel et al., 2017) due to, for instance, increased tidal disruption and reionization, but here we consider subhaloes which are still present in the full physics run, and since the matching is not complete due to mergers we end up with fewer matched systems in the gravity-only run. The central distances for the matched subhaloes agree reasonably well between the two runs, allowing us to probe baryonic effects also for the satellite lensing signal, but this subsample is biased with respect to the full satellite sample.

We see in Fig. 5.8 that the innermost small-scale satellite signals for Illustris and IllustrisTNG agree between the whole full physics and matched full physics selections to $r \sim 40 - 50\,h^{-1}$ kpc where the convergence is attained to $r \sim 30 - 40\,h^{-1}$ kpc for the $10.3 <$

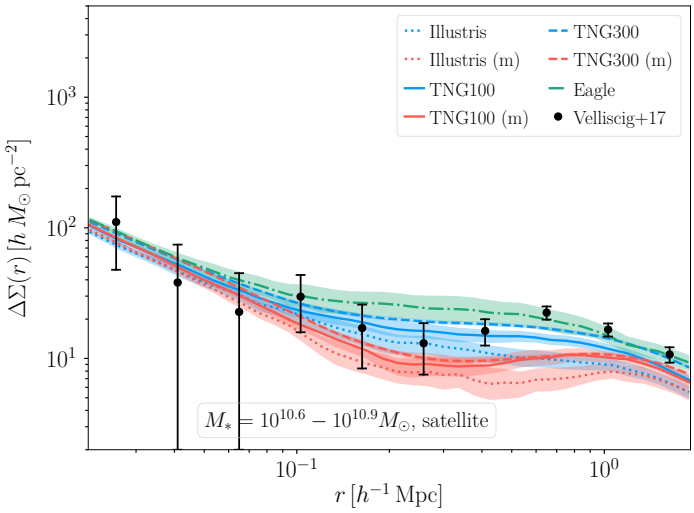

Figure 5.8: Comparison of lensing predictions from the different hydrodynamical simulations and the Velliscig et al. (2017) measurements for the satellite lensing signal for $10.6 < \log M_* \, [M_\odot] < 10.9$ using bound masses. We note significant departures between the matched and total full physics signals in the amplitude and location of the central bump. All of the simulations converge to a similar solution in the centre, but the Illustris and TNG100 simulations have the best performance in the region between the centre and the central bump, where Eagle is the only simulation to accurately capture the amplitude.

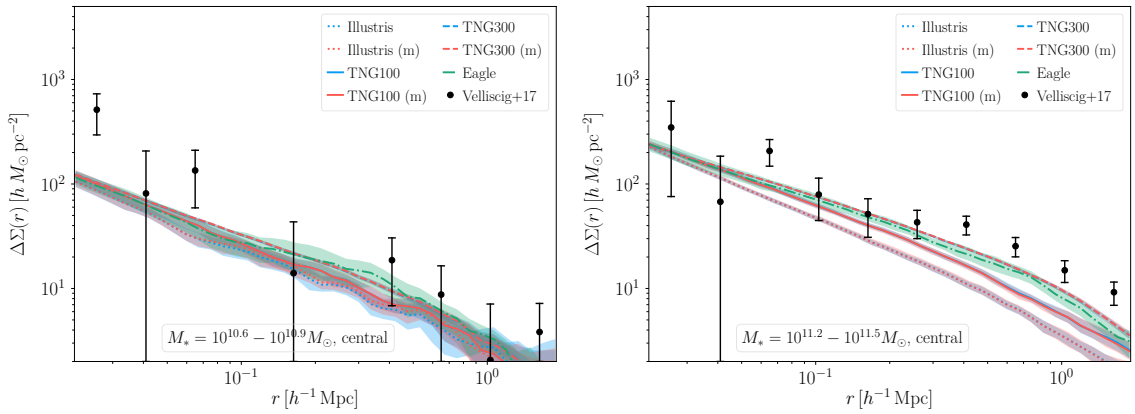

Figure 5.9: Lensing predictions for the different simulations compared to observations from Velliscig et al. (2017) for central galaxies with $10.6 < \log M_* \, [M_\odot] < 10.9$ using the bound mass definition. All simulations give comparable results. In panel II we show the same for stellar masses in the $11.2 < \log M_* \, [M_\odot] < 11.5$ mass range. Across the radial range covered, the TNG100 and TNG300 give different results with amplitude differences of the same order of magnitude as between TNG100 and Illustris which have different galaxy formation models. These differences are slightly alleviated in Fig. 5.10 where we show the predictions after the resolution correction, where we now have excellent agreements for this mass end (there are still residual differences for other mass bins).

$\log M_* [M_\odot] < 10.6$ mass bin and exceeds slightly beyond $100\,h^{-1}\,\mathrm{kpc}$ for $M_* > 10^{11.2}\,M_\odot$. The divergence is caused by the relative displacement of the whole full physics sample of satellites, where the central bump is further away for the matched subsample, but also that the amplitude is higher reflecting a higher host M_{200c} in the full physics run. This is expected as subhaloes in more massive hosts are more likely to have merged, thus reducing the average host halo masses in the matched signal. Mass convergence is once again reached at $r \sim 1 - 2\,h^{-1}\,\mathrm{Mpc}$ for Illustris and slightly larger projected radii for TNG100 and yet further out for TNG300. Although we have not fitted NFW profiles, we can see that the satellite lensing signal is more concentrated than the corresponding central signal, reflecting previous results (e.g. Moliné et al., 2017) for the concentration-mass relation for subhaloes. Deviations from NFW profiles due to tidal stripping are yet too small to be detected observationally (e.g. Sifón et al., 2018). Still, this is not easily discerned in Fig. 5.10 due to the impact of baryons with the contraction due to presence of the stellar term. As the satellite subhaloes are relatively less massive, the central baryonic enhancement continues to larger radii. Concerning the amplitude of the the central bump it is best captured by Eagle, followed closely by the TNG300, where an even better concordance can be seen in Fig. 5.10 for the resolution-corrected TNG300 signal with 30 pkpc aperture masses.

In Fig. 5.9, we compare the predictions for centrals for two stellar mass bins between the different hydro-runs, where the lower mass bin results in panel I extends to the least massive bin, and the more massive bin in panel II for stellar masses $M_* > 10^{10.9}\,M_\odot$. Illustris displays some scatter between the full physics and matched full physics signals in panel I for the bootstrap resample, but otherwise the two signals agree for all simulations due to the high matching rates for centrals. This bodes well for a unified parameterisation for central galaxies. At the low stellar mass end, the models predict different host halo masses but the error bars are large enough so that all of them are consistent with data. Similarly as seen for the van Uitert et al. (2016) comparison previously, the Illustris predict too low signals across the whole stellar mass range (more easily distinguished in Fig. 5.10), whereas Eagle and the TNG300, and partly TNG100, give consistent results with one another. The deficiency at the high mass end for $M_* > 10^{11.2}\,M_\odot$ on scales $r \gtrsim 0.4\,h^{-1}\,\mathrm{Mpc}$ visible in panel II of Fig. 5.9 can partly be reconciled by switching to 30 pkpc masses for the TNG100 and TNG300, but it still persists as seen in the panels of Fig. 5.10 with the central signals. As it is robust to volume variations, this suggests that the average halo masses for the simulations at the high mass end should be higher. If we compare the host halo masses to those predicted by SAMs, which are consistent with the observations in this radial range as explored previously in Chapter 4, the masses for IllustrisTNG are too low by about $0.2 - 0.3\,\mathrm{dex}$ for the $11.2 < \log M_* [M_\odot] < 11.5$ mass bin and by about $0.3 - 0.4\,\mathrm{dex}$ for the $11.5 < \log M_* [M_\odot] < 11.8$ bin. We do not see this discrepancy for the stellar mass only selection for the van Uitert et al. (2016) datasets as those samples also have the central bump from the satellite lensing signals offsetting the joint signal in this mass range, which we can observe in predictions for the joint central-satellite signal from the TNG300 in Fig. 5.10.

To ease the comparisons between Illustris, TNG100 and TNG300, we show the stacked predictions for all mass bins in Fig. 5.10. With the resolution correction, we obtain a better agreement between the different TNG volumes for the central signal, large scale satellite signal around $r \sim 1\,h^{-1}\,\mathrm{Mpc}$ and the joint signal. Especially we recognise a very good agreement for the TNG300 predictions for the large scale satellite signal for all stellar masses, which propagates into concordance for the joint signal in the last column. As expected the statistical errors are comparable for Illustris and TNG100, whereas the TNG300 curves are smoother

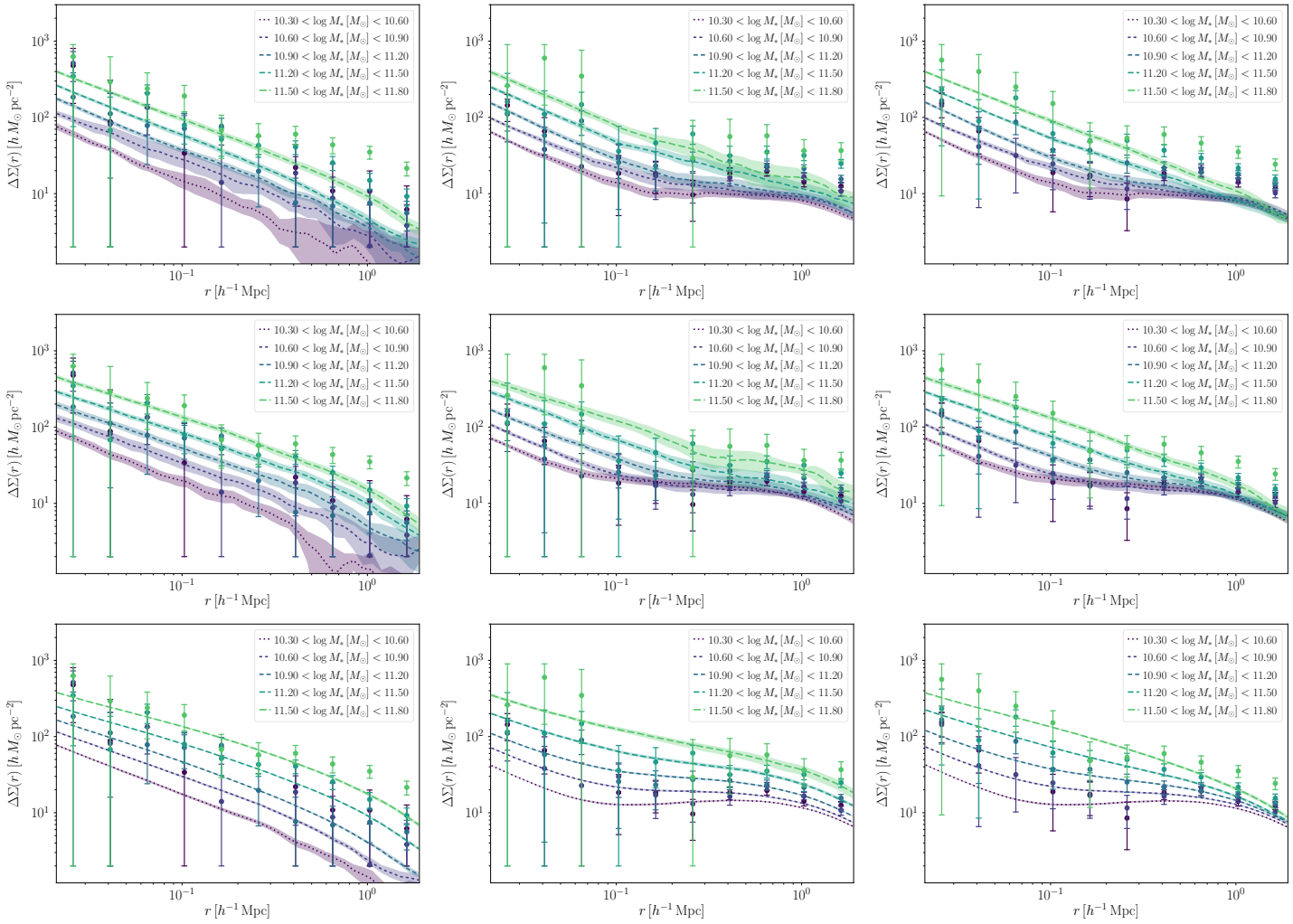

Figure 5.10: Predicted lensing signals for 30 pkpc aperture masses from Illustris (first row), TNG100 (middle row) and TNG300 (last row) compared to observations for galaxy group members from Velliscig et al. (2017) for centrals (first column), satellites (middle column) and the joint combined signal (last column).

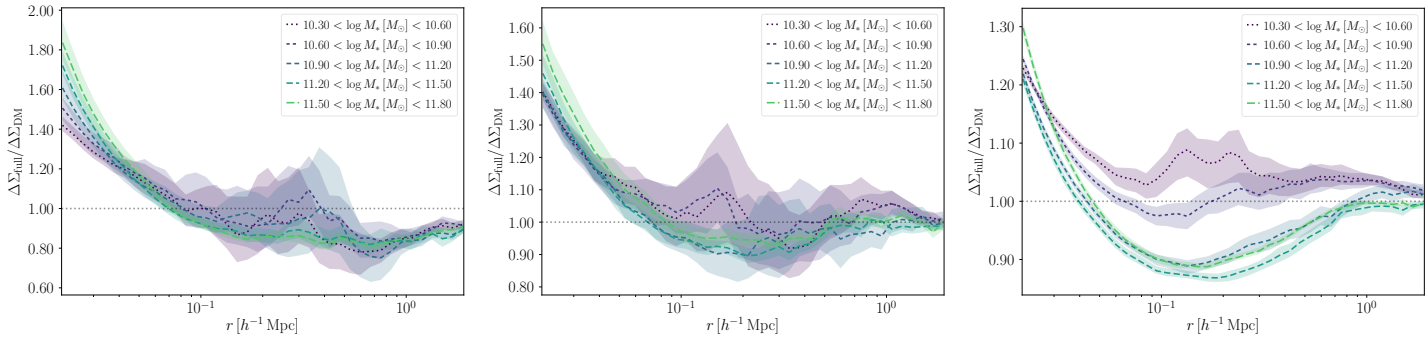

Figure 5.11: The effect of baryons on matched subhaloes in the joint signal from Velliscig et al. (2017) for Illustris (left), TNG100 (middle) and TNG300 (right) with 30 pkpc stellar masses. Although we are more likely to retain central galaxies as matches, the three lowest bins are dominated by satellites which causes a large spread in the effect due to the mismatched positions in the two runs.

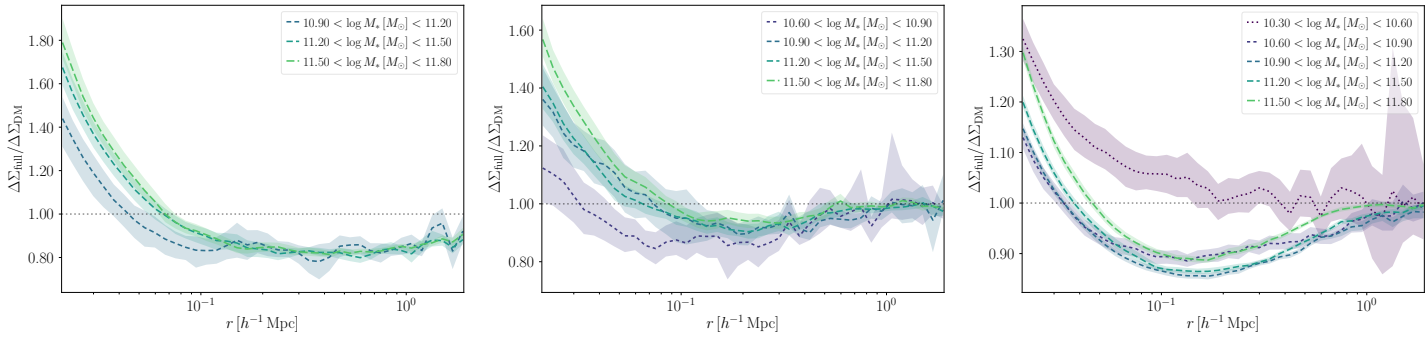

Figure 5.12: Baryonic effects on the central galaxy signals for the Velliscig et al. (2017) comparison for Illustris (left), TNG100 (middle) and TNG300 (right). Here the scatter in the 1-halo to 2-halo transition regime is substantial for the least massive bins for Illustris and TNG100 and thus they are not shown.

due to larger volume. As already apparent in Fig. 5.8, there are only small differences between the Illustris and TNG100 for the small-scale satellite lensing signal. We attribute the drop for $M_* < 10^{11.2}\,M_\odot$ for the TNG300 in Fig. 5.10 to a miss-calibration of the resolution correction as all simulations are consistent in Fig. 5.8, including Eagle. The biggest improvement can be distinguished for the central signal and the central bump for the satellite signal for the TNG100 with respect to Illustris, reflecting the improved recipe for the radio-mode AGN feedback, yielding a higher stellar-to-halo mass ratio for the centrals and more satellites in massive hosts.

For the baryonic deformations, we show the impact on the matched joint signal in Fig. 5.11 and for matched centrals in Fig. 5.12. The residuals for the low mass centrals in Illustris and TNG100 diverge in the 1-halo to 2-halo transition regime due to poor statistics and presence of more massive structures which can cause negative lensing signals and this limits the comparison to the more massive bins. This divergence partly manifests itself in the low mass central residuals for the TNG300 given in panel III of Fig. 5.12 which have a drastically different form than the curves for the other mass bins, but the results for this stellar mass bin also suffers from the resolution correction. If we compute the same quantity for the bound masses, the scatter in the transition regime subsides slightly and the model predicts a mild

suppression of the lensing signal to $60\,h^{-1}\,\mathrm{kpc}$.

Comparing the imprint for the joint signal in Fig. 5.11 and Figs. 5.5, 5.6 and 5.7, there is now a larger scatter from $0.1\,h^{-1}\,\mathrm{Mpc}$ owing to the large satellite fractions of the group samples, which still persist once the matching rate has been taken into account. From $M_* > 10^{10.9}\,M_\odot$ onwards the result is similar for the two selection functions. The peaks of the scatter for the low mass bins lie slightly closer to the halo centres for TNG100 and TNG300 compared to Illustris, reflecting the larger average distances between the satellites and their centrals listed in Tables 5.1, 5.2 and 5.3. Analogously as for the whole sample, Illustris predicts the largest central enhancement and this also applies for the central signals in Fig. 5.12, whereas the TNG300 has the smallest due to the prevalence of more massive host haloes. Similarly as seen in Figs. 5.6 and 5.7 for the TNG100 and TNG300, as we also spot here for central Illustris galaxies in Fig. 5.12, there is a trend with smaller suppressions for low mass centrals, with maximum suppression for the $10.9 < \log M_*\,[M_\odot] < 11.2$ mass bin for TNG300 (and Illustris due to the plotting constraint) and for $10.6 < \log M_*\,[M_\odot] < 10.9$ and then subsequently less suppression towards the massive end of the SMF. We attribute this effect to the AGN feedback being most efficient at deforming haloes at this intermediate mass range of $M_{200\mathrm{c}} \sim 10^{13}\,h^{-1}\,M_\odot$. This is also visible for the large scale deformation in panel III for the TNG300 where the mass suppression continues beyond $r \sim 2\,h^{-1}\,\mathrm{Mpc}$ for the $10.6 < \log M_*\,[M_\odot] < 10.9$ mass bin and where convergence already comes around $r \sim 1\,h^{-1}\,\mathrm{Mpc}$ for the $11.5 < \log M_*\,[M_\odot] < 11.8$ bin. For the TNG100, convergence is attained around $r \sim 1\,h^{-1}\,\mathrm{Mpc}$ for all mass bins and the maximum suppression lies around $5-10\,\%$ for the most massive bins. As we have already seen, the suppression is greater in the TNG300, reaching approximately $\sim 15\,\%$ at its maximum, and for Illustris around $\sim 20\,\%$ continuing past $r > 2\,h^{-1}\,\mathrm{Mpc}$.

5.6.3 Red and blue lenses

If we examine the lensing signals for red and blue galaxies using the TNG300 in Fig. 5.13 compared to observations from SDSS-DR7, we see that simulation manages to capture the most massive red lensing signal and predicts an excessive blue signal for the most massive bin, which we attribute to poor statistics. In general, the simulation produces excessive central bumps for the satellite signals visible around $r \sim 0.7\,h^{-1}\,\mathrm{Mpc}$. In the two lower panels, we restrict the comparisons to centrals and show the baryonic imprint for the two samples. We discover that the suppression for red centrals is larger than for blue centrals, which have more pronounced stellar terms. By fitting NFW profiles (Navarro et al., 1996, 1997) to the lensing signal (Wright & Brainerd, 2000) for $0.1 < r\,[h^{-1}\,\mathrm{Mpc}] < 1.0$ for centrals in the $10.7 < \log M_*\,[M_\odot] < 11.0$ mass bin, we are able to translate this difference into a bias in the observed host halo bimodality. Using observationally motivated $1/r^2$ weights and assuming a lens redshift of $z = 0.11$, we find the best-fit parameter values in Table 5.4. Baryons cause a shift of almost 0.1 dex in the best fit host halo mass for the red sample, and while we still observe a host halo bimodality with red galaxies residing in more massive haloes by a factor of ~ 1.40, it is reduced by $\sim 25\,\%$ from the gravity-only run where the red-to-blue mass ratio is ~ 1.64. For the fitted masses for red galaxies, the suppression is $\sim 15\,\%$ for $10.4 < \log M_*\,[M_\odot] < 11.4$, after which the effect decreases and vanishes for the most massive centrals with $11.6 < \log M_*\,[M_\odot] < 15.0$. Baryonic effects also influence the measured concentrations c, with a shift of $\Delta c \sim 1$ for red systems with $10.7 < \log M_*\,[M_\odot] < 11.6$, whereas there are only small differences for blue galaxies with decreases of the order of

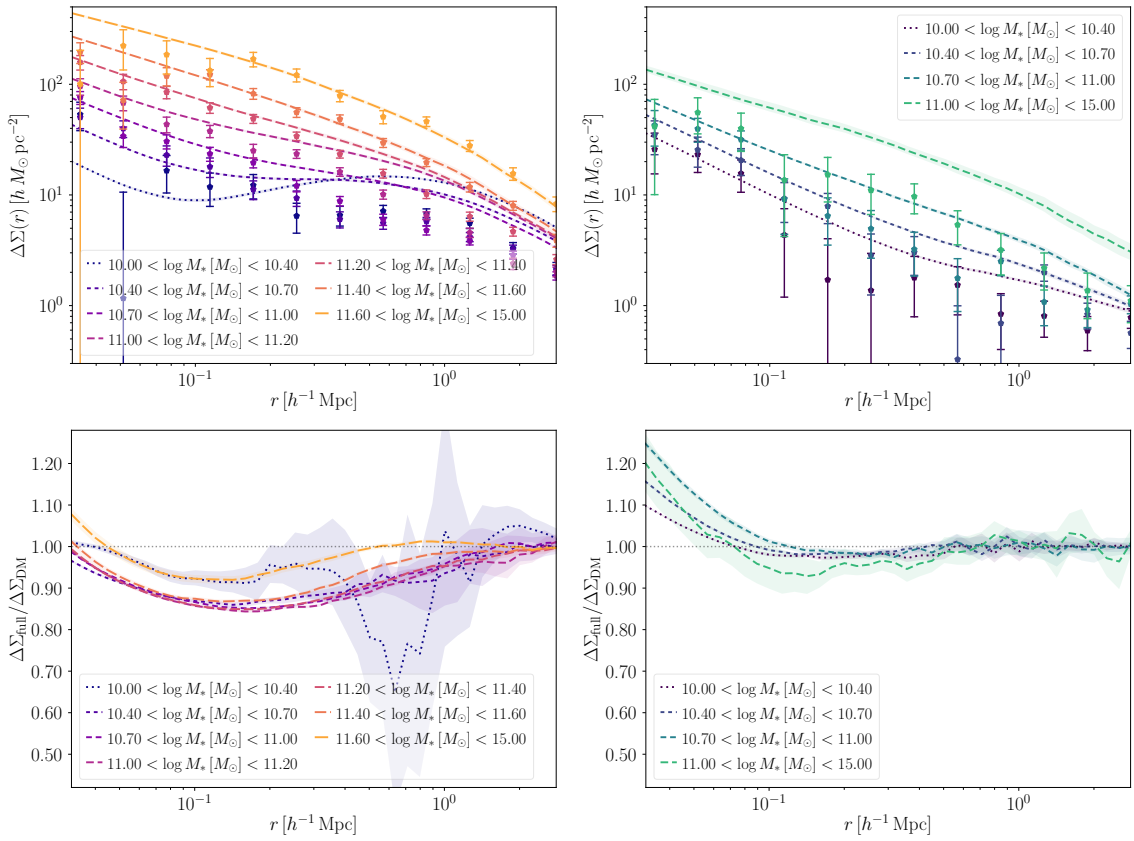

Figure 5.13: The predicted lensing signals from the TNG300 for red (first column) and blue galaxies (second column) at $z = 0$ compared to measurements from SDSS-DR7 for the all main sample using a ${}^{0.1}(g-r) = 0.8$ colour cut with the dust extinction model from Nelson et al. (2018b). We realise that the impact of baryons, given in the bottom row panels, is different for red and blue central galaxies where the lowest $10.0 < \log M_* < 10.4$ mass bin for red centrals comes with a large scatter due to the large spread in host halo masses.

Fitted parameter	Full physics	Gravity-only
$\log M_{200c}\,[h^{-1}\,M_\odot]$ (red)	12.30	12.37
$\log M_{200c}\,[h^{-1}\,M_\odot]$ (blue)	12.15	12.16
Concentration (red)	5.76	6.95
Concentration (blue)	6.21	6.11

Table 5.4: Fitted NFW parameters for central red and blue galaxies with $10.7 < \log M_* \,[M_\odot] < 11.0$ compared to their matches in the dark matter-only run of the TNG300.

$\Delta c \sim 0.3 - 0.4$. In Table 5.4, the host haloes are actually less concentrated in the gravity-only run but we consider this a coincidence additionally susceptible to the reassignment of stellar masses from the Pillepich et al. (2018b) resolution correction, where effects are prominent at the knee of the stellar mass function. The observed decrease in concentration in the full physics run conforms to previous findings in the literature for 3D density profiles (e.g. Duffy et al., 2010; Mummery et al., 2017). For this mass range, red central galaxies in the baryonic run reside in less concentrated host haloes in the full physics run than blue galaxies, but these correspond to more concentrated haloes in the dark matter only run. It is well-known that concentration correlates with formation time (e.g. Navarro et al., 1997; Gao & White, 2007), with older haloes on average being more concentrated which would host older[3] galaxies which on average are redder. However, in the full physics run, feedback processes, whose effects appear to be irreversible (e.g. Zhu et al., 2017), have had more time to change the appearance of these older haloes, thus lowering their concentrations with respect to the subhaloes hosting younger blue systems.

5.6.4 Quantified baryonic impact

We plot $f_{\rm bgas}$ vs. M_{500c} in Fig. 5.14 for TNG300 to arrive at the best fits for Eq. (5.4.7) for the bound gas fractions. Similar to other hydrodynamical simulations (e.g. Horizon-AGN Chisari et al., 2018), the gas fractions inside r_{500c} are generally too high w.r.t X-ray observations. However, if one introduces a hydrostatic mass bias to account for non-thermal pressure components violating the assumption of hydrostatic equilibrium, observational halo masses could be biased high by about $\sim 10\,\%$ (Eckert et al., 2018; Ettori et al., 2018). Moreover, lensing mass estimates indicate up to $\sim 40\,\%$ lower masses (Lieu et al., 2016), albeit subject to large errors. Hence, the discrepancy between the best fit models and the fiducial ST15 model should be taken with a grain of salt. We use the simulation best fit parameters subsequently in the analysis.

In Figs. 5.15 and 5.16 we compare the predicted gas fractions from the BCM model with those measured for stacked halo profiles from TNG300. The models are able to capture the overall shape of the gas fractions but have difficulties to match the inner slope and position of the turnover point, switching to the ejected gas profile. With respect to the power spectrum measurements, these profiles indicate only a mild evolution of η with redshift for TNG300. These profiles are in tension with the measurements presented in Battaglia et al. (2013) which were used for comparisons in Schneider & Teyssier (2015). If we increase the radius from which

[3]Colour can of course also be influenced by metallicity, as stars with higher metallicities are redder (e.g. Mo et al., 2010).

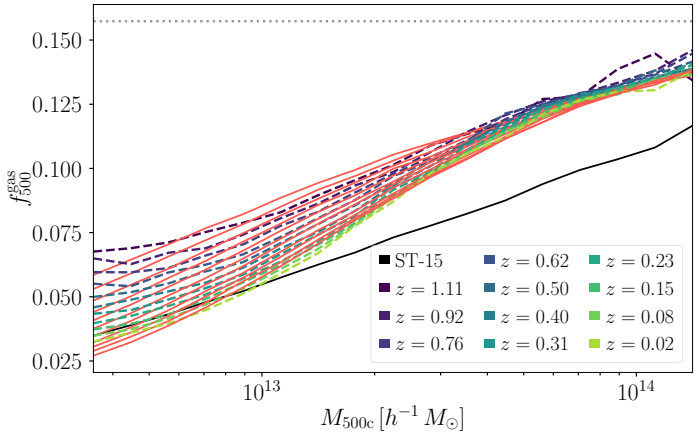

Figure 5.14: Gas fractions inside r_{500c} vs. M_{500c} for TNG300 for stacked systems in 0.1 dex bins for a range of redshifts with the best fit models of Eq. (5.4.7) plotted on top compared to the fiducial ST15 model in black fitted to observations. The best fit pairs (M_c, β) have a linear redshift evolution (for M_c linear in $\log M$) spanning approximately $\beta \in [0.65, 0.95]$ and $\log M_c \in [13.1, 13.4]$ for M_{200c} masses with decreasing redshift.

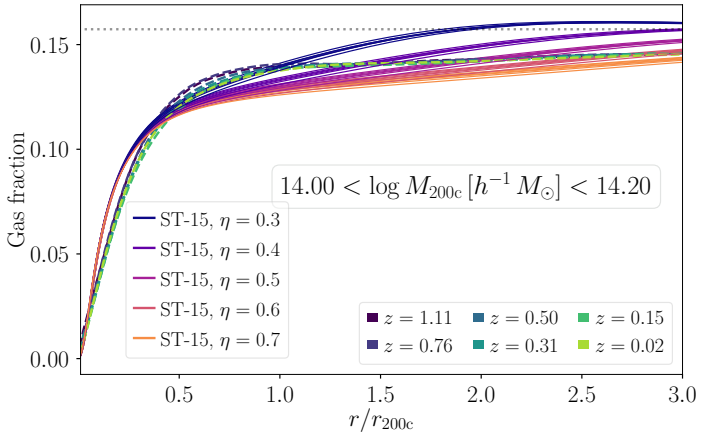

Figure 5.15: Gas fractions (including wind cells) for stacked TNG300 haloes with $10^{14} < M_{200c}\left[h^{-1}\,M_\odot\right] < 10^{14.2}$ for a range of redshifts compared to the BCM model with different η parameters with the cosmic baryon fraction as a dotted line. The slight redshift evolution is captured from the bound gas parameters β and M_c. At large scales $\sim 10\,r_{200c}$ we do not arrive at a convergence with the model since we measure an excess $0.5 - 0.6\,\%$ residual contribution from stars.

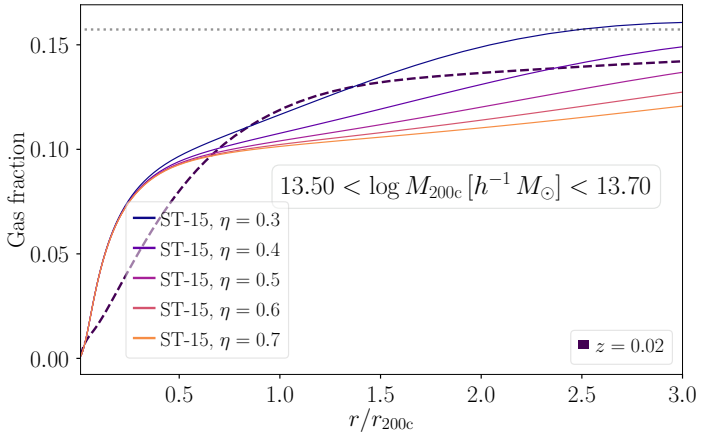

Figure 5.16: Gas fractions for stacked TNG300 haloes with $10^{13.5} < M_{200c}\,[h^{-1}\,M_\odot] < 10^{13.7}$ as in Fig. 5.15 at $z = 0.02$. While we are unable to obtain a good fit for the central region, $\eta = 0.3$ and $\eta = 0.4$ provide the best fits in the outskirts. The shape is generally more poorly captured than for galaxy clusters.

the bound gas profile starts to trace the NFW profile to $c/\sqrt{2}$ we obtain a better fit in the inner region below the turnover point but are unable to match the amplitude at the turnover point. In Fig. 5.16 we see that this problem extends and is aggravated in group scale systems. If we switch to the halo profiles themselves, in Figs. 5.17 and 5.18, for stacked cluster haloes at $z = 0.02$, we find that the dark matter component is well matched on intermediate scales but is too contracted in the centre and slightly too expanded in the halo outskirts. This excessive contraction is caused by the excessive stellar component in the centre. The underlying issue could be that galaxies in the TNG300 at the high mass end of the SMF form too few stars which was already established in Pillepich et al. (2018b). A better match on intermediate scales is obtained by fitting an Einasto profile to $r \sim 0.2\,h^{-1}\,\mathrm{Mpc}$ with best fit $\alpha \sim 0.2$ and from $r \sim 0.2\,h^{-1}\,\mathrm{Mpc}$ to $r \sim 1\,h^{-1}\,\mathrm{Mpc}$ with $\alpha \sim 0.08$ or with a simple power law $\sim r^{-2.6}$ for the whole range to $1\,h^{-1}\,\mathrm{Mpc}$. If we switch to the gas profiles, the amplitude is overpredicted to $\sim 0.2\,r_{200c}$ but the shapes are overall consistent with the measured values. As expected, the different η values only impact the outer gas profile from about $0.4\,r_{200c}$ with a mismatch in the amplitude between $1-2\,r_{200c}$ otherwise suggesting a low value $\eta = 0.3$ to be preferential. The situation is similar for group-scale systems although the gas profile excess up to $\sim 0.2\,r_{200c}$ is even larger implied by Fig. 5.16. If we consider the total density profile computed from Eq. (5.4.6) w.r.t. the full physics profile taking into account the Lagrangian displacements in Fig. 5.19, the small but crude model mismatches impedes a complete agreement with the fractional differences shown in the lower panel of Fig. 5.18. In the centre, both the stellar and DM components are too high, which leads to an excess of the order of $\sim 50\,\%$ compared to the mild suppression from using the gravity-only profiles as a model. We are able to attain a better agreement on scales $\sim 100\,h^{-1}\,\mathrm{kpc}$ and at the halo outskirts the gas and dark matter densities are too high w.r.t. the measurements leading to a worse agreement for all model η values. To conclude, the BCM model is capable to capture the overall trends in the differences between the profile components in the dark matter and full physics run, but refined recipes and fits are needed to obtain a better agreement at the profile level (it may already be sufficient for a power spectrum treatment) for the TNG suite. The fact that the

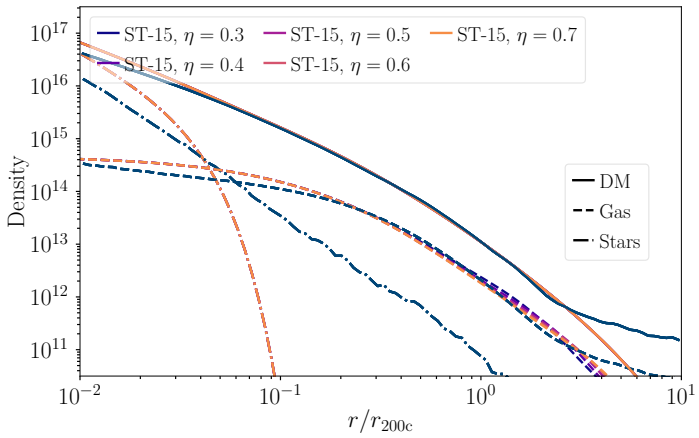

Figure 5.17: Comparisons between the component-wise TNG300 stacked full physics profiles for $10^{14.0} < M_{200c}\,[h^{-1}\,M_\odot] < 10^{14.2}$ haloes at $z = 0.02$ and the BCM model predictions. The stellar profile is not well matched, suggesting that an incorporation of the satellite contribution and ICL is necessary. From $r \sim r_{200c}$ the 2-halo term takes on, which we model with the fiducial $N-$body result.

impact of the different η choices linger to around $3 - 4\,r_{200c}$ might suggest that the model is more suitable for simulations with stronger AGN feedback for gas ejection such as Illustris as seen in Fig. 5.5.

5.6.5 Redshift evolution for mock clusters and groups

It is interesting to quantify the baryonic effects for clusters selected in upcoming deep surveys such as HSC and Euclid. Neglecting the details of the cluster finding algorithm and assuming that clusters can be reliably selected, we plot the redshift evolution of the baryonic imprint for FOF groups with $M_{200m} \geqslant 10^{14}\,h^{-1}\,M_\odot$ in Fig. 5.20 from $z = 1.1$ to today in the TNG300. At $z = 1.1$ 20 clusters initially satisfy the criteria, 96 at $z = 0.5$ and 252 at $z = 0.02$. The poor statistics at high redshift are reflected as oscillations in the signals in Figs. 5.20 and 5.22. The inner region is dominated by the stellar component, which as discerned in Fig. 5.21, is fairly constant with redshift whereas the dark matter and gas components of the signal grow. For a galaxy-galaxy lensing analysis at $z = 1.1$, failure to accurately model the stellar component excludes all radial bins below $100\,h^{-1}$ kpc, whereas this is only a problem below $50\,h^{-1}$ kpc at low redshift. At high redshift, there is almost no suppression of the baryonic profiles between $100\,h^{-1}$ kpc and $1\,h^{-1}$ Mpc. The gas component almost perfectly traces the dark matter part. If we compare the dark matter component in the full physics and dark matter only run, the haloes in the latter simulation are more massive and less concentrated as seen in Fig. 5.22. This is especially important at higher redshift.

We can perform the same analysis using group-scale lenses, seen in Figs. 5.23 and 5.24. Here we have better statistics with 205 groups passing the criteria at $z = 1.1$, 557 at $z = 0.5$ and 872 at $z = 0.02$. For the baryonic imprint, the contribution from the stellar component is not as prominent at high z as for the cluster lenses, $\sim 50\,\%$ instead of $\sim 100\,\%$, and the contribution almost vanishes at $z = 0.02$. Instead there is a smooth suppression of the profiles between $100\,h^{-1}$ kpc and $1\,h^{-1}$ Mpc at $z = 1.1$ and $\sim 30\,h^{-1}$ kpc and $1\,h^{-1}$ Mpc at $z = 0.02$, which gradually deepens at lower z. If one looks at the baryonic components, the stellar part is slightly larger at higher z and also the gas mass profiles in the inner regions with a

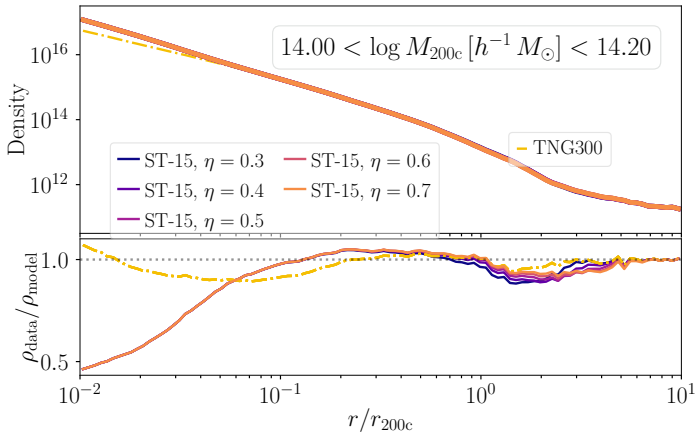

Figure 5.18: Comparisons between the TNG300 stacked full physics profiles and the BCM model predictions. The largest discrepancy lies in the central stellar term whereas the BCM model added to the gravity-only profiles according to Eq. (5.4.6) are able to yield an improved agreement on scales $\sim 100\,h^{-1}$ kpc with respect to the unmodified profiles (dot-dashed line). At the halo outskirts around the splashback radius, the gas component is generally too large with respect to the fiducial $N-$body results.

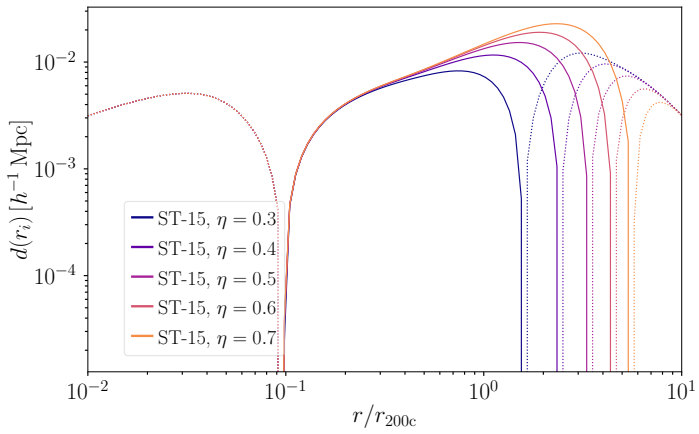

Figure 5.19: Lagrangian displacements between initial and final positions for stacked $10^{14.0} < M_{200c}\,[h^{-1}\,M_\odot] < 10^{14.2}$ haloes at $z = 0.02$ with dotted and solid lines indicating negative and positive displacements respectively. The higher the η, the greater the ejection radius $r_{\rm ej.}$ which we can see as a positive displacement extending to larger scales.

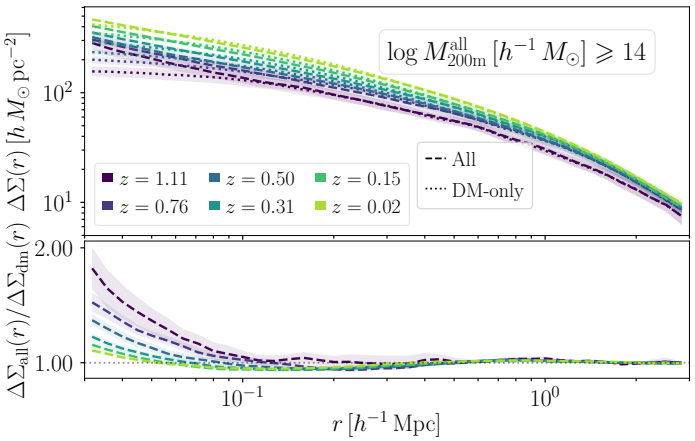

Figure 5.20: Baryonic effects on galaxy cluster profiles from $z = 1.1$ to $z = 0.02$. The relative enhancement in the inner region of the baryonic profiles ('all'), as seen in the lower panel, decreases at lower redshift due to the growth of the dark matter component. There is a slight enhancement at $r = 1\,h^{-1}\,{\rm Mpc}$ which starts at $\sim 500\,h^{-1}\,{\rm kpc}$ for the baryonic profiles due to the ejection of gas which is more pronounced at higher redshift due to the shallower potential wells.

transition point at $100\,h^{-1}\,{\rm kpc}$ from which on the lower z gas profiles are more massive to $1\,h^{-1}\,{\rm Mpc}$. This trend is not present for clusters in Fig. 5.21. The transition scale at which the gas component starts to constitute more of the total signal than the stellar component is roughly the same for clusters and massive groups at $\sim 200\,h^{-1}\,{\rm kpc}$.

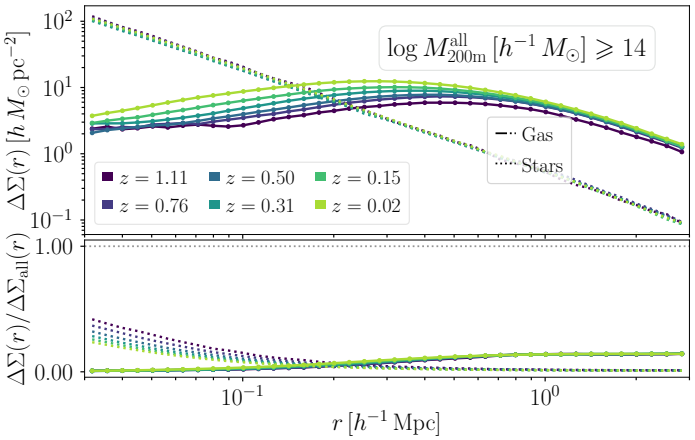

Figure 5.21: Redshift evolution of the gas and stellar components of the $\Delta\Sigma$ profiles, with respect to the dark matter component (lower panel). The gas profiles grow with decreasing redshift, but their contribution to the overall signal remains constant due to the simultaneous growth of the dark matter component.

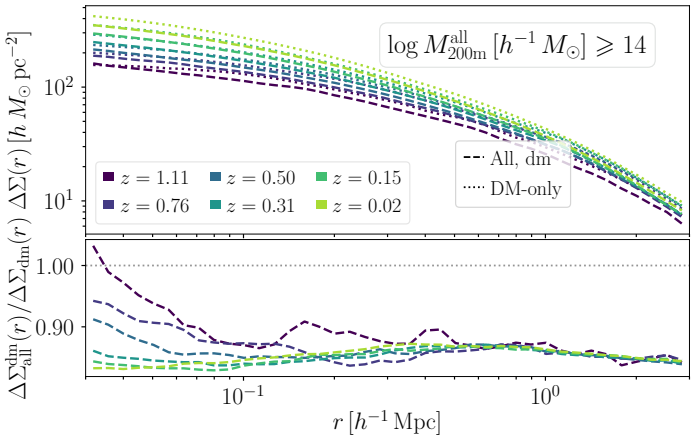

Figure 5.22: Comparison between the dark matter components in the full physics and dark matter only runs. The dark matter only signal is roughly 1.2 times higher than the $\Delta\Sigma$ in the full physics run.

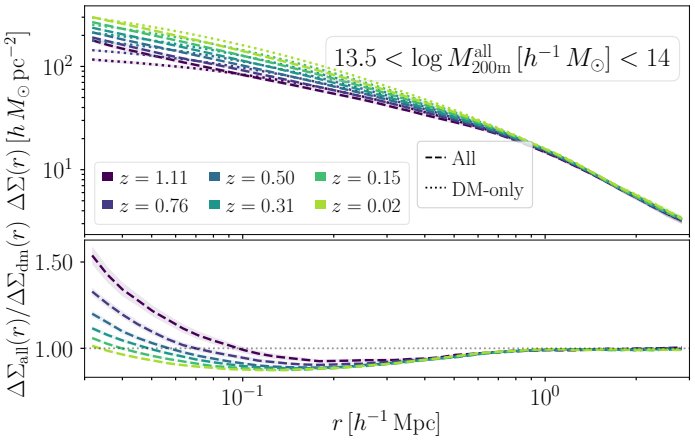

Figure 5.23: Baryonic effects on galaxy group profiles from $z = 1.1$ to $z = 0.02$. The relative enhancement in the inner region of the baryonic profiles ('all') is lower than for the cluster size lenses at high redshift seen in Fig. 5.20. There is also no enhancement at $r = 1\,h^{-1}\,{\rm Mpc}$ for the group lens profiles.

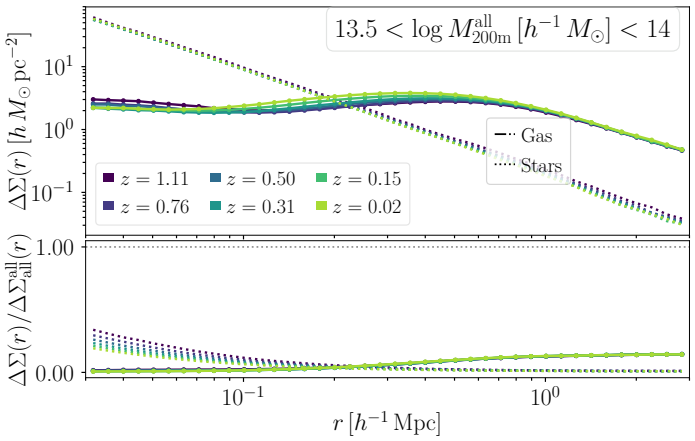

Figure 5.24: Redshift evolution of the gas and stellar components of the $\Delta\Sigma$ profiles for the group lenses w.r.t. the full signal. The relative enhancement in the inner region of the baryonic profiles ('all'), as seen in the lower panel, decreases at lower redshift due to the growth of the dark matter component. The gas profile reservoir in the inner region is slightly larger at higher redshifts which is gradually converted to stars.

5.7 Discussion

In this Chapter we have chiefly compared the baryonic imprint in the Illustris and IllustrisTNG simulations. We will shortly do the same for Eagle where most of the particle and halo catalogue data is public. Moreover, it would be interesting to extend the analysis to other hydrodynamical simulations such as MassiveBlack-II (Khandai et al., 2015) and Horizon-AGN (Dubois et al., 2014), as well as BAHAMAS (McCarthy et al., 2017) going down in resolution[4] for a comparable volume as the TNG300, for a comparable parameterisation framework as in Huang et al. (2018).

We have seen that baryonic effects can suppress the lensing profiles by as much as 20 % for certain stellar mass ranges in the Illustris simulation and mass convergences at $r \sim 5\,h^{-1}\,\mathrm{Mpc}$. This agrees with previous results using the same simulation for a BOSS CMASS emulated sample with matched number densities published by Leauthaud et al. (2017). Compared to the impact on the matter power spectra in Springel et al. (2018), the suppression deformations of the lensing profiles are slightly smaller with $10-15\,\%$ instead of 20 %, proving that these are not comparable probes.

Regarding the parameterisation, we find that the gas profiles from the TNG300 differ from those published in Battaglia et al. (2013), which can partly explain the mismatch of the ST15 model. Further developments should focus on characterising the stellar term as well as the radial scale of the gas ejection, which is too large for the TNG suite.

5.8 Conclusions

We have measured and characterised the imprint of baryonic physics on galaxy-galaxy lensing profiles, and found suppressions on the small-scale signal at $r \sim 0.1\,h^{-1}\,\mathrm{Mpc}$ of the maximum order of $\sim 20\,\%$ (Illustris) and $10-15\,\%$ (IllustrisTNG). Eagle, TNG100 and TNG300 are all able to produce accurate profiles in the observational comparisons, although the red satellite lensing signal for the TNG300 is alleviated. The maximum radial scale of the suppression also varies between the different simulations, up to maximally $r \sim 5-6\,h^{-1}\,\mathrm{Mpc}$ for the Illustris simulation, largely independent of stellar mass. Future surveys should use these scales as conservative limits.

In addition, we find differences in the baryonic suppressions between red and blue galaxies, reflecting the fact that feedback processes have had more time to shape the host haloes of the former. This discrepancy has implications for the mass, as well as the concentration, measurements of the host haloes. Further studies are required to quantify how different feedback processes sets the scale of the suppression of the bimodality.

While the ST15 model represents a step in the right direction towards artificial baryonic modifications, it is not sophisticated enough to capture the features of group and cluster scale systems in the TNG300 between $z = 1.1$ and $z = 0$.

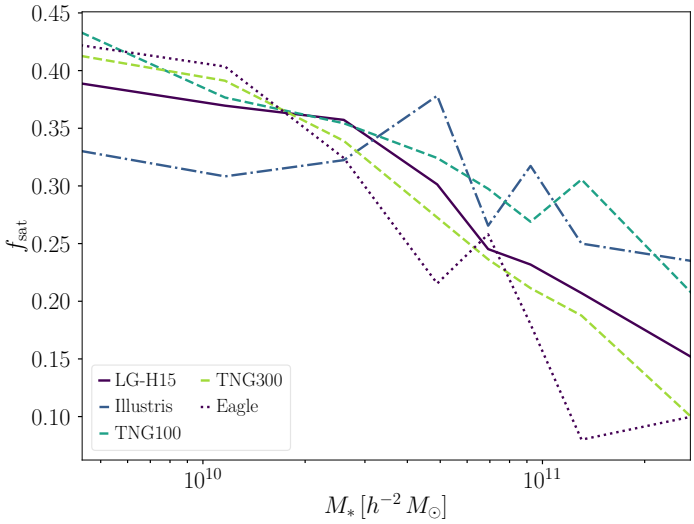

Figure 5.25: Satellite fractions for the different hydrodynamical simulations for the bound mass definition. With respect to Fig. 5.2 for the 30 pkpc apertures, the results for the TNG100 and TNG300 simulations agree better with this mass definition.

$M_*[\log_{10} M_\odot]$	$\bar{d}_{\rm Eagle}$	$M_{\rm 200c}^{\rm cen.,\,E}$	$M_{\rm 200c}^{\rm sat.,\,E}$	$N_{\rm gal}^{\rm E}$	$M_*^{\rm lim,\,E}[\log_{10} M_\odot]$
$10.3 - 10.6$	0.593	12.43	13.79	352	9.60
$10.6 - 10.9$	0.818	12.98	13.95	146	10.03
$10.9 - 11.2$	0.813	13.37	14.11	36	10.40
$11.2 - 11.5$	1.505	13.85	14.04	22	10.48
$11.5 - 11.8$	-	14.10	-	4	-

Table 5.5: Average 3D distance between the satellite galaxies and the central galaxy in each FOF group in units of h^{-1} Mpc for 30 pkpc stellar masses for Eagle.

5.9 30 pkpc lensing predictions for Eagle

In this Chapter, we have found that the lensing predictions differ slightly depending on the stellar mass definition used. This also affects the satellite fractions, where we plot the corresponding satellite fractions in Fig. 5.25. Here the predictions for the TNG100 and the TNG300 agree at the low mass end, but for higher stellar masses the TNG300 gives relatively fewer satellites due to the prevalence of more massive host haloes and the deficiency in star formation produces fewer massive satellites. The result for Eagle is smoother than for the 30 pkpc mass definition beyond the knee of the SMF, reflecting a healthier model.

We present the lensing predictions for the 30 pkpc mass definition for Eagle in Fig. 5.26, corresponding to the same choice as for Illustris, TNG100 and TNG300 already shown in Section 5.6.1. For $M_* > 10^{10.79}\,h^{-2}\,M_\odot$, the curves start to deviate from the observational data points with particularly excessive signals for the three most massive stellar mass bins. These large differences persist if we switch to the group lens sample. We give the most general statistics in Table 5.5 for the host halo masses, central distances and limiting stellar masses for

[4]In BAHAMAS the softening length $\epsilon = 4\,h^{-1}$ kpc in physical coordinates for $z \leqslant 3$ and is fixed in comoving coordinates at higher redshifts for a comoving box length $L = 400\,h^{-1}$ Mpc following cosmo-OWLS (Le Brun et al., 2014).

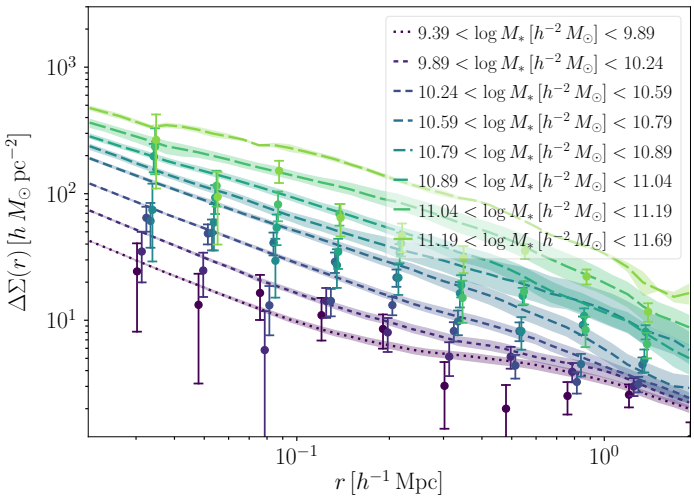

Figure 5.26: Lensing predictions from the Eagle simulation with 30 pkpc aperture stellar masses. Compared to the bound mass result, the predictions for $M_* > 10^{10.79}\,h^{-2}\,M_\odot$ are elevated and do not conform to the observational data points.

the group criteria. Compared to the TNG100 values listed in Table 5.2, the host halo masses for the centrals for the two most massive bins are elevated with 0.5 dex and the number of galaxies have dropped by a factor of four for the three most massive bins.

Chapter 6 Summary and outlook

In this thesis we have investigated various aspects of the modelling of small-scale galaxy-galaxy lensing. We have increased the complexity from gravity-only simulations of dark matter, with focus on host haloes, to include realistic galaxy populations from semi-analytical models of galaxy formation (SAMs) for the N-body simulations to finally compare these results to cosmological simulations using full hydrodynamical schemes. In addition, we have probed the effects from very small dwarf galaxies to galaxy cluster size objects, over a range of redshifts to match mock observations for future lensing surveys, giving our results a large dynamic range. In this Chapter we summarise and provide an outlook on how the main results in this thesis can be extended into future projects.

6.1 One simulation to fit them all

In Chapter 3 we found that the rescaled lensing and 3D density profiles could well approximate the results in direct simulations with biases which we can quantify with the semi-analytical fitting formulae from Ludlow et al. (2016) and Diemer et al. (2017). The correlations between these biases offer an intriguing setup to potentially explore the 1-halo to 2-halo transition region, which is notoriously difficult to treat analytically, through characterisations of the deeply nonlinear regime. Moreover, these relations can be used as further constraints in the optimisation of the rescaling parameters. Further studies should focus on treating the signal from satellite galaxies with the same success[1] and quantify errors for supplementary probes; such as galaxy clustering. In addition, parametrisable fits for new physics such as modified gravity signatures and massive neutrinos could extend the lifecycle for a given cosmological N-body simulation. Naturally this also applies for baryonic corrections, but here different hydrodynamical simulations should be used to probe the range of possible deformations given certain feedback implementations for realistic fits.

The results are also applicable for potential rescaling of the small-scale features of the next generation of N-body simulations with box lengths $L \sim 2\,h^{-1}$ Gpc and particle numbers $\sim 10^{12}$, which are currently in production.

6.2 The future for joint constraint analyses

In Chapter 4 we explored if SAMs and the IllustrisTNG suite were able to produce consistent lensing and clustering predictions with respect to observational constraints. This is a

[1] Still, the consistency between the stellar mass-only lensing profiles which features both central and satellite galaxies in the rescaled Millennium to a Planck 2014 cosmology and the gravity-only TNG100 using a Planck 2016 cosmology in Chapter 4 for the Henriques et al. (2015) SAM suggests that such examinations may prove superfluous.

crucial step for these models to be competitive frameworks to populate (sub)-haloes with galaxies for the cosmological parameter extraction from the next generation of large-scale structure surveys. As already highlighted, the increased modelling complexity pays off in the supplementary observables and correlations which are given simultaneously. We found that the IllustrisTNG produced excellent predictions for both probes, except for the intermediate mass red lensing signal. This was traced back to galaxies residing in unmatched subhaloes preferentially in massive hosts. In the SAMs, the same effect was found for the lensing of (red) orphan galaxies in massive hosts and if we switched to a higher resolution simulation, the trend was still there for the corresponding satellite galaxies. For the integrated HODs from Zu & Mandelbaum (2016), this problem did not arise. It would be interesting to extend this analysis to the other HOD models mentioned in Section 2.1, as well as SHAMs, to see if this is a generic feature of empirical modelling.

We rephrased this discrepancy as a shift in the host halo mass distributions for satellite galaxies in the SAMs compared to the stellar-mass only HOD curves in Zu & Mandelbaum (2015). This points towards necessary modifications of environmental quenching mechanisms in massive hosts to remove these problematic satellites, or to boost the populations in less massive hosts, in both physical modelling frameworks. Recently it was pointed out (Bahé et al., 2019) that complete galaxy disruption in massive groups is rare and that it is probably mostly due to gravitational forces and not baryonic processes, which could play a role for the similarity of the results in the different simulations.

Moreover, the accuracy in predicting the red galaxy clustering signal was significantly affected by the dust model and resolution correction enforced. We investigated the dust correction explicitly for the latest Munich SAM and found impacts of the order of $\sim 40\,\%$ for the red clustering signal, which acts to serve as a cautionary tale that its constraining power requires further studies.

Returning to the lensing predictions, the latest Munich SAM from Henriques et al. (2015) required further tuning in order to be consistent with SDSS LBG lensing and stellar mass only lensing from KiDS+GAMA, as well as general galaxy clustering observations from SDSS. This motivated a decrease in the strength of the radio-mode AGN feedback as well as a shorter merger time for the orphan galaxies. Differences in the clustering signal of massive galaxies pointed to the AGN feedback implementation as the main cause, since the supernovae feedback affect centrals as well as satellites whereas the AGN feedback mostly affects centrals. Using a complementary group lensing dataset from KiDS+GAMA, we verified that the found new parameters also produce satisfactory lensing predictions for central galaxies superior to the fiducial results. In addition, they retained the excellent agreement with the stellar mass function up to redshift $z = 3$. This nice property ensures that the new improved model is suitable for modelling group and cluster lensing profiles for future deep surveys such as HSC and LSST. However, the agreement for the matched fraction satellite lensing signal was compromised, especially above $M_* > 10^{10.9}\,M_\odot$ where the host halo masses were too low. This also points towards the need for a more careful treatment of the satellites, with a potentially stronger dependency on the host halo mass in setting the merger time clock.

Overall, both the IllustrisTNG and L-Galaxies can predict the lensing and clustering signals sufficiently well for them to be used, potentially in combination with HODs, in cosmological parameter analyses pipelines.

6.3 On the effects of baryons

In Chapter 5, we examined the deformations of lensing mass profiles due to the presence of baryons in the Illustris and IllustrisTNG suites. This is still an open area of research and the results should be complemented by measurements in additional hydrodynamical simulations to cover a wider range of feedback prescriptions. For current cosmological analyses, which use large-scale galaxy-galaxy lensing, the most interesting area is the suppressions in the 1-halo to 2-halo transition regime due to AGN feedback for groups and clusters. Here, Illustris and IllustrisTNG gave different answers on how a conservative sample selection has to be designed to mitigate the effect of baryons. In the TNG suite, removing scales below $r \sim 1-2\,h^{-1}\,\mathrm{Mpc}$ was sufficient to obtain accurate mass profiles, whereas the suppression extended to $r \sim 5-6\,h^{-1}\,\mathrm{Mpc}$ in the fiducial Illustris simulation. A way to move forward would be to include different parameterised baryonic fitting formulae, such as modified versions of the BCM from Schneider & Teyssier (2015), and different radial cuts to explore the impact on the constraints of the cosmological parameters. Since the overall lensing predictions are more consistent with observations in the TNG suite than in Illustris, it is probable that $r \sim 1-2\,h^{-1}\,\mathrm{Mpc}$ is a more realistic extent, but there might be an additional covert host halo mass dependency included. Hence, caution must be taken and complementary measurements from e.g. Eagle are advisable. However, the BCM also preferred a similar extent as Illustris, stressing the urgent need for a better connection between AGN activity and particle ejection.

On smaller scales, the fitting formula preferred a more prominent stellar term than what the TNG300 suggested. This could partly be related to the deficiency in star formation in this simulation highlighted in Pillepich et al. (2018b). Still, for halo mass measurements with down-weighted inner radial bins which is the standard case in GGL, this deficiency should be of limited importance.

We also found that baryonic imprint is different for red and blue galaxies, and the implications for halo and galaxy assembly bias (see e.g. Zentner et al., 2014) signatures should be studied further. It would be interesting to use other large hydrodynamical simulations such as cosmo-OWLs (Le Brun et al., 2014) and BAHAMAS (McCarthy et al., 2017) to probe the effects where one has different physics implementations, although extra consideration must be devoted to resolution convergence.

In conclusion, this study has opened the door to many interesting future endeavours which will enrich the field in the years to come.

Bibliography

Abadi M. G., Navarro J. F., Fardal M., Babul A., Steinmetz M., 2010, MNRAS, 407, 435

Abazajian K. N., et al., 2009, ApJS, 182, 543

Abbott T. M. C., et al., 2017a, preprint, p. arXiv:1708.01530 (arXiv:1708.01530)

Abbott B. P., et al., 2017b, Nature, 551, 85

Abbott T. M. C., et al., 2018, preprint, p. arXiv:1801.03181 (arXiv:1801.03181)

Adhikari S., Dalal N., Chamberlain R. T., 2014, JCAP, 11, 019

Agertz O., et al., 2007, MNRAS, 380, 963

Aihara H., et al., 2018, Publications of the Astronomical Society of Japan, 70, S4

Amendola L., et al., 2013, Living Reviews in Relativity, 16

Anderson M. E., Gaspari M., White S. D. M., Wang W., Dai X., 2015, MNRAS, 449, 3806

Angulo R. E., Hilbert S., 2015, MNRAS, 448, 364

Angulo R. E., White S. D., 2010, MNRAS, 405, 143

Angulo R. E., Springel V., White S. D. M., Jenkins A., Baugh C. M., Frenk C. S., 2012, MNRAS, 426, 2046

Applegate D. E., et al., 2016, MNRAS, 457, 1522

Artale M. C., et al., 2017, MNRAS, 470, 1771

Bacon D. J., Refregier A. R., Ellis R. S., 2000, MNRAS, 318, 625

Bagla J. S., 2005, Current Science, 88, 1088

Bahé Y. M., et al., 2019, arXiv e-prints, p. arXiv:1901.03336

Baldauf T., 2018, Advanced Cosmology Statistics, Non-Gaussianity and Non-Linearity, http://www.damtp.cam.ac.uk/user/tb561/AdvCosmo/

Baldauf T., Smith R. E., Seljak U., Mandelbaum R., 2010, Phys. Rev. D., D81, 063531

Baltz E. A., Marshall P., Oguri M., 2009, JCAP, 1, 15

Bardeen J. M., Bond J. R., Kaiser N., Szalay A. S., 1986, ApJ, 304, 15

Barnes J., Hut P., 1986, Nature, 324, 446

Bartelmann M., Schneider P., 2001, Phys.Rep., 340, 291

Battaglia N., Bond J. R., Pfrommer C., Sievers J. L., 2013, ApJ, 777, 123

Bauer A., Springel V., 2012, MNRAS, 423, 2558

Baugh C. M., Gardner J. P., Frenk C. S., Sharples R. M., 1996, MNRAS, 283, L15

Baumann D., 2018, Cosmology, http://cosmology.amsterdam/education/cosmology/

Baxter E., et al., 2017, ApJ, 841, 18

Becker M. R., Kravtsov A. V., 2011, ApJ, 740, 25

Behroozi P. S., Conroy C., Wechsler R. H., 2010, ApJ, 717, 379

Behroozi P. S., Wechsler R. H., Wu H.-Y., 2013a, ApJ, 762, 109

Behroozi P. S., Wechsler R. H., Conroy C., 2013b, ApJ, 770, 57

Behroozi P., Wechsler R., Hearin A., Conroy C., 2018, arXiv e-prints, p. arXiv:1806.07893

Bekki K., 2013, MNRAS, 432, 2298
Benson A. J., 2010, Physics Reports, 495, 33
Berger M. J., Colella P., 1989, Journal of Computational Physics, 82, 64
Berlind A. A., Weinberg D. H., 2002, ApJ, 575, 587
Bertschinger E., 1998, Annual Review of Astronomy and Astrophysics, 36, 599
Bett P., Eke V., Frenk C. S., Jenkins A., Helly J., Navarro J., 2007, MNRAS, 376, 215
Binney J., Tremaine S., 1987, Galactic dynamics. Princeton University Press, Princeton, NJ
Birnboim Y., Dekel A., 2003, MNRAS, 345, 349
Blandford R., Narayan R., 1986, ApJ, 310, 568
Blanton M. R., Roweis S., 2007, The Astronomical Journal, 133, 734
Blazek J., Mandelbaum R., Seljak U., Nakajima R., 2012, Journal of Cosmology and Astro-Particle Physics, 2012, 041
Blumenthal G. R., Faber S. M., Primack J. R., Rees M. J., 1984, Nature, 311, 517
Blumenthal G. R., Faber S. M., Flores R., Primack J. R., 1986, ApJ, 301, 27
Bocquet S., Saro A., Dolag K., Mohr J. J., 2016, MNRAS, 456, 2361
Bond J. R., Myers S. T., 1996, The Astrophysical Journal Supplement Series, 103, 1
Bond J. R., Cole S., Efstathiou G., Kaiser N., 1991, ApJ, 379, 440
Bonvin V., et al., 2017, MNRAS, 465, 4914
Booth C. M., Schaye J., 2009, MNRAS, 398, 53
Bower R. G., Benson A. J., Malbon R., Helly J. C., Frenk C. S., Baugh C. M., Cole S., Lacey C. G., 2006, MNRAS, 370, 645
Boylan-Kolchin M., Ma C.-P., Quataert E., 2008, MNRAS, 383, 93
Boylan-Kolchin M., et al., 2009, MNRAS, 398, 1150
Brainerd T. G., Blandford R. D., Smail I., 1996, ApJ, 466, 623
Bruzual G., Charlot S., 2003, MNRAS, 344, 1000
Bryan G. L., Norman M. L., 1998, ApJ, 495, 80
Bullock J. S., Boylan-Kolchin M., 2017, Annual Review of Astronomy and Astrophysics, 55, 343
Bullock J. S., Kravtsov A. V., Weinberg D. H., 2000, ApJ, 539, 517
Busch P., White S. D. M., 2017, MNRAS, 470, 4767
Castorina E., Paranjape A., Hahn O., Sheth R. K., 2016, preprint, (arXiv:1611.03619)
Cen R., Ostriker J., 1992, ApJ, 393, 22
Chang C., DES Collaboration 2018, ApJ, 864, 83
Chang C., et al., 2013, MNRAS, 428, 2695
Chisari N. E., Mandelbaum R., Strauss M. A., Huff E. M., Bahcall N. A., 2014, MNRAS, 445, 726
Chisari N. E., et al., 2018, MNRAS, 480, 3962
Chua K. E., Pillepich A., Vogelsberger M., Hernquist L., 2018, arXiv e-prints, p. arXiv:1809.07255
Cole S., Lacey C., 1996, MNRAS, 281, 716
Cole S., Aragon-Salamanca A., Frenk C. S., Navarro J. F., Zepf S. E., 1994, MNRAS, 271, 781
Colless M., et al., 2001, MNRAS, 328, 1039
Conroy C., Wechsler R. H., 2009, ApJ, 696, 620
Conroy C., Wechsler R. H., Kravtsov A. V., 2006, ApJ, 647, 201
Cooray A., Sheth R., 2002, Physics Reports, 372, 1
Correa C. A., Wyithe J. S. B., Schaye J., Duffy A. R., 2015, MNRAS, 452, 1217
Crain R. A., et al., 2015, MNRAS, 450, 1937
Croton D. J., et al., 2006, MNRAS, 365, 11

D'Souza R., Vegetti S., Kauffmann G., 2015, MNRAS, 454, 4027
Davis M., Peebles P. J. E., 1983, ApJ, 267, 465
Davis M., Efstathiou G., Frenk C. S., White S. D. M., 1985, ApJ, 292, 371
De Lucia G., Blaizot J., 2007, MNRAS, 375, 2
De Lucia G., Boylan-Kolchin M., Benson A. J., Fontanot F., Monaco P., 2010, MNRAS, 406, 1533
Dekel A., Silk J., 1986, ApJ, 303, 39
Desjacques V., Jeong D., Schmidt F., 2018, Phys. Rept., 733, 1
Despali G., Vegetti S., 2017, MNRAS, 469, 1997
Di Matteo T., Springel V., Hernquist L., 2005, Nature, 433, 604
Diemer B., 2017, ApJs, 231, 5
Diemer B., Kravtsov A. V., 2014, ApJ, 789, 1
Diemer B., Mansfield P., Kravtsov A. V., More S., 2017, ApJ, 843, 140
Dodelson S., 2003, Modern cosmology. Academic Press
Driver S. P., et al., 2011, MNRAS, 413, 971
Dubois Y., et al., 2014, MNRAS, 444, 1453
Duffy A. R., Schaye J., Kay S. T., Dalla Vecchia C., Battye R. A., Booth C. M., 2010, MNRAS, 405, 2161
Dutton A. A., et al., 2016, MNRAS, 461, 2658
Dvornik A., et al., 2017, MNRAS, 468, 3251
Dvornik A., et al., 2018, MNRAS, 479, 1240
Dyer C. C., Ip P. S. S., 1993, ApJ, 409, 60
Eckert D., et al., 2018, preprint, p. arXiv:1805.00034 (arXiv:1805.00034)
Efron B., 1979, Annals of Statistics, 7, 1
Efstathiou G., Eastwood J. W., 1981, MNRAS, 194, 503
Eifler T., Krause E., Dodelson S., Zentner A. R., Hearin A. P., Gnedin N. Y., 2015, MNRAS, 454, 2451
Einasto J., 1965, Trudy Astrofizicheskogo Instituta Alma-Ata, 5, 87
Einstein A., 1915, Sitzungsberichte der Königlich Preußischen Akademie der Wissenschaften (Berlin, pp 844–847
Eisenstein D. J., Hu W., 1998, ApJ, 496, 605
Eisenstein D. J., et al., 2005, ApJ, 633, 560
Ettori S., et al., 2018, preprint, p. arXiv:1805.00035 (arXiv:1805.00035)
Evrard A. E., 1988, MNRAS, 235, 911
Fabian A. C., 2012, Annual Review of Astronomy and Astrophysics, 50, 455
Feng Y., Chu M.-Y., Seljak U., McDonald P., 2016, MNRAS, 463, 2273
Fischer P., et al., 2000, Astronomical Journal, 120, 1198
Foreman S., Becker M. R., Wechsler R. H., 2016, MNRAS, 463, 3326
Frenk C. S., White S. D. M., 2012, Annalen der Physik, 524, 507
Friedrich O., DES Collaboration 2018, Phys. Rev. D, 98, 023508
Gabor J. M., Davé R., Oppenheimer B. D., Finlator K., 2011, MNRAS, 417, 2676
Gao L., White S. D. M., 2007, MNRAS, 377, L5
Gao L., De Lucia G., White S. D. M., Jenkins A., 2004, MNRAS, 352, L1
Gao L., Navarro J. F., Cole S., Frenk C. S., White S. D. M., Springel V., Jenkins A., Neto A. F., 2008, MNRAS, 387, 536
Garrison-Kimmel S., et al., 2017, MNRAS, 471, 1709
Genel S., et al., 2014, MNRAS, 445, 175

Ghigna S., Moore B., Governato F., Lake G., Quinn T., Stadel J., 1998, MNRAS, 300, 146
Ghigna S., Moore B., Governato F., Lake G., Quinn T., Stadel J., 2000, ApJ, 544, 616
Gillis B. R., et al., 2013, MNRAS, 431, 1439
Gingold R. A., Monaghan J. J., 1977, MNRAS, 181, 375
Gnedin O. Y., Kravtsov A. V., Klypin A. A., Nagai D., 2004, ApJ, 616, 16
Gordon Y. A., et al., 2018, MNRAS, 475, 4223
Greengard L., Rokhlin V., 1987, Journal of Computational Physics, 73, 325
Gruen D., DES Collaboration 2018, Phys. Rev. D, 98, 023507
Gruen D., et al., 2016, MNRAS, 455, 3367
Gunn J. E., Gott J. Richard I., 1972, ApJ, 176, 1
Guo Q., White S., Li C., Boylan-Kolchin M., 2010, MNRAS, 404, 1111
Guo Q., White S., Boylan-Kolchin M., De Lucia G., Kauffmann G., et al., 2011, MNRAS, 413, 101
Guo Q., White S., Angulo R. E., Henriques B., Lemson G., Boylan-Kolchin M., Thomas P., Short C., 2013a, MNRAS, 428, 1351
Guo Q., White S., Angulo R. E., Henriques B., Lemson G., Boylan-Kolchin M., Thomas P., Short C., 2013b, MNRAS, 428, 1351
Guo Q., et al., 2016, MNRAS, 461, 3457
Guzik J., Seljak U., 2001, MNRAS, 321, 439
Habib S., Morozov V., Frontiere N., Finkel H., Pope A., Heitmann K., 2013, in SC '13 Proceedings of SC13: International Conference for High Performance Computing. p. 6, doi:10.1145/2503210.2504566
Hahn O., Paranjape A., 2014, MNRAS, 438, 878
Hamilton A. J. S., 2001, MNRAS, 322, 419
Harnois-Déraps J., van Waerbeke L., Viola M., Heymans C., 2015, MNRAS, 450, 1212
Hayashi E., White S. D. M., 2008, MNRAS, 388, 2
Hearin A. P., Zentner A. R., van den Bosch F. C., Campbell D., Tollerud E., 2016, MNRAS, 460, 2552
Heitmann K., et al., 2008, Computational Science and Discovery, 1, 015003
Heitmann K., Lawrence E., Kwan J., Habib S., Higdon D., 2014, ApJ, 780, 111
Henriques B. M. B., Thomas P. A., Oliver S., Roseboom I., 2009, MNRAS, 396, 535
Henriques B. M. B., White S. D. M., Thomas P. A., Angulo R. E., Guo Q., Lemson G., Springel V., 2013, MNRAS, 431, 3373
Henriques B. M. B., White S. D. M., Thomas P. A., Angulo R., Guo Q., Lemson G., Springel V., Overzier R., 2015, MNRAS, 451, 2663
Henriques B. M. B., White S. D. M., Thomas P. A., Angulo R. E., Guo Q., Lemson G., Wang W., 2017, MNRAS, 469, 2626
Henson M. A., Barnes D. J., Kay S. T., McCarthy I. G., Schaye J., 2017, MNRAS, 465, 3361
Hernquist L., Katz N., 1989, The Astrophysical Journal Supplement Series, 70, 419
Hernquist L., Bouchet F. R., Suto Y., 1991, The Astrophysical Journal Supplement Series, 75, 231
Heymans C., 2015, Physics Online Journal, 8, 74
Heymans C., et al., 2012, MNRAS, 427, 146
Heymans C., et al., 2013, MNRAS, 432, 2433
Hikage C., et al., 2018, preprint, p. arXiv:1809.09148 (arXiv:1809.09148)
Hilbert S., White S. D. M., 2010, MNRAS, 404, 486
Hilbert S., Hartlap J., White S. D. M., Schneider P., 2009, A&A, 499, 31
Hildebrandt H., et al., 2017, MNRAS, 465, 1454
Hildebrandt H., et al., 2018, arXiv e-prints, p. arXiv:1812.06076

Hinshaw G., et al., 2013, ApJS, 208, 19
Hirata C. M., Seljak U., 2004, Physical Review D, 70, 063526
Hirata C. M., et al., 2004, MNRAS, 353, 529
Hirata C. M., Mandelbaum R., Ishak M., Seljak U., Nichol R., Pimbblet K. A., Ross N. P., Wake D., 2007, MNRAS, 381, 1197
Hockney R. W., Eastwood J. W., 1988, Computer simulation using particles. Taylor & Francis
Hoekstra H., Hartlap J., Hilbert S., van Uitert E., 2011, MNRAS, 412, 2095
Hopkins P. F., 2013, MNRAS, 428, 2840
Hopkins P. F., Richards G. T., Hernquist L., 2007, ApJ, 654, 731
Hopkins P. F., Quataert E., Murray N., 2012, MNRAS, 421, 3522
Hopkins P. F., Kereš D., Oñorbe J., Faucher-Giguère C.-A., Quataert E., Murray N., Bullock J. S., 2014, MNRAS, 445, 581
Hoyle B., et al., 2018, MNRAS, 478, 592
Huang H.-J., Eifler T., Mandelbaum R., Dodelson S., 2018, arXiv e-prints, p. arXiv:1809.01146
Ivezić Ž., et al., 2008, arXiv e-prints, p. arXiv:0805.2366
Jenkins A., et al., 1998, ApJ, 499, 20
Jiang F., van den Bosch F. C., 2016, MNRAS, 458, 2848
Jing Y. P., Suto Y., 2002, ApJ, 574, 538
Jing Y. P., Zhang P., Lin W. P., Gao L., Springel V., 2006, ApJ, 640, L119
Joudaki S., et al., 2018, MNRAS, 474, 4894
Kaiser N., Wilson G., Luppino G. A., 2000, preprint, pp astro–ph/0003338 (arXiv:astro-ph/0003338)
Kauffmann G., White S. D. M., Guiderdoni B., 1993, MNRAS, 264, 201
Kauffmann G., Colberg J. M., Diaferio A., White S. D. M., 1999, MNRAS, 303, 188
Kennicutt R. C., Evans N. J., 2012, Annual Review of Astronomy and Astrophysics, 50, 531
Kereš D., Katz N., Weinberg D. H., Davé R., 2005, MNRAS, 363, 2
Khandai N., Di Matteo T., Croft R., Wilkins S., Feng Y., Tucker E., DeGraf C., Liu M.-S., 2015, MNRAS, 450, 1349
Kilbinger M., 2015, Reports on Progress in Physics, 78, 086901
Kitching T. D., Verde L., Heavens A. F., Jimenez R., 2016, MNRAS, 459, 971
Klypin A., Gottlöber S., Kravtsov A. V., Khokhlov A. M., 1999, ApJ, 516, 530
Klypin A. A., Trujillo-Gomez S., Primack J., 2011, ApJ, 740, 102
Knebe A., Arnold B., Power C., Gibson B. K., 2008, MNRAS, 386, 1029
Knebe A., et al., 2011, MNRAS, 415, 2293
Knebe A., et al., 2013, MNRAS, 435, 1618
Knebe A., et al., 2015, MNRAS, 451, 4029
Komatsu E., Seljak U., 2001, MNRAS, 327, 1353
Komatsu E., et al., 2009, ApJs, 180, 330
Komatsu E., et al., 2011, ApJs, 192, 18
Kormendy J., Ho L. C., 2013, Annual Review of Astronomy and Astrophysics, 51, 511
Krause E., et al., 2017, arXiv e-prints, p. arXiv:1706.09359
Kravtsov A. V., Berlind A. A., Wechsler R. H., Klypin A. A., Gottlöber S., Allgood B., Primack J. R., 2004, ApJ, 609, 35
Kravtsov A. V., Vikhlinin A. A., Meshcheryakov A. V., 2018, Astronomy Letters, 44, 8
Kuhlen M., Vogelsberger M., Angulo R., 2012, Physics of the Dark Universe, 1, 50
Kuijken K., et al., 2015, MNRAS, 454, 3500

Lacey C., Cole S., 1993, MNRAS, 262, 627
Lahav O., Lilje P. B., Primack J. R., Rees M. J., 1991, MNRAS, 251, 128
Laureijs R., et al., 2011, preprint, (arXiv:1110.3193)
Lawrence E., et al., 2017, ApJ, 847, 50
Le Brun A. M. C., McCarthy I. G., Schaye J., Ponman T. J., 2014, MNRAS, 441, 1270
Leauthaud A., Tinker J., Behroozi P. S., Busha M. T., Wechsler R. H., 2011, ApJ, 738, 45
Leauthaud A., et al., 2012, ApJ, 744, 159
Leauthaud A., et al., 2017, MNRAS, 467, 3024
Lehmann B. V., Mao Y.-Y., Becker M. R., Skillman S. W., Wechsler R. H., 2017, ApJ, 834, 37
Lemson G., Virgo Consortium t., 2006, preprint, pp astro–ph/0608019 (arXiv:astro-ph/0608019)
Leonard C. D., Ferreira P. G., Heymans C., 2015, Journal of Cosmology and Astro-Particle Physics, 2015, 051
Lewis A., 2013, Phys. Rev. D., 87, 103529
Lewis A., Bridle S., 2002, Phys. Rev. D., 66, 103511
Lewis A., Challinor A., Lasenby A., 2000, ApJ, 538, 473
Li C., White S. D. M., 2009, MNRAS, 398, 2177
Lieu M., et al., 2016, A&A, 592, A4
Lim E. A., 2012, Advanced Cosmology : Primordial non-Gaussianities, http://www.damtp.cam.ac.uk/user/eal40/AdvCos/lecture2.pdf
Limber D. N., 1953, ApJ, 117, 134
Liske J., et al., 2015, MNRAS, 452, 2087
Lovell M. R., Frenk C. S., Eke V. R., Jenkins A., Gao L., Theuns T., 2014, MNRAS, 439, 300
Lovell M. R., et al., 2018, MNRAS, 481, 1950
Lucy L. B., 1977, The Astronomical Journal, 82, 1013
Ludlow A. D., Angulo R. E., 2017, MNRAS, 465, L84
Ludlow A. D., Porciani C., 2011, MNRAS, 413, 1961
Ludlow A. D., Navarro J. F., Li M., Angulo R. E., Boylan-Kolchin M., Bett P. E., 2012, MNRAS, 427, 1322
Ludlow A. D., Navarro J. F., Angulo R. E., Boylan-Kolchin M., Springel V., Frenk C., White S. D. M., 2014, MNRAS, 441, 378
Ludlow A. D., Bose S., Angulo R. E., Wang L., Hellwing W. A., Navarro J. F., Cole S., Frenk C. S., 2016, MNRAS, 460, 1214
Macciò A. V., Dutton A. A., van den Bosch F. C., Moore B., Potter D., Stadel J., 2007, MNRAS, 378, 55
Mandelbaum R., 2018, Annual Review of Astronomy and Astrophysics, 56, 393
Mandelbaum R., et al., 2005, MNRAS, 361, 1287
Mandelbaum R., Slosar A., Baldauf T., Seljak U., Hirata C. M., Nakajima R., Reyes R., Smith R. E., 2013, MNRAS, 432, 1544
Mandelbaum R., Wang W., Zu Y., White S., Henriques B., More S., 2016, MNRAS, 457, 3200
Mandelbaum R., et al., 2018a, Publications of the Astronomical Society of Japan, 70, S25
Mandelbaum R., et al., 2018b, MNRAS, 481, 3170
Mansfield P., Kravtsov A. V., Diemer B., 2017, ApJ, 841, 34
Marian L., Smith R. E., Angulo R. E., 2015, MNRAS, 451, 1418
Marinacci F., et al., 2018, MNRAS, 480, 5113
Martin C. L., 1999, ApJ, 513, 156
Martizzi D., Teyssier R., Moore B., 2013, MNRAS, 432, 1947

Matthee J., Schaye J., Crain R. A., Schaller M., Bower R., Theuns T., 2017, MNRAS, 465, 2381
McAlpine S., et al., 2016, Astronomy and Computing, 15, 72
McCarthy I. G., et al., 2010, MNRAS, 406, 822
McCarthy I. G., Schaye J., Bird S., Le Brun A. M. C., 2017, MNRAS, 465, 2936
McConnell N. J., Ma C.-P., 2013, ApJ, 764, 184
Mead A. J., Peacock J. A., 2014a, MNRAS, 440, 1233
Mead A. J., Peacock J. A., 2014b, MNRAS, 445, 3453
Mead A. J., Peacock J. A., Heymans C., Joudaki S., Heavens A. F., 2015, MNRAS, 454, 1958
Mead A. J., Heymans C., Lombriser L., Peacock J. A., Steele O. I., Winther H. A., 2016, MNRAS, 459, 1468
Miralda-Escudé J., 1991, ApJ, 370, 1
Mitchell P. D., et al., 2018, MNRAS, 474, 492
Mo H. J., White S. D. M., 1996, MNRAS, 282, 347
Mo H., van den Bosch F. C., White S., 2010, Galaxy Formation and Evolution. Cambridge University Press
Mohammed I., Gnedin N. Y., 2018, ApJ, 863, 173
Mohammed I., Martizzi D., Teyssier R., Amara A., 2014, preprint, p. arXiv:1410.6826 (arXiv:1410.6826)
Moliné Á., Sánchez-Conde M. A., Palomares-Ruiz S., Prada F., 2017, MNRAS, 466, 4974
Monaghan J. J., 1992, Annual Review of Astronomy and Astrophysics, 30, 543
Moore B., Lake G., Katz N., 1998, ApJ, 495, 139
More S., Diemer B., Kravtsov A. V., 2015, ApJ, 810, 36
More S., et al., 2016, ApJ, 825, 39
Moster B. P., Somerville R. S., Maulbetsch C., van den Bosch F. C., Macciò A. V., Naab T., Oser L., 2010, ApJ, 710, 903
Moster B. P., Naab T., White S. D. M., 2013, MNRAS, 428, 3121
Moster B. P., Naab T., White S. D. M., 2018, MNRAS, 477, 1822
Mukhanov V. F., Chibisov G. V., 1981, Soviet Journal of Experimental and Theoretical Physics Letters, 33, 532
Muldrew S. I., Pearce F. R., Power C., 2011, MNRAS, 410, 2617
Mummery B. O., McCarthy I. G., Bird S., Schaye J., 2017, MNRAS, 471, 227
Musso M., 2016, Analytical models of large-scale structure, https://wwwmpa.mpa-garching.mpg.de/~komatsu/lecturenotes/Marcello_Musso_on_LSS.pdf
Musso M., Sheth R. K., 2012, MNRAS, 423, L102
Naab T., Ostriker J. P., 2017, Annual Review of Astronomy and Astrophysics, 55, 59
Nadler E. O., Mao Y.-Y., Wechsler R. H., Garrison-Kimmel S., Wetzel A., 2018, ApJ, 859, 129
Naiman J. P., et al., 2018, MNRAS, 477, 1206
Navarro J. F., Frenk C. S., White S. D. M., 1996, ApJ, 462, 563
Navarro J. F., Frenk C. S., White S. D. M., 1997, ApJ, 490, 493
Nelson D., et al., 2015, Astronomy and Computing, 13, 12
Nelson D., et al., 2018a, arXiv e-prints, p. arXiv:1812.05609
Nelson D., et al., 2018b, MNRAS, 475, 624
Neto A. F., et al., 2007, MNRAS, 381, 1450
O'Shea B. W., Nagamine K., Springel V., Hernquist L., Norman M. L., 2005, The Astrophysical Journal Supplement Series, 160, 1
Oguri M., Takada M., 2011, Phys. Rev., D83, 023008

Okumura T., Jing Y. P., Li C., 2009, ApJ, 694, 214
Onions J., et al., 2012, MNRAS, 423, 1200
Osato K., Shirasaki M., Yoshida N., 2015, ApJ, 806, 186
Padmanabhan T., 2010, Gravitation: Foundations and Frontiers. Cambridge University Press
Paranjape A., Sheth R. K., 2012, MNRAS, 426, 2789
Paranjape A., Sheth R. K., Desjacques V., 2013, MNRAS, 431, 1503
Parkinson H., Cole S., Helly J., 2008, MNRAS, 383, 557
Pastor Mira E., Hilbert S., Hartlap J., Schneider P., 2011, A&A, 531, A169
Peacock J. A., 2003, preprint, pp astro–ph/0309240 (arXiv:astro-ph/0309240)
Peacock J. A., Heavens A. F., 1990, MNRAS, 243, 133
Peacock J. A., Smith R. E., 2000, MNRAS, 318, 1144
Peebles P. J. E., 1970, The Astronomical Journal, 75, 13
Peebles P. J. E., 1980, The large-scale structure of the universe. Princeton University Press
Peebles P. J. E., 1993, Principles of Physical Cosmology. Princeton University Press
Peirani S., et al., 2017, MNRAS, 472, 2153
Peng Y.-j., Lilly S. J., Renzini A., Carollo M., 2012, ApJ, 757, 4
Perlmutter S., et al., 1999, ApJ, 517, 565
Pillepich A., et al., 2018a, MNRAS, 473, 4077
Pillepich A., et al., 2018b, MNRAS, 475, 648
Planck Collaboration 2013, A&A, 557, A52
Planck Collaboration 2014, A&A, 571, A16
Planck Collaboration 2016a, A&A, 594, A13
Planck Collaboration 2016b, A&A, 594, A17
Planck Collaboration 2018, preprint, p. arXiv:1807.06209 (arXiv:1807.06209)
Plummer H. C., 1911, MNRAS, 71, 460
Potter D., Stadel J., Teyssier R., 2017, Computational Astrophysics and Cosmology, 4, 2
Prat J., DES Collaboration 2018, Phys. Rev. D, 98, 042005
Press W. H., Schechter P., 1974, ApJ, 187, 425
Pujol A., et al., 2017, MNRAS, 469, 749
Remus R.-S., Burkert A., Dolag K., 2017, in Gil de Paz A., Knapen J. H., Lee J. C., eds, Proceedings IAU Symposium Vol. 321, Formation and Evolution of Galaxy Outskirts. pp 84–86, doi:10.1017/S1743921316011534
Renneby M., Hilbert S., Angulo R. E., 2018, MNRAS, 479, 1100
Renneby M., et al., in prep.b, Baryonic deformations of galaxy-galaxy lensing profiles
Renneby M., Henriques B. M. B., Hilbert S., Nelson D., Vogelsberger M., Angulo R. E., Springel V., Hernquist L., in prep.a, Joint galaxy-galaxy lensing and clustering constraints on galaxy formation
Retana-Montenegro E., van Hese E., Gentile G., Baes M., Frutos-Alfaro F., 2012, A&A, 540, A70
Reyes R., Mandelbaum R., Seljak U., Baldauf T., Gunn J. E., Lombriser L., Smith R. E., 2010, Nature, 464, 256
Reyes R., Mandelbaum R., Gunn J. E., Nakajima R., Seljak U., Hirata C. M., 2012, MNRAS, 425, 2610
Riess A. G., et al., 1998, AJ, 116, 1009
Riess A. G., et al., 2016, ApJ, 826, 56
Riess A. G., et al., 2018, ApJ, 861, 126
Robotham A. S. G., et al., 2011, MNRAS, 416, 2640
Rodríguez-Puebla A., Primack J. R., Avila-Reese V., Faber S. M., 2017, MNRAS, 470, 651

Rubin V. C., Ford W. K. J., Thonnard N., 1980, ApJ, 238, 471
Rudd D. H., Zentner A. R., Kravtsov A. V., 2008, ApJ, 672, 19
Ruiz A. N., Padilla N. D., Domínguez M. J., Cora S. A., 2011, MNRAS, 418, 2422
Saghiha H., Hilbert S., Schneider P., Simon P., 2012, A&A, 547, A77
Saghiha H., Simon P., Schneider P., Hilbert S., 2017, A&A, 601, A98
Sánchez C., et al., 2017, MNRAS, 465, 746
Schaller M., et al., 2015a, MNRAS, 451, 1247
Schaller M., Dalla Vecchia C., Schaye J., Bower R. G., Theuns T., Crain R. A., Furlong M., McCarthy I. G., 2015b, MNRAS, 454, 2277
Schawinski K., et al., 2014, MNRAS, 440, 889
Schaye J., et al., 2015, MNRAS, 446, 521
Schneider P., 1985, A&A, 143, 413
Schneider P., 2003, preprint, pp astro–ph/0306465 (arXiv:astro-ph/0306465)
Schneider A., Teyssier R., 2015, Journal of Cosmology and Astro-Particle Physics, 2015, 049
Schneider P., Ehlers J., Falco E. E., 1992, Gravitational Lenses. Springer Verlag, doi:10.1007/978-3-662-03758-4
Schneider A., Teyssier R., Stadel J., Chisari N. E., Le Brun A. M. C., Amara A., Refregier A., 2018, preprint, p. arXiv:1810.08629 (arXiv:1810.08629)
Schrabback T., et al., 2015, MNRAS, 454, 1432
Schrabback T., et al., 2018, MNRAS, 474, 2635
Schramm T., Kayser R., 1995, A&A, 299, 1
Seitz C., Schneider P., 1997, A&A, 318, 687
Seitz S., Schneider P., Ehlers J., 1994, Classical and Quantum Gravity, 11, 2345
Seljak U., 2000, MNRAS, 318, 203
Seljak U., et al., 2005, Phys. Rev. D, 71, 043511
Semboloni E., Hoekstra H., Schaye J., van Daalen M. P., McCarthy I. G., 2011, MNRAS, 417, 2020
Semboloni E., Hoekstra H., Schaye J., 2013, MNRAS, 434, 148
Sereno M., Fedeli C., Moscardini L., 2016, JCAP, 1, 042
Shankar F., Weinberg D. H., Miralda-Escudé J., 2009, ApJ, 690, 20
Sheth R. K., Tormen G., 1999, MNRAS, 308, 119
Sheth R. K., Mo H. J., Tormen G., 2001, MNRAS, 323, 1
Shi X., 2016, MNRAS, 459, 3711
Shi X., 2017, Self-similar spherical collapse, https://wwwmpa.mpa-garching.mpg.de/~komatsu/lecturenotes/Xun_Shi_on_collapse.pdf
Shirasaki M., Lau E. T., Nagai D., 2018, MNRAS, 477, 2804
Sifón C., Herbonnet R., Hoekstra H., van der Burg R. F. J., Viola M., 2018, MNRAS, 478, 1244
Sijacki D., Springel V., Di Matteo T., Hernquist L., 2007, MNRAS, 380, 877
Sijacki D., Vogelsberger M., Kereš D., Springel V., Hernquist L., 2012, MNRAS, 424, 2999
Sijacki D., Vogelsberger M., Genel S., Springel V., Torrey P., Snyder G. F., Nelson D., Hernquist L., 2015, MNRAS, 452, 575
Silk J., Rees M. J., 1998, A&A, 331, L1
Simon P., Hilbert S., 2018, A&A, 613, A15
Somerville R. S., Davé R., 2015, Annual Review of Astronomy and Astrophysics, 53, 51
Somerville R. S., Primack J. R., 1999, MNRAS, 310, 1087
Spergel D. N., et al., 2003, ApJS, 148, 175
Spergel D. N., et al., 2007, ApJs, 170, 377

Spergel D., et al., 2015, preprint, p. arXiv:1503.03757 (arXiv:1503.03757)
Springel V., 2005, MNRAS, 364, 1105
Springel V., 2010a, Annual Review of Astronomy and Astrophysics, 48, 391
Springel V., 2010b, MNRAS, 401, 791
Springel V., Yoshida N., White S. D. M., 2001a, New Astronomy, 6, 79
Springel V., White S. D. M., Tormen G., Kauffmann G., 2001b, MNRAS, 328, 726
Springel V., Di Matteo T., Hernquist L., 2005a, MNRAS, 361, 776
Springel V., et al., 2005b, Nature, 435, 629
Springel V., et al., 2018, MNRAS, 475, 676
Squires G., Kaiser N., 1996, ApJ, 473, 65
Srisawat C., et al., 2013, MNRAS, 436, 150
Stone J. M., Norman M. L., 1992, The Astrophysical Journal Supplement Series, 80, 753
Suto Y., Sasaki S., Makino N., 1998, ApJ, 509, 544
Tasitsiomi A., Kravtsov A. V., Wechsler R. H., Primack J. R., 2004, ApJ, 614, 533
Tasker E. J., Brunino R., Mitchell N. L., Michielsen D., Hopton S., Pearce F. R., Bryan G. L., Theuns T., 2008, MNRAS, 390, 1267
Tassev S., Zaldarriaga M., Eisenstein D. J., 2013, JCAP, 6, 36
Tassev S., Eisenstein D. J., Wandelt B. D., Zaldarriaga M., 2015, preprint, (arXiv:1502.07751)
Taylor E. N., et al., 2011, MNRAS, 418, 1587
Teyssier R., 2002, A&A, 385, 337
Teyssier R., Moore B., Martizzi D., Dubois Y., Mayer L., 2011, MNRAS, 414, 195
The Dark Energy Survey Collaboration 2005, preprint, pp astro–ph/0510346 (arXiv:astro-ph/0510346)
The EAGLE team 2017, preprint, p. arXiv:1706.09899 (arXiv:1706.09899)
Thomas P. A., Muanwong O., Pearce F. R., Couchman H. M. P., Edge A. C., Jenkins A., Onuora L., 2001, MNRAS, 324, 450
Torrey P., Vogelsberger M., Genel S., Sijacki D., Springel V., Hernquist L., 2014, MNRAS, 438, 1985
Troxel M. A., DES Collaboration 2018, Phys. Rev. D, 98, 043528
Troxel M. A., Ishak M., 2015, Phys. Rep., 558, 1
Vale A., Ostriker J. P., 2006, MNRAS, 371, 1173
Valluri M., Debattista V. P., Quinn T., Moore B., 2010, MNRAS, 403, 525
Van Waerbeke L., et al., 2000, A&A, 358, 30
Velander M., et al., 2014, MNRAS, 437, 2111
Velliscig M., van Daalen M. P., Schaye J., McCarthy I. G., Cacciato M., Le Brun A. M. C., Dalla Vecchia C., 2014, MNRAS, 442, 2641
Velliscig M., et al., 2017, MNRAS, 471, 2856
Viola M., et al., 2015, MNRAS, 452, 3529
Vogelsberger M., Sijacki D., Kereš D., Springel V., Hernquist L., 2012, MNRAS, 425, 3024
Vogelsberger M., Genel S., Sijacki D., Torrey P., Springel V., Hernquist L., 2013, MNRAS, 436, 3031
Vogelsberger M., et al., 2014a, MNRAS, 444, 1518
Vogelsberger M., et al., 2014b, Nature, 509, 177
Wadsley J. W., Veeravalli G., Couchman H. M. P., 2008, MNRAS, 387, 427
Wang W., White S. D. M., Mandelbaum R., Henriques B., Anderson M. E., Han J., 2016, MNRAS, 456, 2301
Wang Y., et al., 2018, arXiv e-prints, p. arXiv:1811.06545
Wechsler R. H., Tinker J. L., 2018, Annual Review of Astronomy and Astrophysics, 56, 435

Weigel A. K., Schawinski K., Bruderer C., 2016, MNRAS, 459, 2150
Weinberg S., 2008, Cosmology. Oxford University Press
Weinberg D. H., Mortonson M. J., Eisenstein D. J., Hirata C., Riess A. G., et al., 2013, Phys. Rept., 530, 87
Weinberger R., et al., 2017, MNRAS, 465, 3291
Wetzel A. R., Hopkins P. F., Kim J.-h., Faucher-Giguère C.-A., Kereš D., Quataert E., 2016, ApJ, 827, L23
White M., 2014, MNRAS, 439, 3630
White S. D. M., Frenk C. S., 1991, SpJ, 379, 52
White S. D. M., Rees M. J., 1978, MNRAS, 183, 341
White S. D. M., Efstathiou G., Frenk C. S., 1993, MNRAS, 262, 1023
Wibking B. D., et al., 2018, MNRAS, p. 2206
Wilson G., Kaiser N., Luppino G. A., Cowie L. L., 2001, ApJ, 555, 572
Wittman D. M., Tyson J. A., Kirkman D., Dell'Antonio I., Bernstein G., 2000, Nature, 405, 143
Wright C. O., Brainerd T. G., 2000, ApJ, 534, 34
Wright A. H., et al., 2018, arXiv e-prints, p. arXiv:1812.06077
Yoo J., Seljak U., 2012, Phys. Rev. D., D86, 083504
Yoo J., Tinker J. L., Weinberg D. H., Zheng Z., Katz N., Davé R., 2006, ApJ, 652, 26
York D. G., et al., 2000, The Astronomical Journal, 120, 1579
Zaldarriaga M., Seljak U., 2000, The Astrophysical Journal Supplement Series, 129, 431
Zel'Dovich Y. B., 1970, A&A, 500, 13
Zentner A. R., Semboloni E., Dodelson S., Eifler T., Krause E., Hearin A. P., 2013, Phys. Rev. D, 87, 043509
Zentner A. R., Hearin A. P., van den Bosch F. C., 2014, MNRAS, 443, 3044
Zhu Q., Marinacci F., Maji M., Li Y., Springel V., Hernquist L., 2016, MNRAS, 458, 1559
Zhu Q., Hernquist L., Marinacci F., Springel V., Li Y., 2017, MNRAS, 466, 3876
Zu Y., Mandelbaum R., 2015, MNRAS, 454, 1161
Zu Y., Mandelbaum R., 2016, MNRAS, 457, 4360
Zuntz J., et al., 2018, MNRAS, 481, 1149
van Daalen M. P., Schaye J., Booth C. M., Dalla Vecchia C., 2011, MNRAS, 415, 3649
van Daalen M. P., Schaye J., McCarthy I. G., Booth C. M., Dalla Vecchia C., 2014, MNRAS, 440, 2997
van Daalen M. P., Henriques B. M. B., Angulo R. E., White S. D. M., 2016, MNRAS, 458, 934
van Uitert E., et al., 2016, MNRAS, 459, 3251
van Uitert E., et al., 2018, MNRAS, 476, 4662
van den Bosch F. C., 2017, MNRAS, 468, 885
van den Bosch F. C., Tormen G., Giocoli C., 2005, MNRAS, 359, 1029
van den Bosch F. C., More S., Cacciato M., Mo H., Yang X., 2013, MNRAS, 430, 725
van den Bosch F. C., Ogiya G., Hahn O., Burkert A., 2018, MNRAS, 474, 3043

Acknowledgements

I would like to acknowledge financial support by the DFG cluster of excellence 'Origin and Structure of the Universe' and express my gratitude to the Max Planck Institute for Astrophysics (MPA) and the Max Planck Computing and Data Facility for computational resources. Moreover, I would like to thank the MPA for office space during the completion of this work and for the opportunity to participate in its rich scientific environment, particularly in the activities organised by the large-scale structure and galaxy groups, as well as for my many fruitful and amiable discussions with my colleagues there. I would like to convey thanks to my official supervisor Prof. Dr. Andreas Burkert for administrative help, as well as Prof. Eiichiro Komatsu, PhD.

This work had not been possible without the warm and enthusiastic support of my project supervisor Dr. Stefan Hilbert. Thank you for your unwavering faith in my abilities and your encouragement for me to pursue new ideas.

I would also like to express gratitude for the help and support from my main collaborators, Prof. Raúl E. Angulo, PhD, and Bruno Henriques, PhD, without whose scientific guidance and thoughtful insights the results of this thesis would have been less profound and impactful.

In addition, I would especially like to thank the following friends and colleagues for spreading joy during my time in Munich: Dr. Haakon Andresen, Durand D'Souza, Dr. Isabella Söldner-Rembold, Dr. Jeffrey Chan, Dijana Vrbanec, Marius Berge Eide, Dr. Koki Kakiichi, Dr. Inh Jee, Dr. Titouan Lazeyras, Damien Coffey, Dr. Philipp Plewa, Dr. Vlas Sokolov, Linda Baronchelli, Dr. Christine Schulz, Dr. Graham Wagstaff, Dr. Fabian Knust, Raffaella Capasso and Dr. Steffen Hagstotz.

To continue, Chris Byrohl, my fantastic adventurous office mate, and Timo Halbesma truly made Office 014 Coffee the *place-to-be*. Thank you for making my days full of smiles.

Although we have not (*yet*) managed to open the physical door between our offices, it feels like it was never there. I would like to thank Matteo Frigo, Philipp Busch and Aoife Boyle for many great moments filled with boisterous, wholehearted laughter during this research roller-coaster ride, and for being there in the darkest hours. I will miss you dearly.

Last but not least, I would like to thank my guiding light through the PhD program, my wonderful former office mate Dr. Anabele Pardi. Thank you for keeping my spirits (and chilli levels) high during gloomy as well as marvellous times and for being an amazing friend.

Moreover, I would like to thank my friends in Sweden, Estonia and elsewhere, especially Sara, Agnes, Hannes, Nigul, Frida, Anna, Sara and Martin, and Henrik. Thank you for the moral support, for bringing me down to earth and for scintillating light throughout the years.

Finally, I would like to express my extreme gratitude for the love and support from my family. Thank you for sparking my curiosity and helping me throughout this long journey and for standing by my side during whatever challenges, opportunities and triumphs the future holds in store. I would like to close by thanking those who were with me during the start of

this academic endeavour but could not be present near its completion. You will always be with me in my heart.

In the words of my personal hero and role model: By Endurance, We Conquer. I am looking forward to the next Chapter.